

ABSTRACT

LEMAIRE, PAUL CHARLES. Atomic Layer Deposition and Controlling Film and Crystal Nucleation. (Under the direction of Gregory N. Parsons).

Typically, conformally coating fibers or high aspect ratio substrates with thin films has proven problematic. Two techniques that are well suited for overcoming these challenges include atomic layer deposition (ALD) and molecular layer deposition (MLD). ALD and MLD are vapor-phase techniques that use sequential half reactions to deposit highly conformal films with angstrom-level thickness control. By purging excess unreacted reactants, ALD and MLD are able to deposit thin films only on substrate surfaces, making them ideal for conformally coating fibers or porous substrates in order to impart new chemical functionality to substrate surfaces.

ALD has proven especially applicable for the continued development of metal organic framework (MOF) multifunctional materials. MOFs are chemically functionalized micro- and mesoporous materials with high surface areas, and are attractive for multiple applications including filtration, gas storage, and catalysis. The amount of MOF loading on fiber substrates has been increased by coating fibers with ALD in order to generate nucleation sites. In addition, ALD modification of the MOFs themselves through post-synthetic modification is a strategy to impart new properties, including improved chemical stability and selective catalytic activity.

The highly controlled ALD surface reactions also make ALD ideal for selective deposition, in which a film is only deposited in predetermined regions. Area-selective thin film deposition is expected to be important for advanced sub-10 nanometer semiconductor devices, enabling feature patterning, alignment to underlying structures and edge definition.

There are multiple strategies to achieve selective ALD, including utilizing inherent differences in the surface chemistry of different material surfaces or through periodic etching of undesired nuclei on specific surfaces.

In order to make ALD, MLD, and MOF deposition even more applicable it is important to understand the underlying nucleation mechanisms. Nucleation is defined as the initial process that occurs in the formation of a crystal from a solution, a liquid, or a vapor. A small number of ions, atoms, or molecules become arranged in a pattern characteristic of a crystalline solid, forming a site upon which additional particles are deposited as the crystal or film grows.¹ Accordingly this dissertation focuses on understanding nucleation reactions in order to increase crystal loading on substrates, limit unwanted substrate degradation, and achieve controlled selective deposition.

The first half of this dissertation focuses on the interactions between ALD and organic-inorganic materials, including MOFs. By studying CuBTC MOF nucleation mechanisms, we show that ALD oxide surfaces facilitate CuBTC nucleation by enhancing copper nitrate adsorption and through the formation of intermediary hydroxy double salts. We then analyze ALD precursor interactions with the MOF, UiO-66-NH₂. The ALD precursors react induce reversible distortion of the MOF metal clusters, reacting predominantly at the MOF surface region. We also discuss the MLD deposition of organic-inorganic porous films with swelling properties due to the formation of a quaternary ammonium salt functionality.

In the second half of this dissertation, we discuss the selective deposition and etching of thin films. We investigated the causes of metallic tungsten nucleation on SiO₂ and other “non-growth” surfaces during the WF₆/SiH₄ W-ALD process. We provide evidence that WF₆ and

SiH_4 react with vicinal hydroxyl sites on oxide surfaces, initiating undesired nucleation. Using this information, we investigated strategies to widen the “selectivity window” or increase the amount of tungsten selectively deposited on one surface versus another. We widened the W-ALD selectivity window by lowering the process temperature, diluting the ALD vapor precursors, and utilizing different carrier gases. Finally, based on observed etching during the W-ALD incubation period, we developed a thermal-driven and self-limiting TiO_2 atomic layer etching (ALE) process using WF_6 and BCl_3 .

© Copyright 2017 Paul Charles Lemaire

All Rights Reserved

Atomic Layer Deposition and Controlling Film and Crystal Nucleation

by
Paul Charles Lemaire

A dissertation submitted to the Graduate Faculty of
North Carolina State University
in partial fulfillment of the
requirements for the degree of
Doctor of Philosophy

Chemical Engineering

Raleigh, North Carolina

2017

APPROVED BY:

Dr. Gregory N. Parsons
Committee Chair

Dr. Jan Genzer

Dr. Michael D. Dickey

Dr. Saad Khan

DEDICATION

To my family, friends, research group, and adviser. They all helped me towards my doctorate degree and put up with my sense of humor.

BIOGRAPHY

Paul Lemaire was born in Morristown, NJ to Paul and Laura Lemaire, and grew up in Madison, NJ. After graduating from Madison High School, Paul went to Villanova University in Villanova, PA to study chemical engineering. While at Villanova University, he was fortunate to learn the importance and joys of service and research. Paul took part in multiple service trips to areas including Fort Smith AK, Marion SC, Antigua Guatemala, and San Salvador El Salvador. Paul also co-led a trip to Winston Salem NC. He worked with the local communities to help construct affordable homes and learned about the hardships that all too many people fall victim to and are forced to live with on a daily basis. Paul was also able to take part in undergraduate research with Professor Weinstein and Professor Skaf at Villanova and with Professor Riman at Rutgers University in New Brunswick NJ. After graduating with his bachelors from Villanova University, Paul continued his studies at North Carolina to pursue his doctorate in chemical engineering. Here he was fortunate to receive a position in Dr. Gregory Parsons' research group. In June 2017, will be driving cross country to start a position at LAM Research in Portland OR.

ACKNOWLEDGMENTS

No person is truly an island and I am no exception. There are several people to whom I am greatly indebted for the completion of this dissertation. First I must thank my parents. They have been my greatest confidants, providing an endless supply of support and insight, shaping me into the man I am today. My father helped foster my love of math, science, and just tinkering in general, whereas my mother helped keep me from becoming a cliché engineer, playing a large role in my “personality.” I also have to thank my older sisters, Caitlin, Danielle, and Sarah who helped raise me and will always be lifelong friends.

I would also be remiss if I failed to thank Professor Gregory N. Parsons and his entire research group. Professor Parsons made sure to always be available when I needed help. But possibly even more important, he let me make my own mistakes and discoveries, allowing me to develop into a true researcher. I am also extremely fortunate to work with past and present group members whose experience and knowledge was invaluable, but more importantly cultivated into true friendships. Without this support, I am confident the past five years would not have gone by so quickly.

TABLE OF CONTENTS

LIST OF TABLES	xiv
LIST OF FIGURES	xv
CHAPTER 1. INTRODUCTION	1
<i>1.1 Principles of Atomic Layer Deposition and Molecular Layer Deposition</i>	1
<i>1.1.1 Atomic Layer Deposition (ALD)</i>	1
<i>1.1.2 Atomic Layer Deposition on Polymer Substrates</i>	3
<i>1.1.3 Selective Atomic Layer Deposition (S-ALD)</i>	4
<i>1.1.4 Molecular Layer Deposition (MLD)</i>	6
<i>1.2 Chemical Vapor Etching and Atomic Layer Etching</i>	8
<i>1.2.1 Chemical Vapor Etching</i>	8
<i>1.2.2 Atomic Layer Etching (ALE)</i>	9
<i>1.3 Metal Organic Frameworks (MOFs)</i>	11
<i>1.3.1 General Metal Organic Framework Properties</i>	11
<i>1.3.2 Properties of the UiO-66 MOF and MOF Analogs</i>	12
<i>1.3.3 Properties of the CuBTC MOF</i>	13
<i>1.3.4 Investigating Nucleation and Deposition of the CuBTC MOF</i>	15
<i>1.3.4.1 Homogenous and Heterogeneous MOF Nucleation</i>	15

1.3.4.2	<i>Role of Substrate Surface Charge on CuBTC Nucleation</i>	15
1.3.4.3	<i>CuBTC Nucleation on Chemically Functionalized Surfaces</i>	17
1.3.5	<i>Post-Synthetic Modification of MOF Substrates</i>	17
CHAPTER 2. EXPERIMENTAL TOOLS		19
2.1	<i>Atomic Layer Deposition Reactor</i>	19
2.2	<i>Quartz Crystal Microbalance (QCM) Analysis</i>	20
2.3	<i>Fourier Transform Infrared Spectroscopy (FTIR) Analysis</i>	20
2.4	<i>Spectroscopic Ellipsometry (SE)</i>	22
2.5	<i>X-Ray Photoelectron Spectroscopy (XPS)</i>	23
CHAPTER 3. COPPER BENZENETRICARBOXYLATE METAL-ORGANIC FRAMEWORK NUCLEATION MECHANISMS ON METAL OXIDE POWDERS AND THIN FILMS FORMED BY ATOMIC LAYER DEPOSITION		25
3.1	<i>Abstract</i>	25
3.2	<i>Introduction</i>	26
3.3	<i>Experiment</i>	28
3.3.1	<i>MOF Precursors and Materials</i>	28
3.3.2	<i>Substrate Preparation and Growth of Crystalline Materials</i>	29
3.3.3	<i>Material Characterization</i>	33
3.4	<i>Results</i>	34

3.4.1	<i>Reaction products on ALD-coated fibers after Cu(NO₃)₂/BTC solvothermal exposure</i>	34
3.4.2	<i>Products on ALD-coated fibers exposed to BTC only under solvothermal conditions</i>	39
3.4.3	<i>Reaction products after sequential BTC + Cu(NO₃)₂ solvothermal exposure</i> .	40
3.4.4	<i>Reaction products after Cu(NO₃)₂ exposure</i>	41
3.4.5	<i>Products on ALD metal oxides after Cu(NO₃)₂ + BTC sequential exposure</i> ...	43
3.5	<i>Discussion of Results</i>	46
3.6	<i>Conclusions</i>	49
3.7	<i>Acknowledgement</i>	49
 CHAPTER 4. REACTANT-DEPENDENT SURFACE NODE DISTORTION DURING ATOMIC LAYER DEPOSITION ON UIO-66-NH₂ METAL ORGANIC FRAMEWORK		50
4.1	<i>Abstract</i>	50
4.2	<i>Introduction</i>	51
4.3	<i>Experimental</i>	55
4.3.1	<i>List of materials</i>	55
4.3.2	<i>Synthesis of UiO-66-NH₂ powder</i>	55
4.3.3	<i>Immobilization of UiO-66-NH₂ crystals on substrates</i>	56

4.3.4	<i>Reactant exposure and ALD reactor conditions</i>	56
4.4	<i>Ex-situ characterization of UiO-66-NH₂ powders</i>	57
4.5	<i>In-situ characterization of ALD processes</i>	58
4.6	<i>Results</i>	59
4.6.1	<i>As-formed UiO-66-NH₂ MOF</i>	59
4.6.2	<i>UiO-66-NH₂ Reactions with TiCl₄ and TMA</i>	62
4.6.3	<i>ALD Precursor Penetration into UiO-66-NH₂</i>	65
4.6.4	<i>Sequential ALD precursor/water exposure steps on UiO-66-NH₂</i>	67
4.6.5	<i>Interactions between ALD precursors and dehydroxylated UiO-66-NH₂</i>	70
4.6.6	<i>Ex-situ TEM characterization of ALD-modified UiO-66-NH₂</i>	72
4.7	<i>Discussion</i>	74
4.7.1	<i>Precursor Reactions on Hydroxylated and Dehydroxylated UiO-66-NH₂</i>	74
4.7.2	<i>Reversible Surface Node Distortion during ALD on UiO-66</i>	77
4.8	<i>Conclusion</i>	78
4.9	<i>Acknowledgement</i>	79
CHAPTER 5. RAPID VISIBLE COLOR CHANGE AND PHYSICAL SWELLING DURING WATER EXPOSURE IN TRIETHANOLAMINE-METALCONE FILMS FORMED BY MOLECULAR LAYER DEPOSITION		80
5.1	<i>Abstract</i>	80

5.2	<i>Introduction</i>	81
5.3	<i>Experiment</i>	82
5.3.1	<i>MLD Precursors and Materials</i>	82
5.3.2	<i>Reactor setup for triethanolamine-metalcone deposition</i>	83
5.3.3	<i>Ex-situ characterization</i>	84
5.3.4	<i>Results</i>	85
5.3.4.1	<i>Deposition of triethanolamine-metalcone films</i>	85
5.3.5	<i>Characterization of triethanolamine-metalcone films</i>	91
5.3.6	<i>Triethanolamine-metalcone film stability</i>	94
5.3.7	<i>Surface energy and physical swelling of triethanolamine-metalcone films</i>	98
5.3.8	<i>Assessing the role of HCl in film structure and physical response</i>	100
5.3.9	<i>Applying swelling properties to other solvents and gases</i>	104
5.4	<i>Discussion</i>	106
5.5	<i>Conclusion</i>	110
5.6	<i>Acknowledgements</i>	111
 CHAPTER 6. UNDERSTANDING INHERENT SUBSTRATE SELECTIVITY DURING ATOMIC LAYER DEPOSITION: EFFECT OF SURFACE PREPARATION, HYDROXYL DENSITY AND METAL OXIDE COMPOSITION ON NUCLEATION MECHANISMS DURING TUNGSTEN ALD		112

6.1	<i>Abstract</i>	112
6.2	<i>Introduction</i>	113
6.3	<i>Experimental</i>	116
6.3.1	<i>List of supplies and materials</i>	116
6.3.2	<i>Substrate surface preparation</i>	116
6.3.3	<i>W-ALD reactor design</i>	118
6.3.4	<i>ALD reaction sequence</i>	118
6.3.5	<i>Sample characterization</i>	118
6.4	<i>Results</i>	120
6.4.1	<i>Comparison of W-ALD nucleation on silicon, metal, and metal oxide substrates</i> 120	
6.4.2	<i>Role of surface hydroxyl groups in the loss of W-ALD selectivity</i>	122
6.4.3	<i>SiH₄ and WF₆ interaction with SiO₂, Al₂O₃, and TiO₂</i>	126
6.4.4	<i>Expanding the W-ALD selectivity window</i>	129
6.5	<i>Discussion</i>	131
6.5.1	<i>Surface hydroxyls as tungsten nucleation sites</i>	132
6.5.2	<i>Fluorination of oxide substrates</i>	133
6.5.3	<i>SiH₄ reactions with surface hydroxyls</i>	135
6.5.4	<i>Limiting WF₆ and SiH₄ reactions with surface hydroxyls</i>	135

6.6	<i>Conclusion</i>	136
6.7	<i>Acknowledgements</i>	137
CHAPTER 7. INFLUENCE OF TEMPERATURE AND CARRIER GAS FLOW RATE ON THE TUNGSTEN ATOMIC LAYER DEPOSITION “SELECTIVITY WINDOW”		
		138
7.1	<i>Abstract</i>	138
7.2	<i>Introduction</i>	139
7.3	<i>Experimental</i>	142
7.3.1	<i>List of supplies and materials</i>	142
7.3.2	<i>Substrate surface preparation</i>	142
7.3.3	<i>W-ALD reactor design</i>	143
7.3.4	<i>ALD reaction sequence</i>	143
7.3.5	<i>Sample characterization</i>	144
7.4	<i>Results</i>	145
7.4.1	<i>Process Temperature and Tungsten Nucleation on Si and Oxide Surfaces</i>	145
7.4.2	<i>Tungsten Nucleation versus Process Pressure/Carrier Flow Rate</i>	148
7.4.3	<i>Modulating Process Temperature/Pressure with Inert Gas Dosing</i>	150
7.5	<i>Discussion</i>	153
7.6	<i>Conclusion</i>	156

**CHAPTER 8. SELECTIVE SELF-LIMITING THERMAL ATOMIC LAYER
ETCHING OF TiO₂ USING SEQUENTIAL EXPOSURES OF WF₆ AND BCL₃..... 158**

8.1	<i>Abstract</i>	158
8.2	<i>Introduction</i>	159
8.3	<i>Experimental</i>	162
8.3.1	<i>List of supplies and materials</i>	162
8.3.2	<i>W-ALD reactor design and reaction sequence</i>	163
8.3.3	<i>Sample characterization</i>	164
8.3.4	<i>Thermodynamic modeling</i>	165
8.4	<i>Results and Discussion</i>	165
8.4.1	<i>Vapor Chemical Etching of TiO₂ using WF₆</i>	165
8.4.2	<i>Thermodynamic Modeling of Metal Oxide Etching by WF₆</i>	167
8.4.3	<i>TiO₂ Surface Characterization following Etching by WF₆</i>	169
8.4.4	<i>Effect of TiO₂ Thickness on Vapor Etch Rate</i>	173
8.4.5	<i>Schematic of the WF₆ Vapor Etch Reaction Process</i>	175
8.4.6	<i>Addition of Surface Modifiers to Increase Etching Rate</i>	176
8.4.7	<i>TiO₂ Atomic Layer Etching using WF₆/BCL₃</i>	178
8.4.8	<i>Schematic of the WF₆/BCL₃ ALE Reaction Process</i>	183
8.5	<i>Summary and Conclusions</i>	184

8.6 Acknowledgements	185
REFERENCES	186
APPENDICES	209
APPENDIX A. CO-AUTHORED PUBLICATIONS	210
A.1 <i>Highly Adsorptive, MOF-Functionalized Nonwoven Fiber Mats for Hazardous Gas Capture Enabled by Atomic Layer Deposition</i>	210
A.2 <i>Conformal and Highly Adsorptive Metal–organic Framework Thin Films via Layer-by-Layer Growth on ALD-Coated Fiber Mats</i>	211
A.3 <i>Platinum-Free Cathode for Dye-Sensitized Solar Cells Using Poly(3,4-ethylenedioxythiophene) (PEDOT) Formed via Oxidative Molecular Layer Deposition</i>	212
A.4 <i>Wafer-Scale Selective-Area Deposition of Nanoscale Metal Oxide Features Using Vapor Saturation into Patterned Poly(methyl methacrylate) Templates</i>	213
A.5 <i>Facile Conversion of Hydroxy Double Salts to Metal-Organic Frameworks Using Metal Oxide Particles and Atomic Layer Deposition Thin Film Templates</i>	214
A.6 <i>Using Hydrogen to Expand the Inherent Substrate Selectivity Window During Tungsten Atomic Layer Deposition</i>	215

LIST OF TABLES

Table 3.1: List of Cu-BTC solvothermal precursors, intermediate species, and products	29
Table 4.1. Reported vapor-phase deposition of materials on MOF substrates	54
Table 5.1. Experimental film composition (± 2 at. %) based on high resolution XPS scans of ~300 nm Ti-TEA films deposited at 150°C. Expected atomic composition based on the stoichiometric composition: $\text{Ti}_3(\text{C}_6\text{H}_{12}\text{NO}_3)_4$	93
Table 5.2. Experimental film composition (± 2 at. %) based on high resolution XPS scans of ~300 nm Al-TEA films deposited at 150°C. Expected atomic composition based on the stoichiometric composition: $\text{Al}(\text{C}_6\text{H}_{12}\text{NO}_3)$	93
Table 5.3: Film composition (± 2 at. %) based on high resolution XPS scans of Al-TEA-HCl films deposited at 150°C. Expected Al-TEA-HCl film composition based on the stoichiometric composition: $\text{Al}(\text{C}_6\text{H}_{12}\text{NO}_3)(\text{Cl})$, assuming one chloride anion per protonated nitrogen.	102

LIST OF FIGURES

Figure 1.1: Schematic representation of the Al ₂ O ₃ ALD reaction sequence.	1
Figure 1.2: Schematic representation of the metallic tungsten ALD reaction sequence.	3
Figure 1.3: Reaction sequence for an alucone film deposited with a) TMA and b) ethylene glycol.....	7
Figure 1.4: General reaction scheme for a thermally-driven ALE process, in which unlike the energy-enhanced, surface volatilization depends on a ligand exchange reaction.....	10
Figure 1.6: CuBTC structure in which the green and pink spheres denote the primary and secondary MOF pores respectively.....	14
Figure 2.1: Schematic view of viscous flow reactor for ALD, fitted with an in-situ quartz crystal microbalance (QCM) probe.	19
Figure 2.2 Configuration for in-situ FTIR analysis of ALD processes	22
Figure 3.1. Schematic of the standard and sequential solvothermal Cu-BTC synthesis. The fiber mat substrates coated with ALD metal oxides are added to the mixed solution where they wet and settle on the bottom of the PTFE-container. After full reaction at 120°C, the fiber mats are rinsed and dried.....	31
Figure 3.2: Cu-BTC nucleation on PP/ALD with (a) images (b) XRD after exposure to Cu-BTC solvothermal solution at room temperature for ~30 s and (c) percent Cu-BTC mass loading on PP/ALD plotted versus reaction time at 120°C. The PP/ZnO samples show a rapid Cu-BTC nucleation as shown by XRD and accompanied by a rapid color change from white to blue and an early initial mass loading.....	36
Figure 3.3: Zeta-potential as a function of pH for PP and PP/ALD samples	37

Figure 3.4: XRD of powders generated by oxide facilitated synthesis showing rapid Cu-BTC deposition on ZnO, CdO, and MgO powders, and little growth on Cu₂O, NiO, TiO₂, and Al₂O₃. 38

Figure 3.5: (a) XRD of PP/ALD samples after 20 h in BTC solution, showing patterns consistent with Zn-BTC and Al-BTC MOFs. (b) Percent Cu-BTC mass loading as a function of reaction time using PP/Al₂O₃ and PP/Al-BTC substrates. The relatively slow MOF growth on Al-BTC indicates that this compound is not an important intermediate in the growth of Cu-BTC on Al₂O₃. 40

Figure 3.6: (a) FTIR of O-NO₂ stretching band for samples after exposure to Cu(NO₃)₂ solution for 1 h at 120°C. The narrower band splitting for the symmetric and asymmetric O-NO₂ stretching band suggests formation of a monodentate hydroxyl double salt (HDS) on PP/ZnO and predominantly bidentate Cu(NO₃)₂ on PP and PP/Al₂O₃ as shown in the structure diagrams. (b) XRD analysis of PP/ALD samples after 16 hours in Cu(NO₃)₂ solution. The reflections corresponding to a HDS are visible on each substrate, with the most intense signal on the ZnO surface. 42

Figure 3.7: XRD spectra of PP/ALD samples after 16 h in Cu(NO₃)₂ solution followed by 0.5 h in BTC solution. Reflections from Cu-BTC are seen on the PP/ZnO sample, indicating that the HDS produced during the Cu(NO₃)₂ exposure (shown in Figure 3.4) converts rapidly to Cu-BTC on this surface. Reflections from Cu-BTC are not observed on the PP/TiO₂ or PP/Al₂O₃ substrates. 44

Figure 3.8: FTIR spectra of (a) (Cu,Cu)-HDS and (b) (Cu,Zn)-HDS powders prior to and following exposure to a BTC solution at room temperature for 5 minutes. The relative change

in C=O, C=C, and =C-H bands suggest BTC is incorporated into the (Cu,Zn)-HDS and not the (Cu,Cu)-HDS. A reference Cu-BTC spectrum is included..... 45

Figure 3.9: FTIR spectra of powders generated by ZnO facilitated Cu-BTC deposition using different copper precursors. The results suggest that Cu-BTC was formed for each of the copper precursors except copper acetate (Cu(OAc)₂)..... 46

Figure 4.1: SEM image and XRD patterns of as-formed UiO-66-NH₂ powder. The UiO-66-NH₂ XRD pattern is compared to a UiO-66 pattern simulated from CCDC 837796. 59

Figure 4.2: a) FTIR spectra of UiO-66-NH₂ at 150 (black) and 250°C (red) and differential spectra (blue) and b) an expanded view from 2000-600 cm⁻¹, showing loss of the hydroxyl bands (OH) and loss of the carboxylate bands (COO⁻) with elevated heating. Panel c) shows molecular structure of the hydroxylated (Zr₆O₄(OH)₄) and dehydroxylated (Zr₆O₆) metal clusters, including 4 carboxylate groups out of the expected 12 aminoterephthalic acid linkers. Potential reaction sites for the ALD precursors include: 1) hydroxide groups, 2) bridging oxygens, and 3) coordinated oxygen on the carboxylate groups. 62

Figure 4.3: Differential FTIR spectra of hydroxylated UiO-66-NH₂ powders exposed to repeated exposures of a) TiCl₄ and b) H₂O at 150°C. The H₂O exposure in b) follows a TiCl₄ exposure equivalent to the first exposure in a). The starting UiO-66-NH₂ spectrum at 1/20th scale collected before any exposure is included in each panel as reference. 63

Figure 4.4: QCM analysis of a) repeated TiCl₄ /repeated H₂O and b) similar repeated doses of TMA and H₂O on hydroxylated UiO-66-NH₂ at 150°C..... 65

Figure 4.5: FTIR spectra of hydroxy stretching band of UiO-66-NH₂ prior to and following a) 10 TiCl₄ exposures and b) 3 TMA exposures, both at 150°C. 67

Figure 4.6: Differential FTIR spectra of sequential exposures of a) $\text{TiCl}_4/\text{H}_2\text{O}$ and b) $\text{TMA}/\text{H}_2\text{O}$ on hydroxylated UiO-66-NH_2 at 150°C . The initial UiO-66-NH_2 spectrum is included as reference at $1/20^{\text{th}}$ scale. 68

Figure 4.7: QCM analysis of sequential exposures of a) $\text{TMA}/\text{H}_2\text{O}$ and b) $\text{TiCl}_4/\text{H}_2\text{O}$ on hydroxylated UiO-66-NH_2 at 150°C . Panels c), e) and d), f) show expanded views of a) and b) respectively. 70

Figure 4.8: Differential FTIR spectra of dehydroxylated UiO-66-NH_2 at 250°C following sequential exposures to a) $\text{TiCl}_4\text{-H}_2\text{O}$ and b) $\text{TMA-H}_2\text{O}$. The initial UiO-66-NH_2 spectrum is included as reference at $1/20^{\text{th}}$ scale. 71

Figure 4.9: QCM analysis of sequential exposures of a) $\text{TiCl}_4\text{-H}_2\text{O}$ on hydroxylated UiO-66-NH_2 at 150 and on dehydroxylated UiO-66-NH_2 at 250°C , with b) showing an expanded view during cycles 5 and 6. The data at 150°C is reproduced from Figure 5.7..... 72

Figure 4.10: TEM images and corresponding diagrams of UiO-66-NH_2 with a) and c) 100 cycles of $\text{TMA}/\text{H}_2\text{O}$ and b) and d) 200 cycles of $\text{TiCl}_4/\text{H}_2\text{O}$, both deposited at 150°C . The resulting TiO_2 and Al_2O_3 films were 20 and ~ 7.5 nm thick respectively, with TiO_2 -modified UiO-66-NH_2 exhibiting an interfacial layer..... 73

Figure 4.11: Differential FTIR spectra comparing dehydroxylation of UiO-66-NH_2 . The spectra of the samples after annealing is shown at $1/5^{\text{th}}$ its actual scale. The initial UiO-66-NH_2 spectrum is included as reference at $1/20^{\text{th}}$ scale. 77

Figure 5.1: Al-TEA reaction sequence with successive a) TMA and b) TEA exposure 86

Figure 5.2. Al-TEA film thickness per cycle at 150°C as a function of a) TMA and b) TEA dose time and c) film thickness versus cycle number. Lines are meant to guide eyes. 87

Figure 5.3: Ti-TEA film thickness per cycle at 150°C as a function of a) TiCl₄ and b) TEA dose time and c) film thickness versus cycle number. Lines are meant to guide eyes. 88

Figure 5.4: Growth rate versus reactor temperature for a) Al-TEA and b) Ti-TEA. Lines are meant to guide eyes..... 89

Figure 5.5: Quartz crystal microbalance (QCM) analysis: a) Al-TEA at 150°C, b) Ti-TEA at 150°C, c) Al-TEA at 200°C, d) Ti-TEA at 200°C..... 90

Figure 5.6: Mid-range FTIR spectra for ~300 nm Al-TEA and Ti-TEA films deposited at 150°C. 92

Figure 5.7: High resolution XPS scans of Cl 2p and N 1s peaks for the ~300 nm Al-TEA and Ti-TEA films deposited at 150°C. 94

Figure 5.8: Changes in triethanolamine-metalcone film b) thickness and b) refractive index at a wavelength of 632.8 nm over time in open laboratory conditions. Lines are meant to guide eyes. 96

Figure 5.9: QCM results of 100 cycles of a) Ti-TEA and b) Al-TEA films deposited at 150°C which then remain in the heated conditions with flowing carrier gas for ~14 hours..... 97

Figure 5.10: Time-resolved goniometric analysis monitoring the water droplet contact angle versus time on ~300 nm Al-TEA and Ti-TEA films deposited at 150°C. 98

Figure 5.11: Thickness of Al-TEA and Ti-TEA films versus relative humidity..... 99

Figure 5.12: Images of a 500 cyc Ti-TEA film in which the process humidity increases from a) < 1% relative humidity, to e) ~65% relative humidity. 100

Figure 5.13: QCM analysis Al-TEA-HCl MLD process at 150°C..... 101

Figure 5.14: FTIR spectra for the Al-TEA-HCl and Al-TEA films deposited at 150°C..... 101

Figure 5.15: High resolution XPS scans of Cl 2p and N 1s peaks for the Al-TEA-HCl and Al-TEA films deposited at 150°C..... 103

Figure 5.16: Thickness of Al-TEA and Al-TEA-HCl films versus relative humidity..... 104

Figure 5.17: QCM analysis of a) methanol and b) ammonia loading on ~300 nm Ti-TEA film..... 105

Figure 5.18. Ti-TEA reaction sequence with successive a) $TiCl_4$ and b) TEA exposure, showing byproduct HCl protonating the TEA nitrogen..... 108

Figure 6.1: Results of W-ALD on Si, Au, and SiO_2 surfaces from a) in-situ QCM analysis and b) XPS analysis of W 4f peaks after 30 W ALD cycles. 121

Figure 6.2: In-situ QCM analysis of a) W-ALD on ZnO, Al_2O_3 , SiO_2 , and TiO_2 surfaces and b) an enlarged view of W-ALD on TiO_2 , which shows film etching during the nucleation period. 122

Figure 6.3: In-situ FTIR of thermal SiO_2 on PS following piranha clean, measured at 100, 200 and 300°C, showing loss of surface bound water, with some surface bound water remaining after 300°C..... 123

Figure 6.4: a) Ex-situ FTIR of thermal SiO_2 on PS at room temperature before and after piranha clean, and the resulting difference spectrum, showing removal of isolated hydroxyls and an increase in the concentration of germinal hydroxyls and adsorbed water. b) SE delta parameter at 700 nm for piranha-cleaned and as-is SiO_2 wafers. 124

Figure 6.5: Impact of ex-situ annealing samples at 600 and 800°C prior to W-ALD: a) Ex-situ FTIR spectra of thermal SiO_2 on PS and difference spectra of the hydroxylated thermal

SiO₂ after 600 and 800°C anneal. Difference spectra referenced to SiO₂+Piranha spectra, b) SE delta parameter at 700 nm for SiO₂ samples following W-ALD at 220°C..... 125

Figure 6.6: SE delta parameter at 700 nm for SiO₂ samples after 30 W ALD cycles following x SiH₄ pre-exposure cycles. The delta data from the piranha-cleaned SiO₂ in Figure 4 is repeated for clarity. 127

Figure 6.7: XPS spectra of TiO₂ and Al₂O₃ ALD films exposed to 0 (black), 10 (red), and 50 (blue) SiH₄ exposures. With increasing number of SiH₄ exposures, the Si 2p peak increases on both the TiO₂ and Al₂O₃ surfaces. 128

Figure 6.8: In-situ QCM analysis comparing W-ALD on a) TiO₂ and b) Al₂O₃ for the as-is oxide (red), oxide with 50 SiH₄ pre-exposures (black), and oxide with 50 WF₆ pre-exposures (blue). 129

Figure 6.9: Ex-situ XPS W 4f high resolution scans for Si and SiO₂ samples following: a) 50 W-ALD cycles at 160°C, b) 30 W-ALD cycles at 220°C, and c) 20 W-ALD cycles at 300°C. d) Ratio of W 4f Area on Si versus SiO₂ at different reactor temperatures..... 131

Figure 7.1: SE delta parameter at 700 nm versus deposition temperature for SiO₂ and Si samples following 50 W-ALD cycles. 146

Figure 7.2. Ex-situ XPS high resolution scans of the a) W 4f and b) F 1s regions for SiO₂ samples after 20, 30, and 50 W-ALD cycles at 300, 220, and 160°C respectively. The number of W-ALD cycles for each temperature was chosen based on when the delta parameter, Δ, decreased to ~30°, indicative of tungsten nucleation as described above..... 147

Figure 7.3: In-situ QCM analysis of W-ALD nucleation on TiO₂ surfaces at different process temperatures. 148

Figure 7.4: a) Operating pressure versus Ar carrier flow rate b) SE delta parameter at 700 nm versus flow rate for SiO₂ (black) and Si (blue) substrates after 40 W-ALD cycles at 220°C. 149

Figure 7.5: In-situ QCM analysis of W-ALD nucleation on TiO₂ surfaces with an Ar carrier gas flow rate of 105 (black), 210 (red), and 900 (blue) sccm at 220°C..... 150

Figure 7.6: QCM analysis steady state W-ALD at 220°C with a reactor volume of 4700 cm³, where a) He and b) H₂ are dosed immediately before the WF₆ for 5 s. During the He and H₂ dosing, there is an observed decrease in the QCM loading, consistent with sample heating. 152

Figure 7.7: QCM analysis of W-ALD in smaller reactor volume (~750 cm³) where H₂ was dosed for 5 s a) immediately before and b) 45 s before the WF₆ dosing. In the smaller reactor volume, the decrease in the QCM signal during the H₂ dosing due to sample heating is more pronounced, but returns to the initial mass loading during a sufficiently long Ar purge step. 152

Figure 7.8: Ex-situ high resolution XPS scans of the a) W 4f and b) Si 2p regions for SiO₂ samples following 40 W-ALD cycles at 220°C. Three reaction sequences were used: SiH₄/Ar/WF₆/Ar (red), SiH₄/Ar/CH₄/WF₆/Ar (blue), and SiH₄/Ar/He/WF₆/Ar (black). Samples in which CH₄ and He were dosed immediately prior to the WF₆ exhibit lower tungsten concentration and a more pronounced Si signal from the underlying SiO₂ wafer. 153

Figure 8.1: QCM analysis of a) 200 cycles of Al₂O₃ or TiO₂ followed immediately by 50 WF₆/Ar exposures of 1/60 s each; and b) 100 TiO₂ ALD cycles followed by 1 WF₆ exposure of 50 s..... 166

Figure 8.2: Equilibrium concentrations of species from 25 to 400°C for a system initially containing a) 1 mole WF_6 and 1 mole TiO_2 and b) 1 mole WF_6 and 0.667 mole Al_2O_3 168

Figure 8.3: a) QCM analysis TiO_2 ALD followed by 50 WF_6 doses at 120 and 220°C and b) an enlarged view of the mass loading during the WF_6 doses, showing net mass loss during each WF_6 step at 220°C and little to no change at 120°C..... 169

Figure 8.4: High resolution XPS scans of a) Ti 2p, b) Si 2p, c) W 4f, and d) F 1s regions for ~6.5 nm TiO_2 films exposed to 0, 1, 5 and 15 WF_6 doses at 220°C..... 171

Figure 8.5: Peak intensity of high resolution XPS scans of a) Ti 2p (459.1 eV) and Si 2p (99.3 eV) and b) W 4f and (38 eV) and F 1s (685.2 eV) for 5.5 nm TiO_2 films exposed to 0, 10, 25, 50, 100 WF_6 doses at 220°C. Lines are meant to guide eyes. 172

Figure 8.6: a) Thickness and b) refractive index at 632.8 nm of samples with 5.5 nm TiO_2 followed by 0, 15, 25, 50, and 100 WF_6 doses at 220°C, measured with spectroscopic ellipsometry. Lines are meant to guide eyes. 173

Figure 8.7: QCM analysis of WF_6 etching following 50, 100, and 200 TiO_2 ALD cycles on a bare Au QCM crystal at 220°C and 1.75 Torr. 174

Figure 8.8: Proposed etching mechanism for TiO_2 films exposed to WF_6 at 220°C: 1) WF_6 adsorbs on thick TiO_2 surface, forming surface-bound TiO_vF_z and WO_xF_y . 2) Additional WF_6 exposure further fluorinates the TiO_vF_z and WO_xF_y , creating volatile WF_2O_2 and TiF_4 , etching the TiO_2 film. 175

Figure 8.9: High resolution XPS scans of a) Ti 2p, b) F 1s, c) W 4f, and d) Sn 3d regions for 6.5 nm TiO_2 films following 0, 15, 25 $\text{WF}_6/\text{Ar}/\text{Sn}(\text{acac})_2/\text{Ar}$ cycles at 220°C and 1.75 Torr. 177

Figure 8.10: a) QCM analysis at 170°C and 1.75 Torr of TiO₂ ALD followed by 25 BCl₃/Ar doses (pink), 50 WF₆/Ar doses (red), 50 WF₆/Ar/Sn(acac)₂/Ar cycles (black), or 50 WF₆/Ar/BCl₃/Ar cycles (blue). b) Expanded view of the WF₆/Ar/BCl₃/Ar etch sequence.. 179

Figure 8.11: a) Thickness and b) refractive index of 7 nm TiO₂ versus WF₆/BCl₃ ALE cycle number as measured by spectroscopic ellipsometry. The TiO₂ ALD and ALE were performed at 170°C with an ALE dosing sequence of WF₆/Ar/BCl₃/Ar (1/60/2.5/60 s). Lines are meant to guide eyes. 180

Figure 8.12: High resolution XPS scans of a) W 4f and b) F 1s regions for 7 nm TiO₂ film (black), 7 nm TiO₂ following 50 WF₆/BCl₃ cycles at 170°C (red), and 5.5 nm TiO₂ following 50 WF₆ doses at 220°C (blue)..... 181

Figure 8.13: QCM analysis of a) WF₆/Ar/BCl₃/Ar sequence at 110, 130, 150, 170 and 190°C and b) 10 WF₆/Ar followed by 10 BCl₃/Ar (repeated 3 times), at 110, 130, 150, and 170°C. 182

Figure 8.14: Proposed etch mechanism for the TiO₂ ALE process using WF₆ and BCl₃ at 170°C: 1) WF₆ adsorbs on thick TiO₂ surface, forming surface-bound TiO_vF_z and WO_xF_y. 2) BCl₃ volatilizes the surface metal oxy fluoride species, forming TiCl₄, WCl₂O₂ and BF₃.. 184

CHAPTER 1. INTRODUCTION

1.1 Principles of Atomic Layer Deposition and Molecular Layer Deposition

1.1.1 Atomic Layer Deposition (ALD)

Atomic layer deposition (ALD) is a vapor-phase technique to deposit nano-scale coatings on substrates while maintaining thickness control and conformality.² ALD coatings can be thin enough that there are no obvious changes to visual characteristics, feel, and flexibility.³ It consists of two sequential self-limiting reactions as shown in Figure 1.1.⁴ In a typical reaction sequence, a substrate is first exposed to one of the reactants, which selectively reacts with the surface. The unconverted reactant is purged from the system by carrier gas. Without sufficient purge times, unremoved precursors can react by chemical vapor deposition (CVD), causing thicker and less uniform coatings.⁵ The system is then dosed with the second reactant which reacts with the first and restores the original surface functionality. This cycle is repeated to add additional layers.

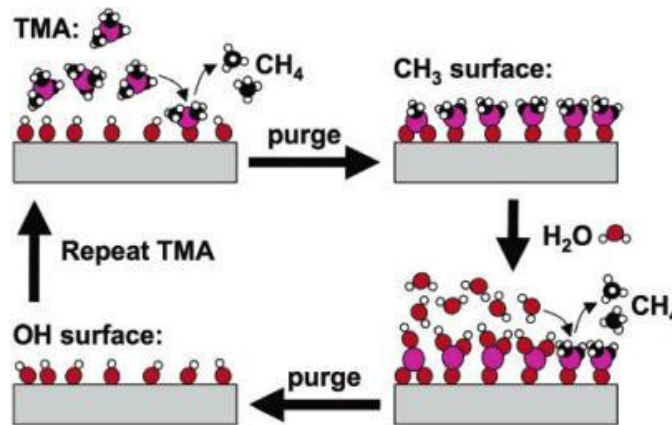
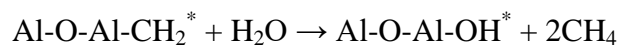
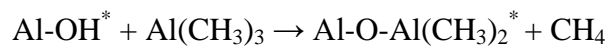


Figure 1.1: Schematic representation of the Al₂O₃ ALD reaction sequence.

Figure 1.1 shows the model reaction for atomic layer deposition, Al₂O₃ ALD. Al₂O₃ is deposited through the sequential exposure of trimethylaluminum (TMA) and water, in which the surface undergoes the chemistry shown in the reactions below, with asterisks denoting surface species.⁵ The Al₂O₃ and similar oxide ALD processes consist of Lewis acid-base reactions. These reactions are ligand exchanges and not oxidative or reductive reactions.



The net Al₂O₃ ALD reaction sequence is highly exothermic. The reactions are spontaneous even at low temperatures, without undesired reactant decomposition, desorption, or condensation.^{2,5} TiO₂ and ZnO ALD sequences can also be accomplished at low temperature.⁵ For an ALD process, there is typically a temperature range in which the growth per ALD cycle is not largely dependent on the temperature. This is referred to as the “temperature window.” Outside this window, deposition becomes temperature dependent, in which the growth rate per cycle can increase or decrease due to incomplete surface reaction, desorption of surface sites, precursor condensation, or precursor decomposition.⁵ A broad temperature window is especially significant for temperature sensitive substrates like polypropylene which can have a melting point as low as 135 °C.⁶

In addition to oxides; metals, carbides, nitrides, and sulfides can also be deposited through ALD.^{5,7} Unlike the Al₂O₃ ALD process, depositing metal films via ALD requires reduction reactions. A lack of viable reducing agents limits the number of metals that can be deposited

via ALD because most metals have a relatively large positive reduction potential.^{8,9} Metallic tungsten can be deposited at relatively low temperatures (as low as $\sim 150^\circ\text{C}$) using tungsten hexafluoride (WF_6) and a reducing agent such as monosilane (SiH_4)¹⁰⁻¹³ or disilane (Si_2H_6).¹⁴⁻¹⁷ Figure 1.2 shows the proposed reaction mechanism for the deposition on Si-H_x and SiO_2 surfaces.¹⁸ During normal steady state growth, WF_6 adsorbs and reacts on a metal surface. SiH_4 then removes fluorine from the adsorbed WF_x species and reduces the tungsten to W^0 . SiH_4 adsorbs on the reduced tungsten surface, creating a reducing layer.^{11,13,15,16} Analogous to Al_2O_3 ALD, these two steps can then be repeated to increase the film thickness.

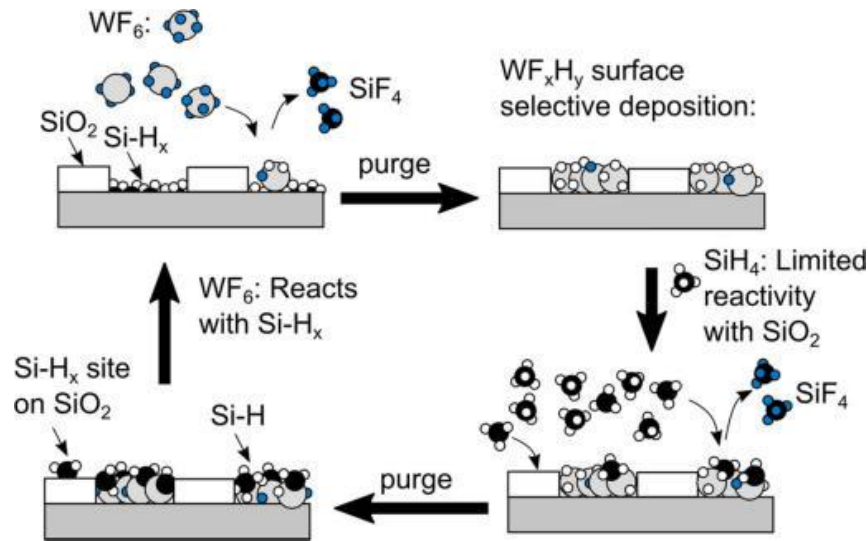


Figure 1.2: Schematic representation of the metallic tungsten ALD reaction sequence.

1.1.2 Atomic Layer Deposition on Polymer Substrates

One can utilize Al_2O_3 ALD to deposit Al_2O_3 films on nearly every substrate including polymers.¹⁹ Al_2O_3 ALD introduces additional hydroxyl groups, typically making substrates more hydrophilic. ALD coating can make fibers more rigid, imparting hydrophobicity

because of reduced contact area between the water droplet and the fibers.³ Typically, ALD will have better results when a substrate surface already has hydroxyl groups to help initiate nucleation.¹⁹ For example, ALD of thin films on cotton or nylon fibers are highly conformal, with TEM showing an abrupt interface between the fiber and film because these polymers have a high concentration of surface active sites.²⁰⁻²² In contrast, non-hydroxylated surfaces can inhibit nucleation or yield incomplete nucleation focused on substrate defect areas.⁵ Al₂O₃ deposition on polypropylene occurs when TMA diffuses into the polymer subsurface.^{20,23} Sub-surface diffusion causes retention of excess precursors even upon purging. This leads to Al₂O₃ film nucleation and non-ideal CVD growth that increases the film thickness by introducing impurities.³

1.1.3 Selective Atomic Layer Deposition (S-ALD)

As companies begin work producing integrated circuits with less than 10 nm feature sizes, standard patterning techniques, such as lithography, become much less applicable because of challenges maintaining edge definition and alignment to the underlying features. One solution to this problem is to limit the number of patterning steps and instead selectively deposit the desired material, such as a metal or dielectric. There are multiple strategies for selective atomic layer deposition (S-ALD). The simplest strategy is inherent selectivity, which takes advantage of the different surface chemistries of a patterned substrate. For example, the tungsten ALD schematic shown in Figure 1.2 shows that the precursors will selectively react with a Si-H or metal surface over an oxide surface. The Si-H or a metal surface reduces the WF₆ to W⁰ leading to film deposition. In contrast, the stability of an oxide

surface leads to a high energy barrier for precursor adsorption and accordingly tungsten nucleation.²⁴⁻²⁶ Using less reactive precursors can create an even larger barrier for deposition on “non-growth” surface. For example, using an alcohol instead of water as an oxygen source improved the selectivity of ZrO₂ ALD on patterned substrates.²⁷ Yet despite the theoretically high thermodynamic barriers, deposition eventually occurs on the non-growth surface, typically due to the presence of defects.

Another common strategy is to passivate or block one of the surfaces on a patterned substrate and selectively deposit on the “unblocked” surface with ALD. These blocking layers are typically photoresists or self-assembled monolayers (SAMs).²⁸⁻³⁵ For example, the SAM octadecylphosphonic acid was used to selectively passivate copper surfaces over SiO₂ surfaces.³⁶ For a SAM layer to be an effective blocking layer, it is crucial to form densely packed, highly hydrophobic monolayers.²⁸ Yet regardless of the quality of the SAM film, deposition eventually occurs on the passivated surface, with nucleation occurring due to defect sites or as a result of non-planar substrates.³¹ One solution is to intermittently remove and regenerate the passivating SAM layer with an in-situ vapor-phase process.³⁷

Competitive adsorption of gaseous species can be utilized to generate a more selective S-ALD process. Instead of using a solid mask or SAM layer, ALD deposition is inhibited on non-growth surfaces by blocking precursor adsorption by simultaneously dosing a volatile reagent that will preferentially adsorb on the non-growth surface. For example, a ZrO₂ ALD process using tetrakis(dimethylamido)zirconium(IV) and water preferentially deposits ZrO₂ on an oxide surface over a metal surface, but selectivity is quickly lost. But by dosing

trimethylamine (TEA) simultaneously with the two reactants, the TEA will adsorb on the copper surface, preventing the ZrO_2 precursors from reacting on the non-growth surface.³⁸ The shortcoming of this process is that deposition on the growth surface is often also depressed.

Finally, the overall selectivity of an S-ALD process can be increased by utilizing a selective etching process. An initial etch step can remove active sites on the non-growth surface to passivate it from undesired deposition. For example, ethanol vapor can etch the native oxide layer on copper, removing hydroxyl sites that could react with the ALD precursors.^{27,39} In addition, an etch-back step can be used periodically during a deposition. The etch step ideally removes or getters the nuclei on the non-growth surface with minimal etching of the film deposited on the desired growth surface.⁴⁰

1.1.4 Molecular Layer Deposition (MLD)

Molecular layer deposition (MLD) is a deposition process analogous to ALD, but instead of depositing inorganic films such as an oxide or metal, MLD deposits purely organic or organic-inorganic films. For example, purely organic nylon-66 films have been deposited with adipoyl chloride and 1,6-hexanediamine.⁴¹ Another technique to generate organic films is through oxidative molecular layer deposition (oMLD), in which a monomer precursor is polymerized with an oxidant, generating a polymer film such as poly(3,4-ethylenedioxythiophene) (PEDOT).^{42,43}

Deposition of organic-inorganic films referred to as “metalcones” involves self-limiting half-reactions between organic and organometallic (or metal-halide) reactants. The metal precursors are typically metal precursors used in metal oxide ALD (e.g. TMA). These MLD include alucone,^{44,45} zincone,^{46,47} titanicone,⁴⁸ and others.^{49,50} Figure 1.3 shows a proposed reaction sequence for an alucone film deposited with the precursors TMA and ethylene glycol.^{5,44} Most film reaction studies to date have focused on metal precursors reacting with ethylene glycol,^{44-46,48-50} glycerol,^{48,51} glycidol,⁵² and various carboxylic acids,⁵³⁻⁵⁵ generally leading to polymeric O-M-O-(CH_x)_y-O-M-O repeat units as determined by spectroscopic and other analyses. Metalcone films have multiple possible applications including flexible electronics,⁴⁷ sacrificial films to form conductive carbon-rich⁵⁶ or porous oxide films,^{57,58} encapsulation and protective layers on chemically reactive fibers, and antireflective coatings.⁴⁴

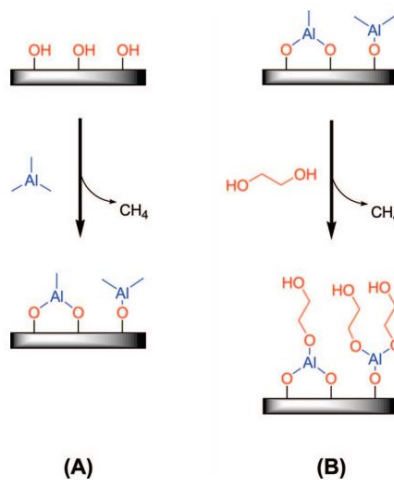


Figure 1.3: Reaction sequence for an alucone film deposited with a) TMA and b) ethylene glycol.

1.2 Chemical Vapor Etching and Atomic Layer Etching

1.2.1 Chemical Vapor Etching

The semiconductor industry is looking towards controllable etching techniques to supplement currently used thin film deposition techniques in order to design and manufacture smaller and more complicated transistor nodes. For example vapor phase etching of native oxide on silicon (Si) is an etching process of interest to the semiconductor industry. Hydrogen fluoride (HF) liquid etching of Si native oxide⁵⁹⁻⁶¹ is ubiquitously utilized in the semiconductor industry, but in-situ vapor etching helps limit the reformation of an interfacial oxide layer between Si and a deposited film.^{10,62-66} For both solution and vapor phase etching, H₂O plays a significant role in HF etching of the native oxide, with significantly lower etch rates in anhydrous conditions.⁶⁷⁻⁷⁰ In vapor phase etching, water creates a interfacial layer between the substrate and gas and acts as a proton donor and acceptor to catalytically activate the HF etch.^{60,68,69} Although HF is a promising etchant, the high HF concentrations can lead to uncontrolled etching.

1,1,1,5,5,5-Hexafluoroacetone (hHfac) is another acid that can dry etch oxides. Like HF, hHfac can break metal –oxygen bonds, forming volatile metal complexes. For example, hHfac⁷¹ and a hHfac and O₃/H₂O₂^{72,73} processes were used to etch ZnO and copper respectively. The etch products, Zn(hfac)₂ and Cu(hfac)₂ volatilize at temperatures as low as 150°C, enabling low temperature etching.⁷¹⁻⁷³ Issues arise for these etching techniques at higher temperatures, where above 200°C there is increased chemical degradation, leading to carbon and fluorine contamination in the films.⁷¹⁻⁷³

Steady-state plasma etching is a more common way to continuously dry etch a broader range of materials. By using high-energy species in techniques such as reactive ion etching (RIE), magnetron reactive ion etching, electron cyclotron resonance etching, ion beam etching, and plasma etching, it is possible to volatilize a much larger range of species than by chemical etching alone at relatively high etch rates.⁷⁴ For example, RIE uses a partially ionized plasma glow discharge that generates reactive and non-reactive ions, electrons, photons, and multiple other species.⁷⁵ By biasing the substrate it is possible to achieve directional or anisotropic etching, which is advantageous for creating trenches and other patterns.⁷⁵ Yet these highly reactive species are prone to recombination and transport limited phenomena, making them less applicable for high-aspect ratio substrates.^{75,76} In addition, the reactive species can damage sensitive structure features, due to roughening or contamination, which is a major concern for the semiconductor industry.⁷⁴

1.2.2 Atomic Layer Etching (ALE)

Atomic layer etching (ALE) is an etching technique based on the principles of ALD. ALE consist of a sequence of self-limiting surface reactions, but instead of depositing a film, ALE instead removes a layer of the substrate with each cycle.⁷⁷ A typical ALE consists of two half reactions: an adsorption and activation step. In the adsorption step, the precursor modifies the substrate surface in a manner that reduces the activation energy required to remove that layer.⁷⁸ For example, Si substrate is exposed to chlorine gas to form a SiCl_x layer and an oxide is typically chlorinated or fluorinated with BCl_3 ^{75,79} or HF respectively.⁸⁰⁻⁸³ The adsorption step ideally modifies only the surface layer, passivating the substrate from further

modification. The modified layer is then removed via volatilization through an activation step. The activation step can consist of a thermally-driven ligand exchange⁸⁰⁻⁸³ as shown in Figure 1.4⁴⁰ or energy enhanced species such as argon bombardment as shown in Figure 1.5.^{75,77-79} The nature of the activation step can impact whether the etching is anisotropic or isotropic. ALE processes enable more conformal etching processes,⁷⁷ with thermal-driven ALE having the added bonus of enabling etching in high aspect ratio structures.⁴⁰

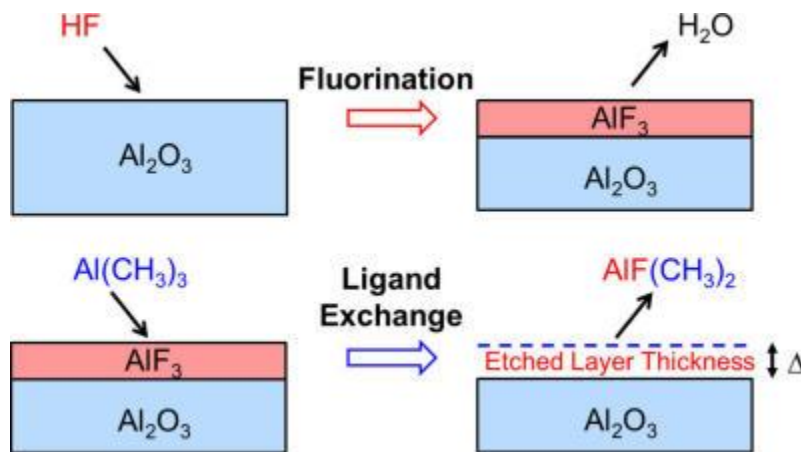


Figure 1.4: General reaction scheme for a thermally-driven ALE process, in which unlike the energy-enhanced, surface volatilization depends on a ligand exchange reaction.

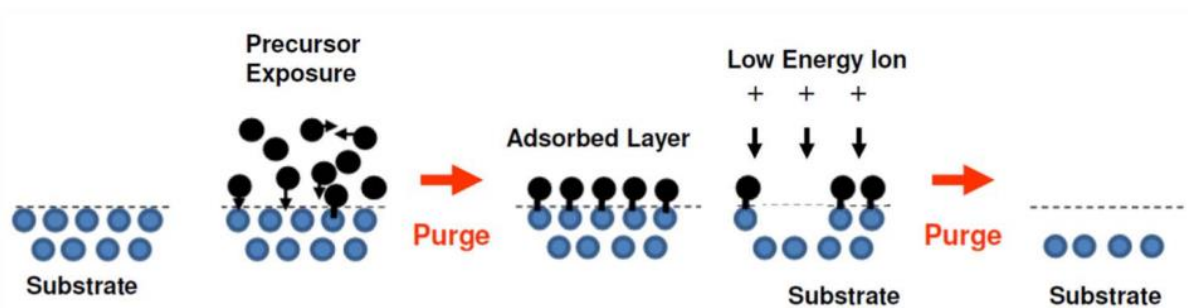


Figure 1.5: General reaction scheme for an energy-enhanced ALE process, consisting of an adsorption and activation step.

There has been considerable work by George et al. studying selective etching of oxides using hydrofluoric acid (HF) in combination with different metal coreagents.⁸⁰⁻⁸³ Specifically, HF was used to fluorinate metal oxides including Al_2O_3 , HfO_2 , and ZrO_2 creating a passivating metal fluoride layer.⁸⁰⁻⁸³ Exposing the metal fluoride layer to a co-reagent such as trimethylaluminum (TMA),^{80,83} tin acetylacetonate ($\text{Sn}(\text{acac})_2$),^{80-82,84} diethylaluminum chloride (DMAC),⁸⁰ or silicon tetrachloride (SiCl_4)⁸⁰ can lead to a ligand-exchange reaction. Depending on the metal fluoride and the extent of the ligand-exchange, the modified surface layer will be volatilized, reforming the original substrate surface termination. For example, a AlF_3 surface layer is proposed to react with $\text{Sn}(\text{acac})_2$ to form volatile $\text{Al}(\text{acac})_3$ and $\text{SnF}(\text{acac})_2$.^{81,82} Selective oxide etching has been achieved by adjusting the process temperature and selecting specific metal precursors that serve as ligand sources. For example, a HF/TMA ALE process was observed to etch Al_2O_3 but not ZrO_2 at 300°C .⁸⁰

1.3 Metal Organic Frameworks (MOFs)

1.3.1 General Metal Organic Framework Properties

Metal organic frameworks (MOFs) are inorganic-organic solid state compounds formed through coordination bonds between metal cations and organic ligands.⁸⁵ The MOF structure consists of rigid pores that retain their structure upon solvent removal.^{86,87} MOFs exhibit a high degree of crystallinity, relatively high thermal stability, very high surface area, and a maximum porosity that exceeds that of zeolites.⁸⁸ In addition, these inorganic-organic compounds can be tuned for specific applications, such as adjusting MOF pore size to control

transport through the pores or the replacement of ligands with other molecules.⁸⁹ As a result, MOF materials are of considerable interest for gas storage and toxic gas adsorption.⁹⁰

1.3.2 *Properties of the UiO-66 MOF and MOF Analogs*

The UiO-66⁹¹ and NU-1000⁹² series of MOF contain Zr_6 octahedral clusters and carboxylate linkers, giving rise to strong coordination bonds.⁹³ This imparts these MOFs with strong thermal and chemical stability, in addition to the high surface area and porosity typical for MOF materials. It is also possible to tune the properties of UiO-66 by replacing the organic benzene dicarboxylate linker with analogous linkers with side groups including amine, nitro, and bromide side groups.⁹⁴ The amine functionalized UiO-66-NH₂ creates more Lewis base sites and makes the MOF more “electron rich” in comparison to standard UiO-66.⁹⁴ As a result, UiO-66-NH₂ can adsorb and degrade chemical warfare agents (CWA's),⁹⁵ act as a visible-light photocatalyst,⁹⁶ and has double the CO₂ and CH₄ storage capacity relative to UiO-66.⁹⁷

Another special property of the UiO-66 and NU-1000 MOF series is that they can transition between a hydroxylated and dehydroxylated state. In their hydroxylated state, the metal clusters are Zr_6O_8 cores in octahedral geometry, with each octahedral face bridged by a μ_3 -OH or μ_3 -O moiety, corresponding to $Zr_6O_4(OH)_4$ stoichiometry. Treatment at elevated temperatures first leads to loss of physisorbed water and solvent, followed by release of two H₂O from each metal cluster, yielding dehydroxylated Zr_6O_6 that takes on a distorted structure.^{98,99} Rehydroxylation allows repopulation of the bridging hydroxyl groups. Dehydroxylation, generating missing linker sites, and tuning the zirconium nodes sites with

solvents such as methanol can increase the concentration of active sites available for catalysis and other applications.^{100,101}

1.3.3 *Properties of the CuBTC MOF*

Another MOF of particular interest is copper benzene tricarboxylate ($\text{Cu}_3(\text{BTC})_2$), referred to as CuBTC, HKUST-1, or MOF-199. CuBTC consists of $\text{Cu}_3(\text{H}_2\text{O})_2$ dimer units linked by 1,3,5-benzenetricarboxylate groups (BTC). CuBTC is typically synthesized solvothermally by heating the MOF precursor solution for extended periods of time. The copper and organic precursor react to form sub-structures referred to as secondary building units (SBUs), which then combine to form the complete three-dimensional MOF structure.⁸⁶ Each copper metal fills the residual axial coordination sites with weakly bound axial water ligands.^{87,102} The CuBTC structure as shown in Figure 1.6 consists of channels $\sim 9 \text{ \AA}$ in diameter surrounded by tetrahedral side pockets $\sim 5 \text{ \AA}$ in diameter.¹⁰³ The channels and pockets are then interconnected by triangular windows $\sim 3.5 \text{ \AA}$.^{86,104} Collectively, this generates the electrically neutral and three dimensional open framework.¹⁰⁴

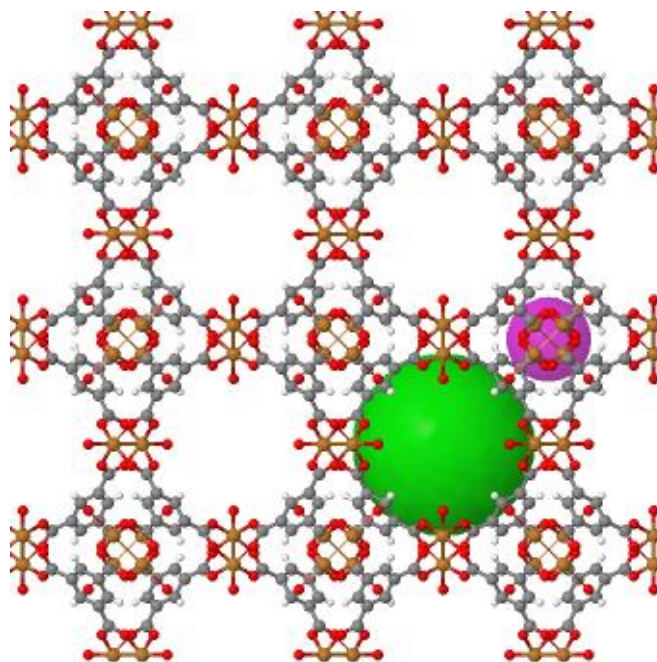


Figure 1.6: CuBTC structure in which the green and pink spheres denote the primary and secondary MOF pores respectively.

Due to its structure and composition, CuBTC is extremely hydrophilic and acts as a Lewis acid.^{102,105} MOF structures are fairly resilient due to the coordination bonds, but dissociation of the cluster-link bond will destroy the framework.⁸⁷ Exposure to high temperatures and moisture can therefore cause CuBTC decomposition. Finally, CuBTC can be readily modified by removing water ligands from the copper center in order to expose metal sites for applications such as gas adsorption.¹⁰⁶

1.3.4 Investigating Nucleation and Deposition of the CuBTC MOF

1.3.4.1 Homogenous and Heterogeneous MOF Nucleation

Immobilizing MOF materials on substrates demands an understanding of homogenous and heterogeneous nucleation. Homogenous nucleation occurs when crystals self-nucleate in solution.¹⁰⁷ In the specific context of MOFs, homogenous nucleation likely occurs through the rapid SBU formation in solution.¹⁰⁸ In comparison, heterogeneous nucleation occurs on pre-existing surfaces and is typically thermodynamically favored because of the lower energy barrier.¹⁰⁷ For that reason, lowering the reaction temperature is one way to favor heterogeneous nucleation over homogenous nucleation. Heterogeneous growth on a substrate tends to yield strong attachment and helps limit unnecessary reactant depletion.¹⁰²

1.3.4.2 Role of Substrate Surface Charge on CuBTC Nucleation

Metal oxide properties such as surface charge and dissolution rates are a function of the specific oxide and solution environment. Under aqueous conditions, metal oxides can consist in three main forms: MO^- , MOH , or MOH_2^+ .¹⁰⁹ The dominant state will make the oxide surface behave more like an acid (electron recipient) or a base (electron donor). The isoelectric point (IEP) value is a way to quantify the relative acidity-basicity of a surface. The zeta potential is measured over varying pH values and the IEP is the pH value where the surface has a zero net charge (aka MOH). The reported IEP value ranges for the metal oxides of interest are as follows: Al_2O_3 : 8-8.5, TiO_2 : 5-6.5, and ZnO : 8.6-9.1.¹⁰⁹ These values convey that Al_2O_3 and ZnO can be considered basic surfaces while TiO_2 is considered more acidic.

In addition, certain oxides dissociate in aqueous conditions in order to maintain thermodynamic equilibrium.¹⁰⁹ A Pourbaix diagram shows the equilibrium phases at different solution pH and applied potentials, as shown in Figure 1.7.¹¹⁰ This shows that without an applied potential, ZnO will form Zn^{2+} cations and etch under acidic aqueous conditions. Through similar analysis, one can determine that Al_2O_3 will also etch in acidic aqueous conditions, but TiO_2 is relatively stable.^{111,112}

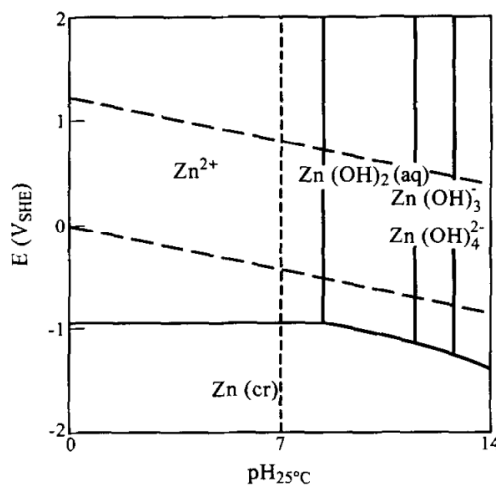


Figure 1.7: Pourbaix diagram for zinc at 25°C.

Work studying heterogeneous CuBTC nucleation has shown that favorable copper adsorption increases overall CuBTC loading onto a substrate.^{113–117} For example, Abbasi et al. increased the heterogeneous CuBTC nucleation on silk fibers by dipping the fibers in alkaline solution prior to MOF deposition. It was hypothesized that the alkaline solution deprotonates the silk carboxylic groups and the negative surface charge improves Cu^{2+} retention.¹¹³ In agreement, Pinto et al. showed that there was only minimal heterogeneous CuBTC nucleation on their modified “acidic” cellulose.¹¹⁴ Finally, Zacher et al. observed that little to no growth

occurred on acidic SiO₂ surfaces while more basic Al₂O₃ substrates showed dense growth under the same reaction conditions.³² These results suggest that negatively charged or basic surfaces support CuBTC nucleation.

1.3.4.3 *CuBTC Nucleation on Chemically Functionalized Surfaces*

A substrate surface functionality can control if and how CuBTC nucleates or adheres to a surface. Through the use of SAMs, it was observed that CuBTC attaches to carboxylic acid (COOH) and hydroxyl (OH) terminated surfaces through the (111) and (100) crystal face respectively.^{33,34} The COOH sites interact with the copper metal centers by replacing the carboxylic acid groups from the MOF organic linker, BTC. OH sites on the other hand, coordinate to the MOF metal centers by replacing the axially coordinated water groups. The oriented attachment initiated during nucleation is maintained with additional MOF growth.³⁴ Furthermore, Zacher et al. noted that CF₃ surfaces inhibited MOF nucleation.³²

1.3.5 *Post-Synthetic Modification of MOF Substrates*

Post-synthetic modification of MOFs is a strategy to impart desirable stability,^{118–120} catalytic activity,^{121,122} other functionality to the MOFs that are not present in the as-synthesized system. Solvent assisted linker exchange (SALE)^{123,124} or solvent assisted linker incorporation (SALI)^{125,126} are two techniques to generate MOFs that cannot be synthesized directly through *de novo* synthesis techniques. A general scheme for the concept of post-synthetic modification of MOFs is included in Figure 1.8.¹²² For example, different carboxylate-derived functionalities were inserted into the NU-1000 MOF via SALI in order

to create charge compensating sites.¹²⁵ Kim et al. also showed that the zirconium metal centers in UiO-66 readily exchange with titanium (IV) and hafnium (IV) during extended soaking in metal-halide solution.¹²⁷

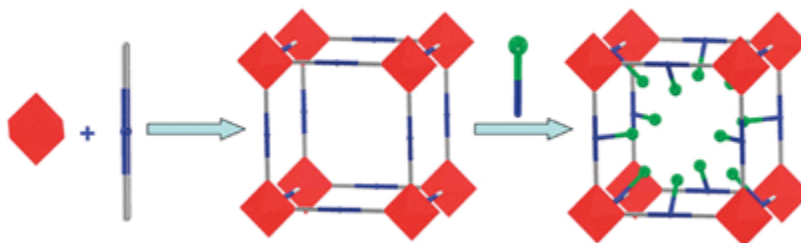


Figure 1.8: Post-synthetic modification of a MOF substrate.

Vapor-phase techniques based on chemical vapor deposition (CVD) and atomic layer deposition (ALD) have also been utilized for post-synthetic modification of MOFs.^{92,108,128–136} For example, Peterson et al. made the CuBTC MOF hydrophobic by coating the surface with a perfluorohexane film via plasma CVD.¹³¹ The Farha and Hupp group applied ALD in MOFs (AIM)^{92,132,133} to modify mesoporous NU-1000. The relatively large pore size, channel dimension, thermal stability and availability of reactive hydroxyl groups made them suitable for bulk reactive modification by the common ALD reactants trimethylaluminum (TMA) and diethylzinc (DEZ).⁹² In further work, this same group used bis(di-isopropylacetamidinato)cobalt(II) with either water¹³⁵ or H_2S ¹³³ to uniformly deposit Co^{2+} ions or Co_9S_8 respectively, inside NU-1000. The addition of Co_9S_8 sites makes the NU-1000 catalytically active for selective hydrogenation of m-nitrophenol over m-aminophenol.¹³³

CHAPTER 2. EXPERIMENTAL TOOLS

2.1 Atomic Layer Deposition Reactor

Atomic layer deposition (ALD) of conformal thin films were carried out in a home-built ALD reactors, with a general reactor design included in Figure 2.1. A typical reactor chamber consists of a tube that is ~40-60 cm long and 4-10 cm wide to ensure that the flow is fully developed before reaching the samples. 306 stainless steel lines are plumbed from a carrier gas (nitrogen or argon) to the reactor. The deposition chamber and steel lines are heated resistively with heat tape or tube furnaces using PID controllers. Gas flow and precursor delivery are controlled with pneumatically actuated valves, which allows consistent precursor dosing and purging between exposures.

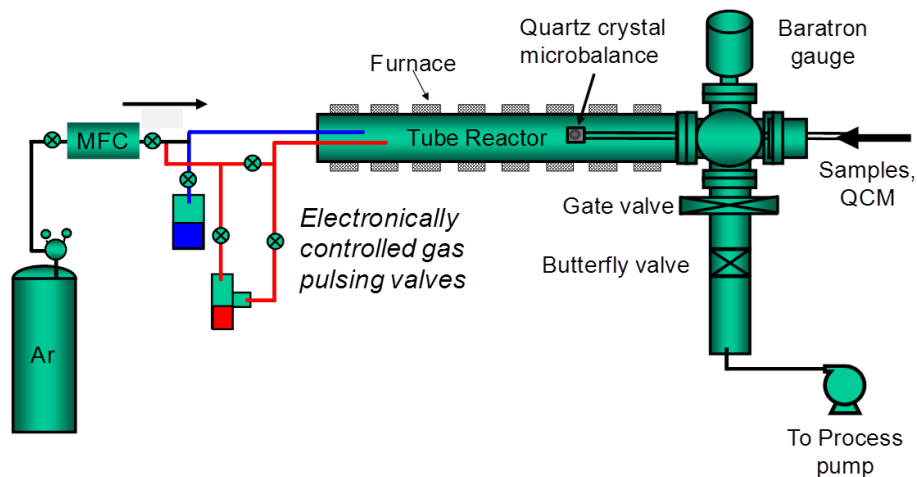


Figure 2.1: Schematic view of viscous flow reactor for ALD, fitted with an in-situ quartz crystal microbalance (QCM) probe.

2.2 Quartz Crystal Microbalance (QCM) Analysis

In-situ real-time monitoring of mass loading or etching on a substrate was monitored using quartz crystal microbalance (QCM) analysis. QCM analysis is based on the fact that quartz is a piezoelectric material. Applying alternating current to a properly cut quartz (typically AT quartz cut at $\sim 35^\circ$) induces oscillations in the crystal.¹³⁷ Keeping other variables constant, the frequency of the oscillation depends on the thickness of the quartz crystal. Equation 2.1 shows how the change in crystal frequency (Δf) correlates to a change in mass loading (Δm).¹³⁷ Where f_0 is the fundamental frequency, C is a frequency constant, and p_f and A are the film density and area respectively. For the QCM analysis included in this document, f_0 and C were set as 6,000,000 Hz and 228.304 Hz/ μg respectively, with a deposition area A of 0.357 cm^2 . This equation holds as long as $\Delta f/f_0$ is less than $\sim 2\%$ because the film thickness is treated as an extension of the overall crystal thickness.¹³⁷ It should also be noted that the crystal frequency is also impacted by changes in process temperature, which is a common source of error in QCM analysis. Finally, to ensure that deposition only occurs on the top crystal face, a gas purge is delivered to the crystal backside to act as a gas shield.^{46,138}

$$\Delta f = -\frac{f_0^2 \Delta m}{C p_f A} \quad (2.1)$$

2.3 Fourier Transform Infrared Spectroscopy (FTIR) Analysis

Fourier Transform Infrared Spectroscopy (FTIR) is an absorption analytical technique that correlates an energy change between two quantized state in a molecule sample to the frequency of absorbed light in the infrared region.¹³⁹ FTIR differs from other absorptive

spectroscopy in that it utilizes broadband light source in order to generate multiple frequencies of light simultaneously.¹³⁹ The raw data, or interferogram, is then processed with a Fourier transform.

Depending on the molecule, a final processed spectrum consists of different vibrational modes, including stretching, bending, scissoring, rocking and twisting modes.¹³⁹ The wavenumber of an absorption band conveys the relative energy of a molecular bond and can be utilized to identify the chemical species present in a sample. Furthermore, the local bonding environment can be characterized by shifts in bands. For example, FTIR analysis of a nitrate anion coordinated to a metal will include symmetric and asymmetric stretching bands in the spectra. The difference in wavenumber between these two bands indicates the degree of ion symmetry and whether the metal-nitrate bonding is monodentate or bidentate.^{140,141} This analysis extends to other moieties as well, such as carboxylate groups.^{142,143}

FTIR analysis was performed in ThermoNicolet 6700 IR bench with DTGS detector for ex-situ analysis and MCT-A detector for in-situ analysis. The FTIR was operated in transmission mode with 200-2050 scans per spectra at 4 cm⁻¹ resolution. A home-built reactor shown in Figure 2.2 was used for in-situ FTIR analysis. This reactor configuration allowed substrates to be analyzed by FTIR without exposing samples to ambient conditions. This was ideal for monitoring changes in surface chemistry following separate ALD half reactions. After each ALD half reaction, the reactor is purged of any reactants and gate-valves are opened, allowing the IR beam to pass through the substrate to the IR detector and

a spectrum is collected. This spectrum can then be analyzed with the previously collected spectrum used as the background.

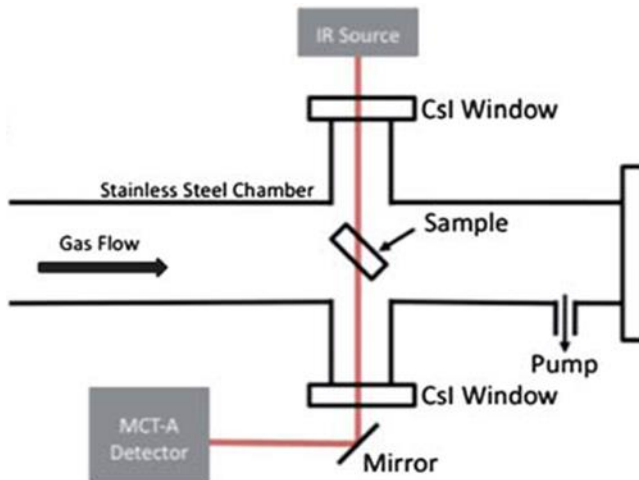


Figure 2.2 Configuration for in-situ FTIR analysis of ALD processes

2.4 Spectroscopic Ellipsometry (SE)

Ellipsometry is an optical technique to measure the thickness of a film based on changes in the polarization of an incident light beam that reflects off a substrate.¹³⁷ Specifically, spectroscopic ellipsometry (SE) utilizes multiple wavelengths in order to determine both the optical constants (n , k) and thickness of a film.¹³⁷ For a transparent film, the raw ellipsometric data, the phase difference (Δ) and the amplitude ratio (ψ), are used in a Cauchy model to determine the film properties. It is also possible to use the raw data itself to monitor the extent of nucleation. For example, Δ is particularly sensitive to changes in surface roughness, making it ideal for monitor the formation and coalescence of nuclei.^{13,18,144} Δ can

also be plotted versus ψ over time or cycle number to determine if growth proceeds through a layer or island growth model.¹³⁷

2.5 X-Ray Photoelectron Spectroscopy (XPS)

X-ray photoelectron spectroscopy (XPS) is a surface-sensitive analytical technique used to monitor and characterize thin film nucleation and composition. Samples are exposed to x-rays (generated by an Al or Mg target), ejecting core electrons from surface atoms in the sample. Electrons that inelastically scatter, returning to their initial energy state, become the spectra background. But electrons ejected from the surface atoms (the first few nm) are less prone to scattering and generate the spectra. This is the basis for why XPS is a surface sensitive technique. These emitted electrons have kinetic energies given by Equation 2.2:

$$KE = hv - BE - \phi_s \quad (2.2)$$

Where KE is the kinetic energy of the ejected electron, hv is the x-ray energy (1487 eV for Al source), BE is the binding energy of the core electron, and ϕ_s is the spectrometer work function. Using the intensity and relative binding energy of the resulting peaks, is it possible to determine quantitative elemental composition analysis and the chemical state of the element within the film. For example, a peak associated with a metal will have a lower binding energy than the corresponding oxidized metal. The electronegative oxygen draws electron density away from the metal, so that the remaining electrons bound to the metal are more strongly bound and require more energy to remove them via the X-rays.

XPS analysis can also be used to determine the thickness of thin films by monitoring the attenuation of a substrate signal. For example, in this document, the extent of SiH₄ and WF₆ adsorption on TiO₂ was estimated by assessing the decay of the Ti 2p 3/2 signal based on equation 2.3 as follows:

$$\frac{I}{I_0} = e^{(-t\lambda)} \quad (2.3)$$

Where I_0 and I are the initial and final intensities of the Ti 2p 3/2 signal before and after adsorption respectively, t is the film thickness, and λ is the inelastic mean-free path (IMFP) of the electron. NIST's Electron Effective-Attenuation-Length (EAL) database was used to determine the IMFP value, which is a measure of photoelectron transport. The IMFP values depends on material properties of both the substrate and deposited film. The kinetic energy of the attenuated Ti 2p 3/2 signal was determined to be 1028.1 eV by subtracting the incident kinetic energy for the Al x-ray source (1486.6 eV) by the binding energy of the Ti 2p 3/2 signal (458.5 eV). The photoionization asymmetry parameter of Ti 2p 3/2 is 1.41 based on the EAL database. Next the IMFP value depends on properties of the deposited film. For example, for a SiO₂ film formed by SiH₄ adsorption, we used a band gap of 9 eV and a density of 2.65 g/cm². Finally, for the Specs XPS used in this study, X-Ray incidence angle is ~30° from surface and x-ray source to analyzer is ~60°.

**CHAPTER 3. COPPER BENZENETRICARBOXYLATE METAL-ORGANIC
FRAMEWORK NUCLEATION MECHANISMS ON METAL OXIDE POWDERS
AND THIN FILMS FORMED BY ATOMIC LAYER DEPOSITION**

The following work is reproduced with permission from Paul C. Lemaire, Junjie Zhao, Philip S. Williams, Howard J. Walls, Sarah D. Shepherd, Mark D. Losego, Gregory W. Peterson, and Gregory N. Parsons. *ACS Applied Material Interfaces* **2016**, 8, 9514–9522.

3.1 Abstract

Chemically functional microporous metal-organic framework (MOF) crystals are attractive for filtration and gas storage applications, and recent results show that they can be immobilized on high surface area substrates, such as fiber mats. However, fundamental knowledge is still lacking regarding initial key reaction steps in thin film MOF nucleation and growth. We find that thin inorganic nucleation layers formed by atomic layer deposition (ALD) can promote solvothermal growth of copper benzene-tricarboxylate MOF (Cu-BTC) on various substrate surfaces. The nature of the ALD material affects the MOF nucleation time, crystal size and morphology, and the resulting MOF surface area per unit mass. To understand MOF nucleation mechanisms, we investigate detailed Cu-BTC MOF nucleation behavior on metal oxide powders and Al₂O₃, ZnO, and TiO₂ layers formed by ALD on polypropylene substrates. Studying both combined and sequential MOF reactant exposure conditions, we find that during solvothermal synthesis ALD metal oxides can react with the MOF metal precursor to form double hydroxy salts that can further convert to Cu-BTC MOF. The acidic organic linker can also etch or react with the surface to form an oxide-metal-

source MOF, which can also function as a nucleation agent for Cu-BTC in the mixed solvothermal solution. We discuss the implications of these results for better controlled thin film MOF nucleation and growth.

3.2 *Introduction*

Metal organic frameworks (MOFs) are inorganic-organic solid state compounds formed through coordination bonds between metal clusters and organic ligands^{85,86,145} and show great potential for filtration^{90,146,147}, catalysis^{148–150}, gas storage^{151,152}, and sensing applications^{153,154}. MOFs exhibit a high degree of crystallinity, relatively high thermal stability, very high surface area that is more defined than activated carbon.¹⁵¹ Despite these advantages, MOF crystals are typically formed as a powder which limits and constrains the way the MOFs can be used. Growing MOF thin films on functional substrates such as fibrous materials could therefore lead to new advances in MOF-based devices and composites.

Many methods have been attempted to integrate MOF materials onto fiber matrices including solvothermal,^{114,155} layer by layer,^{113,116,156} suspension sprays,^{157,158} and microwave-facilitated^{159,160} techniques. Conformal metal oxides or organic-inorganic films formed by atomic layer deposition (ALD) and molecular layer deposition (MLD) respectively can be directly converted into specific MOFs.^{161–165} Recent reports show that ALD metal oxide films can also serve as nucleation layers to promote the heterogeneous nucleation and growth of a wide variety of MOFs on polymer fiber substrates, including Cu-BTC, MOF-74, and UiO-66.^{32,166,167} While these methods are promising for immobilizing MOFs, little is known

about the initial key reaction steps during MOF nucleation and growth on ALD metal oxide thin films.

Several groups have explored nucleation and thin film growth of copper benzene-tricarboxylate (Cu-BTC) MOF^{32,113,114,155,156}, referred to as Cu₃(BTC)₂, HKUST-1, or MOF-199. Results suggest for example, that the copper precursor reacts with the substrate to form stable Cu²⁺ or secondary building unit (SBU) species, thereby promoting subsequent Cu-BTC heterogeneous nucleation.^{113–117} Negatively charged or alkaline substrates appear to have a stronger interaction with the positively charged Cu²⁺ precursors, helping to facilitate Cu-BTC formation.^{32,113,114} Bunge et al.¹⁶⁸ showed that immobilizing copper species via reactive dyes facilitated strong Cu-BTC attachment to fiber substrates. Work also shows that Cu-BTC nucleation can be adjusted to some degree by the substrate surface functionality. For example, the (111) and (100) crystal faces of the Cu-BTC shows preference to attach to COOH and OH substrate surface groups, respectively, whereas CF₃ surface groups tend to inhibit MOF nucleation.^{32–35}

We previously reported that the Cu-BTC MOF crystal size and loading was affected by the substrate ALD metal oxide.¹⁶⁶ We proposed that the different Cu-BTC deposition was possibly due to differences in substrate wettability, surface roughness, and isoelectric point (IEP) values.¹⁶⁶ Herein, we specifically investigate these factors in more detail and show results of subsequent experiments that demonstrate MOF nucleation and growth on metal oxides involves the stabilization of intermediate hydroxy double salts (HDS), where the HDS structure depends strongly on the composition of the metal oxide used.

This work describes experiments exploring Cu-BTC nucleation on three representative ALD oxide thin film coatings, including Al_2O_3 , ZnO and TiO_2 . We analyzed the properties of the ALD functionalized fiber mats (referred to as “PP/ALD”) in aqueous conditions and how these substrates interact individually and sequentially with the two Cu-BTC precursors: copper nitrate ($\text{Cu}(\text{NO}_3)_2$) and 1,3,5-benzene-tricarboxylic acid (BTC) to form Cu-BTC. In addition, we further investigated the nucleation mechanism by using a series of metal oxide powders as catalysts, different copper precursors, and HDS powders.

3.3 *Experiment*

3.3.1 *MOF Precursors and Materials*

A list of the Cu-BTC solvothermal precursors, intermediate species, and products is included in Table 3.1. Non-woven polypropylene (PP) was acquired from the Nonwovens Cooperative Research Center (NCRC) at North Carolina State University. Non-woven PP fiber mats are ~0.3 mm thick, with fiber diameter ranging from 0.6 μm to 9.0 μm . Polypropylene (Type WPP) Membrane Circle, 47 mm in diameter with 0.45 μm diameter pores were purchased from GE Healthcare Life Sciences. 1,3,5-benzene-tricarboxylic acid (BTC), copper nitrate trihydrate ($\text{Cu}(\text{NO}_3)_2$), copper chloride dihydrate (CuCl_2), copper sulfate pentahydrate ($\text{Cu}(\text{SO}_4)_2$), and copper acetate monohydrate ($\text{Cu}(\text{OAc})_2$) were purchased from Sigma Aldrich. Metal oxide powders including Al_2O_3 , TiO_2 , NiO , CaO , Cu_2O , MgO , CdO and ZnO were also purchased from Sigma Aldrich. Materials were used as received.

Table 3.1: List of Cu-BTC solvothermal precursors, intermediate species, and products

Abbreviation	Material	Chemical Formula	Comment
Cu-BTC	Copper BTC or HKUST-1 MOF	$\text{Cu}_3(\text{BTC})_2 \cdot 3\text{H}_2\text{O}$	MOF formed on surface
PP/ALD	Polypropylene fiber with ALD metal oxide	-	Substrate material
$\text{Cu}(\text{NO}_3)_2$	Copper Nitrate	$\text{Cu}(\text{NO}_3)_2 \cdot 3\text{H}_2\text{O}$	MOF precursor
BTC	1,3,5-Benzene-tricarboxylic acid	$\text{C}_9\text{O}_6\text{H}_3$	MOF precursor (deprotonated)
(Cu,Cu)-HDS	Copper Hydroxy Nitrate	$\text{Cu}_2(\text{OH})_3\text{NO}_3$	Surface intermediate
(Cu,Zn)-HDS	Copper, Zinc Hydroxy Nitrate	$(\text{Cu,Zn})_2(\text{OH})_3\text{NO}_3$	Surface intermediate
Cu_2O	Copper (I) Oxide	Cu_2O	Degradation product
Al-BTC	MIL-96	$\text{Al}_{12}\text{O}(\text{OH})_{18}(\text{H}_2\text{O})_3(\text{Al}_2(\text{OH})_4)[\text{BTC}]_6 \cdot 24\text{H}_2\text{O}$	Side product
Zn-BTC	-	$[\text{Zn}_3(\text{BTC})_2(\text{H}_2\text{O})_2] \cdot 2\text{H}_2\text{O}$	Side product

3.3.2 Substrate Preparation and Growth of Crystalline Materials

PP samples were coated with 20 nm of Al_2O_3 , ZnO , or TiO_2 in a lab-made ALD reactor at ~1.0 Torr and 100°C . Clean silicon wafers, placed up- and down-stream of the PP confirmed uniform ALD.

To form Cu-BTC MOFs, 0.42 g BTC (2.0 mmol) in 12 mL of ethanol, and 0.87 g $\text{Cu}(\text{NO}_3)_2$ (3.6 mmol) in 12 mL of deionized water, were added simultaneously to a PTFE-lined pressure vessel containing neat (untreated) or ALD-treated fiber mats. This sequence is written: PP/ALD + $\text{Cu}(\text{NO}_3)_2/\text{BTC}$. (Figure 3.1). The pressure vessel was sealed and heated at 120°C in an IsotempTM vacuum oven for times ranging from 2 to 20 hrs. After cooling for 2 hours, samples were removed under fume hood ventilation, rinsed in equivolume water-ethanol (20 min) and dried under vacuum (0.1 Torr, 120°C , 16 hours).

The PP/ALD fiber mats were massed prior to and following the solvothermal process to determine the Cu-BTC percent mass loading. The Cu-BTC loaded mats were weighed following drying, after sitting in ambient conditions for at least 15 min. Mass effects due to fiber degradation, oxide etching, and ambient water uptake by Cu-BTC were assumed to be negligible when comparing the relative Cu-BTC loading on the three PP/ALD samples.

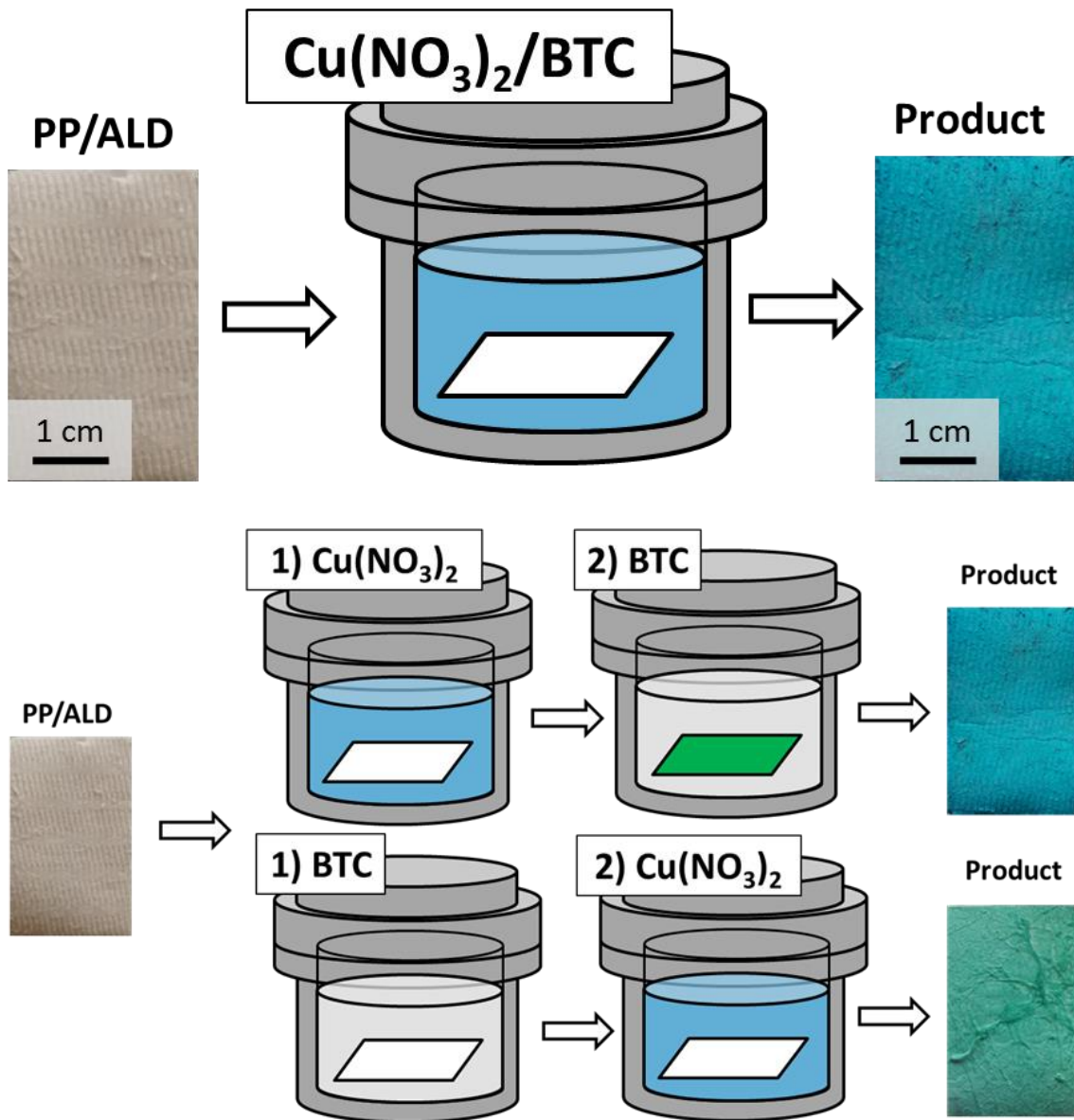


Figure 3.1. Schematic of the standard and sequential solvothermal Cu-BTC synthesis. The fiber mat substrates coated with ALD metal oxides are added to the mixed solution where they wet and settle on the bottom of the PTFE-container. After full reaction at 120°C, the fiber mats are rinsed and dried.

The PP/ALD + $\text{Cu}(\text{NO}_3)_2$ /BTC procedure was adapted for single or sequential reactant exposures, including $\text{Cu}(\text{NO}_3)_2$ or BTC only: (PP/ALD + $\text{Cu}(\text{NO}_3)_2$ or PP/ALD + BTC) or in

sequence (PP/ALD + $\text{Cu}(\text{NO}_3)_2$ + BTC or PP/ALD + BTC + $\text{Cu}(\text{NO}_3)_2$) as shown in Figure 1. For these sequences, the BTC (0.42 g) and $\text{Cu}(\text{NO}_3)_2$ (0.87g) solutions were each 24 mL equivolume ethanol-water solutions.

Metal oxide powders including Al_2O_3 , TiO_2 , NiO, CaO, Cu_2O , MgO, CdO and ZnO were also tested for MOF growth in place of the PP/ALD substrates. For each test, 0.21 g BTC (1.0 mmol) dissolved in 6 mL of ethanol was mixed in a scintillation vial with 0.44 g $\text{Cu}(\text{NO}_3)_2$ (1.8 mmol) dissolved in 6 mL of deionized water. After mixing the BTC and $\text{Cu}(\text{NO}_3)_2$ solutions, 0.18 mmol of the dry metal oxide powder was immediately added to the vial and allowed to react at room temperature for 5 minutes. The final solution was filtered and the collected powder was analyzed by X-ray diffraction (XRD).

To study the interaction of different copper precursors with ZnO powders, CuCl_2 , $\text{Cu}(\text{SO}_4)_2$, or $\text{Cu}(\text{OAc})_2$ were used in place of the $\text{Cu}(\text{NO}_3)_2$, using the same solution concentrations and reaction conditions.

In addition to metal oxide powders, we prepared powders of two hydroxy double salts: $\text{Cu}_2(\text{OH})_3\text{NO}_3$ and $(\text{Zn,Cu})(\text{OH})_3\text{NO}_3$, abbreviated (Cu,Cu)-HDS and (Zn,Cu)-HDS, respectively, to study the Cu-BTC nucleation mechanism. To generate (Cu,Cu)-HDS, 24 ml of the $\text{Cu}(\text{NO}_3)_2$ water-ethanol solution was heated at 120°C for 24 hours. For the (Zn,Cu)-HDS, 0.36 mmol of dry ZnO powder was added to the $\text{Cu}(\text{NO}_3)_2$ solution at room temperature under constant stirring and allowed to react for 5 minutes. The resulting powders were rinsed and dried following the procedure previously described for the MOF/fiber mats.

The collected powder was characterized with Fourier transform infrared spectroscopy (FTIR).

3.3.3 *Material Characterization*

XRD was performed using a Rigaku SmartLabTM X-ray diffraction tool (Cu K α X-ray source). After vacuum drying (120°C, 0.1 Torr, 12 h) the MOF BET surface area and pore size distribution was measured using a QuantachromeTM Autosorb-1C in the P/Po range of 0.05~0.31. The ALD thickness on silicon was measured with spectroscopic ellipsometry (J.A. Woollam Co., Inc.). FTIR was performed with a Thermo NicoletTM 6700 IR bench with a deuterated triglycine sulfate detector operated in transmission mode with 2050 scans at 4 cm⁻¹ resolution.

The isoelectric point of the coated and uncoated fibers was determined by measuring the zeta potential at variable pH with a SurPASSTM electrokinetic analyzer. Each run required 10 16.5 mm PP circular fiber mats with approximately 500 mL of a 0.001 M potassium chloride electrolyte solution. The pH was varied during testing by adding 0.05 M potassium hydroxide or 0.05 M hydrochloric acid solutions.

3.4 Results

3.4.1 Reaction products on ALD-coated fibers after $\text{Cu}(\text{NO}_3)_2/\text{BTC}$ solvothermal exposure

During solvothermal synthesis, the crystal morphology and extent of Cu-BTC MOF growth on metal oxide-coated fibers depends on the composition of the ALD oxide.¹⁶⁶ After 20 hours of solvothermal reaction at 120°C using a mixed $\text{Cu}(\text{NO}_3)_2/\text{BTC}$ solution, we found the Cu-BTC crystals on the PP/ZnO, PP/ Al_2O_3 , and PP/ TiO_2 were approximately 5, 30, and 50 μm in diameter respectively. On the PP/ZnO, PP/ Al_2O_3 and PP/ TiO_2 substrates the resulting Cu-BTC mass loading was found to be: 325%, 302% and 251% respectively. Likewise, the measured BET surface areas of the resulting PP/ALD/MOF samples were 764, 694 and 509 m^2/g respectively. We note that the ZnO substrate showed the highest mass loading and the highest surface area per unit mass.

Using mixed $\text{Cu}(\text{NO}_3)_2/\text{BTC}$ solutions, we investigated the nucleation kinetics of the MOF growth process on each of the ALD coating materials. Upon exposure to the unheated solvothermal solution the PP/ZnO substrate turned blue and XRD confirms formation of Cu-BTC MOF, as shown in Figure 3.2(a) and (b) respectively. In comparison, PP/ Al_2O_3 turned a much lighter blue and PP/ TiO_2 appeared to retain its original yellow color, consistent with less MOF growth. We note that the images in Figure 3.2(a) were collected after only 30 seconds of reaction at room-temperature consistent with very fast MOF formation on the ZnO. Using ZnO for rapid room-temperature Cu-BTC deposition is further discussed by Zhao et. al.¹⁶⁷

Figure 3.2(c) shows the Cu-BTC mass loading on Al₂O₃, TiO₂ and ZnO ALD coated fibers as a function of the solvothermal reaction time. All the substrates show an early nucleation phase followed by a sharp increase in mass gain leading to a plateau. This trend is ascribed to nucleation and initial growth of MOF on fiber substrate (i.e. heterogeneous growth), followed by more rapid homogeneous MOF growth of the MOF nucleation layer. The final mass loading on all three substrates is the same due to similar reactant consumption. After 2 hours, the weight of PP/ZnO substrates increased by 100%, and the weight of PP/Al₂O₃ increased by 50%. On the PP/Al₂O₃, XRD analysis showed formation of Al-BTC. The PP/TiO₂ showed modest measurable weight gain (>~10%) only after 7 hours of solvothermal reaction.

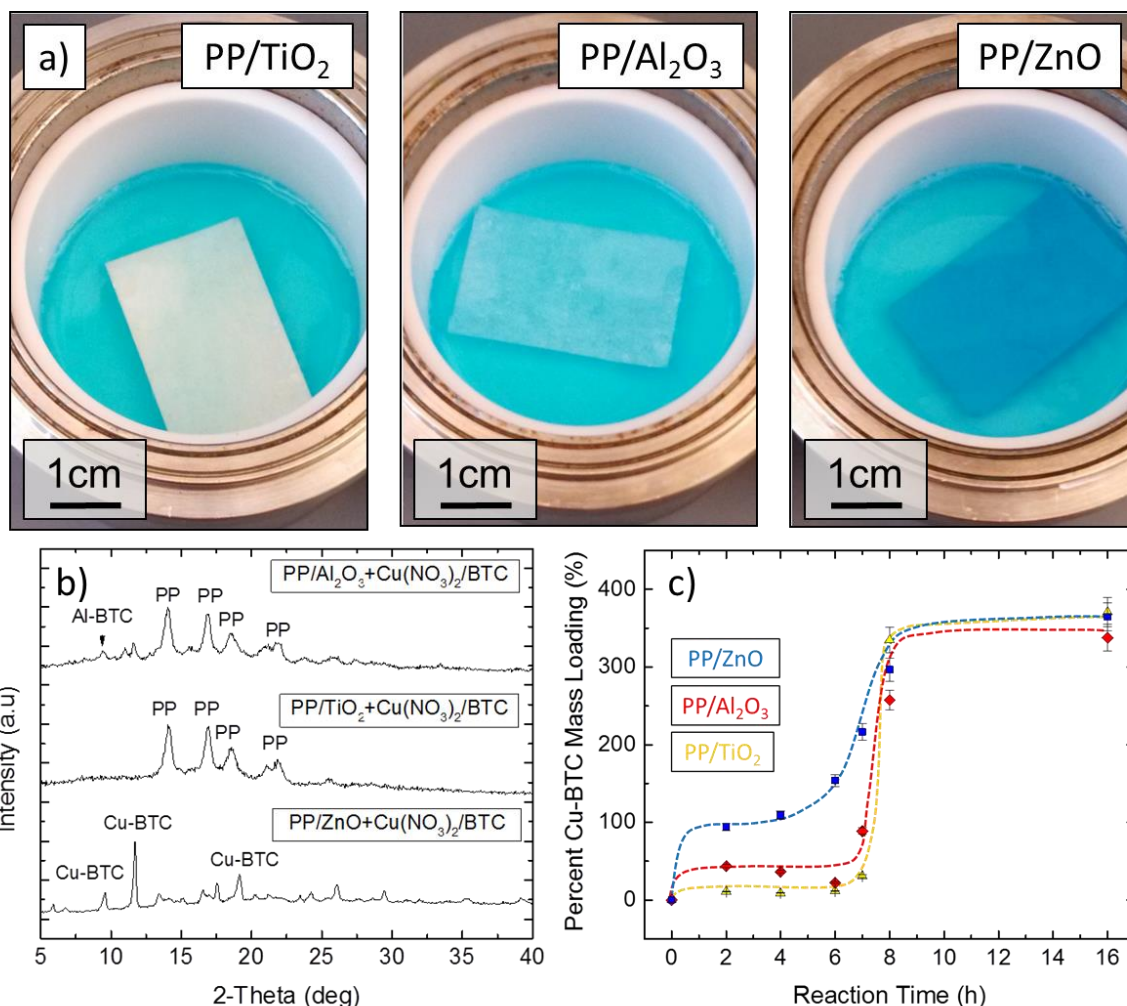


Figure 3.2: Cu-BTC nucleation on PP/ALD with (a) images (b) XRD after exposure to Cu-BTC solvothermal solution at room temperature for ~30 s and (c) percent Cu-BTC mass loading on PP/ALD plotted versus reaction time at 120°C. The PP/ZnO samples show a rapid Cu-BTC nucleation as shown by XRD and accompanied by a rapid color change from white to blue and an early initial mass loading.

To identify possible differences in the metal oxides that could influence MOF nucleation, we measured the surface isoelectric point (IEP) to determine the relative concentration of $M-OH^{2+}$, $M-OH$, or $M-O^-$ surface sites on the ALD oxides at various pH values. The IEP describes the acidity or basicity of a surface, i.e., its tendency to donate or accept protons. As

shown in Figure 3.3, the uncoated PP fibers showed an IEP of 3.83, indicating an acidic surface. After coating with ZnO and Al₂O₃ the IEP increased to 9.52 and 8.88 respectively, indicating more basic surfaces, whereas TiO₂ remained acidic with an IEP near 5.91. These results correspond well with the reported IEP values for these bulk oxide materials.¹⁰⁹

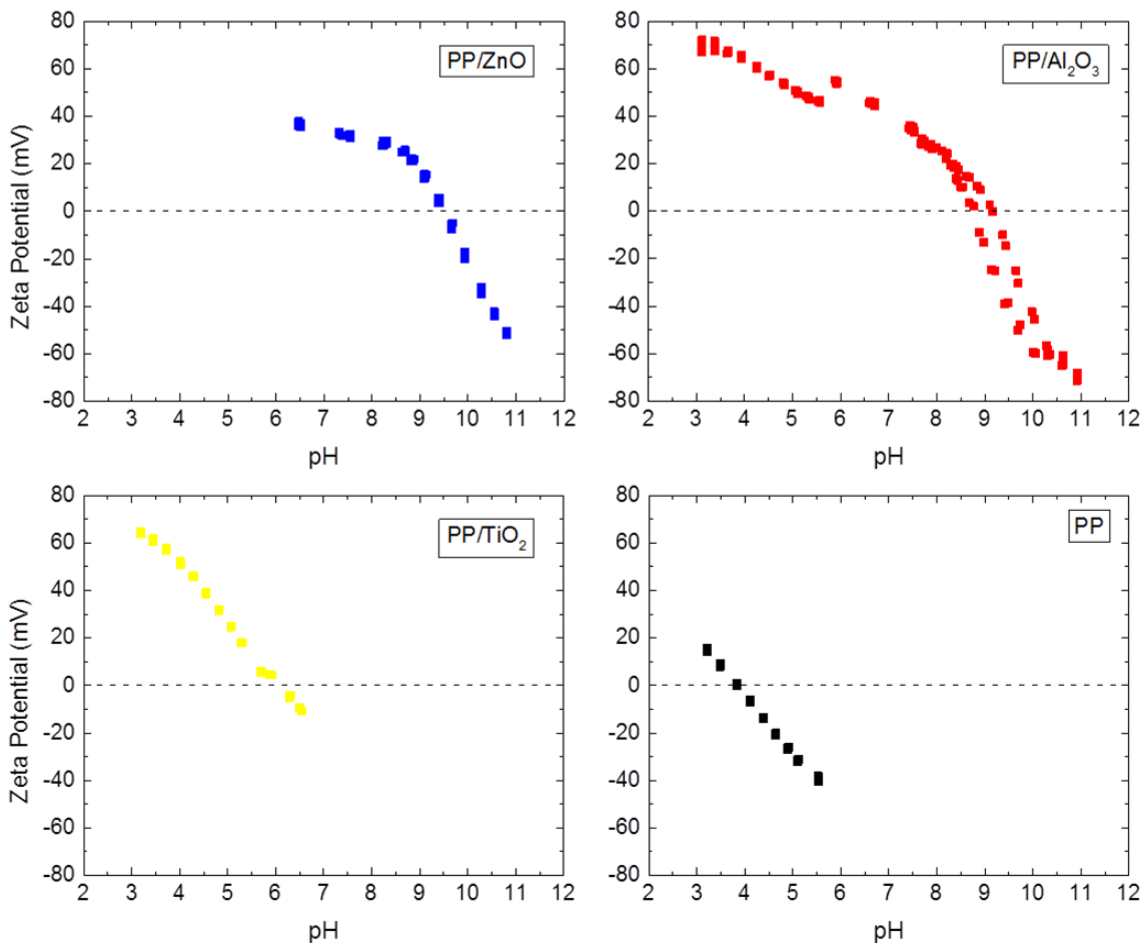


Figure 3.3: Zeta-potential as a function of pH for PP and PP/ALD samples

To further explore the importance of the metal oxide in Cu-BTC nucleation, we tested various metal oxide powders (including oxides of Zn, Cd, Mg, Ni, Ca, Al and Ti) as reactants

for Cu-BTC formation. For each experiment, 0.18 mMol of oxide powder was added to the $\text{Cu}(\text{NO}_3)_2/\text{BTC}$ solvothermal solution and allowed to react at room temperature for 5 minutes. The XRD patterns of the resulting products (Figure 3.4) confirm that Cu-BTC formed in the samples containing ZnO, CdO, and MgO. In addition to Cu-BTC, the MgO, NiO, and TiO_2 powders also led to other crystalline products, including $[\text{Cu}(\text{BTC}-\text{H}_2)_2(\text{H}_2\text{O})_2] \cdot 3\text{H}_2\text{O}$,^{159,169} the one dimensional coordination polymer $[\text{Cu}(\text{C}_9\text{H}_4\text{O}_6)(\text{H}_2\text{O})_3]_n$,¹⁷⁰ and poorly-defined Cu-BTC material.¹⁷¹ Under the conditions studied, the CaO or Al_2O_3 powders led to no measureable crystal products observed by XRD.

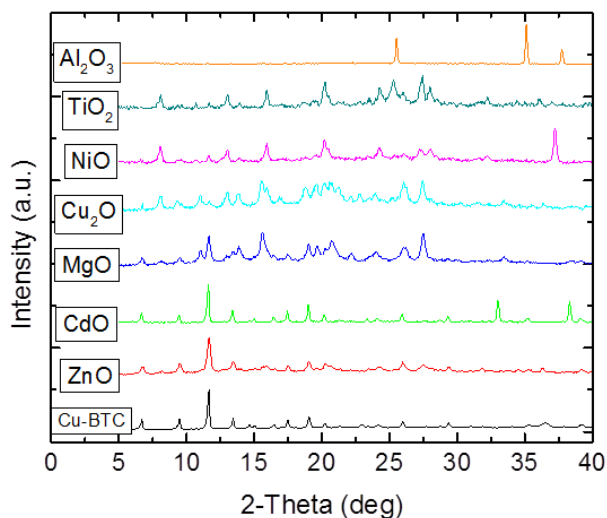


Figure 3.4: XRD of powders generated by oxide facilitated synthesis showing rapid Cu-BTC deposition on ZnO, CdO, and MgO powders, and little growth on Cu_2O , NiO, TiO_2 , and Al_2O_3 .

3.4.2 *Products on ALD-coated fibers exposed to BTC only under solvothermal conditions*

To further isolate the reaction sequence, we studied PP/ALD substrates exposed to BTC in water-ethanol at 120°C. Figure 3.5 presents XRD results for the ALD-coated fiber mats after 20 hours of reaction. The XRD patterns are consistent with MOF products, Al-BTC (MIL-96)^{162,172,173} and Zn-BTC^{174,175} on the PP/Al₂O₃ and PP/ZnO samples respectively. The XRD of the PP/TiO₂ substrates after reaction showed no measureable products. In separate experiments, the ALD oxides were exposed to heated acidic conditions (nitric acid/DI-water/ethanol solution at pH of ~2.5 at 120°C), similar to the Cu-BTC solvothermal conditions. We find that both Al₂O₃ and ZnO etch readily, whereas the TiO₂ was relatively stable, consistent with reported Pourbaix diagrams.^{110,111} Therefore, the Al-BTC and Zn-BTC MOFs may result from etched metal cations that dissolve and react with BTC in solution to redeposit as MOF crystals. Similar mechanisms were proposed by KhALEskaya et al.¹⁶¹ and Bechelany et al.¹⁶² who analyzed conversion of ZnO and Al₂O₃ to ZIF-8 and MIL-53.

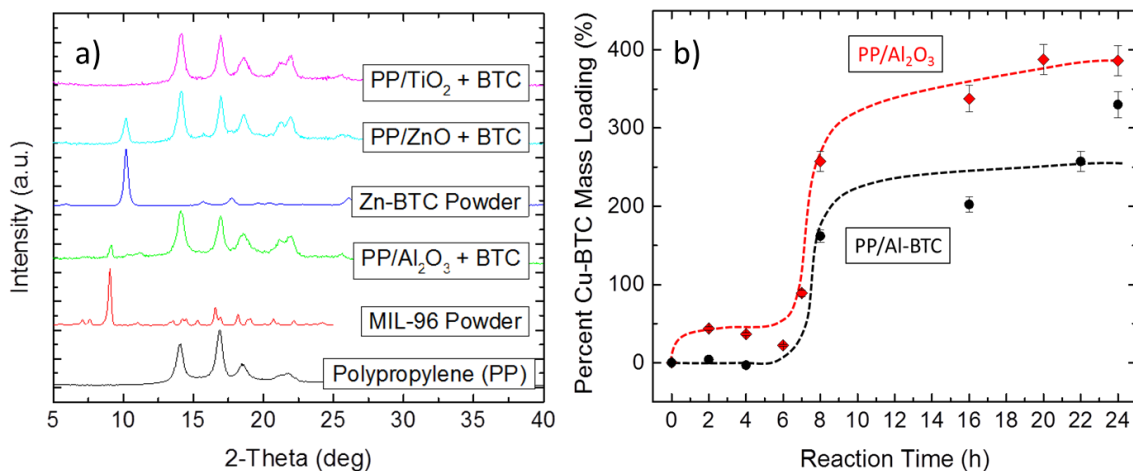


Figure 3.5: (a) XRD of PP/ALD samples after 20 h in BTC solution, showing patterns consistent with Zn-BTC and Al-BTC MOFs. (b) Percent Cu-BTC mass loading as a function of reaction time using PP/Al₂O₃ and PP/Al-BTC substrates. The relatively slow MOF growth on Al-BTC indicates that this compound is not an important intermediate in the growth of Cu-BTC on Al₂O₃.

3.4.3 Reaction products after sequential BTC + Cu(NO₃)₂ solvothermal exposure

Following 20 h of BTC exposure at 120°C, the Al-BTC and Zn-BTC MOFs formed on ALD Al₂O₃ and ZnO were further exposed to 20 hours of Cu(NO₃)₂ solution. After reaction, XRD shows evidence for Cu₂O on both substrates, as well as a HDS. There was no evidence for metal exchange between either Al-BTC or Zn-BTC with dissolved Cu(NO₃)₂ to form Cu-BTC.

The kinetics of MOF formation on PP/Al₂O₃ and PP/Al-BTC during solvothermal growth using mixed Cu(NO₃)₂/BTC solution was also analyzed, and results are shown in Figure 3.5(b). The ~50% mass loading on the PP/Al₂O₃ between 0-4 hours is due to the formation of Al-BTC, which is confirmed by XRD analysis. Therefore, the rate of Cu-BTC nucleation on

Al-BTC is comparable to the ALD Al_2O_3 , indicating that the Al-BTC does not act to facilitate Cu-BTC nucleation on Al_2O_3 .

3.4.4 *Reaction products after $\text{Cu}(\text{NO}_3)_2$ exposure*

Figures 3.6(a) and (b) show infrared transmission and XRD analysis respectively after exposing ALD metal oxides on polypropylene to copper nitrate solution. After 1 hour of $\text{Cu}(\text{NO}_3)_2$ exposure at 120°C , the FTIR shows absorption bands in the $1500\text{-}1300\text{ cm}^{-1}$ range, consistent with O-N-O₂ asymmetric and symmetric stretching modes, respectively,^{140,176,177} as well as absorbance in the $3685\text{-}3150\text{ cm}^{-1}$ region, consistent with significant hydroxyl content. Coordination of nitrate anions to copper affects the ion symmetry and the degeneracy of the ONO₂ modes, leading to splitting of the N-O₂ symmetric and asymmetric stretching bands.¹⁴⁰ A nitrate bound in a monodentate configuration shows a relatively small degree of band splitting, whereas bidentate binding produces a larger band splitting of $\sim 85\text{ cm}^{-1}$.

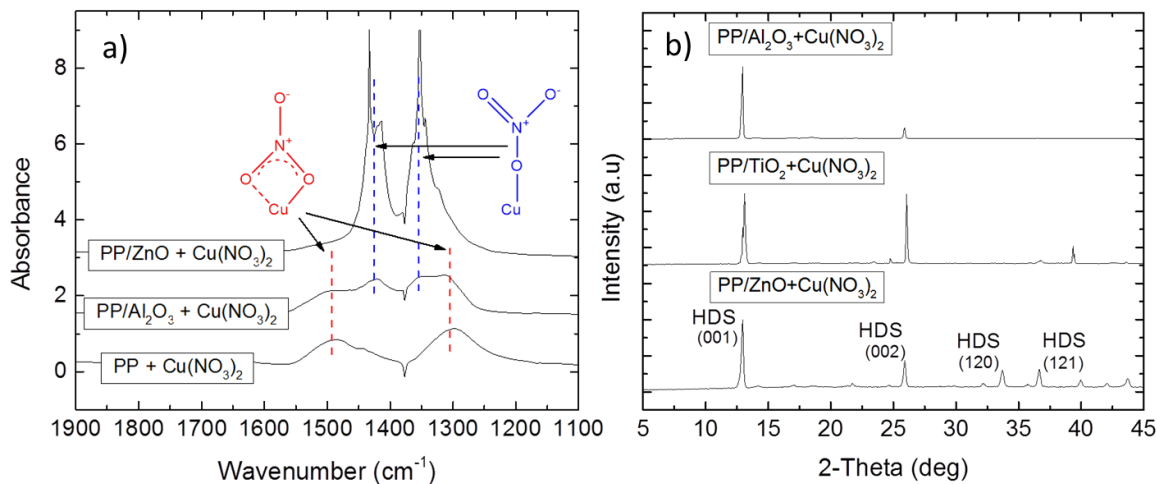


Figure 3.6: (a) FTIR of O-NO₂ stretching band for samples after exposure to Cu(NO₃)₂ solution for 1 h at 120°C. The narrower band splitting for the symmetric and asymmetric O-NO₂ stretching band suggests formation of a monodentate hydroxyl double salt (HDS) on PP/ZnO and predominantly bidentate Cu(NO₃)₂ on PP and PP/Al₂O₃ as shown in the structure diagrams. (b) XRD analysis of PP/ALD samples after 16 hours in Cu(NO₃)₂ solution. The reflections corresponding to a HDS are visible on each substrate, with the most intense signal on the ZnO surface.

For the PP substrate with no ALD metal oxide present, 1 h of Cu(NO₃)₂ exposure leads to relatively weak N-O₂ asymmetric and symmetric stretching modes with a band splitting of 187 cm⁻¹. The same process on the PP/Al₂O₃ substrate also leads to a relative weak signal, but more narrowly split peaks also begin to appear near 1355 and 1430 cm⁻¹. Reaction on the PP/ZnO substrate produces large N-O modes with a narrow band splitting of 62 cm⁻¹.

The wide band splitting observed on polypropylene and PP/Al₂O₃ substrates suggests the copper nitrate coordinates to a surface hydroxide unit, likely through a loss of coordinated water, retaining the bidentate nitrate configuration. On the PP/ZnO, the narrow band splitting

indicates a transition to a more weakly-held nitrate ion in a monodentate bonding configuration, indicative of a HDS.^{140,176,178,179}

After exposing the ALD metal oxide films to $\text{Cu}(\text{NO}_3)_2$ solution for 16 hours, XRD patterns in Figure 3.6(b) are consistent with the crystal structure of (Cu,Cu)-HDS and (Zn,Cu)-HDS (i.e., $\text{Cu}_2(\text{OH})_3\text{NO}_3$ and $(\text{Zn,Cu})(\text{OH})_3\text{NO}_3$ respectively), which are not readily distinguishable by XRD. It is notable that HDS also forms on $\text{PP}/\text{Al}_2\text{O}_3$ and PP/TiO_2 . However, the HDS likely forms more quickly on ZnO because the metal oxide provides a metal source for (Zn,Cu)-HDS formation. After 20 hours of $\text{Cu}(\text{NO}_3)_2$ exposure, XRD analysis of PP/ALD samples show diffraction peaks at 36.5 and 42.4, consistent with conversion of $\text{Cu}(\text{NO}_3)_2$ to Cu_2O .^{180,181}

3.4.5 *Products on ALD metal oxides after $\text{Cu}(\text{NO}_3)_2$ + BTC sequential exposure*

PP/ALD substrate were exposed to the $\text{Cu}(\text{NO}_3)_2$ precursor solution at 120°C for 16 h, followed by 0.5 h in the BTC solution at 120°C, and Figures 3.7 shows XRD results. Following the $\text{Cu}(\text{NO}_3)_2$ + BTC exposure, the XRD indicates Cu-BTC on the PP/ZnO , whereas the $\text{PP}/\text{Al}_2\text{O}_3$ and PP/TiO_2 show peaks only from HDS species. After longer (20 h) $\text{Cu}(\text{NO}_3)_2$ and BTC exposures, XRD shows Cu-BTC on all three oxide substrates. Also after long reaction times, XRD from the PP/ZnO and PP/TiO_2 substrates shows peaks consistent with $\text{Cu}_2(\text{OH})\text{BTC}(\text{H}_2\text{O})$,¹⁸² a known degradation product of Cu-BTC.^{159,183}

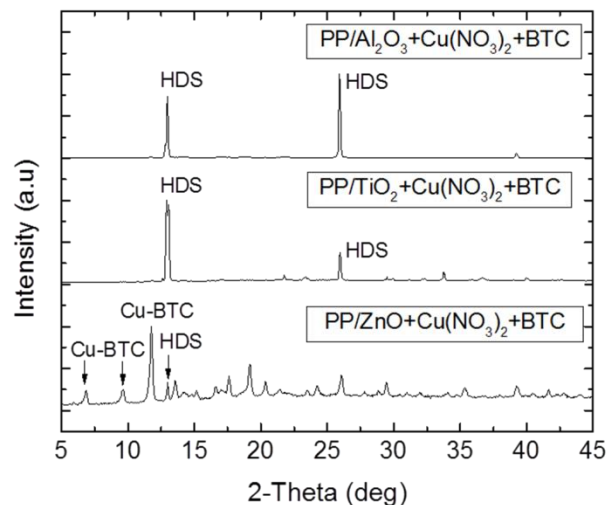


Figure 3.7: XRD spectra of PP/ALD samples after 16 h in $\text{Cu}(\text{NO}_3)_2$ solution followed by 0.5 h in BTC solution. Reflections from Cu-BTC are seen on the PP/ZnO sample, indicating that the HDS produced during the $\text{Cu}(\text{NO}_3)_2$ exposure (shown in Figure 3.4) converts rapidly to Cu-BTC on this surface. Reflections from Cu-BTC are not observed on the PP/ TiO_2 or PP/ Al_2O_3 substrates.

For further analysis, (Cu,Cu)- and (Zn,Cu)-HDS powders were also allowed to react with a 8 mM BTC solution for 5 min at room temperature. Figure 3.8 shows FTIR analysis of the starting HDSs and the resulting products. The starting double salts show peaks at 1450 and 1325 cm^{-1} associated with the O-N-O₂ asymmetric and symmetric stretching, and hydroxyl bands in the 3500-3200 cm^{-1} region. Following the BTC exposure, the (Cu,Cu)-HDS sample did not show a significant change in the FTIR spectra (Figure 3.8(a)). However, starting from (Cu,Zn)-HDS (Figure 3.8(b)) the BTC exposure led to a marked increase in C=O, C=C, and =C-H band intensity, consistent with Cu-BTC MOF, as well as broadening of the hydroxy bands to $\sim 2750 \text{ cm}^{-1}$ indicative of the carboxylic acid O-H stretch in Cu-BTC MOF. The rapid formation (within 5 min) of Cu-BTC from the (Cu,Zn)-HDS suggests that BTC

anion undergoes rapid ion exchange with the nitrate anion in the hydroxy double salt. The FTIR results indicate that similar ion exchange is less rapid for the (Cu,Cu) HDS under the conditions studied.

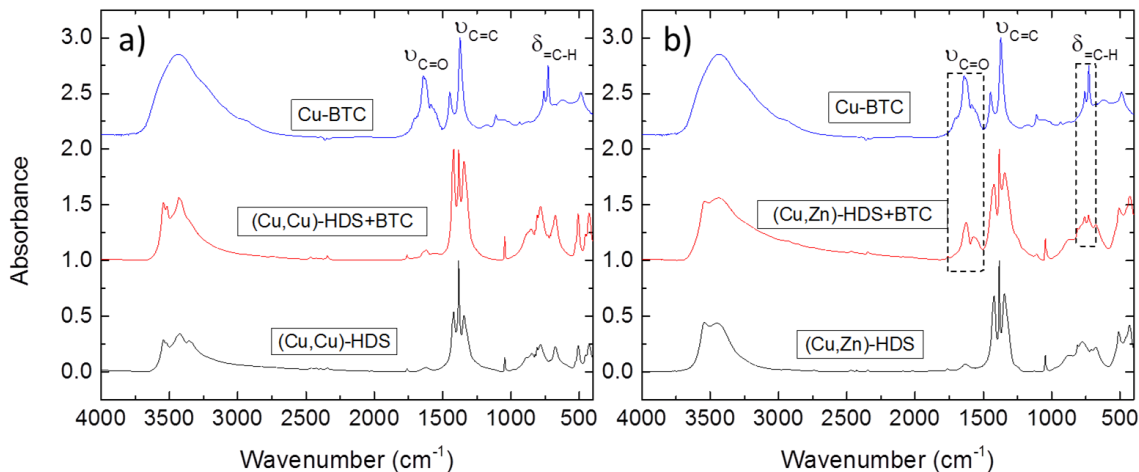


Figure 3.8: FTIR spectra of (a) (Cu,Cu)-HDS and (b) (Cu,Zn)-HDS powders prior to and following exposure to a BTC solution at room temperature for 5 minutes. The relative change in C=O, C=C, and =C-H bands suggest BTC is incorporated into the (Cu,Zn)-HDS and not the (Cu,Cu)-HDS. A reference Cu-BTC spectrum is included.

In addition to $\text{Cu}(\text{NO}_3)_2$, other copper reactants including CuCl_2 , $\text{Cu}(\text{SO}_4)_2$, or $\text{Cu}(\text{OAc})_2$ were combined with BTC and ZnO powder in water/ethanol mixtures to test for formation of hydroxy double salts and Cu-BTC. The resulting powder products were analyzed by FTIR, as shown in Figure 3.9. A reference spectrum for Cu-BTC powder is also shown. Using CuCl_2 , $\text{Cu}(\text{SO}_4)_2$, and $\text{Cu}(\text{NO}_3)_2$, the IR spectra all show prominent peaks at 1623, 1373, and 728 cm^{-1} consistent with Cu-BTC.^{156,159,184} For $\text{Cu}(\text{OAc})_2$ however, the FTIR predominantly shows peaks consistent with unreacted $\text{Cu}(\text{OAc})_2$.

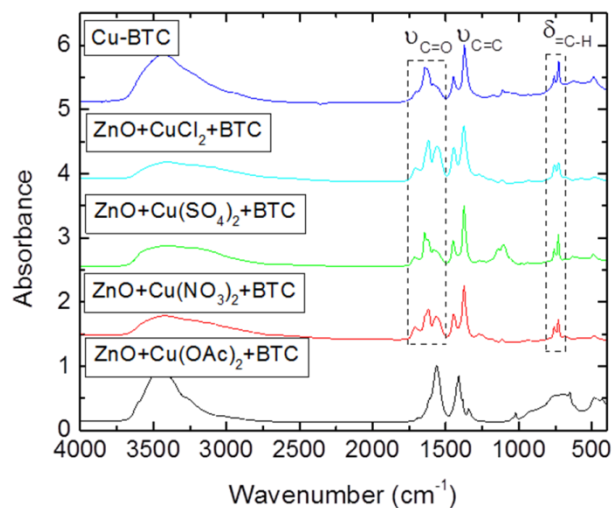


Figure 3.9: FTIR spectra of powders generated by ZnO facilitated Cu-BTC deposition using different copper precursors. The results suggest that Cu-BTC was formed for each of the copper precursors except copper acetate ($\text{Cu}(\text{OAc})_2$)

3.5 Discussion of Results

The results from surface and bulk analyses presented above allow us to consider various mechanisms for Cu-BTC nucleation growth on metal-oxide coated PP fibers and metal oxide powders. The isoelectric point analysis of the metal oxide surfaces showed higher surface pH than the uncoated polymer, and the more basic surface of all the metal oxide films studied likely helps promote precursor adsorption.^{32,113,114}

The XRD results in Figure 3.5(a) shows that the BTC precursor reacts with ZnO and Al_2O_3 to form Zn-BTC and Al-BTC MOFs, respectively. It is likely that these Zn- and Al-BTC MOFs form via etching of the metal oxide to form solvated metal ions that coordinate with the BTC precursor and crystallize on the fiber surface. Further kinetic growth analysis

shown in Figure 3.5(b) using pre-formed Al-BTC on PP/Al₂O₃ suggests that the Al-BTC is relatively inert to further Cu-BTC nucleation and growth. Some Cu-BTC crystals may adhere to these surfaces, consistent with Mao et al. who found that Al-BTC nanorods (MIL-110) can help link Cu-BTC to aluminum oxide,¹⁸⁵ but these crystals are relatively weakly bound to the surface.

For the metal oxide surfaces studied here, the FTIR and XRD results in Figure 3.6 show a fast reaction between ZnO and Cu(NO₃)₂ leading to HDS-related peaks, ascribed to (Zn,Cu)-HDS.^{186,187} This assignment is consistent with reported time-of-flight mass spectroscopy data showing copper diffusion and reaction after exposing ALD ZnO to a room-temperature solution containing Cu(NO₃)₂.¹⁸⁸ The HDS is comprised of stacked metal²⁺ ions (i.e. Cu²⁺ and/or Zn²⁺) in distorted octahedral sites weakly bound to intercalated NO₃⁻ anions.¹⁴⁰ A variety of hydroxy double salts can be readily prepared by precipitation, hydrolysis, or anion exchange techniques,^{176,187} and they are known to support anion exchange,^{140,176,178,189} where the NO₃⁻ coordinated to a metal center can be displaced by various anions including benzoate,^{176,179} alkyl sulfates,¹⁸⁷ and radioactive anions such as iodide.¹⁷⁸

Conversion of ALD ZnO to (Zn,Cu)-HDS could proceed via Cu(NO₃)₂ adsorption followed by rapid Zn²⁺-Cu²⁺ ion exchange, where the Zn cations in (Zn,Cu)-HDS weaken the degree of covalent bonding between Cu²⁺ and NO₃⁻.^{176,179} This mechanism is consistent with Aguirre et al.,¹⁷⁷ who found that Mg(OH)₂ promotes fast formation of (Cu,Cu)-HDS at room temperature, likely through facile nitrate ion transfer from Cu²⁺ to Mg²⁺. The (Zn,Cu)-HDS is an important intermediate for Cu-BTC formation. This is shown in the XRD and FTIR

results in Figure 3.7 and 3.8(b) respectively, which confirm that Cu-BTC forms via sequential reaction of ZnO with Cu(NO₃)₂ and BTC. The (Zn,Cu)-HDS formed upon Cu(NO₃)₂ exposure reacts quickly with BTC to form Cu-BTC.

The XRD results in Figure 3.6(b) also show HDS formation on Al₂O₃ and TiO₂. For the Al₂O₃ and TiO₂, the HDS peaks are ascribed to (Cu,Cu)-HDS, where the Al⁺³ and Ti⁺⁴ ions preclude mixed-metal HDS structures. Figure 3.8(a) shows that the (Cu,Cu)-HDS on the Al₂O₃ and TiO₂ does not readily form Cu-BTC, likely due to relatively slow nitrate-BTC anion exchange at the studied conditions.

The results of experiments using metal oxide powder and different copper salt precursors are also consistent with this scheme for Cu-BTC MOF formation. The XRD results in Figure 3.4 show that MgO, CdO, and ZnO powders all exhibited good Cu-BTC nucleation at room temperature. The Mg,^{176,187} Cd,¹⁹⁰ and Zn^{176,180,187} oxides are known to form hydroxy salts with crystal structure similar to (Zn,Cu)-HDS, in turn promoting Cu-BTC nucleation. Furthermore, in addition to Cu(NO₃)₂, results in Figure 3.9 show that in the presence of ZnO, CuCl₂ and Cu(SO₄)₂ also readily yield Cu-BTC. CuCl₂ and Cu(SO₄)₂ are known reactants for HDS formation.^{186,191–193} The Cu(OAc)₂ can also react with ZnO to yield a HDS, but the reaction is slow and requires relatively high temperature to achieve appreciable rates.¹⁸⁶ Further study is necessary to understand how the lability of HDS ligands affects the Cu-BTC nucleation and structural properties, such as porosity.

3.6 Conclusions

Cu-BTC MOF thin films can form on ALD metal oxides, including Al_2O_3 , ZnO and TiO_2 . The rate of Cu-BTC MOF nucleation depends strongly on the composition of the metal oxide, with notably faster growth on ZnO compared to Al_2O_3 and TiO_2 . The fast rate on ALD ZnO is ascribed to the facile formation of a mixed zinc-copper hydroxy double salt, $(\text{Zn,Cu})(\text{OH})_3\text{NO}_3$, or (Zn,Cu)-HDS, which does form on TiO_2 or Al_2O_3 . The (Zn,Cu)-HDS allows rapid ion exchange with the BTC^{3-} in solution yielding covalently surface-bound Cu-BTC crystals that then facilitate further Cu-BTC growth. The facile reaction between ZnO and $\text{Cu}(\text{NO}_3)_2$ to form (Zn,Cu)-HDS, also extended to CdO and MgO powders to produce analogous HDS structures. Substituting $\text{Cu}(\text{NO}_3)_2$ with other copper salts, including CuCl_2 and $\text{Cu}(\text{SO}_4)_2$ which have not previously been reported for Cu-BTC formation, also yielded (Zn,Cu)-HDS powders that reacted with BTC to form Cu-BTC. This insight into the MOF thin film nucleation can enable MOF crystal and thin film growth processes for a variety of advanced applications.

3.7 Acknowledgement

The authors acknowledge funding from ECBC through grant #W911SR-07-C-0075 and from the Joint Science and Technology Office through Army Research Office grant #W911NF-13-1-0173. The authors acknowledge the use of the Analytical Instrumentation Facility (AIF) at North Carolina State University, which is supported by the State of North Carolina and the National Science Foundation.

CHAPTER 4. REACTANT-DEPENDENT SURFACE NODE DISTORTION DURING ATOMIC LAYER DEPOSITION ON UiO-66-NH₂ METAL ORGANIC FRAMEWORK

The following work is reproduced with permission from Paul C. Lemaire, Dennis T. Lee, Junjie Zhao, and Gregory N. Parsons. “Reactant-Dependent Surface Node Distortion during Atomic Layer Deposition on UiO-66-NH₂ Metal Organic Framework.” Submitted to *The Journal of American Chemistry*. **2017**

4.1 Abstract

Metal organic frameworks (MOFs) are chemically functionalized micro- and mesoporous materials with high surface areas, and are attractive for multiple applications including filtration, gas storage, and catalysis. Post-synthetic modification (PSM), via solution or vapor-based techniques, is a way to impart additional complexity and functionality into these materials. There is a desire to shift towards vapor-phase methods in order to ensure more controlled modification and more efficient reagent and solvent removal from the modified MOF material. In this work we explore how the metal precursors titanium tetrachloride (TiCl₄) and trimethylaluminum (TMA), commonly used in atomic layer deposition, react with UiO-66-NH₂ MOF. Using in-situ quartz crystal microbalance (QCM) and Fourier transform infrared spectroscopy (FTIR) at 150 and 250°C, we find that the ALD precursors react with μ_3 -OH hydroxyl and μ_3 -O bridging oxygen groups on Zr₆ nodes, as well as oxygen from carboxylate linker groups. The reactions occur predominantly at the crystal surface, with TiCl₄ exhibiting greater diffusion into the MOF subsurface. FTIR analysis suggests that

at 150°C, both TiCl_4 and TMA reversibly dehydroxylate the hydroxylated UiO-66- NH_2 , which is accompanied by distortion of the zirconium metal clusters. Finally, we show that TiCl_4 is able to react with the dehydroxylated UiO-66- NH_2 structure, suggesting that TiCl_4 is able to react directly with the carboxylate groups on the organic ligand or the bridging oxygens in the metal-clusters. Better understanding of chemical and thermally-driven MOF dehydroxylation reactions can be important for improved post-synthetic modification of MOFs.

4.2 Introduction

Metal organic frameworks (MOFs) are inorganic-organic solid state compounds formed through coordination bonds between metal clusters and organic ligands^{85,86,145} and show great potential for filtration^{90,146,147}, catalysis^{148–150}, gas storage^{151,152}, and sensing applications.^{153,154} MOFs exhibit a high degree of crystallinity, relatively high thermal stability, very high surface area that is more defined than activated carbon.¹⁵¹ In addition, various isorecticular MOF structures are readily attained with different reactive or surface area properties by modifying metal centers^{194,195} or linker composition^{91,196} during hydrothermal synthesis.

UiO-66⁹¹ and NU-1000⁹² are particularly interesting because of their thermal and chemical stability. These MOFs contain Zr_6 octahedral clusters and carboxylate linkers, giving rise to strong coordination bonds that promote stability.⁹³ In their hydroxylated state, the metal clusters are Zr_6O_8 cores in octahedral geometry with each octahedral face bridged by a $\mu_3\text{-OH}$ or $\mu_3\text{-O}$ moiety, corresponding to $\text{Zr}_6\text{O}_4(\text{OH})_4$ stoichiometry. Treatment at elevated

temperatures first leads to loss of physisorbed water and solvent, followed by release of two H₂O from each metal cluster, yielding dehydroxylated Zr₆O₆ that takes on a distorted structure.^{98,99} Rehydroxylation allows repopulation of the bridging hydroxyl groups. Analysis of the metal clusters in UiO-66 and NU-1000 via X-ray scattering indicates that the distortion coincides with a transition from the original cubic symmetry to the more asymmetric monoclinic geometry, where the phase transition and dehydroxylation are typically coincident but not necessarily physically interrelated.⁹⁹ This structural transition is reversible but kinetically slow, requiring several days to weeks for reconfiguration upon water exposure.⁹⁹

Researchers have also turned attention to understanding post-synthetic modification of MOFs to impart desirable stability,^{118–120} catalytic activity,^{121,122} other functionality to the MOFs that are not present in the as-synthesized system. Solvent assisted linker exchange (SALE)^{123,124} or solvent assisted linker incorporation (SALI)^{125,126} are two techniques to generate MOFs that cannot be synthesized directly through *de novo* synthesis techniques. Kim et al. also showed that the zirconium metal centers in UiO-66 readily exchange with titanium (IV) and hafnium (IV) during extended soaking in metal-halide solution.¹²⁷

Vapor-phase techniques based on chemical vapor deposition (CVD) and atomic layer deposition (ALD) have also been utilized for post-synthetic modification of MOFs.^{92,108,128–136} Table 4.1 summarizes some of the reported efforts using CVD and ALD to deposit metals, metal oxides, sulfides, and other materials in or on various metal-organic frameworks. For example, Peterson et al. made the CuBTC MOF hydrophobic by coating the surface with a

perfluorohexane film via plasma CVD.¹³¹ The Farha and Hupp group applied ALD in MOFs (AIM)^{92,132,133} to modify mesoporous NU-1000. The relatively large pore size, channel dimension, thermal stability and availability of reactive hydroxyl groups made them suitable for bulk reactive modification by the common ALD reactants trimethylaluminum (TMA) and diethylzinc (DEZ).⁹² Diffuse reflectance infrared Fourier transform spectroscopy showed that the TMA reacts with all the terminal hydroxyl groups on the hydroxylated $Zr_6(\mu_3-O)_4(\mu_3-OH)_4$ metal cluster sites in NU-1000, whereas the DEZ tends to react predominantly with the hydroxyl groups pointing into the channels. This selectivity for -OH sites has been ascribed to favorable dispersion interactions between the DEZ precursor and the coordinated linkers, promoting precursor localization and hence more favorable overall reaction kinetics within the small pore regions.¹⁹⁷ In further work, this same group used bis(di-isopropylacetamidinato)cobalt(II) with either water¹³⁵ or H_2S ¹³³ to uniformly deposit Co^{2+} ions or Co_9S_8 respectively, inside NU-1000. The addition of Co_9S_8 sites makes the NU-1000 catalytically active for selective hydrogenation of m-nitrophenol over m-aminophenol.¹³³

Table 4.1. Reported vapor-phase deposition of materials on MOF substrates

MOF	Deposition Technique	Deposited Material	Source
MOF-5	CVD	Fe, Pt, Au, Cu, Zn, Sn	108
MOF-5	CVD	Ru	129
UiO-66	CVD/SVI	Cr(CO) ₃	130
Cu-BTC	PECVD	C ₆ F ₁₄	131
NU-1000	ALD	Al ₂ O ₃ , ZnO	92, 99
NU-1000	ALD	In ₂ O ₃ , Al ₂ O ₃	132
NU-1000	ALD	Co ₉ S ₈	133
MIL-101	ALD	NiO	134
NU-1000	ALD	Co ²⁺ , Ni ²⁺	135, 136
NU-1000	ALD-ME	Cu, Ni, Co	128, 198

The mesoporous structure of NU-1000 provides pores and channels large enough to transport and incorporate TMA and DEZ throughout the MOF. There is also interest in how ALD reactions can be used to selectively modify the surface of microporous MOF crystals. Forming thin surface molecular barrier layers on MOFs have applications as capping layers for retaining weakly adsorbing molecules or selective gas filtration.¹⁹⁹ In this work, we combined in-situ FTIR and quartz crystal microbalance (QCM) analyses with ex-situ TEM to explore ALD vapor-phase routes for modification of UiO-66-NH₂ crystals. We provide evidence that the ALD precursors are able to react with μ_3 -OH hydroxyl and μ_3 -O bridging

oxygen groups on Zr_6 nodes, and oxygen from carboxylate linker groups. The size and steric limitation of the ALD precursors impedes their complete access into the microporous UiO-66-NH₂ network, but we show that some precursor transport can proceed into the near-surface regions of the exposed crystal facets. Additionally, the ALD precursors can promote reversible dehydroxylation and distortion of the $Zr_6(\mu_3-O)_4(\mu_3-OH)_4$ clusters. Transmission electron micrographs confirm atomically abrupt interfaces between UiO-66 and highly conformal ALD thin film over-layers.

4.3 Experimental

4.3.1 List of materials

Aminoterephthalic acid (99%), zirconium tetrachloride (99.99%), and anhydrous dimethylformamide (99.8%) were purchased from Sigma Aldrich and used without further treatment. Trimethylaluminum (TMA) and titanium tetrachloride (TiCl₄) were obtained from Strem Chemicals Inc. and used without further treatment. Deionized water (H₂O) was used as the co-reactant. We monitored the ALD deposition with silicon wafers [100] purchased from WRS Materials and with QCM crystals purchased from Inficon. For the carrier and purge gas, dry nitrogen (99.999%) was passed through an EntegrisTM GateKeeper inert gas purifier to remove any residual water before entering the reactor.

4.3.2 Synthesis of UiO-66-NH₂ powder

To form UiO-66-NH₂ MOFs, 0.08 g of zirconium tetrachloride (0.3 mmol) was added to 20 mL of dimethylformamide and mixed room temperature until completely dissolved. 0.062 g

2-aminoterephthalic acid (0.3 mmol) was added to the zirconium tetrachloride solution, mixed for three minutes and then added to a teflon-lined pressure vessel. The pressure vessel was sealed and heated at 120°C in an IsotempTM vacuum oven for 24 hours. After cooling for 2 hours, the MOF powders were collected by filtering the reactant solution. The powders were washed in DMF and then exchanged in pure ethanol for 3 days and dried under vacuum at 120°C.

4.3.3 *Immobilization of UiO-66-NH₂ crystals on substrates*

To attach the MOF crystals on planar substrates, it was necessary to create a MOF suspension. 0.1 g of UiO-66-NH₂ powder was added to 20 mL of methanol and the suspension was sonicated for 1 hour at room temperature. Using a spin coater, 75 µL of the suspension was dropped onto 1 cm² silicon wafer. The spin coater recipe consisted of spinning the wafer at 500 rpm for 15 sec followed by an increased rate of 2500 rpm to remove any weakly attached crystals. This was repeated 5 times and then the samples were dried using compressed nitrogen. The same procedure was used for immobilizing UiO-66-NH₂ onto QCM crystal substrates.

4.3.4 *Reactant exposure and ALD reactor conditions*

The UiO-66-NH₂ crystals were exposed to the ALD precursors in a homebuilt hot wall viscous flow vacuum reactor described previously.⁵² The nitrogen carrier gas flow rate was maintained at 165 standard cubic centimeters per minute (sccm) for an operating pressure of ~0.6 Torr. The TiCl₄, TMA, and H₂O precursor bottles were maintained at room temperature.

The inlet and outlet gas lines were temperature controlled with heating tape to prevent precursor condensation in the reactor. The reactor temperature was held at 150 or 250°C. Samples were heated at the set-point temperature for at least 2 hr prior to deposition or analysis. For FTIR analysis at 250°C, the reactor was held at 150°C and a sample holder with mounted cartridge heaters was used to heat samples to 250°C.

A typical ALD cycle followed a TiCl₄(Hold)/N₂/H₂O(Hold)/N₂ sequence with dose, exposure and purge times of 1.5(60)/120/1.5(60)120 s respectively. A needle valve reduced the TiCl₄ and TMA precursor dose so that the 1.5 s dose corresponds to ~50 mTorr pressure increase. The longer exposure time during the 60 s hold yielded a ~2.7·10⁶ L exposure.

4.4 *Ex-situ characterization of UiO-66-NH₂ powders*

After vacuum drying (120°C, 0.1 Torr, 12 h) the MOF BET surface area and pore size distribution was measured using a QuantachromeTM Autosorb-1C in the P/P₀ range of 0.02-0.07. The external surface area was estimated using the V-T method in the P/P₀ range of 0.1-0.5. XRD was performed using a Rigaku SmartLabTM X-ray diffraction tool (Cu K α X-ray source). Transmission electron spectroscopy (TEM) was performed on a JEOL 2000FX. UiO-66-NH₂ crystals were imaged using an FEITM Verios 460L scanning electron microscope (SEM), in which samples were sputter-coated with 5~10 nm of Au-Pd before imaging.

4.5 *In-situ characterization of ALD processes*

The ALD process conditions were characterized with two in-situ techniques, quartz crystal microbalance (QCM) and Fourier transform infrared spectroscopy (FTIR) analyses. For QCM analysis, a 6 Hz gold coated QCM crystal sensor (Inficon) was mounted onto the QCM housing with conductive epoxy as previously described.⁴⁶ The mass change signals were detected by an InficonTM SQM-160 monitor and recorded using a home designed LabVIEWTM program. The UiO-66-NH₂ loading on the crystals was estimated using the crystal frequency at 150°C for a bare crystal and the crystal with the immobilized UiO-66-NH₂ crystals. QCM results are shown as mass loading per ng of MOF to compensate for variability in the UiO-66-NH₂ immobilization on the QCM crystals.

In-situ FTIR analysis was performed with a ThermoNicoletTM 6700 FTIR bench with a deuterated triglycine sulfate detector incorporated into a homebuilt ALD reactor described previously.^{22,52} Spectra were taken following the metal and water exposures after the chamber was purged for two minutes. FTIR spectra were collected at the temperature the samples were exposed to the ALD precursors. Gates to the FTIR windows were then opened and 500 scans at 4 cm⁻¹ resolution in the frequency range of 4000 to 650 cm⁻¹. An MCT-A detector was used through CsI FTIR windows. To highlight the changes in the spectrum upon exposure, data were collected, processed and presented in differential mode, using the previous collected spectrum as the reference.

4.6 Results

4.6.1 As-formed UiO-66-NH₂ MOF

The UiO-66-NH₂ powder formed via the solvothermal synthesis was characterized via SEM, XRD, BET, and FTIR. SEM images in Figure 4.1 show ~150-200 nm octahedral crystals consistent with previous reports of UiO-66-NH₂.⁹⁷ Figure 4.1 also shows a comparison of the as-formed UiO-66-NH₂ powder XRD, exhibiting the characteristic peaks of the UiO-66 diffraction pattern. In addition, BET analysis shows that the UiO-66-NH₂ crystals have an overall surface area of 1008 m²/g, and the corresponding external surface area of the crystals is 127 m²/g, consistent with reported values.¹⁹⁶

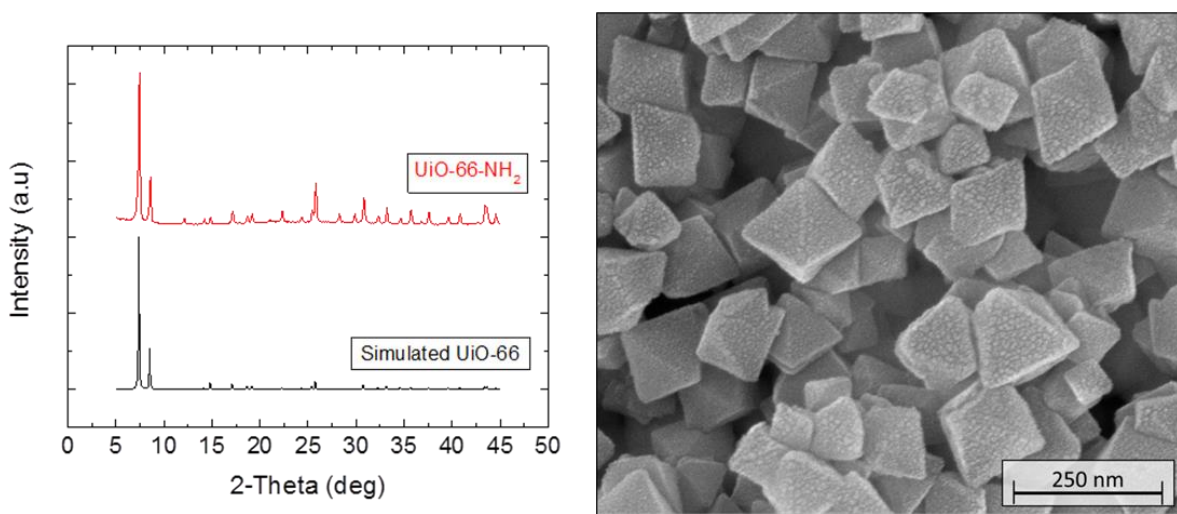


Figure 4.1: SEM image and XRD patterns of as-formed UiO-66-NH₂ powder. The UiO-66-NH₂ XRD pattern is compared to a UiO-66 pattern simulated from CCDC 837796.

Figure 4.2 shows spectra collected from FTIR of the UiO-66-NH₂ structure at 150°C before and after annealing in an inert environment at 250°C. Both spectra show strong peaks at

1569, 1417, and 1380 cm^{-1} consistent with asymmetric and symmetric carboxylate (COO^-) bonding in the organic linker.^{94,97,98,200} The COO^- peak at 1417 cm^{-1} which is present in the UiO-66- NH_2 spectrum^{94,97,200} is typically not observed in the non-amine UiO-66,^{201,202} likely due to differences in the local electron density in the carbon ring induced by the amine group.^{96,203} A peak at 1252 cm^{-1} and peaks at 3512 and 3402 cm^{-1} respectively indicate the C-N stretching and the N-H stretching modes of a primary amine ($-\text{NH}_2$).^{94,97,200} A small shoulder at 1626 cm^{-1} is assigned to the H-N-H scissoring mode.⁹⁴

In the as-formed MOF, the bottom-most FTIR spectrum in Figure 4.2a shows a band at 3668 cm^{-1} assigned to hydroxyl (OH) stretching, and features at 680 and 735 cm^{-1} corresponding to Zr-O bands. After heating the UiO-66- NH_2 to 250°C for 12 hr, there is a small loss at ~1700 cm^{-1} due to the loss of residual DMF,²⁰⁴ along with significant loss of OH modes. We also note a decrease in the Zr-O feature at 735 cm^{-1} and an increase at 764 cm^{-1} . In the skeletal region, the FTIR spectrum of the symmetric cubic ZrO_2 is expected to show three Zr-O features near 530, 625 and 725 cm^{-1} .²⁰⁵ In contrast, in monoclinic ZrO_2 , the Zr atoms are seven-fold coordinated, with half of the oxygen atoms in planar trigonal coordination and the other half arranged in a distorted tetrahedral geometry. This decreased symmetry in the oxygen environment leads to a higher frequency oscillation for asymmetric Zr-O stretching.²⁰⁵ In the as-formed MOF, the FTIR modes at 680 and 735 cm^{-1} agree with the expected cubic structure for the $\text{Zr}_6(\mu_3\text{-O})_4(\mu_3\text{-OH})_4$ node. Upon heat treatment, the decrease at 735 and increase at 764 cm^{-1} is consistent with the node structure transforming from the 8-fold coordinated cubic $\text{Zr}_6\text{O}_4(\text{OH})_4$ to the 7-fold coordinated dehydroxylated monoclinic

Zr_6O_6 , as shown schematically in Figure 4.2c.^{98,99,206} The thermal treatment also leads to loss of the COO^- bands at 1569, 1417, and 1380 cm^{-1} . The positive-going shoulder on the high-wavenumber side of loss peaks indicates peak blue-shift, in agreement with that reported by Valenzano et al.⁹⁸ This shift is further evidence for the expected transition from $Zr_6O_4(OH)_4$ to disordered Zr_6O_6 .^{98,206} Similar trends in COO^- modes upon dehydroxylation were reported after thermal treatment of MOF-74.²⁰⁶

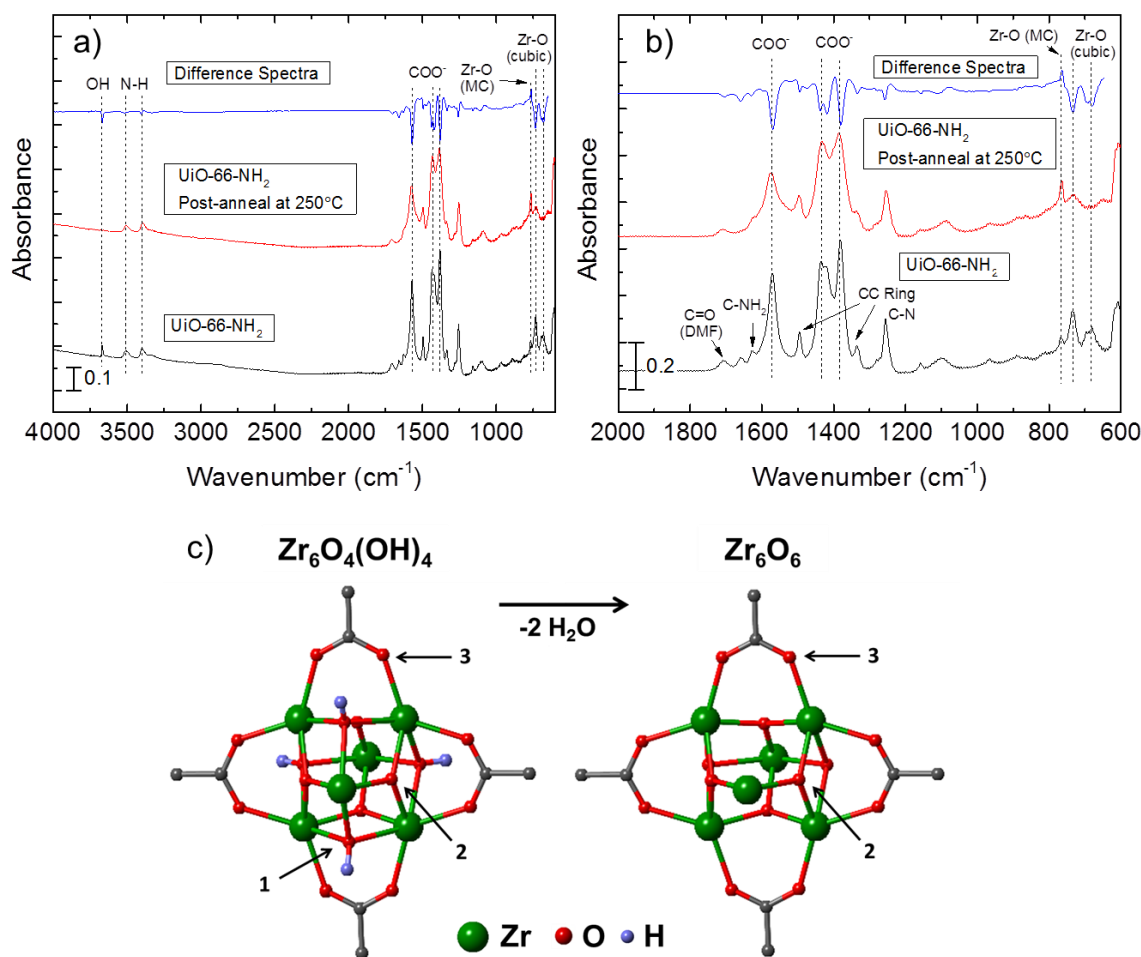


Figure 4.2: a) FTIR spectra of UiO-66-NH₂ at 150 (black) and 250°C (red) and differential spectra (blue) and b) an expanded view from 2000-600 cm⁻¹, showing loss of the hydroxyl bands (OH) and loss of the carboxylate bands (COO⁻) with elevated heating. Panel c) shows molecular structure of the hydroxylated (Zr₆O₄(OH)₄) and dehydroxylated (Zr₆O₆) metal clusters, including 4 carboxylate groups out of the expected 12 aminoterephthalic acid linkers. Potential reaction sites for the ALD precursors include: 1) hydroxide groups, 2) bridging oxygens, and 3) coordinated oxygen on the carboxylate groups.

4.6.2 UiO-66-NH₂ Reactions with TiCl₄ and TMA

As a first experiment, we set out to determine the amount of precursor needed to completely react with or “saturate” the UiO-66-NH₂ MOF. MOF powder samples were exposed to 10

TiCl₄ sequential exposure dose steps as outlined in the Experimental section, and results were monitored by in-situ FTIR and by QCM analysis. Figure 4.3a shows the initial UiO-66-NH₂ FTIR spectra and in-situ difference spectra following the 1, 2, 3, 5, and 10 TiCl₄ exposure steps. The difference spectra represent the net change from the previously collected spectrum. The first TiCl₄ exposure at 150°C produces a loss at 1700 cm⁻¹ attributed to DMF desorption. The C-N and N-H bands at 1252 and 1626 cm⁻¹ exhibit losses, which we attribute to chlorination of the amine groups by byproduct HCl formed upon ligand exchange between TiCl₄ and node hydroxyl groups.²⁰⁷ A red-shift in the N-H stretching modes is also observed (not shown), consistent with amine chlorination. A slight blue shift in the C-N band, possibly indicates that TiCl₄ weakly and reversibly coordinates to the amine group.^{208–211}

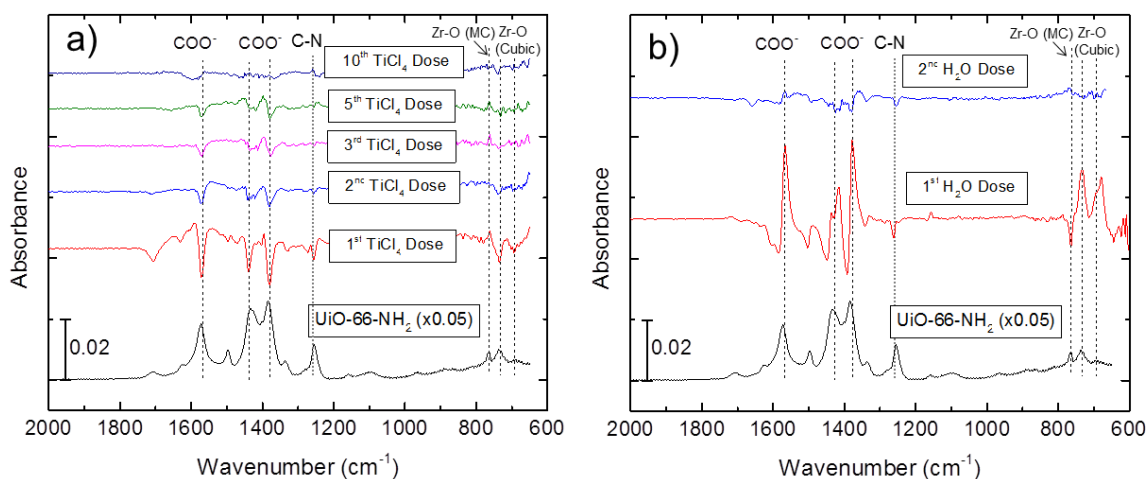


Figure 4.3: Differential FTIR spectra of hydroxylated UiO-66-NH₂ powders exposed to repeated exposures of a) TiCl₄ and b) H₂O at 150°C. The H₂O exposure in b) follows a TiCl₄ exposure equivalent to the first exposure in a). The starting UiO-66-NH₂ spectrum at 1/20th scale collected before any exposure is included in each panel as reference.

The TiCl_4 exposure also produces loss of the of the OH signal at 3668 cm^{-1} the Zr-O bands at 680 and 735 cm^{-1} and the COO^- signals at 1569 , 1417 , and 1380 cm^{-1} . There is also a small increase at 764 cm^{-1} . We note that the observed losses in the COO^- and OH signals, and changes in the Zr-O features follow the trend observed in Figure 4.2 for thermally-driven dehydroxylation. In this case, the dehydroxylation occurs at significantly reduced temperature (150 vs 250°C) and only within the near-surface of the MOF crystals accessed by the ALD precursor (vide infra). Between the 5th and 10th TiCl_4 exposure, the FTIR spectrum undergoes only very small changes, consistent with TiCl_4 reaction saturation.

Following TiCl_4 saturation, the effect of H_2O dosing on the FTIR spectra are given in Figure 4.3b. The initial dose of H_2O produces an increase of the COO^- and the OH signal, indicative of rehydroxylation of the metal node. The water exposure step also reverses the previously observed changes in the Zr-O features; the modes at 680 and 735 cm^{-1} increase, and the feature at 764 cm^{-1} decreases. These changes occur rapidly (on the scale of minutes) within the controlled time used for ALD reactant exposure. A further red-shift in the C-N signal also appears, consistent with weakening of the C-N bond by continued chlorination of the N-H by HCl produced during the second ALD half-reaction. A further H_2O dose results in only small changes in the FTIR signal, indicating rapid saturation for the H_2O reaction step.

In-situ QCM analysis was used to further assess individual precursor reactions with UiO-66- NH_2 . The QCM crystals were loaded with $25\text{-}100\text{ }\mu\text{g}/\text{cm}^2$ of UiO-66- NH_2 crystals and exposed to 10 doses of the ALD precursor followed by 10 doses of the H_2O co-reactant. Figures 4.4a and b show QCM traces collected during $\text{TiCl}_4/\text{H}_2\text{O}$ and TMA/ H_2O exposures,

respectively. Consistent with the FTIR results, saturation in mass uptake coincides with ~7 dose steps of TiCl_4 , and after TiCl_4 , one H_2O dose step is sufficient to completely react with the deposited TiCl_x species.

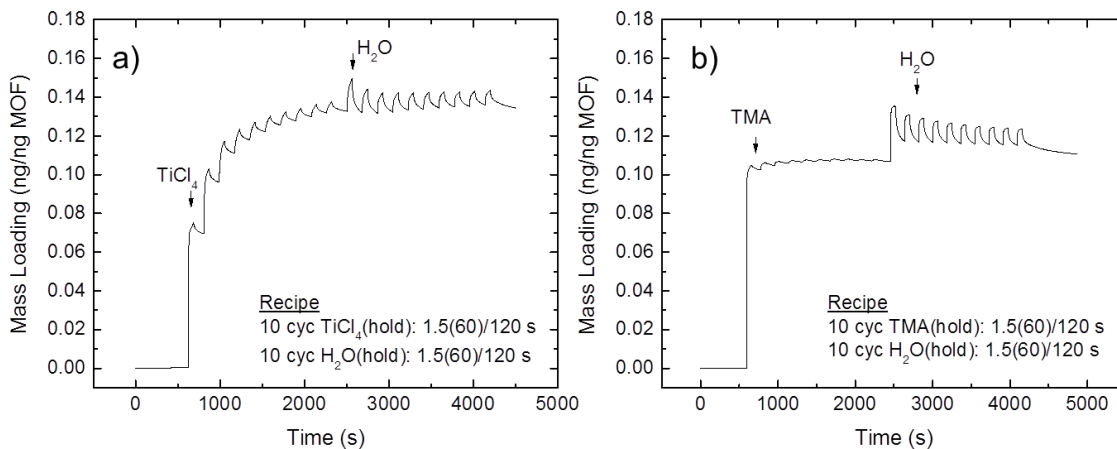


Figure 4.4: QCM analysis of a) repeated TiCl_4 /repeated H_2O and b) similar repeated doses of TMA and H_2O on hydroxylated UiO-66-NH_2 at 150°C .

Repeating this analysis with TMA shows that the reaction with UiO-66-NH_2 is nearly completely saturated after a single TMA exposure, producing a mass increase of 0.1 ng/ng MOF. Additional TMA exposure exhibited negligible increases in the sample loading. As with the TiCl_4 treated sample, one H_2O dose was sufficient to saturate the reaction with the deposited metal ALD precursor.

4.6.3 ALD Precursor Penetration into UiO-66-NH_2

A key question we seek to answer is: to what extent does the ALD precursor react with the available $\text{Zr}_6\text{O}_4(\text{OH})_4$ nodes on the surface and within the bulk of the MOF crystal? We

expected limited molecular diffusion into the MOF pores because the TMA and TiCl_4 molecules have an effective molecular radius of $\sim 4\text{\AA}$,^{212,213} which is close to the UiO-66- NH_2 channel opening dimension of $5\text{-}6\text{\AA}$.^{214,215} To evaluate the extent of precursor diffusion into the UiO-66- NH_2 crystal, we used FTIR to monitor the intensity of the OH band at $\sim 3665\text{cm}^{-1}$ before and after exposure to saturating doses of TiCl_4 and TMA. For the UiO-66- NH_2 crystals used here, the BET analysis shows the total surface area and the external crystal surface area are 1008 and $127\text{ m}^2/\text{g}$, respectively. Therefore, we estimate that full consumption of the hydroxyl groups on the crystal surface facets will decrease the overall OH signal by $\sim 13\%$. Figures 4.5a and b show FTIR spectra associated with the OH peaks before and after exposure to saturating doses TiCl_4 and TMA, respectively. After TiCl_4 exposure, the OH signal intensity decreases by approximately 24% , whereas the TMA leads to $\sim 9\%$ loss. This suggests that TiCl_4 partially diffuses into the MOF, whereas TMA reacts predominantly with hydroxyl sites available on the crystal surface with minimal diffusion into the MOF crystal itself.

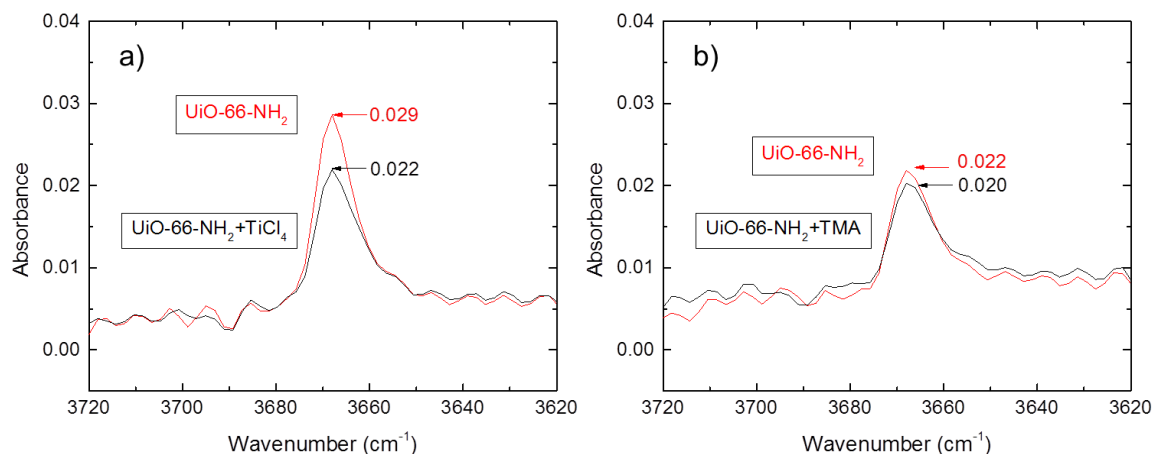


Figure 4.5: FTIR spectra of hydroxy stretching band of UiO-66-NH₂ prior to and following a) 10 TiCl₄ exposures and b) 3 TMA exposures, both at 150°C.

4.6.4 Sequential ALD precursor/water exposure steps on UiO-66-NH₂

The feasibility of continuous ALD on MOF substrates was assessed with FTIR. The differential FTIR spectra for the UiO-66-NH₂ for sequential exposures of TiCl₄/H₂O and TMA/H₂O are shown in Figure 5.6a and b respectively. Consistent with results in Figure 4.3, the TiCl₄ and TMA exposures lead to a decrease in COO⁻ and related changes in Zr-O bands. The addition of H₂O reverses the signal change, i.e. the COO⁻ and cubic Zr-O bands reemerge and the monoclinic Zr-O band signal decreases. This signal gain/loss behavior continued for at least 13 and 10 cycles for the TiCl₄/H₂O and TMA/H₂O processes respectively. This indicates that more than 10 ALD cycles are needed to encapsulate the MOF and block it from further reaction with the ALD precursors.

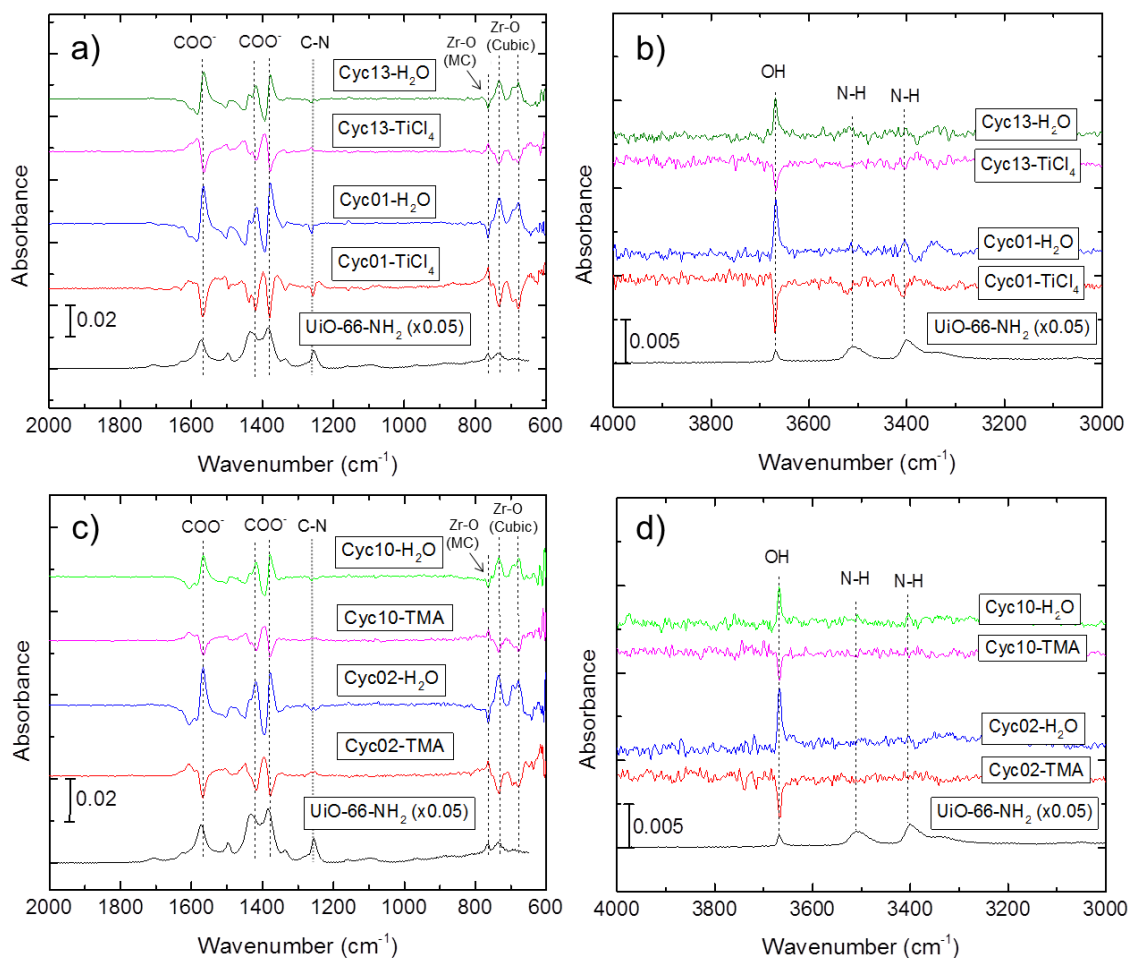


Figure 4.6: Differential FTIR spectra of carboxylate and hydroxyl regions following sequential exposures of a) and b) $\text{TiCl}_4/\text{H}_2\text{O}$ and c) and d) $\text{TMA}/\text{H}_2\text{O}$ on hydroxylated UiO-66-NH₂ at 150°C. The initial UiO-66-NH₂ spectrum is included as reference at 1/20th scale.

Figures 4.7a and b show QCM results collected during the first and subsequent precursor/water exposure cycles for TMA/water and $\text{TiCl}_4/\text{water}$, respectively. The first TMA and TiCl_4 doses produce a large net mass uptake ($\sim 0.1 - 0.2$ ng per ng of MOF), followed by smaller, but consistent mass uptake signals during the following reactant and

water exposures. During the first few cycles of steady state reaction (ALD cycles 5 and 6 in Figure 4.7b and e), the mass uptake during TMA and TiCl_4 exposures followed by mass loss during purging can be ascribed to precursor adsorption/desorption on the MOF at or near the external surface. Also during cycles 5 and 6, there is a more pronounced desorption step following the TiCl_4 exposure than the TMA exposure, which we attribute to the partial TiCl_4 diffusion into the MOF. The water exposure steps show similar trends for both sequences. Later in the steady-state process (ALD cycles 20 and 21 in Figures 4.7c and f), the mass uptake during all exposure steps is significantly smaller for the TMA/ H_2O process, consistent with ALD on a solid surface. In contrast, the TiCl_4 / H_2O process still shows significant mass uptake during the precursor exposures, suggesting that the TiCl_4 can penetrate and react more deeply within the MOF pores.

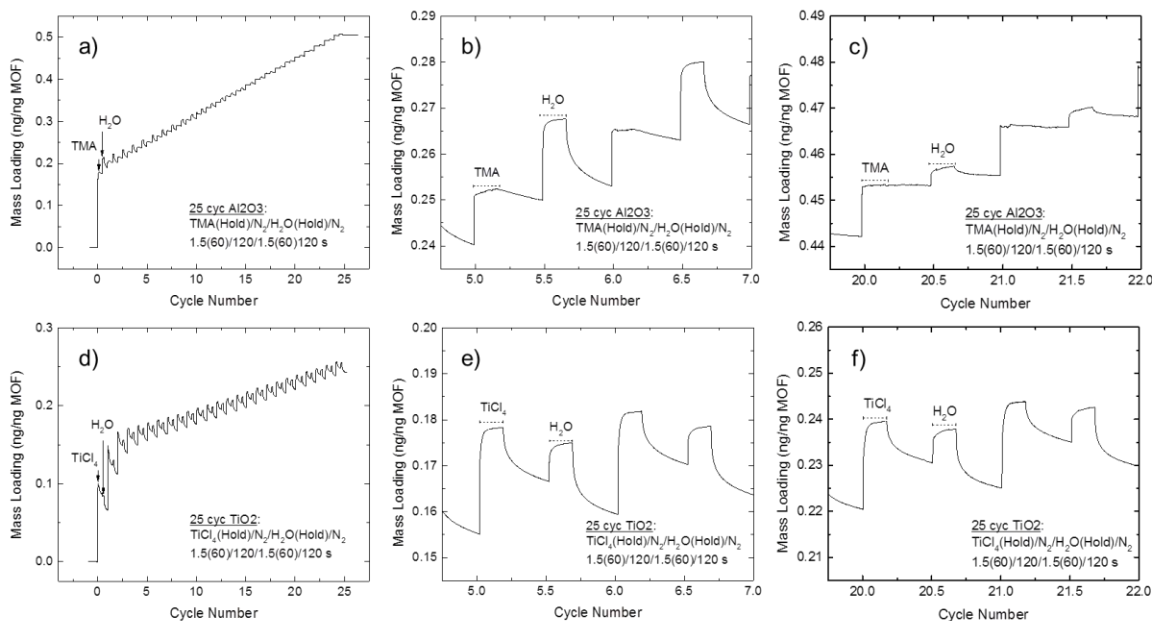


Figure 4.7: QCM analysis of sequential exposures of a) TMA/H₂O and d) TiCl₄/H₂O on hydroxylated UiO-66-NH₂ at 150°C. Panels b), c) and e), f) show expanded views of a) and d) respectively.

4.6.5 Interactions between ALD precursors and dehydroxylated UiO-66-NH₂

To better understand the role of the MOF hydroxyl sites on ALD growth, thermally dehydroxylated UiO-66-NH₂ was sequentially exposed to the ALD precursors to determine if the hydroxyl sites are necessary for precursor adsorption and reaction. Figure 4.8 shows the differential spectra for UiO-66-NH₂ following the first three sequential exposures to TiCl₄-H₂O and TMA-H₂O at 250°C. The FTIR spectra for the UiO-66-NH₂ switch between COO⁻ losses and gains with each subsequent exposure. There are prominent COO⁻ losses for the first TiCl₄ exposure, but for both the TiCl₄/H₂O and TMA/H₂O processes, the extent of feature changes at 250°C is less than that observed under similar exposures on the

hydroxylated MOF at 150°C (Figure 4.6). As expected at 250°C, for both TiCl_4 and TMA, the OH band at 3668 cm^{-1} is relatively small and does not switch with each subsequent exposure.

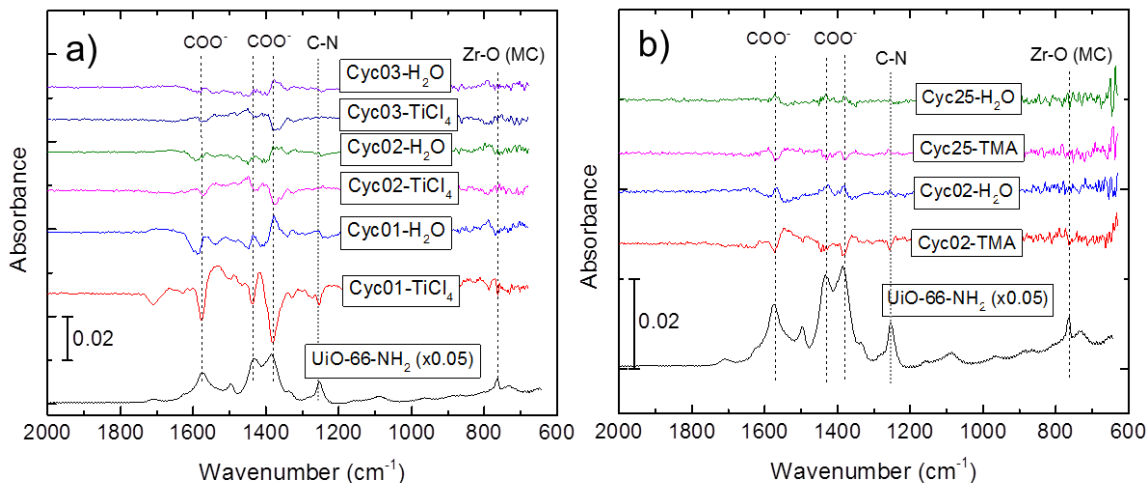


Figure 4.8: Differential FTIR spectra of dehydroxylated UiO-66-NH_2 at 250°C following sequential exposures to a) $\text{TiCl}_4\text{-H}_2\text{O}$ and b) $\text{TMA-H}_2\text{O}$. The initial UiO-66-NH_2 spectrum is included as reference at $1/20^{\text{th}}$ scale.

ALD film growth on dehydroxylated MOF was also monitored by QCM. Figure 4.9 shows QCM results for TiO_2 ALD on hydroxylated and dehydroxylated UiO-66-NH_2 at 150 and 250°C, respectively. As expected, removing the hydroxyl groups reduces the reactivity with TiCl_4 , most notably in the first few ALD cycles. However, the net mass change for one ALD cycle during steady state is approximately 0.004 ng per ng of MOF at both 150 and 250°C, suggesting that ALD film growth proceeds on the outer surface of both hydroxylated and dehydroxylated UiO-66-NH_2 . In Figure 4.9b, the expanded view of QCM results during cycles 5 and 6 shows mass gain during the precursor dose, followed by mass loss during the

purge step. As with the growth on the hydroxylated MOF, we ascribe this trend to precursor adsorption and diffusion into the near-surface region of the MOF followed by expulsion during the purge step. Similar QCM trends are reported during ALD on relatively non-reactive polymers, where subsurface diffusion and reaction readily occurs.²⁰

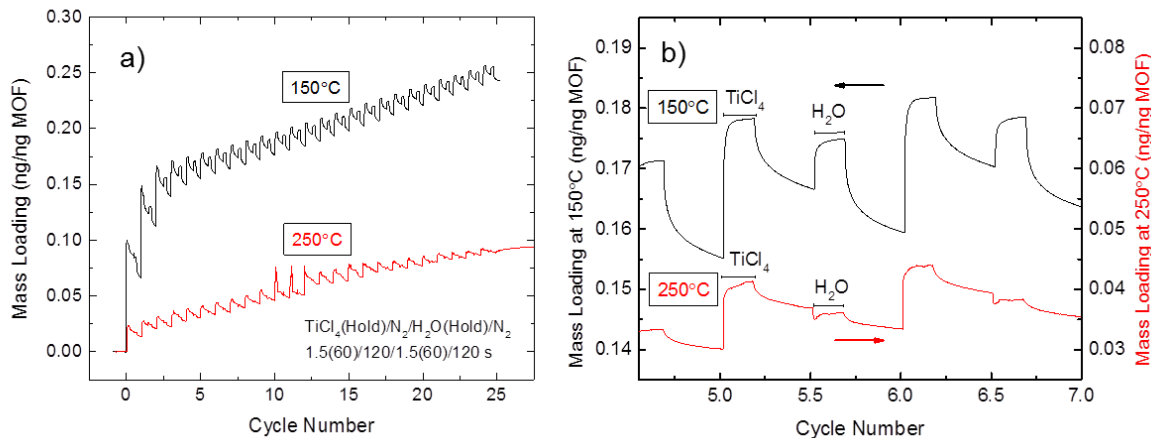


Figure 4.9: QCM analysis of sequential exposures of a) $\text{TiCl}_4\text{-H}_2\text{O}$ on hydroxylated UiO-66- NH_2 at 150 and on dehydroxylated UiO-66- NH_2 at 250°C, with b) showing an expanded view during cycles 5 and 6. The data at 150°C is reproduced from Figure 5.7.

4.6.6 *Ex-situ TEM characterization of ALD-modified UiO-66-NH₂*

The FTIR and QCM results suggest that ALD of Al_2O_3 and TiO_2 can proceed on the external surface of the UiO-66- NH_2 crystals. Results suggest, however, that the TMA reacts readily on the crystal surface, whereas the TiCl_4 tends to diffuse and react in the MOF near-surface region. To explore this result in more detail, we used TEM imaging to observe the structure of the ALD coatings on UiO-66- NH_2 as well as the nature of the ALD metal oxide/MOF

interface. Resulting TEM images are presented in Figures 4.10a and c for ALD Al_2O_3 and TiO_2 respectively, deposited at 150°C on UiO-66- NH_2 crystals.

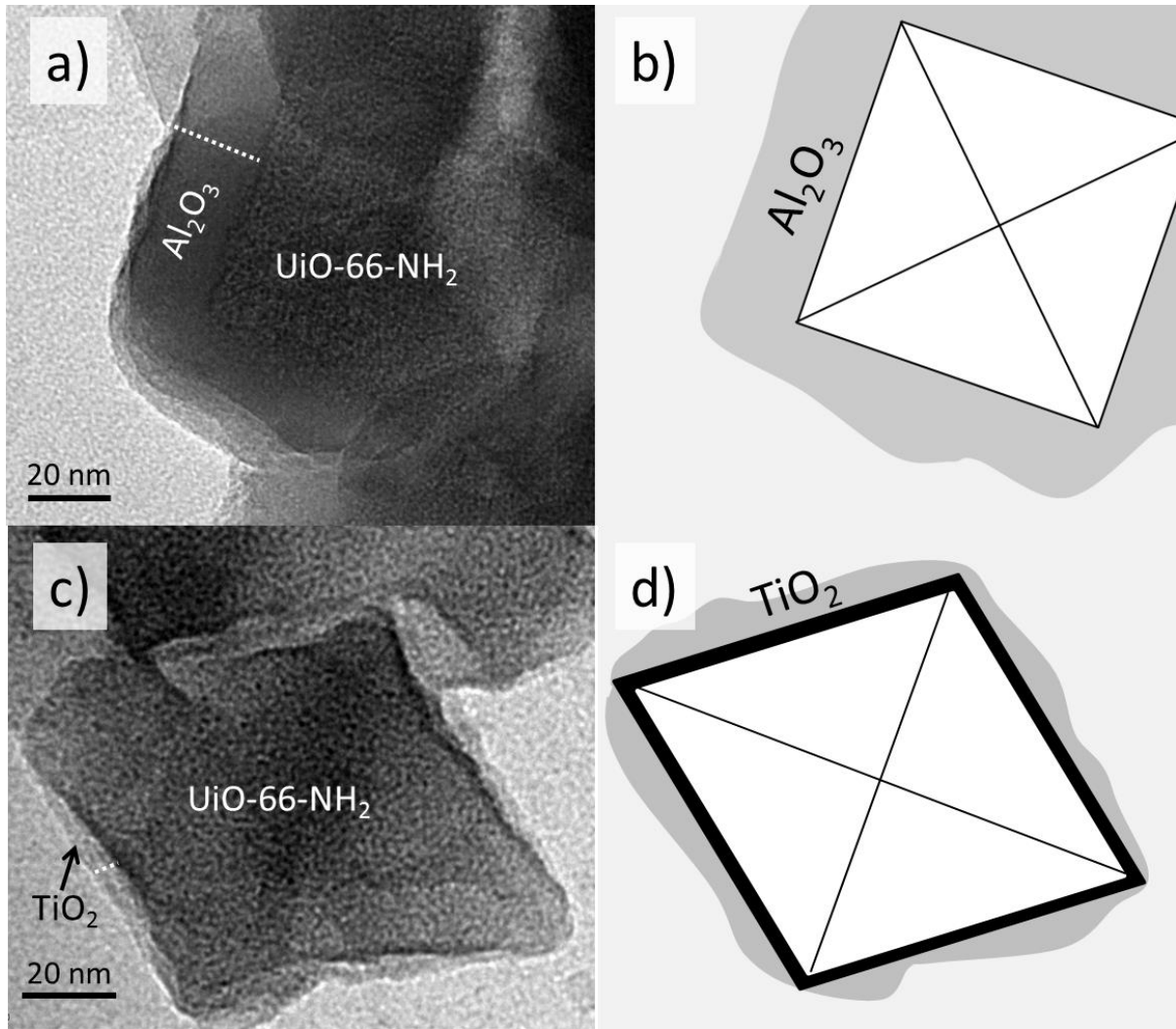


Figure 4.10: TEM images and corresponding diagrams of UiO-66- NH_2 with a) and b) 100 cycles of TMA/ H_2O and c) and d) 200 cycles of TiCl_4 / H_2O , both deposited at 150°C . The resulting TiO_2 and Al_2O_3 films were 20 and ~ 7.5 nm thick respectively, with TiO_2 -modified UiO-66- NH_2 exhibiting an interfacial layer.

At 150°C, the saturated growth per cycle for the ALD Al₂O₃^{20,23} and TiO₂¹⁰ processes used here are expected to be ~1.1 and ~0.4 Å per cycle, respectively. For the ALD layers on UiO-66-NH₂ in Figure 4.10a and c, 100 cycles of TMA/H₂O and 200 cycles of TiCl₄/H₂O produce coatings which are ~20 and ~7.5 nm thick. The thickness on TiO₂ is consistent with the predicted thickness, whereas the Al₂O₃ layer is thicker than expected. The excess Al₂O₃ growth is ascribed to the presence of water during the TMA exposure step. This could result from water that was not fully removed after MOF synthesis or from water infusion during the first few water dose steps before consolidation of oxide nuclei. Careful examination of the TEM images reveals that TMA/H₂O produces an atomically abrupt Al₂O₃/UiO-66 interface, whereas the TiCl₄/H₂O ALD leads to a graded interface, corresponding to a high contrast layer 1-2 nm thick at the boundary between the UiO-66-NH₂ and the ALD TiO₂. As discussed below, this interface layer can result from differences in active reactive sites for TMA and TiCl₄ on the UiO-66-NH₂ MOF, thereby helping TiO₂ to rapidly “seal” the MOF pores and reducing adverse effects associated with water adsorption during ALD.

4.7 Discussion

4.7.1 Precursor Reactions on Hydroxylated and Dehydroxylated UiO-66-NH₂

In a typical ALD reaction sequence for Al₂O₃ or TiO₂, the TMA or TiCl₄ precursors are expected to undergo ligand exchange with surface hydroxyls and in some cases can insert into available bridging oxygen sites.²¹⁶ Figure 4.2c shows molecular structures of the hydroxylated and non-hydroxylated zirconium metal cluster bound to the organic linker via the carboxylate groups. During ALD on the UiO-66-NH₂ MOFs, similar reactions could

proceed with: (1) the μ_3 -OH hydroxyl; and (2) the μ_3 -O bridging oxygen groups on Zr_6 nodes. For hydroxylated MOFs, open cluster sites on the crystal surface will present additional -OH groups, e.g. at missing linker sites or with physisorbed H_2O . As noted above, the pore opening dimension in the microporous UiO-66- NH_2 network will limit ALD precursor access, with near surface penetration depending on the nature of the precursor. This is supported by the structure of metal oxide/MOF interfaces observed here by TEM. On the other hand, Gallington et al. found that for NU-1000 MOFs with similar $Zr_6O_4(OH)_4$ nodes and larger pores, the ALD precursor diethyl zinc (DEZ) can penetrate through the MOF crystal, where it selectively reacts with terminal hydroxyls in the smaller pores. Related work by Gates et al. also found that hydrogen bound water and vicinal hydroxyl groups could also be removed and tuned with methanol vapor.¹⁰¹ The selectivity is ascribed to favorable dispersion force interactions between the organic linkers and the precursor ligands.¹⁹⁷

Carboxylate groups that bind the linker to the metal-oxide node, labeled as (3) in Figure 4.2c, provide another site for precursor interaction with the MOF. For example dye molecules readily bind to metal oxides via carboxylate or phosphate groups and ALD reactions with binding groups are known to enhance adhesion and bonding stability.²¹⁷⁻²¹⁹ FTIR analysis of ALD on carboxylate-linked Ru-dyes bound to TiO_2 ¹⁴² found a Lewis acid/base interaction for $TiCl_4$ and TMA with the carboxyl site. In separate studies, density functional modeling and FTIR also concluded Lewis acid/base adduct formation upon TMA interaction with carbonyl units in poly(methyl)methacrylate thin films.¹⁴³ All of these processes will likely proceed during ALD on MOFs, and within the regions of the MOF crystal that can be accessed by the

vapor reactant (i.e. on the surface of the MOF crystal in our case) and they are expected to substantively impact the node and linker binding structure.

As shown in the QCM results in Figures 4.4 and 4.7, exposing the fully hydroxylated UiO-66-NH₂ to TMA or TiCl₄ leads to rapid initial mass uptake, as expected for substantial reaction on the exposed crystal surface. Correlated FTIR data in Figures 4.3, 4.5 and 4.6 all show loss of the OH bands, consistent with ligand exchange at surface-accessible μ_3 -OH sites. The OH modes remaining after exposure (Figure 4.5) are within the MOF crystal bulk and are therefore not accessed by the ALD precursor. Careful inspection of the FTIR data in Figure 4.3 further reveals that in addition to OH loss, reaction with the ALD precursors produces a loss and blue-shift in the COO⁻ stretching modes and changes in the Zr-O modes stretching features, nearly identical to the changes observed in Figure 4.2 upon UiO-66-NH₂ thermal dehydroxylation. Interestingly, subsequent H₂O exposure after TiCl₄ reverses the COO⁻ mode blue-shift and Zr-O loss, returning the modes to their original position before precursor exposure.

Analysis of the ALD reaction on the dehydroxylated MOF leads to further insight. A lack of hydroxyl groups will impede metal oxide ALD initiation on metal oxide surfaces.¹⁰ As anticipated therefore, we see by QCM (Figure 4.9) that dehydroxylating the UiO-66-NH₂, leads to less mass uptake during the initial TiCl₄ doses. However, even with reduced extent of reaction, the COO⁻ modes in Figure 4.9 show a blue-shift after TiCl₄ and TMA dosing, and like on the hydroxylated MOF, subsequent H₂O exposure steps reverses the COO⁻ mode blue-shift. Moreover, the extent of the change, as estimated by the intensity of the difference

spectra, is similar for the hydroxylated and dehydroxylated materials as summarized in Figure 4.11. In addition, Figure 4.11 also shows that annealing UiO-66-NH₂ causes a much larger loss of the COO⁻ and Zr-O modes than the TiCl₄ exposure at 150°C, reconfirming that the TiCl₄ reaction occurs predominantly at the MOF surface and near-surface regions, while annealing occurs throughout the MOF crystal bulk. We also note that the Zr-O modes are not strongly affected by precursor or water exposure steps at 250°C.

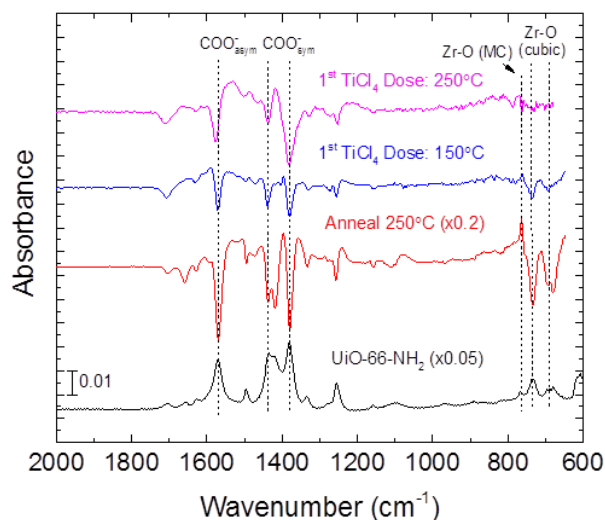


Figure 4.11: Differential FTIR spectra comparing dehydroxylation of UiO-66-NH₂. The spectra of the samples after annealing is shown at 1/5th its actual scale. The initial UiO-66-NH₂ spectrum is included as reference at 1/20th scale.

4.7.2 Reversible Surface Node Distortion during ALD on UiO-66

Based on the above analysis we assert that during ALD on UiO-66 MOFs, TiCl₄ and TMA reacts on the Zr₆ nodes at accessible μ_3 -OH and μ_3 -O bridging sites via ligand exchange and insertion respectively, as well as at COO⁻ sites on accessible linker groups, likely through

acid/base adducts. At low temperature (150°C) on the hydroxylated $Zr_6O_4(OH)_4$ sites, the precursor reaction appears to promote distortion of the Zr-O bonding that is rapidly reversible (within the ~1 min upon subsequent water vapor exposure). This node distortion has an FTIR spectral signature²⁰⁵ consistent with previously observed irreversible node transition from cubic to monoclinic symmetry that occurs at higher temperatures upon thermal dehydroxylation.⁹⁹ The reversibility in this case may reflect the extra degrees of freedom afforded the surface-terminal nodes on the exposed MOF crystal.

4.8 Conclusion

In this work we report site-specific reactions during conformal nanoscale metal oxide coating on UiO-66-NH₂ MOF via atomic layer deposition. The ALD precursors TMA and TiCl₄ react with μ_3 -OH hydroxyl and μ_3 -O bridging oxygen groups on Zr₆ nodes, as well as oxygen from carboxylate linker groups, at sites accessible at or near the crystal terminal surface. When the MOF metal-oxide nodes are hydroxylated, $Zr_6O_4(OH)_4$, low temperature ALD precursor reaction promotes changes in linker bonding a reversible structure transition in Zr-O nodes exposed on the crystal face. When UiO-66-NH₂ is thermally dehydroxylated before ALD, precursor exposure modifies the linker units, consistent with precursor/linker Lewis acid/base interactions, but the FTIR shows no visible change in the Zr-O network, consistent with stable conformational rearrangement during the pre-deposition thermal exposure. We also see distinctions between precursors during ALD on MOFs. From the QCM, FTIR, and TEM data, the TMA as a strong Lewis acid reacts readily on the MOF crystal surface to block transport and promote an atomically sharp metal oxide/MOF interface. However, the TiCl₄

can transport a short distance into the MOF crystal before reacting, leading to a more graded oxide/MOF interface. Low temperature modification or encapsulation of UiO-66-NH₂ has significant implications for catalytic applications and long term storage of MOF materials.

4.9 Acknowledgement

The authors acknowledge the use of the Analytical Instrumentation Facility (AIF) at North Carolina State University, which is supported by the State of North Carolina and the National Science Foundation.

**CHAPTER 5. RAPID VISIBLE COLOR CHANGE AND PHYSICAL SWELLING
DURING WATER EXPOSURE IN TRIETHANOLAMINE-METALCONE FILMS
FORMED BY MOLECULAR LAYER DEPOSITION**

The following work is reproduced with permission from Paul C. Lemaire, Christopher J. Oldham, and Gregory N. Parsons. “Rapid Visible Color Change and Physical Swelling during Water Exposure in Triethanolamine-Metalcone Films Formed by Molecular Layer Deposition.” *Journal of Vacuum Science and Technology A: Vacuum, Surfaces, Film.* **2016**, 34, 01A134.

5.1 Abstract

Molecular layer deposition (MLD) of “metalcones”, including alucone, zincone, titanicone and others, involves self-limiting half-reactions between organic and organometallic (or metal-halide) reactants. Studies have typically focused on metal precursors reacting with ethylene glycol or glycerol to form the films’ polymeric O-M-O-(CH_x)_y-O-M-O repeat units. We report new MLD materials that incorporate tertiary amine groups into the organic linkage. Specifically, reacting triethanolamine (TEA) with either trimethylaluminum (TMA) or titanium tetrachloride (TiCl₄) produces TEA-alucone (Al-TEA) and TEA-titanicone (Ti-TEA), respectively, and the amine group leads to unique physical and optical properties. FTIR analysis confirms that the films have prominent C-H, C-N and M-O-C peaks, consistent with the expected bond structure. When exposed to vapors, including water, alcohol, or ammonia, the Ti-TEA films changed their visible color within minutes and increased physical thickness by >35%. The Al-TEA showed significantly less response. X-ray photoelectron spectroscopy (XPS) and FTIR suggest that HCl generated during MLD

coordinates to the amine forming a quaternary ammonium salt that readily binds adsorbates via hydrogen bonding. The visible color change is reversible, and ellipsometry confirms that the color change results from vapor absorption. The unique absorptive and color-changing properties of the TEA-metalcone films point to new possible applications for MLD materials in filtration, chemical absorption, and multifunctional chemical separations/sensing device systems.

5.2 Introduction

Molecular layer deposition (MLD) of “metalcones”, including alucone,^{44,45} zincone,^{46,47} titanicone,⁴⁸ and others,^{49,50} involves self-limiting half-reactions between organic and organometallic (or metal-halide) reactants. Most film reaction studies to date have focused on metal precursors reacting with ethylene glycol,^{44–46,48–50} glycerol,^{48,51} glycidol,⁵² and various carboxylic acids,^{53–55} generally leading to polymeric O-M-O-(CH_x)_y-O-M-O repeat units as determined by spectroscopic and other analyses.

In their as-deposited form some of these materials are unstable when exposed to ambient atmosphere, resulting in film thickness decrease and bonding degradation.²²⁰ The degradation could result from evolution of unbound organic oligomers or metal oxide species dehydrating or dehydrogenating the organic portion of the metalcone film.^{44,220,221} Metalcone films have multiple possible applications including flexible electronics,⁴⁷ sacrificial films to form conductive carbon-rich⁵⁶ or porous oxide films,^{57,58} encapsulation and protective layers on chemically reactive fibers, and antireflective coatings.⁴⁴ These and other applications will

benefit from more options for MLD material composition and improved understanding of how MLD films interact with the ambient.

In this work, we report unique properties of metalcone thin films formed using triethanolamine, TEA. The TEA is used in a saturated MLD reaction sequence with either Trimethylaluminum (TMA) or titanium tetrachloride (TiCl_4) to form “TEA-alucone”, Al-TEA, or “TEA-titanicone” Ti-TEA thin films, respectively. The Ti-TEA and Al-TEA films are generally stable in air, and upon exposure to vapors (including water, methanol, ethanol, and ammonia) ellipsometry and visual reflectivity show the Ti-TEA undergoes rapid and reversible vapor absorption, whereas the Al-TEA films remain relatively unchanged. We discuss mechanisms to account for the material-dependent vapor adsorption as well as possible novel applications for these materials.

5.3 *Experiment*

5.3.1 *MLD Precursors and Materials*

Trimethylaluminum (TMA) and titanium tetrachloride (TiCl_4) were obtained from Strem Chemicals Inc. and used without further treatment. Anhydrous triethanolamine (TEA) (Sigma-Aldrich) was used as the organic material source and dried through vacuum pumping at room temperature. 12.1 M hydrochloric acid concentrate (HCl) was purchased from Fisher and used as received. We monitored the MLD deposition with silicon wafers [100] purchased from WRS Materials. For the carrier and purge gas, dry nitrogen (99.999%) was passed

through an Entegris GateKeeper inert gas purifier to remove any residual water before entering the reactor.

5.3.2 *Reactor setup for triethanolamine-metalcone deposition.*

Molecular layer deposition of the triethanolamine-metalcone thin films was carried in a homemade hot wall viscous flow vacuum reactor. The nitrogen carrier gas flow rate was maintained at 280 standard cubic centimeters per minute (sccm) for an operating pressure of ~850 mTorr. The inlet and outlet gas lines were temperature controlled with heat tape to prevent precursor condensation in the reactor. The TEA precursor was loaded into a glass flow-over bubbler and heated to 130°C. The TiCl₄, TMA, and HCl precursor bottles were maintained at room temperature.

A typical MLD cycle followed a TMA/N₂/TEA/N₂ sequence (abbreviated as TMA/TEA) with exposure and purge times of 0.1/30/2/45 seconds respectively. In addition to this process sequence, we also explored the effect of vapor HCl dosing on film composition. For the HCl studies, the cycle followed with a TMA/N₂/TEA/N₂/HCl/N₂ sequence (written as TMA/TEA/HCl) with respective times of 0.1/30/2/45/0.1/30 seconds.

Various MLD process conditions were further characterized using in-situ quartz crystal microbalance (QCM) analysis. For these tests, a 6 Hz gold coated QCM crystal sensor (Inficon) was mounted onto the QCM housing with conductive epoxy as previously described.⁴⁶ The epoxy and a dry N₂ crystal back purge of 50 sccm prevented deposition on

the backside of the QCM crystal. The mass change signals were detected by an Inficon SQM-160 monitor and recorded using a home designed LabVIEW program

5.3.3 *Ex-situ characterization.*

The TEA-metalcone film thickness and refractive index at 632.3 nm was measured with a variable-angle alpha-SE spectroscopic ellipsometer (J.A. Woollam Co., Inc.). Ellipsometric measurements were taken after allowing samples to sit at the laboratory temperature and humidity for 15 minutes. We collected humidity-controlled ellipsometry measurements by enclosing the ellipsometer in a sealed Plexiglass case fitted with a humidifier, dry nitrogen (99.999%) gas supply and a humidity sensor and recorder (Omega).

The advancing water contact angle was monitored as a function of time using a Model 200 Rame-Hart contact angle goniometer. The time span was short (<10 seconds) and the water drop was sufficiently large (2–4 mm) so that water evaporation was not significant.

Film composition was characterized using XPS and FTIR analysis. A SPECS X-ray photoelectron spectrometry system operated with an Al anode at 10 kV and 400 W with a PHOIBOS 150 analyzer with a detection limit of ~0.1 at% provided elemental analysis of the deposited films. The collected data was subsequently processed and modeled with CasaXPS software to give elemental analysis. Fourier transform infrared spectroscopy (FTIR) was performed with a ThermoNicolet 6700 IR bench with a deuterated triglycine sulfate detector operated in transmission mode with 2050 scans at 4 cm⁻¹ resolution.

We monitored the color change and mass loading of the deposited TEA-metalcone films by fixing the samples inside a sealed quartz tube and observing the sample visually or monitoring mass change upon exposure to various vapors of interest at atmospheric pressure. Before analysis, the quartz was prepared under dry nitrogen flow. Samples were then placed in the tube and treated under dry nitrogen (99.999%) gas flow at room temperature for 2 hours. To begin exposure, the nitrogen carrier gas was diverted through a bubbler containing water, methanol, or ethanol for 1 minute followed by purging with the dry carrier gas. Ammonia exposure was also performed in the same system using a 5 second exposure to ammonia gas. Color change was monitored via photographic imaging. Mass loading was monitored in the same apparatus via QCM analysis using crystals coated with 500 cycles (250-300 nm) of the TEA-metalcone films.

5.3.4 *Results*

5.3.4.1 *Deposition of triethanolamine-metalcone films*

The proposed reaction scheme for the Al-TEA is shown in Figure 5.1 and discussed in detail in the discussion section. To investigate the validity of this reaction scheme and confirm self-limiting growth, we varied the precursor dose time and monitored film thickness after deposition using ellipsometry. Figure 5.2 shows the growth thickness per cycle as a function of TMA and TEA dose time for the Al-TEA formed at 150°C. The Al-TEA film growth saturates near 7 Å per cycle after 0.1 seconds of TMA exposure, but 3 seconds of TEA exposure is needed to achieve the same growth. For the Ti-TEA process, Figure 5.3 shows a similar trend for TiCl₄ and TEA plateaus after a 4-5 seconds exposure. A longer exposure

time is needed for TEA due to its relatively low vapor pressure (0.01 T at 20°C), and effects of precursor retention within the depositing MLD film.^{44,52,55} These trends, including ‘soft’ saturation in the organic exposure step, are consistent with those reported for other MLD processes.^{44,52,55} To achieve well-controlled and reproducible growth, we maintained the TEA exposure at 2.0 sec, slightly below full saturation. Figure 5.2 and 5.3 also show the film thickness as measured by ellipsometry versus MLD cycle number for the Al-TEA and Ti-TEA films. At set deposition temperature and dose times, the film thickness is linearly dependent on the cycle number with growth thickness per cycle of 6.7 and 5.1 Å/cycle for the Al-TEA and Ti-TEA respectively.

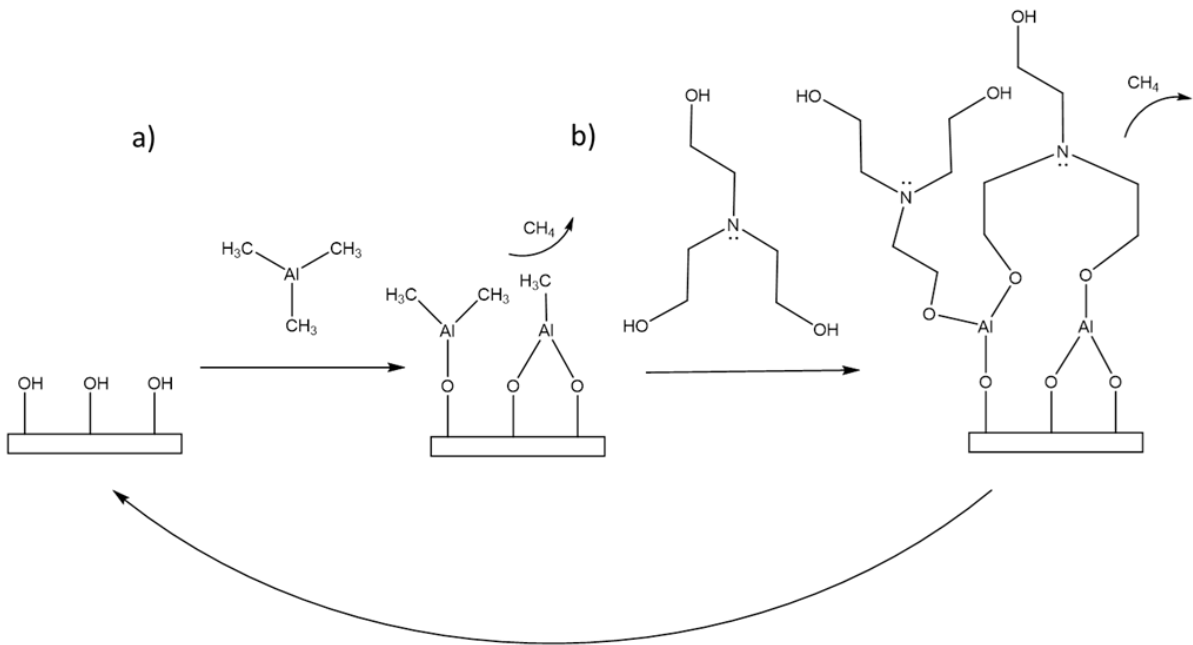


Figure 5.1: Al-TEA reaction sequence with successive a) TMA and b) TEA exposure

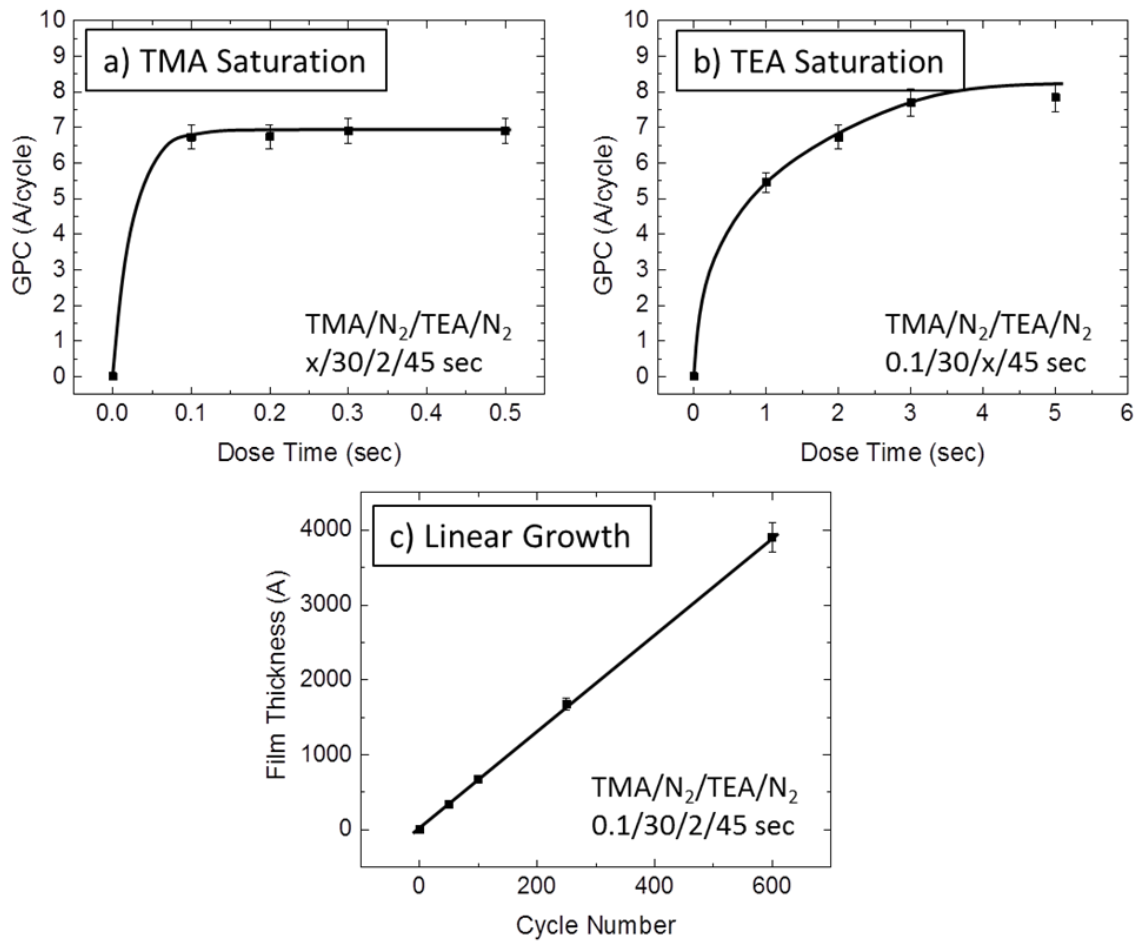


Figure 5.2. Al-TEA film thickness per cycle at 150°C as a function of a) TMA and b) TEA dose time and c) film thickness versus cycle number. Lines are meant to guide eyes.

The growth rate was studied over a temperature range of 150 to 195°C and results are given in Figure 5.4. From 150°C to 195°C, the Al-TEA growth per cycle decreased from 6.7 to 0.8 Å/cycle at 195° Ti-TEA film growth rate also decreases at higher temperatures from 5.2 at 150°C to 2.0 Å/cycle at 195°C.

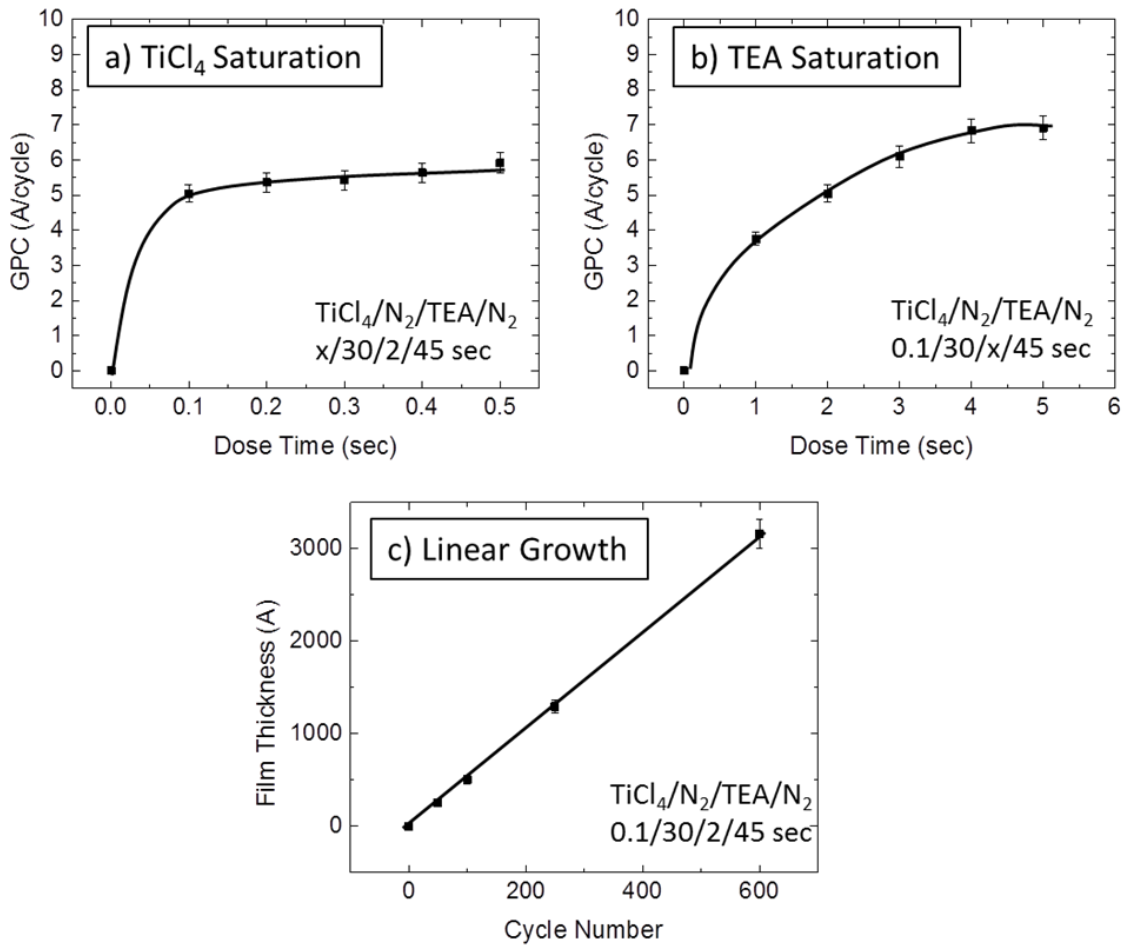


Figure 5.3: Ti-TEA film thickness per cycle at 150°C as a function of a) TiCl₄ and b) TEA dose time and c) film thickness versus cycle number. Lines are meant to guide eyes.

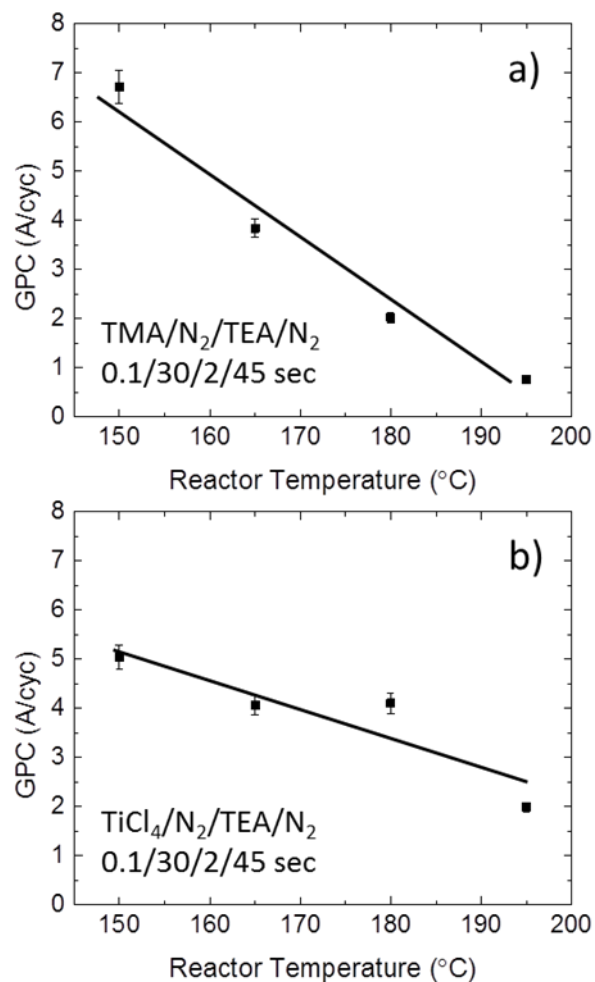


Figure 5.4: Growth rate versus reactor temperature for a) Al-TEA and b) Ti-TEA. Lines are meant to guide eyes

Figure 5.5 shows in-situ QCM analysis demonstrating the mass changes during the metal and TEA exposure steps. Under steady-state MLD at 150°C, Figures 5.5a and b show a mass gain of approximately 65 and 95 ng/cm²/cycle during the TMA and TiCl₄ exposure, respectively. During the TEA exposure, the Al-TEA film (Figure 5.5a) shows a mass gain close to 25 ng/cm²/cycle while the gain is near zero for TEA exposure during Ti-TEA growth

(Figure 5.5b). Figures 5.5c and d show analogous results collected at 200°C. Increasing temperature leads to a significant decrease in the TMA mass uptake (30 ng/cm²/cycle at 200°C) whereas for TiCl₄ the mass uptake decreases only slightly to 75 ng/cm²/cycle. In both processes, increasing the temperature to 200°C decreased the TEA mass uptake per cycle.

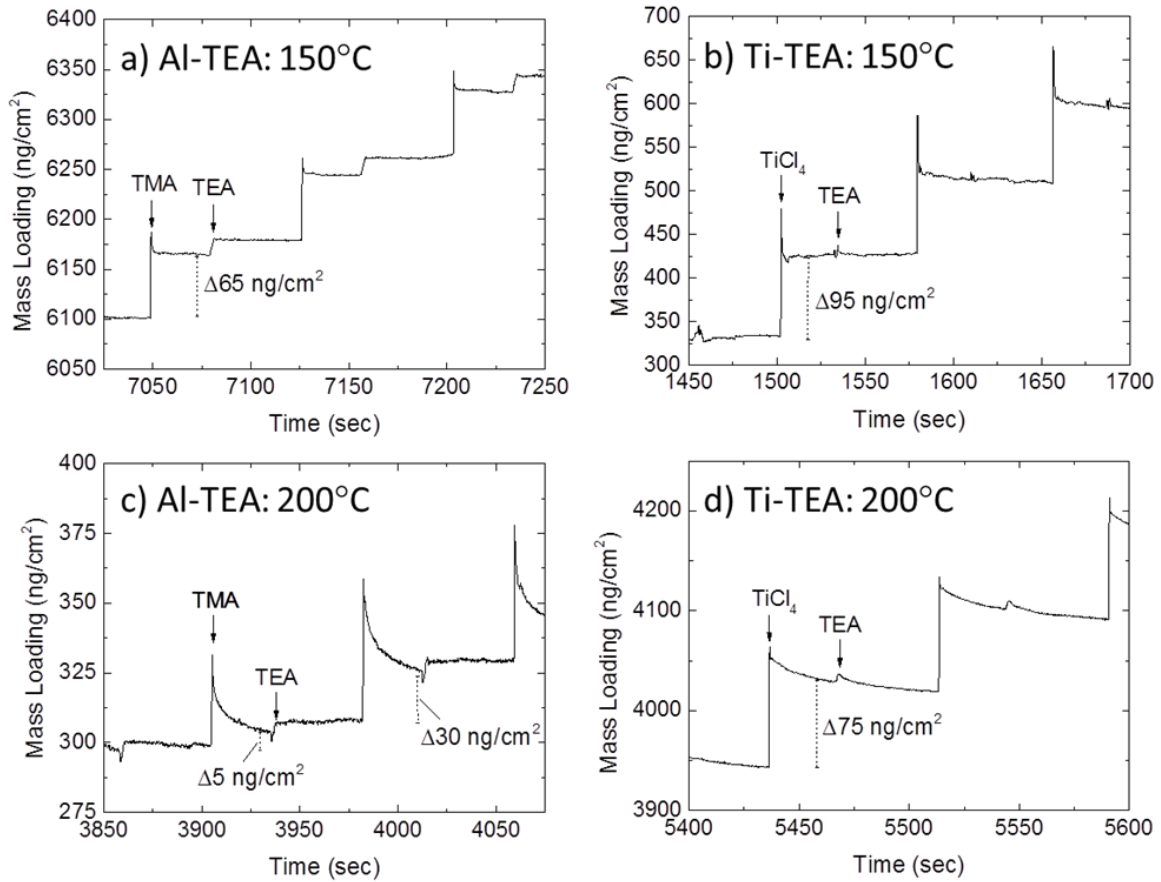


Figure 5.5: Quartz crystal microbalance (QCM) analysis: a) Al-TEA at 150°C, b) Ti-TEA at 150°C, c) Al-TEA at 200°C, d) Ti-TEA at 200°C.

5.3.5 *Characterization of triethanolamine-metalcone films*

We used FTIR analysis to assess the composition of the triethanolamine-metalcone films as shown in Figure 5.6. The bands at 1064 and 1015 cm^{-1} are attributed to the Ti-O-C and Al-O-C linkages respectively, consistent with the expected organic-inorganic amorphous network structure. This is further supported by the broad C-H stretch from 2962-2875 cm^{-1} , the C-H scissoring at 1456 cm^{-1} , and the Ti-O and Al-O bands at 630 and 669 cm^{-1} respectively. There are also large hydroxyl bands from 3700-3000 cm^{-1} , indicating that the triethanolamine-metalcone films have a significant amount of unreacted hydroxyl sites. The sloping background at 2000–3000 cm^{-1} in the Ti-TEA spectrum results from background subtraction. We also observe a small peak at 1226 cm^{-1} for the C-N bond showing that the amine functionality is maintained, predominantly in the Ti-TEA material. Finally, the FTIR data shows a significantly different N-H bending mode structure. For the Ti-TEA film, clear bands are visible at 1633 and 1392 cm^{-1} associated with N-H bending. For the Al-TEA film, the N-H bending modes at 1633 and 1392 cm^{-1} are much less intense. The stronger N-H modes in the Ti-TEA film suggesting that the tertiary amine is protonated during the Ti-TEA MLD process.

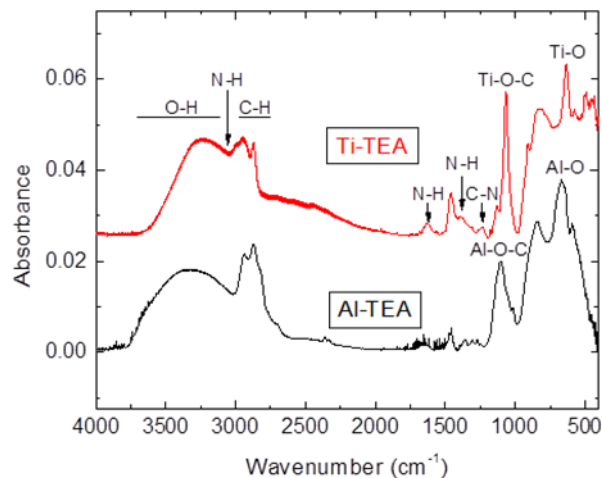


Figure 5.6: Mid-range FTIR spectra for ~300 nm Al-TEA and Ti-TEA films deposited at 150°C.

We used XPS analysis to quantify atomic compositions, and results are given in Table 5.1 and Table 5.2. The table compares atomic composition values derived from XPS to values estimated from the expected organic-inorganic network composition, $\text{Ti}_3(\text{TEA})_4$ ($\text{Ti}_3(\text{C}_6\text{H}_{12}\text{NO}_3)_4$) and $\text{Al}(\text{TEA})$ ($\text{Al}(\text{C}_6\text{H}_{12}\text{NO}_3)$). For Ti-TEA, the experimental and expected film composition corresponds well, except for ~7 at. % chlorine observed in the deposited films. For the Al-TEA, the trends are similar, except the experiment shows less carbon and more oxygen than expected. This result may indicate TMA hydrolysis of the organic reactant.^{44,220,221} Excess water vapor in the organic precursor could also increase oxygen and decrease carbon content, and the effect may be more prevalent in the Al-TEA process due to higher reactivity of water with TMA vs TiCl_4 .

Table 5.1. Experimental film composition (± 2 at. %) based on high resolution XPS scans of ~ 300 nm Ti-TEA films deposited at 150°C . Expected atomic composition based on the stoichiometric composition: $\text{Ti}_3(\text{C}_6\text{H}_{12}\text{NO}_3)_4$.

Ti-TEA	C 1s	O 1s	N 1s	Ti 2p	Cl 2p
Experimental (at. %)	49	29	8	8	7
Expected (at. %)	56	28	9	7	0

Table 5.2. Experimental film composition (± 2 at. %) based on high resolution XPS scans of ~ 300 nm Al-TEA films deposited at 150°C . Expected atomic composition based on the stoichiometric composition: $\text{Al}(\text{C}_6\text{H}_{12}\text{NO}_3)$.

Al-TEA	C 1s	O 1s	N 1s	Al 2p	Cl 2p
Experimental (at. %)	29	50	4	16	1
Expected (at. %)	55	27	9	9	0

The high resolution XPS scans in Figure 5.7 also show the presence of some chlorine in the Al-TEA film. The high resolution scan of the nitrogen 1s for Al-TEA shows a single peak at 398.6 eV, attributed to carbon-nitrogen bonding. In comparison, high resolution analysis of nitrogen in the Ti-TEA film shows two peaks at 399.0 and 400.9 eV. The peak at 399.0 eV is again due to nitrogen-carbon bonds, while the peak at 400.9 eV signifies formation of quaternary nitrogen.^{222–224}

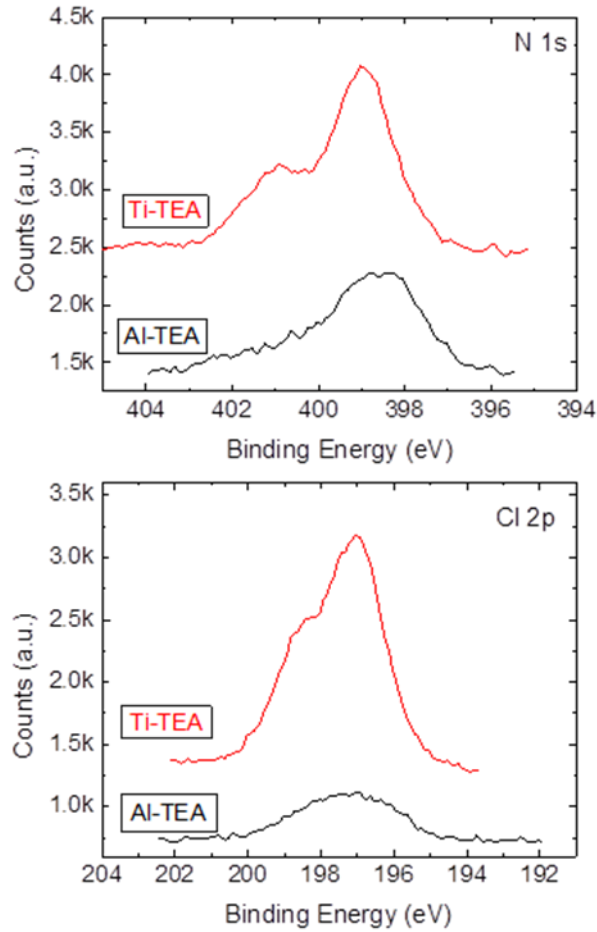


Figure 5.7: High resolution XPS scans of Cl 2p and N 1s peaks for the ~300 nm Al-TEA and Ti-TEA films deposited at 150°C.

5.3.6 *Triethanolamine-metalcone film stability*

A common issue for similar metalcone MLD films is film degradation. We monitored the stability in ambient conditions by measuring the film thickness and refractive index over the course of 25 days. After 24 hours, the Ti-TEA film thickness decreased by 6.2% and 14.1% after 500 hours as shown in Figure 5.8a. In comparison the Al-TEA film thickness increased by 5.1% after 24 hours to a film thickness of 1417 Å which stayed relatively constant over

500 hours. This small increase in film thickness is likely attributed to film swelling in the ambient laboratory conditions. We theorize that the Al-TEA film thickness was relatively stable because any film degradation occurred primarily during the deposition process. To augment the thickness measurements, we also tracked the refractive index of the films at 632.8 nm in order to provide an estimate of changes in film density. Figure 5.8b conveys that the refractive index of the Ti-TEA film increases over time, consistent with the film partially degrading to form TiO_2 . The Al-TEA refractive index decreases initially, again consistent with higher water content in the film and then remained relatively constant with time.

We also monitored the film stability in the dry heated reactor immediately following deposition. Figure 5.9 includes in-situ QCM results for 100 cycles of the triethanolamine-metalcone films deposited at 150°C and then left in the heated reactor for approximately 14 hours with flowing carrier gas. The Al-TEA film thickness stays relatively constant over the course of the 14 hour time period, but the Ti-TEA mass loading decreases by $\sim 25\%$. These results in conjuncture with the previously discussed results suggest that the Al-TEA is more stable than the Ti-TEA film and that the Ti-TEA film degradation occurs regardless of relative humidity.

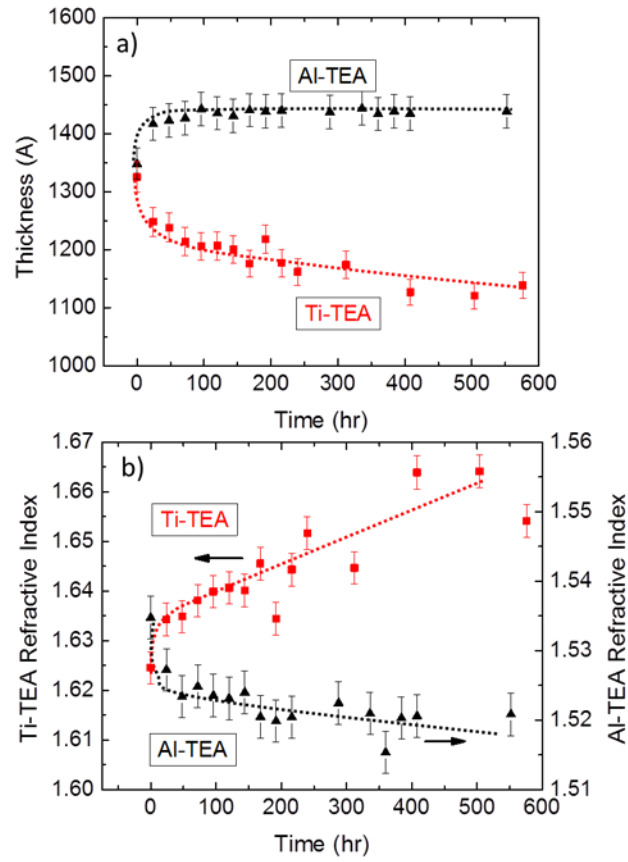


Figure 5.8: Changes in triethanolamine-metalcone film a) thickness and b) refractive index at a wavelength of 632.8 nm over time in open laboratory conditions. Lines are meant to guide eyes.

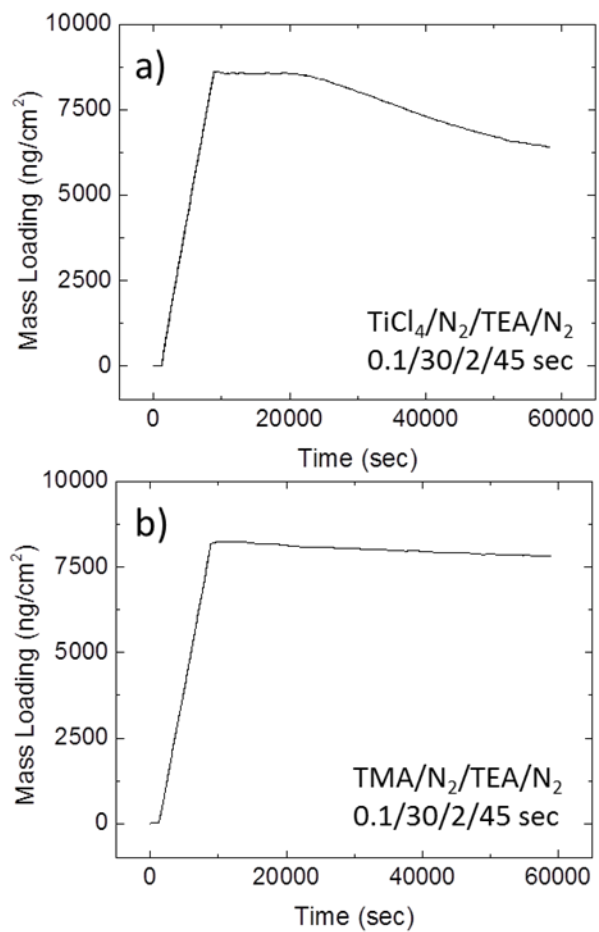


Figure 5.9: QCM results of 100 cycles of a) Ti-TEA and b) Al-TEA films deposited at 150°C which then remain in the heated conditions with flowing carrier gas for ~14 hours.

5.3.7 Surface energy and physical swelling of triethanolamine-metalcone films

We assessed the surface energy of ~300 nm thick Al-TEA and Ti-TEA MLD films via time-resolved goniometric analysis, shown in Figure 5.10. The contact angle for the water droplet immediately decreases upon contact to the Ti-TEA film, decreasing from 42.2 to 26.1° within 5 seconds. The Al-TEA in comparison maintained a relatively constant contact angle of 38.4°. The water droplet contact angle on a native silicon oxide is ~28° indicating that the Al-TEA film is more hydrophobic, likely due to surface roughening.^{21,225}

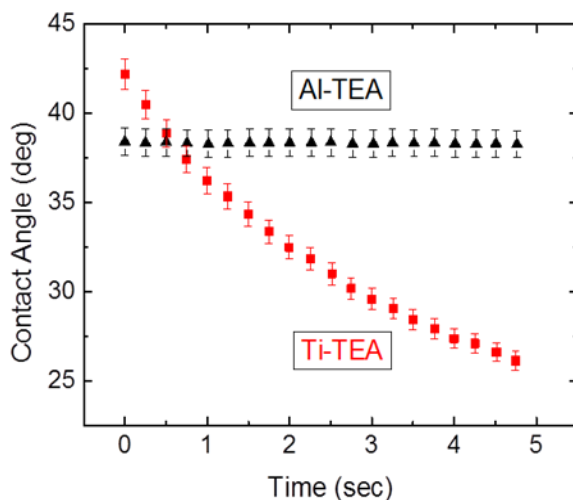


Figure 5.10: Time-resolved goniometric analysis monitoring the water droplet contact angle versus time on ~300 nm Al-TEA and Ti-TEA films deposited at 150°C.

We observed that the triethanolamine-metalcone films exhibited a visual color change immediately upon removing the samples from the heated reactor. This color change was attributed to changes in the film thickness due to film swelling. To test this theory, we monitored the film thickness in a humidity controlled environment. Figure 5.11 shows the

film thickness versus humidity for the two triethanolamine-metalcone films that were approximately 300 nm thick. From 10-65% relative humidity, the Ti- film thickness significantly changes, increasing from 207.0 to 346.9 nm, a ~75% increase in thickness. Accompanied by this thickness change was a visual color change. Figure 5.12 shows images of a Ti-TEA film in a dry environment and changing color after prolonged exposure to a humid environment. The shrinking and swelling behavior was reversible and repeatable unless the relative humidity exceeded ~65%, which lead to film degradation. The Al-TEA film thickness dependence on humidity is significantly lower than the Ti-TEA film in Figure 5.11. The Al-TEA film thickness increases from 266 to 276 nm as the humidity is increased from 10% to 65%, an increase of ~3%.

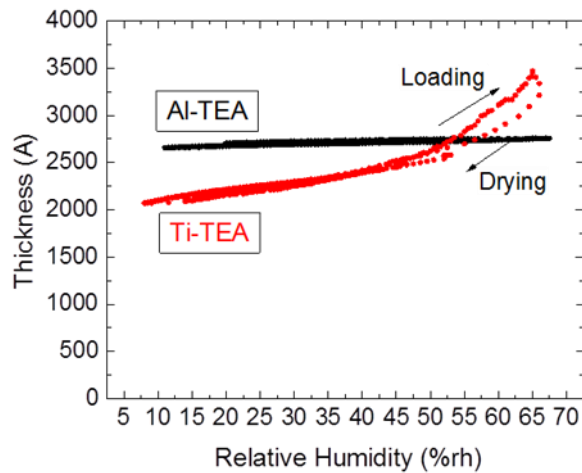


Figure 5.11: Thickness of Al-TEA and Ti-TEA films versus relative humidity.



Figure 5.12: Images of a 500 cyc Ti-TEA film in which the process humidity increases from a) $< 1\%$ relative humidity, to e) $\sim 65\%$ relative humidity.

5.3.8 *Assessing the role of HCl in film structure and physical response*

A modified Al-TEA recipe that included an HCl/H₂O exposure following the TEA exposure was utilized to study how HCl affects the film composition and properties. Figure 5.13 shows QCM results for the TMA-TEA-HCl process. Similar to the TMA-TEA QCM results shown in Figure 5.5a, TMA and TEA doses both result in a mass increase. The additional HCl/H₂O dose also leads to a mass increase which we ascribe to retention of chlorine anions on the protonated nitrogen. Water will also react with available Al-CH₃ sites, leading to negligible mass change. Transmission FTIR results for the Al-TEA and Al-TEA-HCl films are shown in Figure 5.14. The data shows the HCl exposure step leads to an N-H bending band at 1656 and a shoulder at 1633 cm⁻¹, similar to the FTIR spectra for the Ti-TEA film. In addition, the HCl step tends to increase the intensity of the hydroxyl band in the 3700-3000 cm⁻¹ region, consistent with Al-OH formation and possibly some physisorbed water.

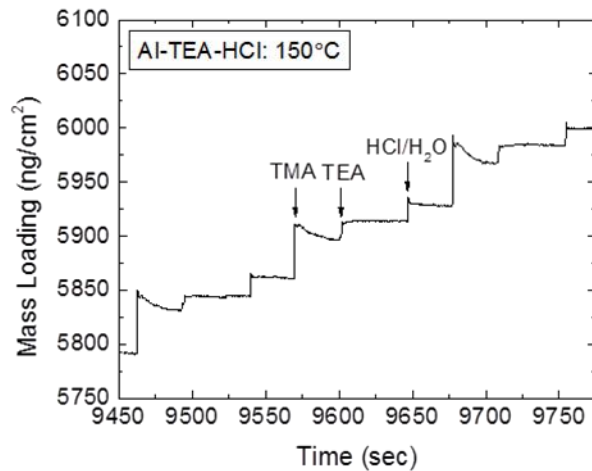


Figure 5.13: QCM analysis Al-TEA-HCl MLD process at 150°C.

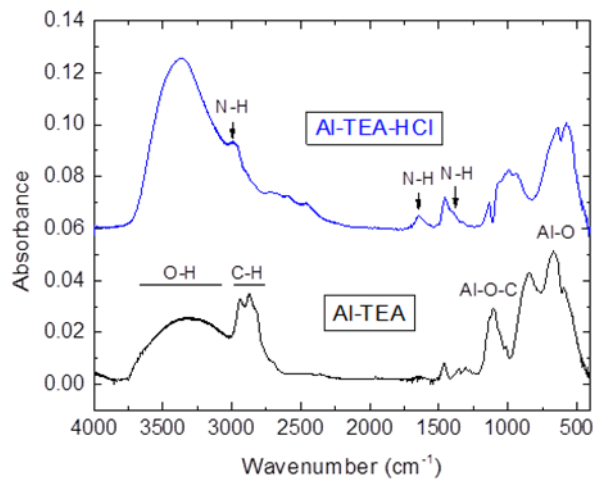


Figure 5.14: FTIR spectra for the Al-TEA-HCl and Al-TEA films deposited at 150°C.

High resolution XPS analysis of the N 1s and Cl 2p peaks and film composition of the Al-TEA and Al-TEA-HCl are shown in Table 5.3 and Figure 5.15. Figure 5.15 shows the chlorine content increases with the Al-TEA-HCl recipe to 7.3 at% versus the 1.4 at% for the Al-TEA film. The Al-TEA-HCl chlorine content is consistent with approximately one

chlorine atom per nitrogen atom. Finally, Al-TEA-HCl sample has a notable peak N 1s peak at 400.6 eV, which is attributed to N-H formation.

We further monitored the swelling properties of the Al-TEA-HCl film versus the Al-TEA films. As shown in Figure 5.16, the Al-TEA-HCl shows significant film shrinking of ~17.5% at 10% relative humidity, which is similar to what was observed for the Ti-TEA film. Above 55% humidity, the films swelled, as determined by the change in visible color, but the increase in thickness was sufficiently large that it could not be accurately quantified with the ellipsometry model.

Table 5.3: Film composition (± 2 at. %) based on high resolution XPS scans of Al-TEA-HCl films deposited at 150°C. Expected Al-TEA-HCl film composition based on the stoichiometric composition: $\text{Al}(\text{C}_6\text{H}_{12}\text{NO}_3)(\text{Cl}^-)$, assuming one chloride anion per protonated nitrogen.

Al-TEA-HCl	C 1s	O 1s	N 1s	Al 2p	Cl 2p
Experimental (at. %)	37	39	5	11	7
Expected (at. %)	50	25	8	8	8

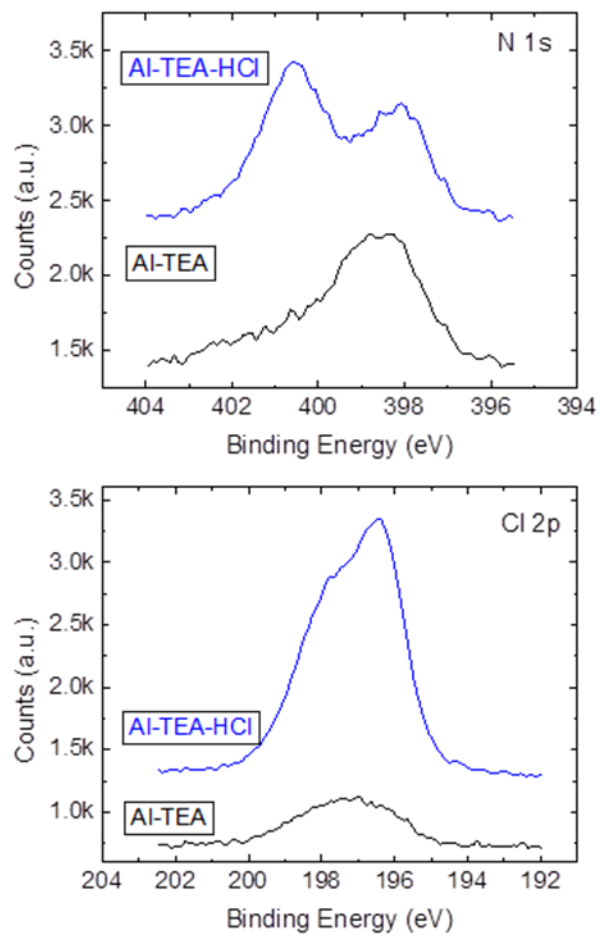


Figure 5.15: High resolution XPS scans of Cl 2p and N 1s peaks for the Al-TEA-HCl and Al-TEA films deposited at 150°C.

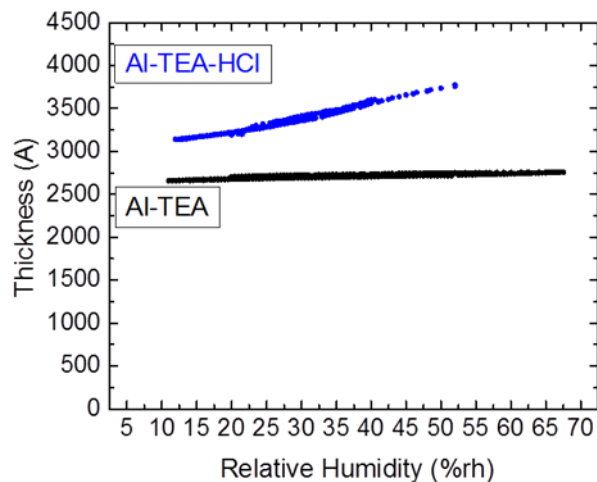


Figure 5.16: Thickness of Al-TEA and Al-TEA-HCl films versus relative humidity.

5.3.9 Applying swelling properties to other solvents and gases

The triethanolamine-metalcone thickness and accompanying color changes due to changes in humidity means that these films could be used for sensor applications. A ~300 nm Ti-TEA film was deposited on a QCM crystal and used in a home-made flow-through reactor. After equilibrating with the dry flowing nitrogen carrier gas, the film was exposed to a solvent for 1 minute at constant pressure. After the exposure, the system was purged with the nitrogen carrier gas. Figure 5.17a shows the change in mass loading after the Ti-TEA film was exposed to methanol, with a sharp mass increase of 1778 ng/cm² followed by a gradual mass loss. Water has the highest mass loading of 3955 ng/cm² and ethanol has the lowest loading of 331 ng/cm².

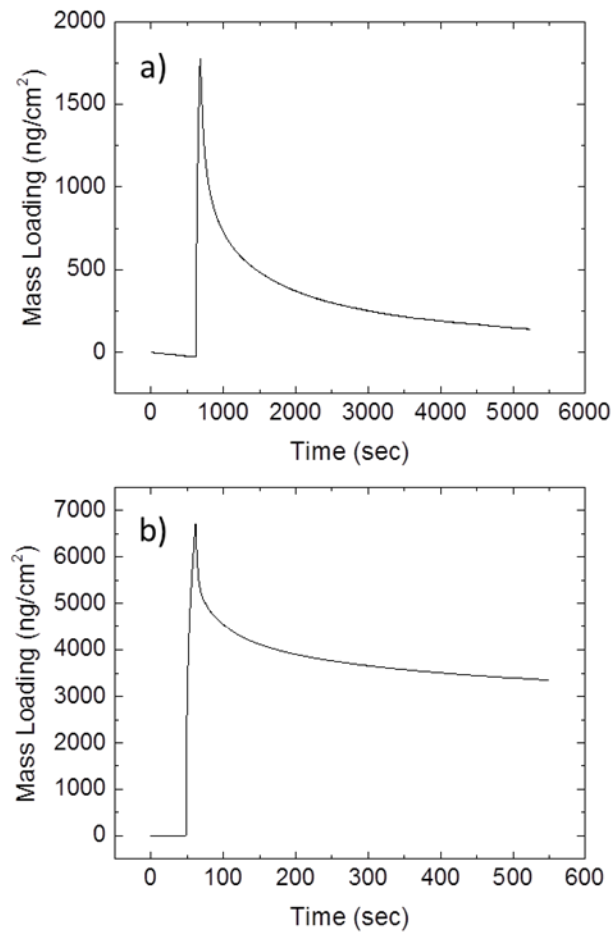


Figure 5.17: QCM analysis of a) methanol and b) ammonia loading on ~300 nm Ti-TEA film.

Finally we tested if these films would load a gas that is of greater interest due to safety concerns: ammonia. Figure 5.17b shows the mass loading for a Ti-TEA film after being exposed to ammonia for 5 seconds. There is a significant mass loading of 6707 ng/cm² after the ammonia exposure and the film appears to retain approximately 3446 ng/cm² of the ammonia after purging. The loading on an uncoated gold QCM crystal was significantly lower (~100 ng/cm²).

5.4 Discussion

The FTIR, XPS, QCM and thickness results in Figures 5.2 through 5.7 indicate that the Al-TEA and Ti-TEA MLD processes produce a coordination polymer of the form $(-O-M-O-(CH_xN_y)_z-O-M-)$, with thickness and structure defined by the number of MLD cycles and deposition temperature. The QCM results in Figure 5.5 show that increasing the process temperature from 150°C to 200°C leads to a decrease in the TMA and TiCl₄ mass uptake during the metal precursor exposure step. Increasing temperature will lead to more rapid metal precursor desorption and less net mass gain during the precursor exposure step. However, increasing the temperature from 150 to 200°C leads to a much larger decrease in TMA mass uptake than for TiCl₄. We believe that the increased retention of the TiCl₄ at higher temperature is due to a higher degree of nitrogen protonation in the Ti-TEA vs the Al-TEA, as described below.

Excess protonation in the Ti-TEA is consistent with XPS and FTIR results in Figure 5.6 and Figure 5.7. Specifically, the XPS shows that the Al-TEA film has a single carbon-nitrogen peak at 399.0 eV. The Ti-TEA peak has an additional peak at the higher binding energy of 400.9 eV signifying nitrogen-hydrogen bonding.^{222,223,226} In addition, the ratio of chlorine to nitrogen based on the Ti-TEA film composition in Table 5.1 is ~1:1, consistent with approximately one chloride anion per positively charged nitrogen. The FTIR analysis further shows that the Ti-TEA films have N-H characteristic bands at 1633 and 1392 cm⁻¹, which is not expected in the TEA tertiary amine structure.²²⁷ The excess protonation in the Ti-TEA

could result from the byproduct HCl reacting with the tertiary amine to form a quaternary ammonium salt ($\text{HR}_3\text{N}^+\text{Cl}^-$).^{228–230} This sequence is shown schematically in Figure 5.18.

The ionic interaction between the nitrogen and chlorine creates Lewis base sites²³⁰ which can bind with acidic TiCl_4 thereby promoting precursor retention, even at elevated temperatures, consistent with the QCM results in Figure 5.5d. Methane generated in the Al-TEA process does not generate the quaternary ammonium salt functionality, so even though TMA is a stronger Lewis acid than TiCl_4 , this mechanism is not active during the TMA-TEA process.

Based on the reaction schematics in Figures 5.1 and 5.18, the TEA exposure step is expected to produce a net mass gain. However, the mass gain observed by QCM in Figure 5.5 is smaller than expected. This is ascribed to excess consumption of Ti-Cl sites, where more than one Ti-Cl reacts with each TEA (i.e. through double- or triple- reactions), or by reaction with water, produced by thermal degradation of the Ti-TEA film²³¹ (Figure 5.9a). Consumption of multiple Ti-Cl surface sites by the organic monomer was previously reported during MLD using TiCl_4 and ethylene glycol.⁴⁸

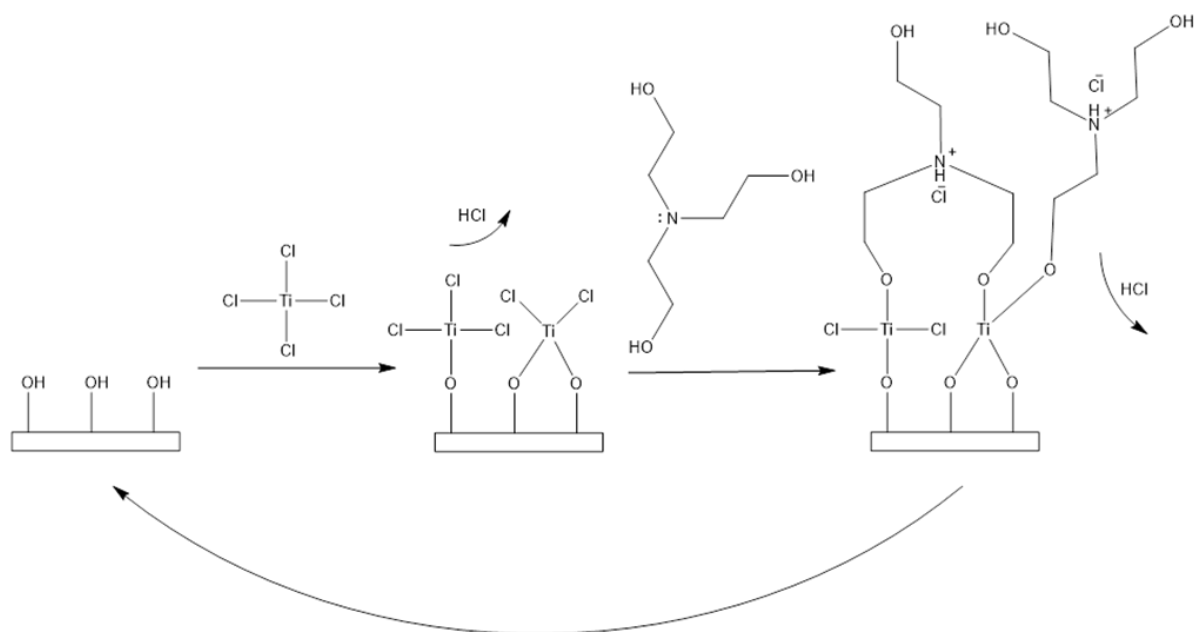


Figure 5.18. Ti-TEA reaction sequence with successive a) TiCl_4 and b) TEA exposure, showing byproduct HCl pronating the TEA nitrogen.

The quaternary ammonium salt functionality can also account for the physical swelling properties of the Ti-TEA films. The protonated nitrogen acts as the hydrogen bond donor, enabling hydrogen bonding with water vapor. The strong hydrogen bonding of the Ti-TEA films is due to the positively charged nitrogen which attracts the electron cloud from around the hydrogen nucleus, leaving the hydrogen atom with a positive partial charge.^{228,229} The films swell as they adsorb water and the change in film thickness manifests as a color change on the reflective silicon surface due to optical interference. A higher concentration of nitrogen protonation is expected to create a more hydrophilic film that can swell to a greater degree.

Using QCM, we tested whether polymer swelling could be induced by other hydroxylated vapors including methanol and ethanol. During the vapor exposure, water showed the highest mass increase of 3955 ng/cm², followed by methanol and ethanol with loadings of 1777 and 330 ng/cm² respectively. The extent of Ti-TEA swelling appears to be dependent on the size of the adsorbent (water < methanol < ethanol). In addition, Figure 5.17b shows that Ti-TEA film showed a high propensity for ammonia, with a loading of 6687 ng/cm² versus ~100 ng/cm² for an uncoated gold QCM crystal. This suggests that the high ammonia loading on the Ti-TEA film is not solely due to hydrogen-bonding physisorption. Furthermore there is some evidence that the ammonia is retained in the film even after purging. It is possible that the Ti-TEA film is forming an ammonium cation which is readily retained in the MLD film.^{232,233} Additional work needs to be done to determine the true capacity for toxic gas adsorption in these triethanolamine-metalcone films.

In some instances it was noted that the Al-TEA films exhibited swelling properties similar to that of the Ti-TEA films. The XPS results in Figure 5.7 and Table 5.2 show that the Al-TEA films contain ~1 at. % chlorine, likely due to residual chlorine on the reactor walls, remaining from the Ti-TEA process. We confirmed the correlation between the quaternary ammonium salt and the physical swelling properties with the Al-TEA-HCl process. Nitrogen-hydrogen FTIR bands at 1656 and 1633 cm⁻¹ in Figure 5.14 and the XPS peak at 400.6 eV in Figure 5.15 both suggest that the HCl exposure protonates the nitrogen in the Al-TEA film. Chloride anions balance the positively charged nitrogen consistent with the formation of a quaternary

ammonium salt. After HCl vapor exposure, the Al-TEA films showed physical swelling response similar to that observed for the Ti-TEA.

5.5 *Conclusion*

In this work, we report unique properties of metalcone MLD films formed using triethanolamine (TEA) with either trimethylaluminum (TMA) or titanium tetrachloride (TiCl_4) producing TEA-alucone (Al-TEA) and TEA-titanicone (Ti-TEA), respectively. We adjusted the reactant dose times, showing that the film thickness per cycle was more dependent on the TEA exposure than the metal precursor exposure. The Al-TEA growth rate decreased at higher deposition temperatures due to TMA diffusion out of the film. In comparison, the Ti-TEA growth rate was less dependent on the reactor temperature because of higher TiCl_4 retention.

We characterized the composition and chemical functionality of the TEA-metalcone films through FTIR and XPS analysis. FTIR showed the expected functionality with prominent C-H, C-N and M-O-C peaks for the two TEA-metalcone films. XPS showed that the experimental Ti-TEA film composition matched calculated values, while the Al-TEA film showed lower carbon content, suggesting partial film hydrolysis. XPS and FTIR also provided evidence that HCl formed in the Ti-TEA process generated a quaternary ammonium salt functionality. As a result the Ti-TEA film in particular exhibited a unique reversible visible color changes when exposed to vapors including water, methanol, ethanol, and ammonia. The color change was attributed to thickness swelling and shrinking and we were able to impart similar properties to the Al-TEA film by exposing the film to HCl vapor.

Finally we studied the loading capacity of these films, which appears to be in part dependent on the adsorbent molecule size. The responsive properties of the TEA-metalcone films make these materials appealing for sensor and filtration applications.

5.6 Acknowledgements

The authors acknowledge the use of the Analytical Instrumentation Facility (AIF) at North Carolina State University, which is supported by the State of North Carolina and the National Science Foundation.

**CHAPTER 6. UNDERSTANDING INHERENT SUBSTRATE SELECTIVITY
DURING ATOMIC LAYER DEPOSITION: EFFECT OF SURFACE
PREPARATION, HYDROXYL DENSITY AND METAL OXIDE COMPOSITION
ON NUCLEATION MECHANISMS DURING TUNGSTEN ALD**

The following work is reproduced with permission from Paul C. Lemaire, Mariah King, and Gregory N. Parsons. *J. Chem. Phys.* **2017**, *146*, 52811.

6.1 Abstract

Area-selective thin film deposition is expected to be important for advanced sub-10 nanometer semiconductor devices, enabling feature patterning, alignment to underlying structures and edge definition. Several atomic layer deposition (ALD) processes show inherent propensity for substrate-dependent nucleation. This includes tungsten ALD (W-ALD) which is more energetically favorable on Si than on SiO₂. However, the selectivity is often lost after several ALD cycles. We investigated the causes of tungsten nucleation on SiO₂ and other “non-growth” surfaces during the WF₆/SiH₄ W-ALD process to determine how to expand the “selectivity window.” We propose that hydroxyls, generated during the piranha clean, act as nucleation sites for non-selective deposition and show that by excluding the piranha clean or heating the samples, following the piranha clean, extends the tungsten selectivity window. We also assessed how the W-ALD precursors interact with different oxide substrates through individual WF₆ and SiH₄ pre-exposures prior to W-ALD deposition. We conclude that repeated SiH₄ pre-exposures reduce the tungsten nucleation delay, which is attributed to SiH₄ adsorption on hydroxyl sites. In addition, oxide surfaces were repeatedly

exposed to WF_6 , which appears to form metal fluoride species. We attribute the different tungsten nucleation delay on Al_2O_3 and TiO_2 to the formation of nonvolatile and volatile metal fluoride species respectively. Through this study we have increased the understanding of ALD nucleation and substrate selectivity, which are pivotal to improving the selectivity window for W-ALD and other ALD processes.

6.2 Introduction

For over 40 years, the number of transistors on an integrated circuit have doubled approximately every two years. Yet as companies begin work producing integrated circuits with less than 10 nm feature sizes, standard patterning techniques, such as lithography, become much less applicable because of challenges maintaining edge definition and alignment to the underlying features. Chemical vapor deposition (CVD) and atomic layer deposition (ALD) processes offer a possible solution to such issues. CVD is a vapor-phase process where one or more volatile inorganic or organic precursors are dosed into a reactor chamber simultaneously. The precursors then decompose on a heated substrate, depositing a thin film and generating volatile byproducts.²³⁴ ALD in comparison, is vapor-phase process that uses two or more sequential self-limiting reactions to deposit conformal films with high thickness control.^{5,11} There are multiple CVD and ALD processes which show a propensity to selectively deposit material on energetically favorable surfaces. For example, a tungsten ALD (W-ALD) process, which uses tungsten hexafluoride (WF_6) and silane (SiH_4)¹⁰⁻¹² or disilane (Si_2H_6)¹⁴⁻¹⁷ as reactants will selectively deposit tungsten on Si and metal surfaces^{25,235,236} with slower nucleation on “non-growth” surfaces such as SiO_2 where growth

is not desired. The stability of SiO_2 leads to a high energy barrier for tungsten deposition because the oxidized silicon atoms are unable to act as sacrificial reductants.^{25,26,237}

Although deposition on non-growth surfaces is thermodynamically much less favorable, deposition will occur after a nucleation period. In order to take full advantage of selective ALD processes, it is pivotal to extend the “selectivity window” or maximize the amount of material deposited on the growth surface before growth begins on the non-growth surface. Previous studies on tungsten CVD provides evidence that the loss of selective tungsten deposition can be attributed to either SiH_4 or WF_6 adsorption on SiO_2 . For example, tungsten nucleation delay is enhanced on non-growth surfaces TiN and SiO_2 by using a SiH_4 ²³⁸ or B_2H_6 ¹² pretreatment respectively. Kobayashi et al. suggests that selective tungsten CVD depends on the selective dissociation of a reducing agent (H_2 or SiH_4) on the metal growth surface.^{236,239}

There is also evidence that WF_6 is predominantly responsible for loss of selective tungsten deposition. For example, although WF_6 cannot readily react with surfaces at low temperatures,^{235,236} it can condense and weakly adsorb on cooled surfaces.^{236,237} Chang et al. proposed that WF_6 can react will react with SiO_2 substrates via surface silanol groups generated during wet sample preparation.²⁶ Additionally, in the presence of hot tungsten, WF_6 can also disproportionate to form highly reactive tungsten subfluorides (WF_x) that can deposit on SiO_2 surfaces.^{25,240–242}

Despite the similarities between CVD and ALD processes, it is important to acknowledge that selectivity loss mechanism for CVD processes will not always apply to ALD processes.

For example, because W-CVD process mixes both precursors simultaneously, these processes generate a higher concentration of vapor-phase products, such as silicon subfluorides of SiH_xF_y species, than a W-ALD process; byproducts often linked with non-selective tungsten deposition.^{236,239,242,243} Also, the relatively high deposition rates for CVD processes can mask phenomena such as etching, which are more apparent during ALD processes.²³⁶

This work expands understanding of metal ALD nucleation mechanisms on “non-growth” substrates (i.e. where growth is not desired) during selective area ALD. Specifically, we explore the role of substrate surface preparation and composition on the rate of growth initiation, and propose mechanisms for selectivity loss that can broaden the understanding of selective ALD methods. Specifically, we report results for WF_6/SiH_4 W-ALD nucleation on various metal oxides and demonstrate that the tungsten nucleation delay is dependent on both the oxide composition and the surface hydroxyl concentration. In order to increase the tungsten selectivity window we tested methods to reduce the hydroxyl concentration on metal oxides via pre-annealing and deposition of a halogenated-passivation layer. We investigate how hydroxyl sites interact with the individual WF_6 and SiH_4 reactants. We find that on SiO_2 , SiH_4 exposure enhances tungsten nucleation which we attribute to SiH_4 adsorption, whereas WF_6 pre-exposure appears to convert the oxide substrates to metal fluorides, promoting metallic tungsten nucleation.

6.3 *Experimental*

6.3.1 *List of supplies and materials*

Tungsten hexafluoride (WF_6) and a dilute 2% silane in argon mixture (SiH_4) were purchased from Galaxy Chemical (Claremore, OK) and Custom Gas Solutions (Durham, NC) respectively and used without further treatment. Trimethylaluminum (TMA), titanium tetrachloride (TiCl_4), and diethyl zinc (DEZ) were obtained from Strem Chemicals Inc. and used without further treatment. The Si substrates were boron doped Si(100) 6-10 Ω -cm (WRS Materials). The SiO_2 substrates were Si(100) 6-10 Ω -cm with 100 nm thermal SiO_2 (WRS Materials), cut into 12 x 12 mm pieces. For the carrier and purge gas, dry 99.999% argon (Ar) was passed through an Entegris GateKeeper inert gas purifier to remove any residual water before entering the reactor.

6.3.2 *Substrate surface preparation*

The SiO_2 substrates were cut into 12 x 12 mm pieces. SiO_2 samples were cleaned in hot piranha solution (1:1 H_2SO_4 : H_2O_2 by volume) for 30 minutes, rinsed with deionized (DI) water, and stored in DI water. Immediately prior to W-ALD, the SiO_2 pieces were rinsed in DI water and dried under flowing N_2 (100 psi). To form hydrogen-terminated silicon, 12 x 12 mm Si pieces were cleaned in the piranha solution described above and stored in DI water. Immediately prior to W-ALD, the Si wafers were dipped in dilute hydrofluoric acid (5 vol%) for 30 s followed by a DI water rinse (30 s) and N_2 drying.

High surface area porous silicon (PS) was prepared using 3 x 3 cm boron doped Si(100) 6-10 Ω -cm wafers. Wafers were secured in a 1.5 cm diameter TeflonTM cell with a platinum wire counter-electrode. Wafers were electrochemically etched for 30 min in a 20 mL solution of 1:1:2 volume ratio of hydrogen fluoride, water, and ethanol at a current density of 15 mA/cm². After etching, silicon surfaces were hydrogen terminated. Porous silicon samples were heated at a ramp rate of 20°C/min to 950°C and held at temperature for 1 hr to form a thermal oxide layer. To hydroxylate the thermal oxide layer, wafers were then placed in a piranha bath for 30 min.

To assess the role of surface hydroxyl sites, piranha-cleaned SiO₂ samples were annealed under air prior to W-ALD. SiO₂ samples were heated at a ramp rate of 20°C/min to 600 or 800°C and held at temperature for 30 min. After cooling to ~300°C, samples were removed from the furnaces and immediately loaded into the ALD reactor for deposition or the ex-situ Fourier transform infrared spectroscopy (FTIR) for characterization.

Approximately 100 nm SiO₂ and Si films were deposited on 6 Hz gold-coated quartz-crystal microbalance (QCM) crystals with the use of a custom-made stainless steel mask. SiO₂ films were deposited at room temperature with a PECVD process with a tetraethyl orthosilicate source. Amorphous Si films were deposited in a LPCVD system at 550°C and 160 mTorr using a 100% Si₂H₆ source, with a ~6 nm/min deposition rate.

6.3.3 *W-ALD reactor design*

Depositions were carried out in a chamber home-built ALD reactor (60 cm long, 10 cm in diameter) described in previous publications.^{11,18} The deposition chamber was heated resistively to 220°C using PID controllers. The operating pressure was maintained at 1.5 Torr with an Ar carrier flow rate of 210 sccm.

6.3.4 *ALD reaction sequence*

Tungsten deposition was achieved by alternately pulsing SiH₄ and WF₆ with inert Ar purge steps following each exposure. Silicon substrates were loaded into the reactor and allowed to reach thermal equilibrium with the walls by flowing carrier gas for 30 min prior to deposition. The conditions for the starting base-line W-ALD process used the SiH₄/Ar/WF₆/Ar (45/45/1/60 s) sequence at 220°C. Selectivity loss mechanisms were investigated by using SiH₄/Ar (45/45 s) and WF₆/Ar (1/60 s) sequences to repeatedly expose samples to the individual precursors prior to the standard SiH₄/Ar/WF₆/Ar sequence. Finally, Al₂O₃, TiO₂, and ZnO ALD films were deposited prior to the W-ALD process using a x/Ar/H₂O/Ar sequence where x is TMA, TiCl₄, and DEZ respectively, with a timing sequence of 0.25/45/0.25/45 s.

6.3.5 *Sample characterization*

Film nucleation and growth were characterized using ex situ analytical tools. Spectroscopic ellipsometry (SE) data were obtained with a J.A. Woollam alpha-SE ellipsometer at an incidence angle of 70°. FTIR analysis was performed with a ThermoNicolet 6700 IR bench

with a deuterated triglycine sulfate detector operated in transmission mode with 2050 scans at 4 cm⁻¹ resolution. Chemical analysis was done using a SPECS X-ray photoelectron spectroscopy (XPS) system with a PHOIBOS 150 analyzer. Spectra were generated using an Al K α X-ray source operated at 400 W. For all analyses, data reduction and fitting was carried out using CasaXPS software with charge compensation based on the C 1s (C-C, C-H) peak set to 285 eV. For some analyses, we utilized the Ti 2p XPS peak intensity to estimate the thickness of SiO₂ films formed as a result of SiH₄ adsorption. For this analysis, we measured the attenuation of the Ti 2p 3/2 peak and modeled the film thickness using parameters available from the NIST Effective Attenuation Length Database,²⁴⁴ coupled with electron inelastic mean-free path values determined using the TPP-2M equation.²⁴⁵ For this equation, we used a bandgap of 3.05 eV and density of 4.23 g/cm³, consistent with bulk amorphous SiO₂.

Process conditions were further characterized using in-situ QCM analysis. For these tests, a 6 Hz gold coated QCM crystal sensor (Inficon) was placed into the QCM housing. A dry Ar crystal back purge that yielded a ~250 mTorr pressure increase was sufficient to prevent deposition on the backside of the QCM crystal. The mass change signals were detected by an Inficon SQM-160 monitor and recorded using a home designed LabVIEW program.

6.4 Results

6.4.1 Comparison of W-ALD nucleation on silicon, metal, and metal oxide substrates

We first worked to quantify the selectivity for W nucleation on Si versus SiO₂ substrates under well-defined ALD conditions.¹⁸ Figure 6.1 shows results from a) in-situ QCM and b) XPS analysis respectively. The QCM results show mass uptake on as-received (Au) and externally coated (Si, SiO₂) quartz crystals during the initial cycles of W-ALD at 220°C. On Si, growth proceeds readily during the first ALD cycles, whereas the Au surface shows that a few cycles are needed to achieve full growth. The SiO₂ surface however requires ~35 ALD cycles before mass uptake is recorded, which is consistent with previous reports.¹⁰

X-ray photoelectron spectra of Si and Si/SiO₂ substrates after 30 cycles of W-ALD are given in Figure 6.1b. Peaks at 33 and 30.8 eV are associated with W⁰, whereas the features at 37.5 and 35.3 eV are due to oxidized W. Surface oxidation is expected during open-air transport of the samples from the ALD reactor to XPS analysis. Overall, the intensity of the W 4f peaks, and in particular the W⁰ signature, are larger on the Si surface versus the SiO₂ surface, consistent with more facile nucleation on Si.

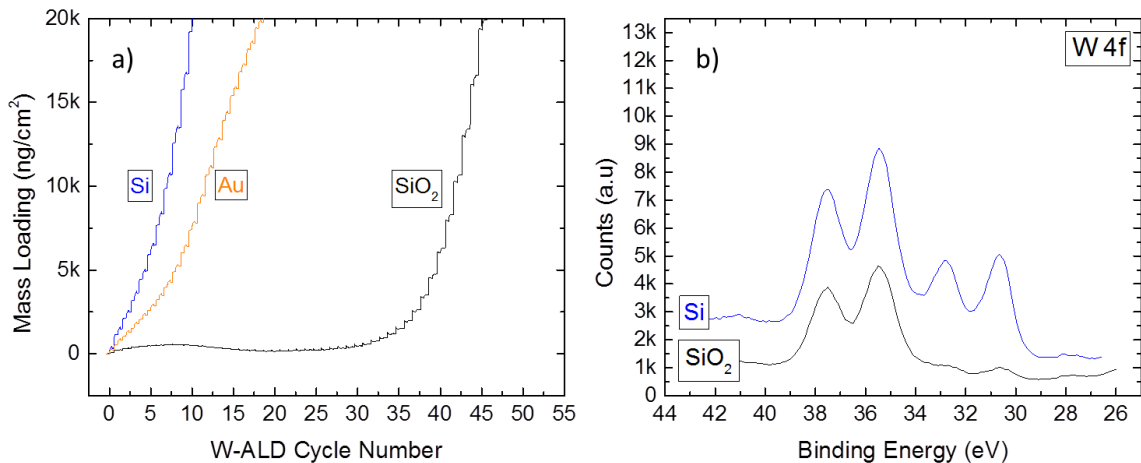


Figure 6.1: Results of W-ALD on Si, Au, and SiO₂ surfaces from a) in-situ QCM analysis and b) XPS analysis of W 4f peaks after 30 W ALD cycles.

The rate of tungsten nucleation was further investigated by comparing QCM mass uptake during W-ALD on various oxide surfaces. It is known that substrates including polymer fiber mats conditioned with Al₂O₃ ALD exhibit more rapid tungsten nucleation.²⁴⁶ Figure 6.2a includes results for W-ALD growth initiation on QCM crystals coated with SiO₂ and ALD Al₂O₃, ZnO and TiO₂. Results show that ZnO and Al₂O₃ surfaces exhibit a small nucleation delay of ~10 W-ALD cycles. In comparison, the SiO₂ and TiO₂ surfaces require between 30-35 W-ALD cycles before there is an appreciable mass increase. Furthermore, prior to the mass gain, the TiO₂ surface shows a prominent mass loss between 10-30 W-ALD cycles, which is attributed to TiO₂ surface etching. An enlarged view of this etching is shown in Figure 6.2b, showing that the mass losses occur during the WF₆ exposures.

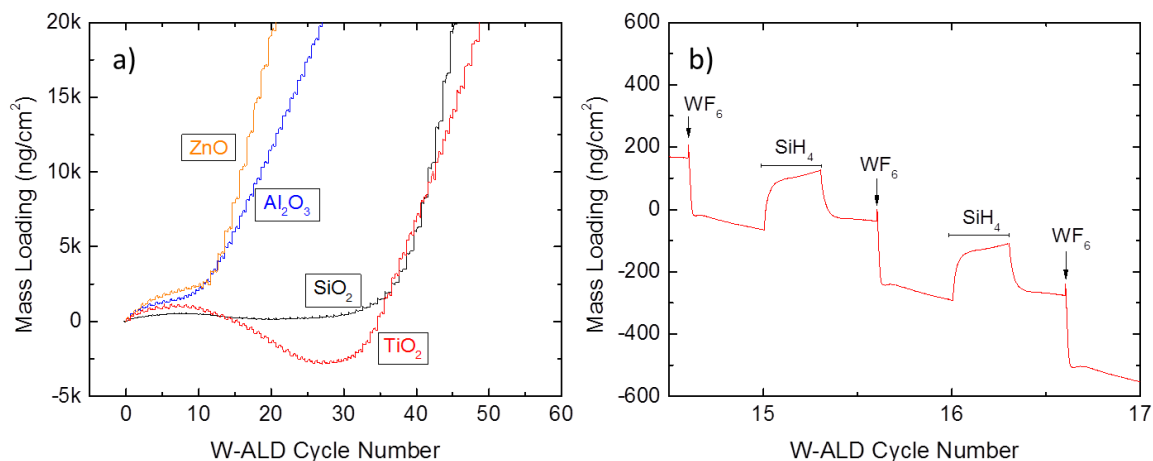


Figure 6.2: In-situ QCM analysis of a) W-ALD on ZnO, Al₂O₃, SiO₂, and TiO₂ surfaces and b) an enlarged view of W-ALD on TiO₂, which shows film etching during the nucleation period.

6.4.2 Role of surface hydroxyl groups in the loss of W-ALD selectivity

The effect of SiO₂ surface preparation on W-ALD nucleation was assessed using FTIR and ex-situ ellipsometry. The extent of surface hydroxyl concentration was varied by in-situ thermal treatment and the rate of change of the ellipsometric response was monitored during tungsten nucleation. To alleviate issues with modeling ellipsometry data, we use a previously published approach to trace tungsten nucleation by directly monitoring the ellipsometry delta parameter, Δ , at 700 nm.¹⁸

Figures 6.3 shows in-situ FTIR spectra of the hydroxyl region for a thermal oxide film on a porous silicon (PS) substrate. As the sample temperature is increased from 100-300°C, the broad peak at 3690-3060 cm⁻¹ decreases, attributed to loss of hydrogen-bound water. The FTIR results suggest that there is some adsorbed water on SiO₂ surfaces at the process

conditions of 220°C and 1.5 Torr. In addition, within the studied temperature range the intensity of the isolated hydroxyl feature at 3740 cm^{-1} remains relatively constant.

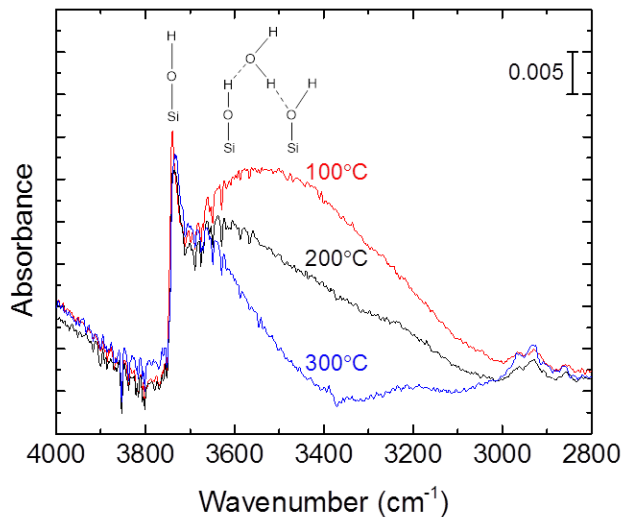


Figure 6.3: In-situ FTIR of thermal SiO₂ on PS following piranha clean, measured at 100, 200 and 300°C, showing loss of surface bound water, with some surface bound water remaining after 300°C.

Figure 6.4a shows spectra from the as-formed porous thermal oxide and after piranha treatment. As formed, the surface shows predominantly isolated hydroxyl features at 3740 cm^{-1} . The difference spectra, after the piranha clean, shows a decrease in the isolated hydroxyl signal and positive-going broad peaks at 3690-3060 cm^{-1} due to an increase in hydrogen-bound water. We also note an increase in the peak shoulder at 3735 cm^{-1} which is ascribed to formation of vicinal hydroxyl groups upon piranha cleaning.²⁴⁷

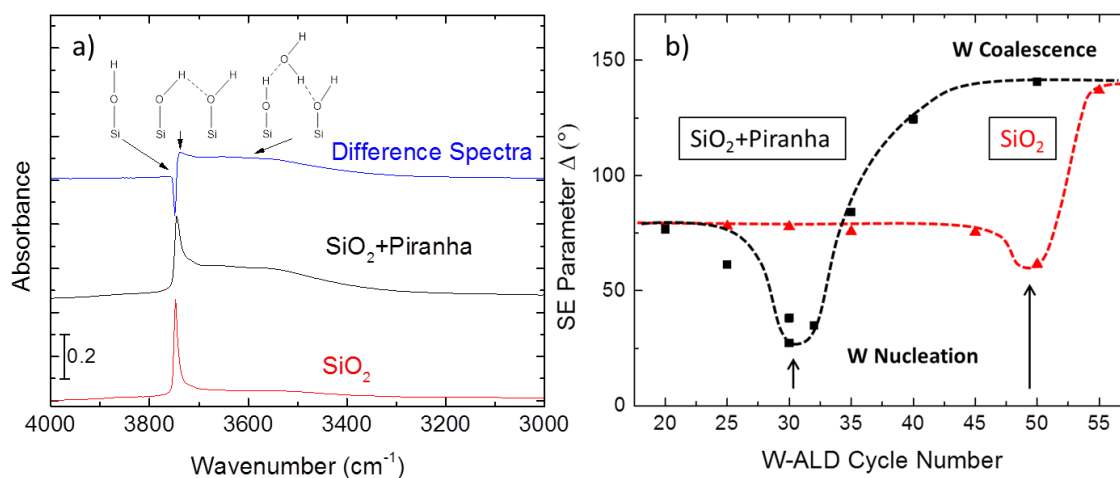


Figure 6.4: a) Ex-situ FTIR of thermal SiO₂ on PS at room temperature before and after piranha clean, and the resulting difference spectrum, showing removal of isolated hydroxyls and an increase in the concentration of germinal hydroxyls and adsorbed water. b) SE delta parameter at 700 nm for piranha-cleaned and as-is SiO₂ wafers.

Figure 6.4b shows the ellipsometry Δ factor versus W-ALD cycle at 220°C on planar SiO₂ thermal oxide prepared with: i) isolated hydroxy groups (as oxidized); and ii) a larger number of vicinal hydroxyl groups (after piranha treatment). For both SiO₂ surfaces, the delta parameter is initially measured to be $\Delta \approx 78^\circ$, and it decreases to 50-30° as the tungsten begins to nucleate. The subsequent increase to 145° correlates with tungsten film coalescence.¹⁸ On SiO₂ with predominantly vicinal hydroxyl groups, the Δ value decreases after ~25-30 cycles, consistent with the QCM analysis (Figure 6.1a). However, the SiO₂ with mostly isolated hydroxyl exhibits an increased nucleation delay of approximately 50 cycles, suggesting that vicinal hydroxyls on SiO₂ are more receptive to tungsten nucleation than the isolated hydroxyl groups.

To further explore the role of adsorbed water and hydroxyl groups on tungsten nucleation, SiO₂ samples with predominantly vicinal hydroxyl groups (i.e. piranha cleaned) were annealed ex-situ in air at 600 and 800°C followed by the W-ALD deposition. FTIR spectra of thermal SiO₂ on PS collected before ALD are given in Figure 6.5a. At both temperatures, annealing leads to loss of the broad hydroxyl bands at 3690-3060 cm⁻¹ and an increase in the isolated hydroxyl band at 3740 cm⁻¹. After 600°C, hydrogen-bonded vicinal hydroxyl groups are visible at 3735 cm⁻¹, but they are lost after 800°C.

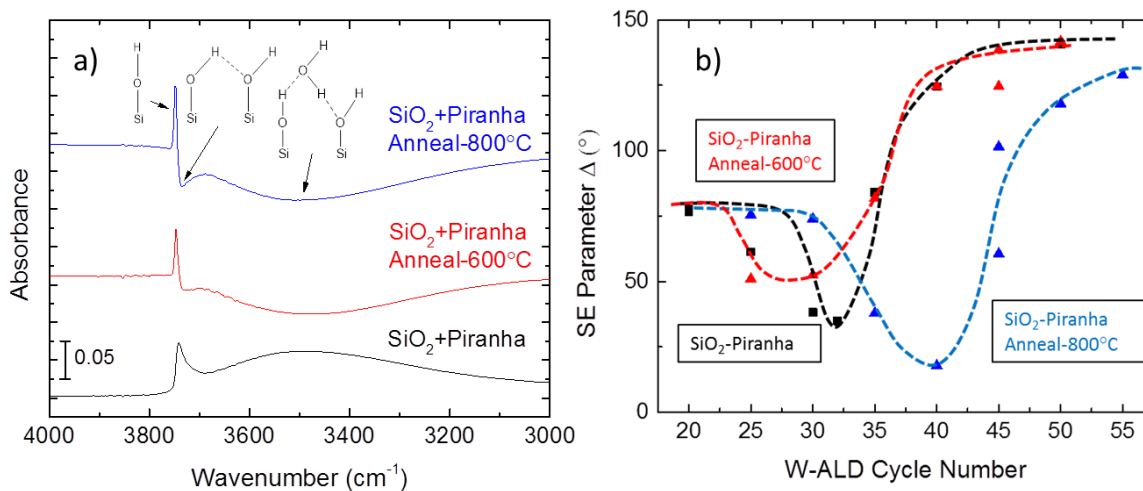


Figure 6.5: Impact of ex-situ annealing samples at 600 and 800°C prior to W-ALD: a) Ex-situ FTIR spectra of thermal SiO₂ on PS and difference spectra of the hydroxylated thermal SiO₂ after 600 and 800°C anneal. Difference spectra referenced to SiO₂+Piranha spectra, b) SE delta parameter at 700 nm for SiO₂ samples following W-ALD at 220°C.

The values for Δ versus W-ALD cycle number for SiO₂ samples with and without annealing are presented in Figure 5b. On SiO₂ with predominantly isolated hydroxyls (i.e. after 800°C) the W-ALD nucleation delay increases by ~10 cycles compared to samples without anneal. In comparison, removing surface water (600°C anneal) promotes nucleation, leading to a ~5

cycle reduction in nucleation delay. Similar to the results in Figure 6.4, this data suggests that vicinal hydroxyl groups on SiO_2 are more favorable for tungsten nucleation. The data further indicates that physisorbed water, observed in Figure 6.3, can impede tungsten nucleation.

6.4.3 *SiH_4 and WF_6 interaction with SiO_2 , Al_2O_3 , and TiO_2*

Results shown above indicate that hydroxyl groups on SiO_2 play an important role in W-ALD nucleation. We further hypothesized that exposing oxide substrates to extended doses of one of the W-ALD reactants (SiH_4 or WF_6) would also influence nucleation. To examine the effect of SiH_4 exposure, piranha-cleaned SiO_2 samples were pre-exposed to sequential doses of SiH_4 followed by SiH_4/WF_6 W-ALD cycles at 220°C . Figure 6.6 shows that the film delta parameter after 30 W-ALD cycles increases with increasing number of SiH_4 pre-exposures, demonstrating that SiH_4 promotes W nucleation on SiO_2 .

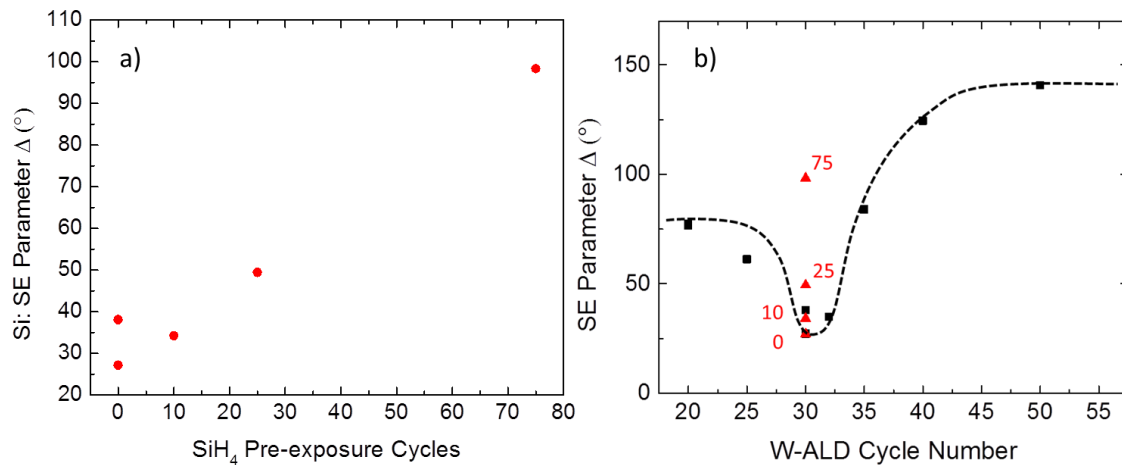


Figure 6.6: SE delta parameter at 700 nm for SiO_2 samples after 30 W ALD cycles following x SiH_4 pre-exposure cycles. The delta data from the piranha-cleaned SiO_2 in Figure 4 is repeated for clarity.

Likewise, silicon wafers coated with ALD TiO_2 and Al_2O_3 were repeatedly exposed to SiH_4 . Figure 6.7 shows Si 2p XPS spectra collected ex-situ on ALD TiO_2 and Al_2O_3 surfaces after increasing number of SiH_4 exposures. The intensity of the Si 2p peak at 102.7 (consistent with oxidized silicon) increases with SiH_4 exposure on both TiO_2 and Al_2O_3 , likely due to SiH_4 adsorption and reaction with surface-bound water.

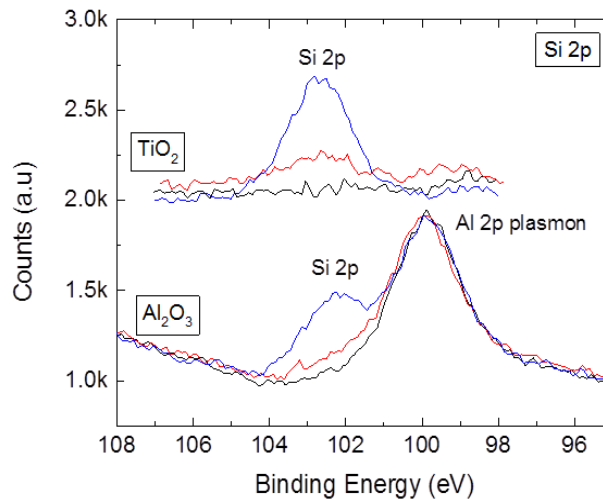


Figure 6.7: XPS spectra of TiO_2 and Al_2O_3 ALD films exposed to 0 (black), 10 (red), and 50 (blue) SiH_4 exposures. With increasing number of SiH_4 exposures, the Si 2p peak increases on both the TiO_2 and Al_2O_3 surfaces.

The SiH_4 pretreatment on TiO_2 and Al_2O_3 also promoted tungsten nucleation, as shown in the QCM results in Figure 6.8. By using 50 SiH_4 exposure cycles before W-ALD, nucleation was observed 6-8 cycles sooner. In addition, mass loss ascribed to chemical etching is observed on TiO_2 , likely due to the volatilization of TiF_4 , regardless of whether a SiH_4 pre-exposure step was applied.

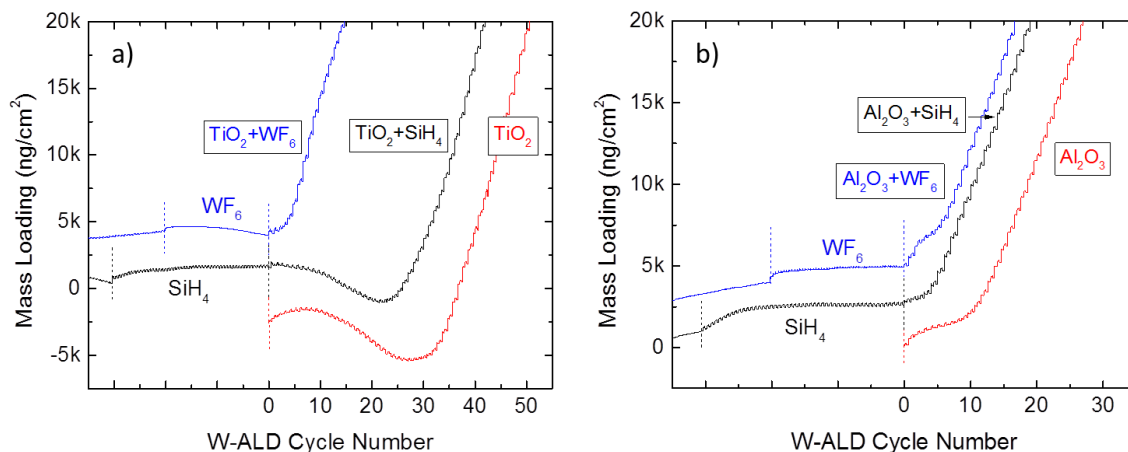


Figure 6.8: In-situ QCM analysis comparing W-ALD on a) TiO₂ and b) Al₂O₃ for the as-is oxide (red), oxide with 50 SiH₄ pre-exposures (black), and oxide with 50 WF₆ pre-exposures (blue).

The interactions between WF₆ and the oxide substrates were investigated by pre-exposing substrates to WF₆ followed by the W-ALD process as shown in Figure 6.8. During the 50 WF₆ pre-exposures, there is an initial mass gain on the Al₂O₃ surface which plateaus after 1-2 WF₆ pre-exposures. The TiO₂ substrate also shows an initial mass gain, but further WF₆ exposures result in mass loss. For both the Al₂O₃ and TiO₂ surfaces, the WF₆ exposure steps lead to more rapid tungsten nucleation. Comparing the results for WF₆ versus SiH₄ pre-exposure, the W-ALD nucleation on oxides is more dependent on WF₆ adsorption than SiH₄ adsorption.

6.4.4 Expanding the W-ALD selectivity window

Using insights and results from surface preparation and individual precursor reaction experiments, we seek to adjust the W-ALD process to expand the ALD selectivity window,

i.e. further slow tungsten nucleation on SiO_2 while maintaining high growth per cycle on silicon. Specifically, since results in Figure 6.3 and Figure 6.5 show that a high density of surface bound water can impede tungsten nucleation on SiO_2 , we hypothesize that a reduced deposition temperature would favor selectivity. Moreover, since SiO_2 reacts with SiH_4 or WF_6 to promote tungsten nucleation, reducing the deposition temperature would also slow the reactions that form active nucleation sites. Results from XPS analysis in Figure 9a-c show the high resolution W 4f scans on Si and SiO_2 at different process temperatures. The ratio of the W 4f signals for the Si versus SiO_2 as measure of the selectivity is included in Figure 9d. For each temperature, the number of cycles deposited corresponds to the negative-going inflection point in ellipsometry Δ parameter on the SiO_2 substrate, i.e. 30 cycles at 220°C as shown in Figure 6.5b (other data not shown). At this inflection point, a larger relative W XPS signal on Si vs SiO_2 corresponds to more W on Si and therefore improved selectivity. At 300°C the area of the tungsten 4f signal is $\sim 1.7\times$ larger on Si than on SiO_2 . At 220°C this ratio increases to ~ 2.4 and reaches ~ 3.3 at 160°C , demonstrating improved selectivity at lower temperature. We attribute the improved selectivity to the temperature dependence of the WF_6 reaction,^{16,248} in which the probability of the SiOH-WF_6 reaction is more significantly reduced than the SiH-WF_6 reaction.

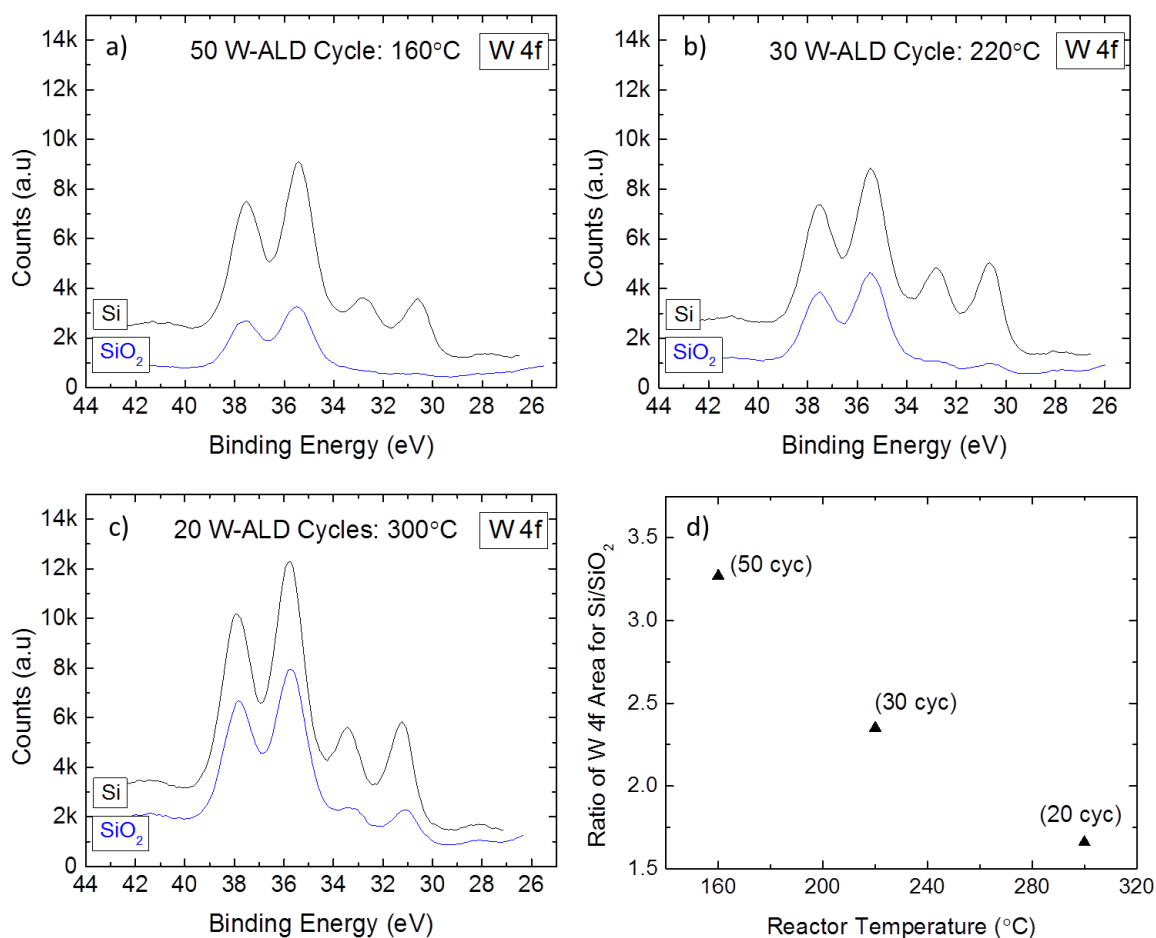


Figure 6.9: Ex-situ XPS W 4f high resolution scans for Si and SiO₂ samples following: a) 50 W-ALD cycles at 160°C, b) 30 W-ALD cycles at 220°C, and c) 20 W-ALD cycles at 300°C. d) Ratio of W 4f Area on Si versus SiO₂ at different reactor temperatures.

6.5 Discussion

The ellipsometry, XPS, FTIR, and QCM results shown above demonstrate that the composition of a metal oxide substrate as well as the concentration of reactive hydroxyl groups on oxide surfaces play a key role in the rate of tungsten metal nucleation during W-ALD. In this section, we discuss in greater detail how the W-ALD precursors react with the

defect hydroxyl sites in the context of controlling tungsten nucleation, and then present suggestions to further expand substrate selectivity.

6.5.1 *Surface hydroxyls as tungsten nucleation sites*

A pristine SiO₂ surface has a large concentration of stable Si-O bonds that are inert towards most reactants,²⁶ and preliminary modeling results suggest that there is a large thermodynamic barrier for WF₆ to react with a hydroxyl-free SiO₂ surface. But SiO₂ surfaces are typically populated by silanol sites which can react with precursors, such as WF₆, to form a Si-O-WF_x linkage and stable HF.²⁶ Results in Figure 6.3, 6.4 and 6.5 show that treating SiO₂ with a piranha cleaning step introduces vicinal hydroxyl groups which are retained during annealing at 600°C. With this surface preparation, relatively rapid tungsten nucleation is observed on SiO₂ by ellipsometry, indicating that vicinal hydroxyl groups promote tungsten nucleation during WF₆/SiH₄ ALD. Ellipsometry also shows slower nucleation on SiO₂ after 800°C anneal, where FTIR shows loss of vicinal hydroxyl species.

We find that tungsten nucleation on SiO₂ surfaces occurs at vicinal hydroxyl sites, which is further validated by results for similar tungsten processes. Using triethylborane, tungsten hexafluoride, and ammonia as reactants in an ALD sequence, Hoyas et al. used energy dispersive X-ray fluorescence to monitor WN_xC_y nucleation on chemical and thermal SiO₂, and at 300°C they observed more rapid nucleation on chemical SiO₂ as compared to thermal SiO₂.²⁴⁹ They suggested that the WN_xC_y nucleation behavior could be related to the fact that the density of reactive hydroxyls is 2 times larger on chemical SiO₂ vs thermal SiO₂ (3 and 1.5 nm⁻² respectively).²⁴⁹ Without surface hydroxyl groups, WF₆ adsorption is severely

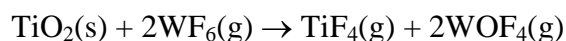
hindered. For example, when surface hydroxyls were removed from quartz samples via in-situ annealed at 1100 K, Groenen et al. observed that the tungsten nucleation time was independent of the WF_6 pre-exposure time.²⁵⁰ Although isolated hydroxyls are often considered to be relatively reactive,²⁵¹ during studies of BCl_3 , TiCl_4 , and TMA reactions with silica surfaces, Morrow et al.²⁴⁷ concludes that hydrogen bonded vicinal groups are more reactive towards specific ALD precursors such as TiCl_4 because they promote bifunctional reactions with more than one vicinal silanol. Based on the results in Figures 6.4, 6.5, and 6.8, we propose that WF_6 also preferentially reacts with the vicinal hydroxyl sites on SiO_2 surfaces through bifunctional reactions.

6.5.2 *Fluorination of oxide substrates*

Results in Figures 6.4, 6.5, and 6.8 suggest that WF_6 reacts at hydroxyl sites, leading to tungsten nucleation on SiO_2 and other oxides. Although WF_6 is generally considered a weak fluorinating agent²⁵² it is able to react with hydroxyl sites, converting the metal oxide substrate to a metal fluoride.^{14,17,26,253} Our results suggest that the different tungsten nucleation behavior for Al_2O_3 and ZnO versus TiO_2 and SiO_2 substrates is due to the difference in volatility of the formed metal fluorides. QCM analysis in Figure 6.2 and Figure 6.8, shows that repeated exposures of WF_6 etches TiO_2 , while Al_2O_3 shows an initial mass loading that plateaus with additional WF_6 doses. The different etching behavior is attributed to the fact that TiF_4 ^{254,255} is more volatile than AlF_3 ^{81,82,256–258} at low temperatures. It should also be noted that QCM analysis (not included) also suggests repeated WF_6 exposures can

etch SiO₂ film. Like TiF₄, SiF₄ is volatile at low temperatures,^{236,239,243,250} whereas ZnF₂ is a non-volatile solid,²⁵⁷ analogous to AlF₃.

In the case of TiO₂, we propose that the initial WF₆ exposures fluorinate the TiO₂ to form fluorinated titanium and oxidized tungsten surface species, consistent with the initial mass increase observed by QCM analysis in Figure 6.8. These surface-bound species are likely a mix of nonvolatile TiF₃,^{254,255} TiOF₂,²⁵⁹ and WO₃.^{236,255,260,261} Additional WF₆ exposures then increases the substrate fluorine concentration, forming volatile TiF₄^{26,238,253,254} and WOF₄.^{236,261} The overall etch reaction would then be written as:



This is consistent with the work of Kobayashi et al., in which they show that WF₆ reacts with SiO₂ to form volatile WOF₄ and SiF₄.²³⁶ The etching rate depending highly on how the SiO₂ was formed (aka plasma CVD SiO₂ versus thermally grown SiO₂), likely because of differences in hydroxyl concentration.²³⁶ Furthermore, in a similar system, NbCl₅ was observed to etch Nb₂O₅ films by forming volatile NbOCl₃.²⁶² Initially, oxide etching removes potential surface sites for tungsten nucleation, but tungsten or WOF_x species eventually deposit on the surface during the WF₆ exposures, allowing tungsten film growth. This explains why following WF₆ etching, there is little to no W-ALD nucleation delay on TiO₂ as shown in Figure 6.8. Collectively, this provides evidence that WF₆ adsorption is the rate-limiting step for tungsten nucleation on an oxide surface.

6.5.3 *SiH₄ reactions with surface hydroxyls*

The tungsten nucleation time is also dependent on SiH₄ exposure time. We suggest that like WF₆, SiH₄ can also adsorb on oxide surfaces by reacting with surface hydroxyls. XPS results in Figure 6.7 indicate that the silicon content on Al₂O₃ and TiO₂ surfaces increases with increasing number of SiH₄ pre-exposures. Attenuation of the Ti 2p 3/2 XPS signal suggests that the TiO₂ sample had a ~4 Å thick SiO₂ over-layer following 50 SiH₄ pre-exposures. In comparison, based on a bulk amorphous density of 2.3 g/cm³, a SiO₂ monolayer is ~3.5 Å thick. This suggests that the in-situ SiH₄ pre-exposures form a Si monolayer on the oxide surfaces, consistent with the observation that approximately one monolayer of SiH₄ adsorbs on oxidized TiN sites by forming Si-O bonds.^{263,264} The Si monolayer then acts as a reducing layer, hence the earlier tungsten nucleation on SiO₂, Al₂O₃, and TiO₂ following SiH₄ pre-exposures shown in Figure 6.6 and 6.8. This is consistent with the more conformal tungsten films following SiH₄^{263,264} or B₂H₆¹² pre-exposures. Nevertheless, we do not consider SiH₄ the predominant selectivity loss reactant. Considering that for TiO₂, 50 SiH₄ pre-exposures enhanced W-ALD nucleation by 5-10 cycles compared to the 30-35 cycle for 50 WF₆ pre-exposures.

6.5.4 *Limiting WF₆ and SiH₄ reactions with surface hydroxyls*

We have provided evidence that both WF₆ and SiH₄ can react with surface hydroxyls, which leads to metallic tungsten nucleation. FTIR results in Figure 6.3 shows that within the 200-300°C temperature range there is still surface bound water on SiO₂ surfaces. There is approximately a monolayer of water on piranha cleaned SiO₂ surfaces²⁶⁵ that can react with

and deplete SiH_4 ²³⁶ and or WF_6 ²⁶¹ forming non-growth oxide films (SiO_2 and WO_3 respectively). We conclude that tungsten nucleation on the hydroxylated oxide surface does not proceed until the physisorbed water layer is consumed. This conclusion is supported by the results in Figure 6.5 that shows removing surface bound water by annealing samples at 600°C leads to earlier tungsten nucleation. This may also explain the improved selectivity observed at 160°C than 300°C in Figure 6.9.

In summary, the following three factors are shown to have significant influence on delaying tungsten nucleation on oxide surfaces: 1) having physisorbed water on the non-growth surface, 2) reducing the concentration of surface vicinal hydroxyls, and 3) etching the oxide substrate and removing possible metal nucleation sites. Based on these conclusions, we suggest three strategies to improve the tungsten selectivity: 1) Based on data in Figure 6.9, operating at lower deposition temperatures will improve the selectivity window, which we attribute to the temperature dependence of the WF_6 reaction, 2) in-situ annealing or plasma cleaning to minimize the prevalence of surface hydroxyls, and 3) non-volatile metal fluoride species could be removed by incorporating an additional reagent, similar to an ALE process.^{82,256,257} Overall, a better understanding of selectivity loss mechanism is pivotal for improving the selectivity window for the W-ALD and other selective ALD processes.

6.6 Conclusion

In this paper we investigate W-ALD nucleation mechanisms for SiO_2 and other oxide substrates. Our results indicate that tungsten nucleation on SiO_2 occurs at hydroxyl sites generated on the surface by the piranha sample preparation. By annealing SiO_2 samples prior

to tungsten deposition we show that vicinal hydroxyls help promote WF_6 adsorption, while physisorbed water tends to delay tungsten nucleation. On oxide surfaces, we found that SiH_4 pre-exposure helped promote tungsten nucleation, which we attribute to the formation of a reducing Si layer. Also on oxide surfaces, WF_6 reacts to form metal fluoride species. In the case of TiO_2 and SiO_2 , the metal fluoride species were volatile and lead to film etching. Finally, we demonstrate that the W-ALD selectivity window can be widened by reducing the process temperature, due to the temperature dependence of the WF_6 interaction with the oxide surface. Understanding selectivity loss mechanisms is the first step to determining the necessary precursors and reactor conditions for extending the selectivity window of an ALD process.

6.7 *Acknowledgements*

The work included in this manuscript was funded by the semiconductor research corporation (SRC). The authors acknowledge the use of the Analytical Instrumentation Facility (AIF) at North Carolina State University, which is supported by the State of North Carolina and the National Science Foundation.

CHAPTER 7. INFLUENCE OF TEMPERATURE AND CARRIER GAS FLOW RATE ON THE TUNGSTEN ATOMIC LAYER DEPOSITION “SELECTIVITY WINDOW”

Paul C. Lemaire and Gregory N. Parsons

This chapter is an article in preparation and may be revised for future publication.

7.1 Abstract

Area-selective thin film deposition is expected to be important for overcoming limitations in conventional patterning techniques for manufacturing semiconductor devices. A tungsten ALD process (W-ALD) has shown propensity for selective deposition of tungsten on Si-H and metal surfaces preferentially over oxide surfaces, but selectivity is lost after a number of W-ALD cycles. In order to expand the “selectivity window” we investigated how the process temperature, carrier flow rate, and choice of carrier gas could delay W-ALD nucleation on oxide surfaces. We assessed these process parameters with spectroscopic ellipsometry (SE), quartz crystal microbalance (QCM), and x-ray photoelectron spectroscopy (XPS) analyses. Reducing the process temperature was observed to extend the W-ALD incubation period on oxides, but at the cost of reduced deposition rates on growth surfaces. Increasing the carrier flow rate expanded the W-ALD selectivity window without significantly reducing tungsten deposition on Si. We propose that increasing the carrier flow rate reduces the precursor concentration in the gas phase, which in turn limits precursor adsorption on the non-growth oxide surfaces. Finally we show that dosing carrier gases (H_2 , He, and CH_4) before the WF_6

exposure also extends the W-ALD incubation period on oxide surfaces. We attribute this to a combined effect of precursor dilution, precursor desorption, and blocking of potential active sites on the oxide surfaces. Adjusting process parameters such as temperature and precursor concentration offer simple routes to widen the selectivity window without the need for significant chemical modification of surfaces.

7.2 Introduction

As transistor devices continue to get smaller, there is a growing need for selective deposition techniques as standard patterning techniques become more limited at smaller feature scales. Selective deposition is a way to deposit materials, such as metals or dielectrics, in predetermined regions. Selective atomic layer deposition (S-ALD) is a vapor phase technique that uses two self-limiting half reactions to preferentially deposit conformal films on specific substrates, with angstrom level thickness control.^{5,11} Typically, S-ALD requires chemical modification of a surface in order to widen the selectivity window. For example, self-assembled monolayers (SAMs) have been used to selectively passivate surfaces to inhibit deposition in the patterned regions. Yet SAMs are typically costly, cannot completely passivate a surface, and do not lend themselves to conventional semiconductor manufacturing.^{29,30} One solution is to instead take advantage of the inherent differences in surfaces energy of unmodified surfaces. For example, a tungsten ALD (W-ALD) process, which uses tungsten hexafluoride (WF_6) and silane (SiH_4)¹⁰⁻¹² or disilane (Si_2H_6)¹⁴⁻¹⁷ selectively deposits tungsten on Si and metal surfaces.^{25,235,236} In contrast, “non-growth”

surfaces such as SiO₂ exhibit lower rates of tungsten nucleation because the oxidized silicon atoms are unable to act as sacrificial reductants.²⁴⁻²⁶

Although deposition on non-growth surfaces is thermodynamically much less favorable, deposition will occur after an incubation period. In order to take full advantage of selective ALD processes, it is pivotal to extend the “selectivity window” or maximize the amount of material deposited on the growth surface before growth begins on the non-growth surface. Recent results suggest that WF₆ reaction with surface hydroxyls is the predominant cause for selectivity loss.^{13,26} Therefore, limiting WF₆ adsorption and reactions with oxide substrates is one strategy to extend the selectivity window.

Adjusting the process temperature is one means of widening the selectivity window. For example, nucleation can be inhibited by lowering the temperature because there is insufficient energy to overcome activation energy barriers.⁵ In contrast, increasing the process temperatures can also depress nucleation because of higher precursor desorption rates.⁵ These parameters not only vary among different process chemistries but also across different substrates. For example, the incubation time for copper chemical vapor deposition (CVD) on growth (e.g. aluminum) and non-growth surfaces (e.g. SiO₂) decreases as the deposition temperature increases because of reduced activation barriers for the copper precursor adsorption.²⁶⁶⁻²⁶⁸ Adsorption and subsequent deposition is inhibited when the copper-ligand bond strength is stronger than the copper-SiO₂ bonding.²³⁴

In addition to reactor temperature, process pressure and the carrier gas affects nucleation and selectivity. Increasing the reactant partial pressure reduces the incubation time because the

molecular flux density condensing on the surface is directly proportional to the reactant partial pressure.²⁶⁷⁻²⁷⁰ Selective deposition of tungsten by WF_6/SiH_4 CVD is enhanced by operating at lower pressures and at lower SiH_4 concentrations. The carrier gas itself can impact the selectivity by acting as a reducing agent, changing the concentration of active sites on a substrate, or enabling different reaction pathways.^{267,268} Precursors will also have different diffusivities in certain carrier gases, which in turn impacts the frequency of precursor molecule collisions with surface sites.^{271,272}

The majority of the work studying the impact of process parameters such as reactor temperature or pressure has focused on CVD processes. Although CVD and ALD processes bear many similarities, separating the reactant exposures with inert purging can drastically impact how process parameters can impact deposition rates and selectivity. Accordingly, in this paper, we investigate how process temperature and pressure/carrier flow rate affects the selectivity window for a tungsten atomic layer deposition process (W-ALD). We used spectroscopic ellipsometry (SE), quartz crystal microbalance (QCM), and x-ray photoelectron spectroscopy (XPS) to assess tungsten nucleation on a growth surface (Si) versus non-growth surfaces (SiO_2 and TiO_2). We observed that lowering the process temperature decreased the tungsten growth per cycle on Si, SiO_2 , and TiO_2 but nevertheless widened the selectivity window. Operating at higher carrier flow rates and overall process pressures depresses tungsten nucleation on SiO_2 and TiO_2 surfaces without significantly impacting the deposition on the Si surfaces. Based on these results we then investigated how

H₂, He, and CH₄ dosing can be used to modify the process temperature and pressure to further improve the W-ALD selectivity.

7.3 *Experimental*

7.3.1 *List of supplies and materials*

Tungsten hexafluoride (WF₆) and a dilute 2% silane in argon mixture (SiH₄) were purchased from Galaxy Chemical (Claremore, OK) and Custom Gas Solutions (Durham, NC) respectively and used without further treatment. Titanium tetrachloride (TiCl₄) was obtained from Strem Chemicals Inc. and used without further treatment. The Si substrates were boron doped Si(100) 6-10 Ω-cm (WRS Materials). The SiO₂ substrates were Si(100) 6-10 Ω-cm with 100 nm thermal SiO₂ (WRS Materials), cut into 12 x 12 mm pieces. For the carrier and purge gas, dry 99.999% argon (Ar) was passed through an Entegris GateKeeper inert gas purifier to remove any residual water before entering the reactor.

7.3.2 *Substrate surface preparation*

The SiO₂ substrates were cut into 12 x 12 mm pieces. SiO₂ samples were cleaned in hot piranha solution (1:1 H₂SO₄:H₂O₂ by volume) for 30 minutes, rinsed with deionized (DI) water, and stored in DI water. Immediately prior to W-ALD, the SiO₂ pieces were rinsed in DI water and dried under flowing N₂ (100 psi). To form hydrogen-terminated silicon, 12 x 12 mm Si pieces were cleaned in the piranha solution described above and stored in DI water. Immediately prior to W-ALD, the Si wafers were dipped in dilute hydrofluoric acid (5 vol%) for 30 s followed by a DI water rinse (30 s) and N₂ drying.

7.3.3 *W-ALD reactor design*

Depositions were carried out in a chamber home-built ALD reactor described in previous publications.^{11,18} Precursor and inert gases were diverted to one of two cylindrical process chambers by gas switching valves. The larger deposition chamber was a hot-walled stainless steel tube (60 cm long, 10 cm diameter tube) and second reaction chamber made of fused quartz (60 cm long, 4 cm diameter tube) was positioned in parallel to the steel reactor and shared the same upstream and downstream gas piping. The steel and quartz tube were heated resistively with PID controllers, but the quartz chamber was only heated near the substrate in order to minimize exposed hot metal surfaces. The operating standard operating conditions were a temperature of 220°C and a pressure of 1.5 Torr with an Ar carrier flow rate of 210 sccm.

7.3.4 *ALD reaction sequence*

Tungsten deposition was achieved by alternately pulsing SiH₄ and WF₆ with inert Ar purge steps following each exposure. Silicon substrates were loaded into the reactor and allowed to reach thermal equilibrium with the walls by flowing carrier gas for 30 min prior to deposition. The conditions for the starting base-line W-ALD process used the SiH₄/Ar/WF₆/Ar (45/45/1/60 s) sequence at 220°C. Finally TiO₂ ALD films were deposited prior to the W-ALD process using a TiCl₄/Ar/H₂O/Ar sequence with a timing sequence of 0.25/45/0.25/45 s.

7.3.5 *Sample characterization*

Film nucleation and growth were characterized using ex situ analytical tools. Spectroscopic ellipsometry (SE) data were obtained with a J.A. Woollam alpha-SE ellipsometer at an incidence angle of 70°. To alleviate issues with modeling ellipsometry data, we use a previously published approach to trace tungsten nucleation by directly monitoring the ellipsometry delta parameter, Δ , at 700 nm.^{13,18} It was observed that the Δ value is 78° for the initial SiO₂ surface but decreases to ~30°. During film coalescence, the Δ value increases to 130°, similar to the Δ value on the Si wafers.^{13,18} Chemical analysis was done using a SPECS X-ray photoelectron spectroscopy (XPS) system with a PHOIBOS 150 analyzer. Spectra were generated using an Al K α X-ray source operated at 400 W. For all analyses, data reduction and fitting was carried out using CasaXPS software with charge compensation based on the C 1s (C-C, C-H) peak set to 285 eV.

Process conditions were further characterized using in-situ QCM analysis. For these tests, a 6 Hz gold coated QCM crystal sensor (Inficon) was placed into the QCM housing. A dry Ar crystal back purge that yielded a ~250 mTorr pressure increase was sufficient to prevent deposition on the backside of the QCM crystal. The mass change signals were detected by an Inficon SQM-160 monitor and recorded using a home designed LabVIEW program.

7.4 Results

7.4.1 Process Temperature and Tungsten Nucleation on Si and Oxide Surfaces

Tungsten deposition on Si and SiO₂ surfaces as a function of temperature was monitored by tracking the delta parameter Δ , at 700 nm.^{13,18} Δ is strongly dependent on surface roughness and inhomogeneity and therefore a good measure of nuclei formation and coalescence.^{18,144} It was observed that on SiO₂, the Δ value was 78° during the W-ALD incubation period. With additional W-ALD cycles, the Δ value decreased to 30° with the formation of tungsten nuclei on the SiO₂ surface. Then, with additional W-ALD cycles, the nuclei fully coalesced and the Δ value increased to ~130°. In contrast, the Δ value decreases from 152° to ~130° with increasing tungsten film thickness on a Si substrate.^{13,18}

Figure 7.1 shows a similar trend when the W-ALD cycle number is held constant (50 cycles) and the deposition temperature is increased. Below 160°C, ellipsometry suggest there is little to no tungsten nucleation on the SiO₂ surface. At 190°C, 50 W-ALD cycles deposits disjointed tungsten nuclei, whereas fully coalesced films are deposited at and above 220°C. In addition, the Δ value on the Si also decreases with increasing temperature, consistent with deposition of thicker tungsten films at higher temperatures.¹⁸

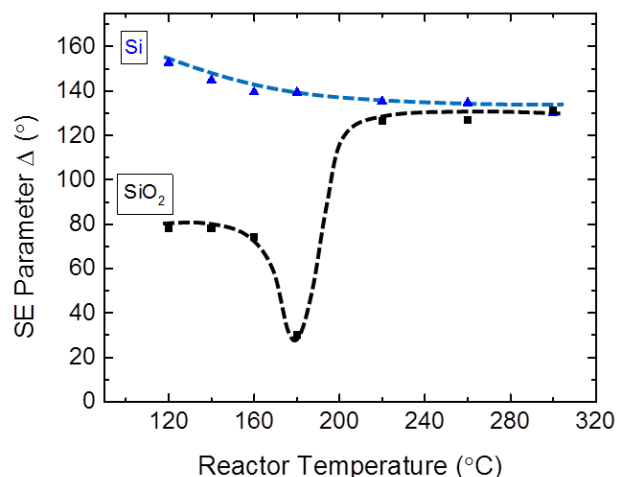


Figure 7.1: SE delta parameter at 700 nm versus deposition temperature for SiO₂ and Si samples following 50 W-ALD cycles.

SiO₂ surfaces following W-ALD deposition at different process temperatures were then characterized with XPS. We chose to vary the number of W-ALD cycles at different process temperatures in order to characterize the surfaces when tungsten was first detected (aka samples with a Δ value of $\sim 30^\circ$). Figure 7.2 shows the high resolution W 4f and F 1s XPS scans for SiO₂ samples after 20, 30, and 50 W-ALD cycles at 300, 220, and 160°C respectively. Figure 7.2a shows that there are approximately equal amounts of tungsten on the SiO₂ surfaces. The W 4f signal is slightly higher with the 300°C deposition, despite the lower number of W-ALD cycles. This is due to the higher deposition rates at the higher temperatures. We previously showed that more W-ALD cycles at lower process temperature exhibited the highest selectivity of tungsten deposition on Si versus SiO₂.¹³

Figure 7.2b shows that at 160°C, there is a detectable fluorine signal on the SiO₂ substrate. It was previously observed that WF₆ can react with SiO₂²³⁶ and TiO₂^{254,255,273} to form SiF₄ and

TiF₄. By fluorinating the oxides substrates, the WF₆ accepts oxygen and forms WO_xF_y.¹³ At 220°C, WO_xF_y species are volatile, but are non-volatile at and below 170°C. Accordingly, the longer W-ALD incubation delay at lower temperatures is possibly the combined result of higher concentration of nonvolatile fluorinated surface species and lower reactivity of SiH₄ at lower temperatures.^{16,24,26,239,243,250}

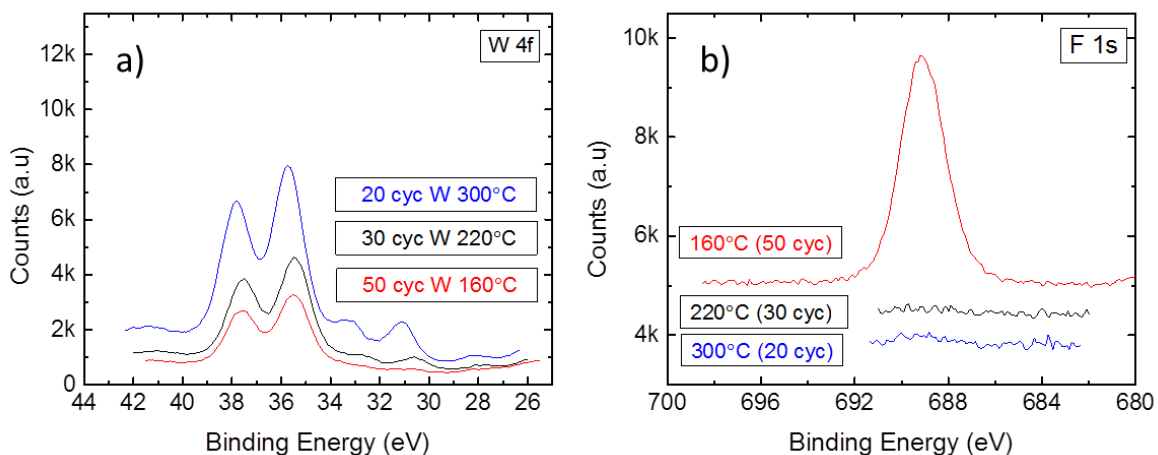


Figure 7.2. Ex-situ XPS high resolution scans of the a) W 4f and b) F 1s regions for SiO₂ samples after 20, 30, and 50 W-ALD cycles at 300, 220, and 160°C respectively. The number of W-ALD cycles for each temperature was chosen based on when the delta parameter, Δ , decreased to $\sim 30^\circ$, indicative of tungsten nucleation as described above.

W-ALD was also monitored on TiO₂ surfaces with in-situ QCM analysis. Figure 7.3 shows that at a higher process temperature (250°C) the nucleation delay is ~ 10 W-ALD cycles. In contrast, at lower temperatures (190 and 220°C), the incubation time increases to 30-35 W-ALD cycles. Finally at 160°C, we did not observe steady state tungsten deposition within 50 W-ALD cycles. A process temperature of 160°C may be too low to overcome the activation barrier for the precursor adsorption or reduction reaction. It may also be related to reactor

poisoning by halogenated species from the TiCl_4 or WF_6 precursors at 160°C .¹¹ It should also be noted there was etching of the TiO_2 substrate during the incubation period at 220°C , but not the other process temperatures. We propose that at 220°C , there is a balance between a long enough incubation time and high enough temperature to volatilize etch products. Etching of active sites or WO_xF_y surfaces species may account for the slightly longer delay at 220°C than 190°C .

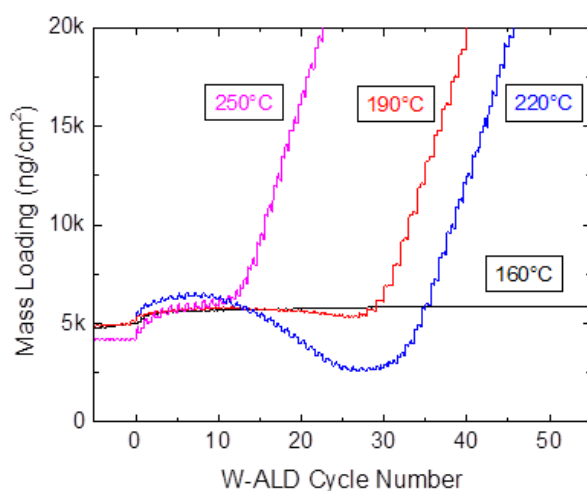


Figure 7.3: In-situ QCM analysis of W-ALD nucleation on TiO_2 surfaces at different process temperatures.

7.4.2 Tungsten Nucleation versus Process Pressure/Carrier Flow Rate

We next assessed how modulating the reactor pressure by increasing the carrier flow rate impacted the W-ALD incubation period. Figure 7.4a shows the reactor pressure increases linearly with an increase in carrier flow rate. In addition, Figure 7.4b shows the Δ value for Si and SiO_2 surfaces after 40 W-ALD cycles versus carrier flow rate. At lower pressure

(~0.75 Torr), 40 W-ALD cycles is sufficient to deposit nearly coalesced films. When the overall reactor pressure is increased to ~5.5 Torr, 40 W-ALD cycles results in disjointed tungsten nuclei. Both the vapor pressure of SiH_4 and WF_6 are high enough that this reduced tungsten nucleation at higher process pressures is not attributed to reduced precursor exposure. Instead, we propose that operating at higher carrier flow rates dilutes the reactant concentration, reducing the probability of adsorption on the non-growth surfaces. Furthermore, tracking the Δ value on the Si surfaces stays relatively constant from 0.75-5.5 Torr. The WF_6 and or SiH_4 adsorption is thermodynamically favorable enough on the Si or deposited tungsten surface that varying the reactant concentration does not significantly impact the deposition kinetics.^{15,24,250}

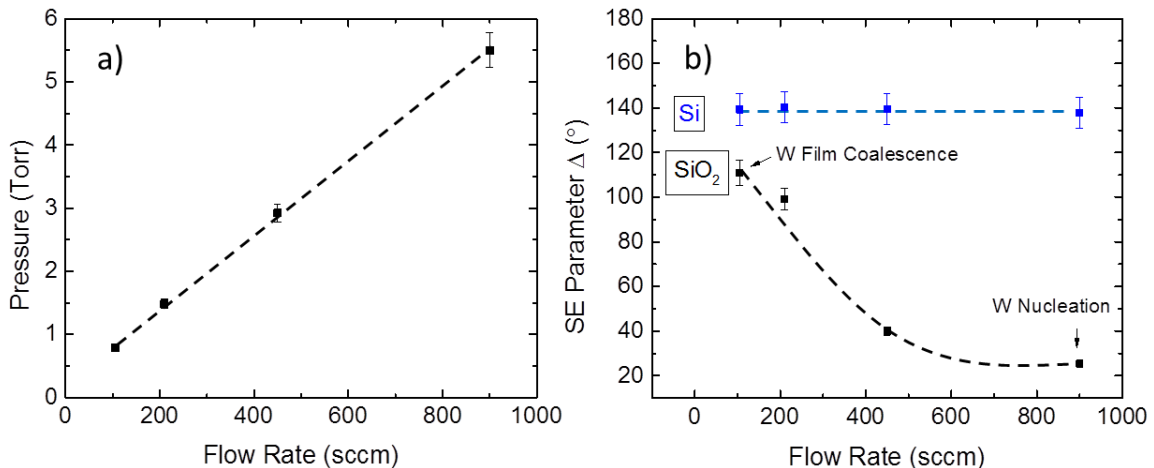


Figure 7.4: a) Operating pressure versus Ar carrier flow rate b) SE delta parameter at 700 nm versus flow rate for SiO_2 (black) and Si (blue) substrates after 40 W-ALD cycles at 220°C.

To support the ellipsometric analysis, we assessed tungsten nucleation on TiO_2 surfaces as a function of reactor pressure using QCM analysis. Figure 7.5 shows that as the pressure was

increased from 0.9 to 5.5 Torr by increasing the carrier flow rate, the tungsten nucleation delay increased from ~25 to 50 W-ALD cycles. Again we attribute this to precursor dilution and reduced precursor adsorption on the TiO₂ surface. We also observed less pronounced etching at higher process pressures. This is possibly a result of reduced volatilization of etch products at higher pressures. The lower etching may also be due to reduced substrate fluorination because of reduced precursor adsorption at the lower precursor concentration.

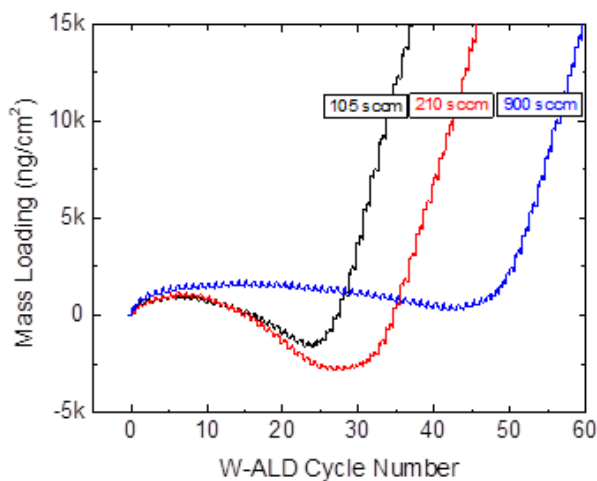


Figure 7.5: In-situ QCM analysis of W-ALD nucleation on TiO₂ surfaces with an Ar carrier gas flow rate of 105 (black), 210 (red), and 900 (blue) sccm at 220°C.

7.4.3 Modulating Process Temperature/Pressure with Inert Gas Dosing

In prior work, it was observed that dosing molecular H₂ immediately prior to the WF₆ exposure extended the W-ALD nucleation delay on SiO₂ surfaces without reducing growth on Si or Au surfaces.¹⁸ It was proposed that H₂ would partially react with the WF₆ in the gas phase, generating HF that passivated SiO₂ surfaces.¹⁸ Based on the results shown in Figures

7.1-7.5 we decided to further investigate the role of H₂ in tungsten nucleation. H₂ has a high momentum and thermal diffusivity (8700 and 12,300 cm²/s respectively)²⁷¹ and we reasoned that changes in the reactor pressure, temperature, or reactant diffusivity may also account for reduced tungsten nucleation on SiO₂.

Figure 7.6 shows results from QCM analysis of steady state W-ALD in which He or H₂ is dosed for 5 s immediately prior to the WF₆ dose. During He and H₂ dosing, there is an observable decrease in the mass loading, indicating either precursor desorption or surface heating, which would increase the frequency of the QCM crystal.¹³⁸ This was further investigated by using a smaller volume quartz reactor to magnify any thermal effects. Figure 7.7 shows QCM analysis of steady state W-ALD in which H₂ was dosed for 5s either immediately before or 45 s before the WF₆ dose. Figure 7.7a shows a more pronounced decrease in the mass loading during the H₂ dose than in 7.6b. This is consistent with enhanced heat transfer because of the closer proximity between the QCM crystal and the hot reactor walls in the smaller reactor volume. Figure 7.7b shows that when the crystal is allowed to equilibrate for 45 s after the 5 s H₂ dose, the mass loading increases, returning approximately to the mass loading value prior to the H₂ dose. Collectively this suggests that the decrease in the mass loading is due to crystal heating.

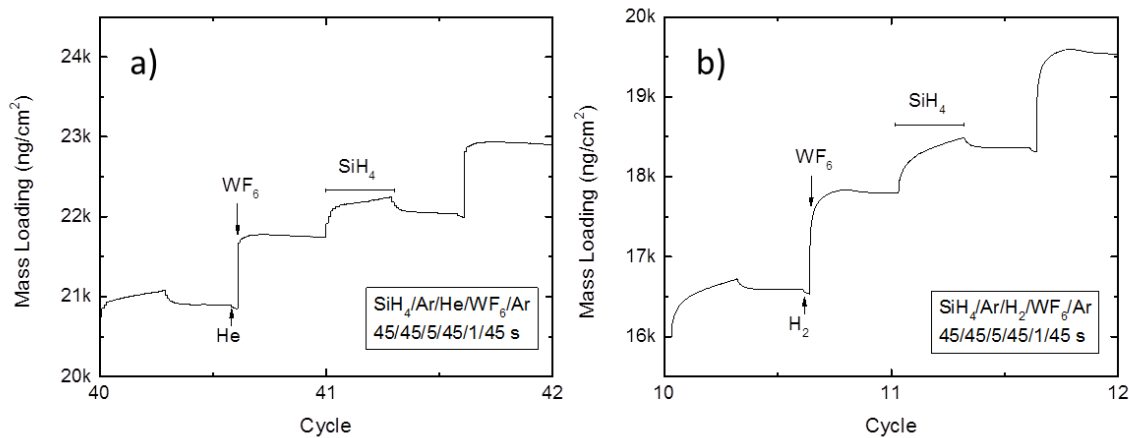


Figure 7.6: QCM analysis steady state W-ALD at 220°C with a reactor volume of 4700 cm³, where a) He and b) H₂ are dosed immediately before the WF₆ for 5 s. During the He and H₂ dosing, there is an observed decrease in the QCM loading, consistent with sample heating.

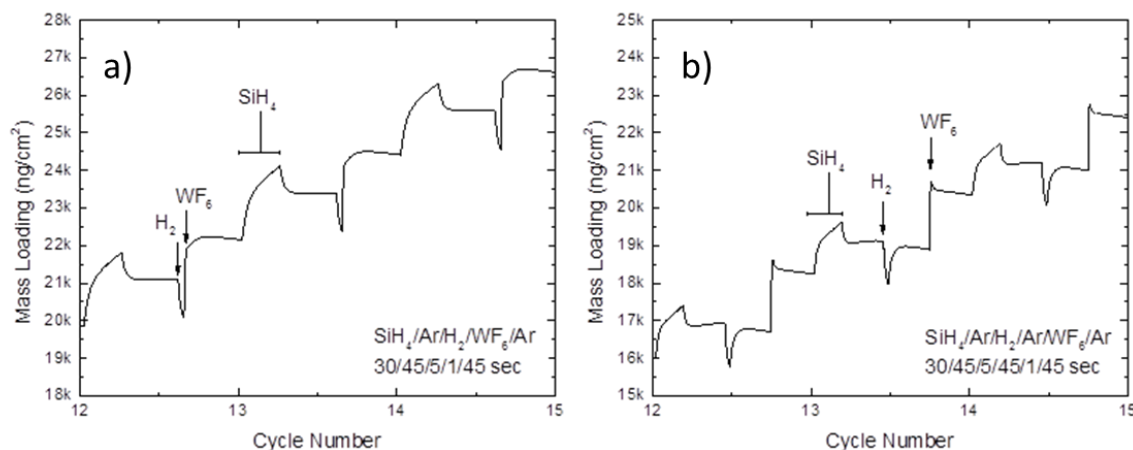


Figure 7.7: QCM analysis of W-ALD in smaller reactor volume (~750 cm³) where H₂ was dosed for 5 s a) immediately before and b) 45 s before the WF₆ dosing. In the smaller reactor volume, the decrease in the QCM signal during the H₂ dosing due to sample heating is more pronounced, but returns to the initial mass loading during a sufficiently long Ar purge step.

Inhibition of tungsten nucleation by dosing inert carrier gases was further assessed with XPS analysis. Figure 7.8 includes high resolution XPS scans of the W 4f and Si 2p regions for

SiO₂ samples following 40 W-ALD cycles at 220°C. For the standard SiH₄/Ar/WF₆/Ar recipe, Figure 7.8a shows that there are prominent W 4f peaks at 33 and 30.8 eV associated with W⁰ and features at 37.5 and 35.3 eV due to oxidized W. In comparison, when CH₄ or He was dosed for 5 s immediately prior to the WF₆ exposure, the peaks associated with metallic and oxidized tungsten are significantly reduced. Furthermore, the Si 2p peaks for the CH₄ and He modified W-ALD sequences are visible, whereas Si is below the detection limit following the standard recipe, due to a thick tungsten film.

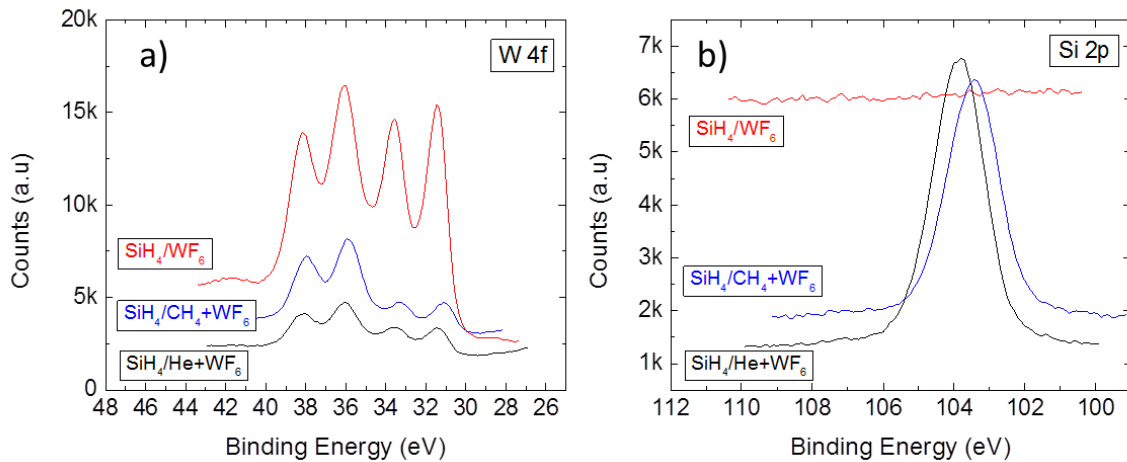


Figure 7.8: Ex-situ high resolution XPS scans of the a) W 4f and b) Si 2p regions for SiO₂ samples following 40 W-ALD cycles at 220°C. Three reaction sequences were used: SiH₄/Ar/WF₆/Ar (red), SiH₄/Ar/CH₄/WF₆/Ar (blue), and SiH₄/Ar/He/WF₆/Ar (black). Samples in which CH₄ and He were dosed immediately prior to the WF₆ exhibit lower tungsten concentration and a more pronounced Si signal from the underlying SiO₂ wafer.

7.5 Discussion

Adjusting the reactor temperature, carrier flow rate, and carrier gas was observed to increase the nucleation delay in two main ways: 1) reduce the probability of WF₆ reacting with active

sites on the oxide surface and 2) limit the ability for SiH₄ to reduce the adsorbed fluoride species. Reducing the process temperature reduces tungsten nucleation predominantly by decreasing the SiH₄ reduction reaction.²⁴⁸ QCM analysis of W-ALD on TiO₂ in Figure 7.3 shows that at 160°C, the initial WF₆ dose increases the mass loading, but additional W-ALD cycles do not lead to additional loading. This suggests that the surface is passivated with TiF_x and WF_y surface species because the temperature is too low to supply the necessary thermal energy for SiH₄ to adsorb and remove surface fluorine. This is consistent with the XPS results in Figure 7.2b in showing significant fluorine concentration following the W-ALD on SiO₂ at 160°C. Reducing the process temperature is not an ideal strategy to widen the selectivity window because it also reduces the deposition rate on the growth surface as shown by the increasing Δ value on the Si surface.

Tungsten nucleation on oxide substrates was also reduced by increasing the argon carrier gas flow rate. We used Equation 7.1 and the results in Figure 7.4b to assess if increasing the flow rate reduced the residence time.

$$\tau = \frac{P}{M} \cdot \frac{V \cdot \tilde{M}}{R \cdot T} \quad (7.1)$$

Where τ is the reactor residence time, \dot{M} is the mass flow rate, V is the reactor volume, \tilde{M} is the molecular weight of argon, R is the ideal gas constant, and T is the temperature. Assuming a constant reactor temperature and volume, the linear increase in pressure with increasing flow rate conveys that the residence time remains relatively constant. This suggests the longer incubation period is not due to a reduction in residence time.

Instead of changing the residence time, we suggest that increasing the carrier gas flow rate extends the W-ALD nucleation delay on SiO₂ by diluting the vapor-phase reactants. Decreasing the vapor-phase concentration decreases the probability of precursor adsorption on a surface. For example, ALD of Al₂O₃ with dilute trimethylaluminum and water leads to incomplete conversion of methyl and hydroxyl species, which reduces the deposition rate per cycle and incorporates unwanted contaminants into the film.²⁷⁰ Similar phenomena were observed for HfO₂ and ZrO₂ ALD, where it was observed that higher carrier gas flow impacted the composition of the adsorbate layer and affected the final film properties, such as increasing the film density.²⁷⁴ In our system, the reduced WF₆ adsorption leads was observed as reduced TiO₂ etching at 900 sccm because the degree of etching is dependent on the extent of oxide fluorination.^{254,255}

Based on the results assessing the role of temperature and pressure, there are a couple explanations for the reduced tungsten nucleation on oxide surfaces when different carrier gases were dosed immediately before the WF₆. First, dosing another gas prior to the WF₆ dilutes the precursor, similar to operating at a higher carrier flow rate. The type of gas (H₂, He, etc) is also potentially significant because of differences in heat capacity and the diffusivity of WF₆ in the gas. For example, the diffusivity of WF₆ in He is ~5x that of in Ar, so WF₆ is more likely to collide with a carrier gas molecule than the substrate in He than in Ar.²⁷¹ Higher diffusivity in a carrier gas will cause convection to dominate molecular motion or diffusion, reducing the number of contacts between WF₆ and the oxide surface and extending the W-ALD nucleation delay on an oxide.²⁷²

The choice of carrier gas may also impact nucleation through thermal effects. The thermal diffusivities of He and H₂ are approximately an order of magnitude higher than Ar,²⁷¹ which allows for better heat transfer between the heated reactor walls and substrate. An increase in the temperature could facilitate in desorption of WF_x species from the substrate,^{248,274} without supplying additional thermal energy needed for the SiH₄ reduction. The increase in the sample temperature was observed during QCM analysis because the QCM frequency is temperature dependent. Finally, gases like H₂ or CH₄ can dissociatively adsorb on surfaces, which could block adsorption of WF₆.²⁷¹ It is likely that a combination of these effects play a role in the longer W-ALD incubation period. For example, He has a higher diffusivity than CH₄, but CH₄ can adsorb on oxide surfaces, which may explain the similar W-ALD delay shown in Figure 7.8.

7.6 Conclusion

In this paper we investigate strategies to widen the W-ALD selectivity window by varying the process temperature and reactant concentration. We observed that the W-ALD nucleation and deposition rate both decreased at lower temperature. The selectivity window was widened at lower process temperatures, but required additional W-ALD cycles to compensate for the lower deposition rates on the growth surface. The longer nucleation delay on the oxide surfaces at the lower process temperature was attributed to surface passivation by fluorine species. Tungsten nucleation was also delayed on SiO₂ surfaces by increasing the carrier gas flow rate. The increase the carrier gas flow rate reduces the probability of WF₆ adsorption on the oxide surfaces due to reactant dilution. Finally, we observed that dosing

H₂, He, or CH₄ prior to the WF₆ exposure also widened the W-ALD selectivity window. We suggest that the addition of these carrier gases may delay tungsten nucleation on oxide surfaces by diluting the WF₆, blocking WF₆ adsorption through competitive adsorption, or facilitating WF₆ desorption through sample heating. Determining new and practical strategies for widening selectivity windows is essential to make vapor-phase deposition processes viable replacements for current patterning techniques.

CHAPTER 8. SELECTIVE SELF-LIMITING THERMAL ATOMIC LAYER ETCHING OF TiO₂ USING SEQUENTIAL EXPOSURES OF WF₆ AND BCL₃

The following work is reproduced with permission from Paul C. Lemaire and Gregory N. Parsons. “Selective Self-Limiting Thermal Atomic Layer Etching of TiO₂ using Sequential Exposures of WF₆ and BCl₃” Submitted to *Chemistry of Materials*. **2017**

8.1 Abstract

Controlled thin film etching is essential for further development of sub-10 nanometer semiconductor devices. Vapor-phase thermal etching of oxides is appealing for achieving highly conformal etching of high aspect ratio features. We show that tungsten hexafluoride (WF₆) can be used to selectively etch amorphous titania (TiO₂) films versus other oxides including alumina (Al₂O₃). WF₆ etching of TiO₂ was studied with quartz crystal microbalance (QCM), spectroscopic ellipsometry, x-ray photoelectron spectroscopy (XPS) analysis, and thermodynamic modeling. XPS shows evidence for a WO_xF_y layer that forms on of the TiO₂ films during the etch process, which may act as a surface surfactant layer to help enable fluorination of the TiO₂. Etching of TiO₂ was observed to be temperature dependent, in which etching was observed at 220°C, but not 120°C. The WF₆ etching depends on the volatilization of the metal fluoride and WF₂O₂, as suggested by thermodynamic modeling. Finally we show that BCl₃ can be used as co-reagents with WF₆ to develop atomic layer etching (ALE) processes, in which the reactor temperature impacts the TiO₂ etch rate per cycle and the ALE saturation behavior. At 170°C, the ALE removal rate

using WF_6/BCl_3 saturates near ~ 0.3 Å/cycle, approximately equivalent to the ALD film growth rate at the same process temperature.

8.2 Introduction

The semiconductor industry foresees multiple challenges in designing and manufacturing transistor devices for the 7 and 5-nm nodes. For example, standard patterning techniques, such as lithography, become much less applicable because of challenges maintaining edge definition and alignment to the underlying features. In addition, semiconductor devices typically utilize three dimensional designs, creating complex high-aspect-ratio features. Accordingly, the semiconductor industry is looking towards controllable etching techniques to supplement currently used thin film deposition techniques.

Vapor phase etching of silicon (Si) native oxide is of interest to the semiconductor industry. Hydrogen fluoride (HF) liquid etching of Si native oxide⁵⁹⁻⁶¹ is ubiquitously utilized in the semiconductor industry, but in-situ vapor etching helps limit the reformation of an interfacial oxide layer between Si and a deposited film.^{62,10,63-66} For both solution and vapor phase etching, H_2O plays a significant role in HF etching of Si native oxide, with significantly lower etch rates in anhydrous conditions.⁶⁷⁻⁷⁰ In vapor phase etching, water creates a interfacial layer between the substrate and gas and acts as a proton donor and acceptor to catalytically activate the HF etch.^{60,68,69} Although HF is a promising etchant, the high HF concentrations can lead to uncontrolled etching.

Extending the anhydrous HF vapor etch to other oxides is often limited, because unlike SiF_4 , many of the formed metal fluorides are non-volatile at typical process temperatures and pressures.²⁵⁷ Yet the non-volatile product formation also creates an opportunity to create a more controlled etching process because the surface fluoride species passivate the substrate from additional fluorination. Surface fluorides or chloride can then be removed anisotropically by a subsequent energy-enhanced technique such as Ar^+ bombardment or plasma species. Ideally, the two individual steps are self-limiting, creating a process known as atomic layer etching (ALE). But even with large control over the bias and the energy of the species, it is possible to get uncontrolled etching or damage to sensitive features.^{79,75,78,77}

In order to limit the issues that arise from energy-enhanced techniques, there is interest in purely thermally-driven chemical ALE processes. Such techniques would enable conformal isotropic etching, which has many applications for etching in high aspect ratio structures.⁴⁰

There has been considerable work by George et al. studying selective etching of oxides using HF in combination with different metal coreagents.⁸⁰⁻⁸³ Specifically, HF was used to fluorinate metal oxides including Al_2O_3 , HfO_2 , and ZrO_2 creating a passivating metal fluoride layer.⁸⁰⁻⁸³ Exposing the metal fluoride layer to a co-reagent such as trimethylaluminum (TMA),^{80,83} tin acetylacetonate ($\text{Sn}(\text{acac})_2$),^{80-82,84} diethylaluminum chloride (DMAC),⁸⁰ or silicon tetrachloride (SiCl_4)⁸⁰ can lead to a ligand-exchange reaction. Depending on the metal fluoride and the extent of the ligand-exchange, the modified surface layer will be volatilized, reforming the original substrate surface termination. For example, a AlF_3 surface layer is proposed to react with $\text{Sn}(\text{acac})_2$ to form volatile $\text{Al}(\text{acac})_3$ and $\text{SnF}(\text{acac})_2$.^{81,82} This

etching approach bears similarities to earlier work in which zinc oxide and copper were etched with hexafluoroacetate (hHfac)⁷¹ and hHfac and O₃/H₂O₂^{72,73} processes respectively. Selective oxide etching has been achieved by adjusting the process temperature and selecting specific metal precursors that serve as ligand sources. For example, a HF/TMA ALE process was observed to etch Al₂O₃ but not ZrO₂ at 300°C.⁸⁰ But in addition to HF, there are other chemicals that can be used in the surface modification step such as BCl₃,²⁷⁵ Cl₂,^{24,25} and WF₆.

WF₆ is an appealing fluorinating agent and etchant. As a higher oxidation state covalently-bound metal fluoride, WF₆ is highly volatile at room temperature.²⁵² Tungsten is also among the most electronegative of the transition metals,²⁷⁷ enabling selective fluoride transfer to other transition metals.²⁵² For example, WF₆ was observed to undergo halogen exchange with TiCl₄ and BCl₃, but was considerably less reactive than MoF₆.²⁵² Yet despite being less reactive, fluorination of TiO₂ with WF₆ proceeds with a Gibbs free energy of -14.9 kcal/mol, whereas HF fluorination is endothermic with $\Delta G = 6.9$ kcal/mol. The thermodynamic fluorination step by HF may in part explain why other reported thermally-driven ALE processes that utilize HF are unable to etch TiN.⁸⁰ In addition, WF₆ has been observed to etch SiO₂²³⁶ and WO₃ films²⁶¹ and in an analogous system NbCl₅ was observed to etch Nb₂O₅.²⁶² WF₆ also has a zero net dipole moment, making it relatively easy to evacuate from a reaction chamber, an attractive feature for a cyclic ALE process. In contrast, HF is “stickier” because of its high dipole moment, which can lead to hydrogen bonding and long residence times.⁴⁰

In this paper, we demonstrate that WF_6 can be used as an etchant for controlled removal of TiO_2 films in both chemical vapor etching and atomic layer etching sequences. We find that WF_6 selectively etches TiO_2 more readily than it etches Al_2O_3 which we ascribe to the ability of TiO_2 to more readily form volatile products at low process temperatures. Using ex-situ XPS analysis, we confirm WF_6 etching of TiO_2 films and provide evidence that etching proceeds through TiO_2 fluorination in the film bulk, and formation of a low density WO_xF_y surface layer on the etching film. Thinner TiO_2 films require less time to become fully fluorinated, resulting in overall more rapid oxide etching than thicker TiO_2 films.

We also find that using a surface coupling agent, the chemical etching via WF_6 can be controlled to achieve a self-limiting ALE process. Specifically we find that coupling exposures of WF_6 with $\text{Sn}(\text{acac})_2$ or BCl_3 in a step-wise sequence acts to volatilize the WO_xF_y surface layer formed during WF_6 etching, enabling etching of a fraction of a monolayer of TiO_2 (i.e. $\sim 0.3 \text{ \AA}$) per ALE cycle.

8.3 *Experimental*

8.3.1 *List of supplies and materials*

99.99% Tungsten hexafluoride (WF_6) and 99.9% boron trichloride (BCl_3) were purchased in stainless steel lecture bottles from Galaxy Chemical and Matheson respectively. Trimethylaluminum (TMA), titanium tetrachloride (TiCl_4) were obtained from Strem Chemicals Inc. and used without further treatment. 99.9% tin acetylacetonate ($\text{Sn}(\text{acac})_2$) was purchased from Sigma Aldrich. The Si substrates were boron doped Si(100) 6-10 $\Omega\text{-cm}$

(WRS Materials) and were used as-received. For the carrier and purge gas, dry 99.999% argon (Ar) was passed through an Entegris GateKeeper inert gas purifier to remove any residual water before entering the reactor.

8.3.2 *W-ALD reactor design and reaction sequence*

Depositions were carried out in a home-built ALD reactor (60 cm long, 10 cm in diameter) described in previous publications.^{18,11} The deposition chamber was heated resistively using PID controllers. The operating pressure was maintained at 1.5 Torr with an Ar carrier flow rate of 210 sccm. Silicon substrates were loaded into the reactor and allowed to reach thermal equilibrium with the walls by flowing carrier gas for 30 min prior to deposition or etching. Al₂O₃ and TiO₂ ALD films were deposited prior to the W-ALD process using a x/Ar/H₂O/Ar sequence where x is TMA and TiCl₄ respectively, with a timing sequence of 0.25/45/0.25/45 s. The WF₆ flow was restricted with a needle valve to generate a pressure change of 300 mTorr and pulsed for etching using a 1.0/60 s time sequence. In some instances, Sn(acac)₂ and BCl₃ were used as co-reagents with the WF₆. The processes were WF₆/Ar/Sn(acac)₂/Ar and WF₆/Ar/BCl₃/Ar with timing sequences of 1/60/1/60 and 1/60/2.5/60 s respectively. Sn(acac)₂ was heated to 105°C to produce a pressure change of ~75 mTorr. The BCl₃ pressure was controlled with a gas regulator and needle valve to generate a pressure change of ~750 mTorr during dosing.

8.3.3 *Sample characterization*

Film deposition and etching were characterized using ex-situ and in-situ analytical tools. Spectroscopic ellipsometry (SE) data were obtained with a J.A. Woollam alpha-SE ellipsometer at an incidence angle of 70° . Chemical analysis was done using a SPECS X-ray photoelectron spectroscopy (XPS) system with a PHOIBOS 150 analyzer. Spectra were generated using an Al $K\alpha$ X-ray source operated at 400 W. For all analyses, data reduction and fitting was carried out using CasaXPS software with charge compensation based on the C 1s (C-C, C-H) peak set to 285 eV. For some analyses, we utilized the Ti 2p $3/2$ XPS peak intensity to estimate the thickness of WO_xF_y films formed as a result of WF_6 adsorption. For this analysis, we measured the attenuation of the Ti 2p $3/2$ peak and modeled the film thickness using parameters available from the NIST Effective Attenuation Length Database,²⁴⁴ coupled with electron inelastic mean-free path values determined using the TPP-2M equation.²⁴⁵ For this equation, we used a bandgap of 3.45 eV ²⁷⁸ and density of 3.58 g/cm^3 ,²⁷⁹ consistent with reported values for amorphous low density WO_3 films.

Process conditions were further characterized using in-situ QCM analysis. For these tests, a 6 MHz gold coated QCM crystal sensor (Inficon) was placed into the QCM housing. A dry Ar crystal back purge that yielded a ~ 250 mTorr pressure increase was sufficient to prevent deposition on the backside of the QCM crystal. The mass change signals were detected by an Inficon SQM-160 monitor and recorded using a home designed LabVIEW program.

8.3.4 *Thermodynamic modeling*

Gibbs free energy values and equilibrium amounts in closed systems were calculated using HSC Chemistry 7.1 software. For the equilibrium composition calculations, the starting input amounts were 5 mol Ar, 1 mol WF_6 and 1 mol oxide (TiO_2 , HfO_2 , ZrO_2 , SiO_2 , and ZnO). The initial moles of Al_2O_3 were set as 0.667 to compensate for reaction stoichiometry. 50 measurements were done from 25 to 400°C at 1.5 Torr (0.002 bar).

8.4 *Results and Discussion*

8.4.1 *Vapor Chemical Etching of TiO_2 using WF_6*

The WF_6 interaction with ALD metal oxide films at 220°C was assessed with in-situ QCM analysis, where the layer to be etched (either Al_2O_3 or TiO_2) is deposited in the reactor on the QCM crystal via ALD immediately before etching experiments. Deposition and etching were performed at the same temperature. Figure 8.1a shows that immediately following steady-state Al_2O_3 or TiO_2 ALD at 220°C, the first 3-5 WF_6 dose steps result in an increase in the mass loading of 355 and 226 ng/cm^2 for Al_2O_3 and TiO_2 respectively. Additional WF_6 exposures on the Al_2O_3 surface leads to saturation, whereas additional WF_6 exposures on the TiO_2 surface leads to mass loss. After ~17 WF_6 doses, the QCM begins to record a net overall mass loss, and further WF_6 dosing leads to additional mass loss, consistent with TiO_2 etching by the WF_6 .

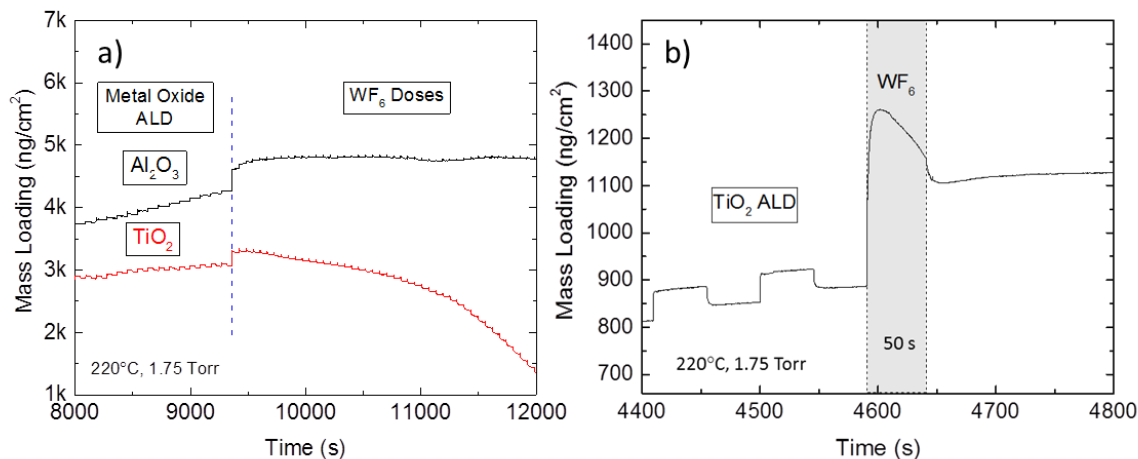


Figure 8.1: QCM analysis of a) 200 cycles of Al₂O₃ or TiO₂ followed immediately by 50 WF₆/Ar exposures of 1/60 s each; and b) 100 TiO₂ ALD cycles followed by 1 WF₆ exposure of 50 s.

The observed TiO₂ etching behavior in Figure 8.1a using a series of WF₆/Ar doses at 1/60 s, respectively, was further assessed in Figure 8.1b to determine the significance of the pulse sequence. Figure 8.1b shows results from QCM analysis of TiO₂ ALD followed by a single continuous WF₆ dose for 50 s. The high vapor pressure of WF₆ ensured that this exposure was equivalent to 50 WF₆/Ar pulses of 1/60 s each. The 50 s WF₆ pulse initially lead to a 360 ng/cm² mass increase, only somewhat larger than for the individual dose steps. As the WF₆ dose continued, the measured mass decreased, but after 50 s, QCM analysis shows a net mass increase of 205 ng/cm² relative to the mass measured immediately following TiO₂ ALD. Based on mechanism studies shown below, we believe that for the continuous and pulsed WF₆ exposure, the initial mass increase corresponds to fluorine and tungsten uptake on the TiO₂ surface, and the later mass decrease is due to etching, likely via removal of TiF₄ and

WF₂O₂ vapor products. The intermittent WF₆ exposure enhances etching by promoting product volatilization during the reactant purge period.

8.4.2 *Thermodynamic Modeling of Metal Oxide Etching by WF₆*

Thermodynamic calculations based on minimizing free-energy were performed to determine probable product species and to shed light on expected differences for etching of Al₂O₃ and TiO₂ by WF₆. Figure 8.2a shows the calculated equilibrium composition for a closed system initially consisting 1:1 molar ratio of TiO₂ to WF₆ as temperatures changes from 25 to 400°C. At room temperature WF₆ reacts with TiO₂ to form solid WO₃ and solid TiF₄, and at ~125°C the solid TiF₄ completely volatilizes. At ~150°C, WF₆ begins to etch the solid WO₃ to form volatile WF₂O₂. Similar modeling also indicates that WF₆ will etch SiO₂, though SiO₂ differs from TiO₂ because unlike TiF₄, SiF₄ is volatile even at room temperature. It should be noted that in the calculations, when either the initial WF₆:oxide ratio or the Ar partial pressure is increased, the temperature required to generate the volatile products decreases, indicating more favorable etching. This analysis is strictly accurate only for closed systems, where products are not purged.

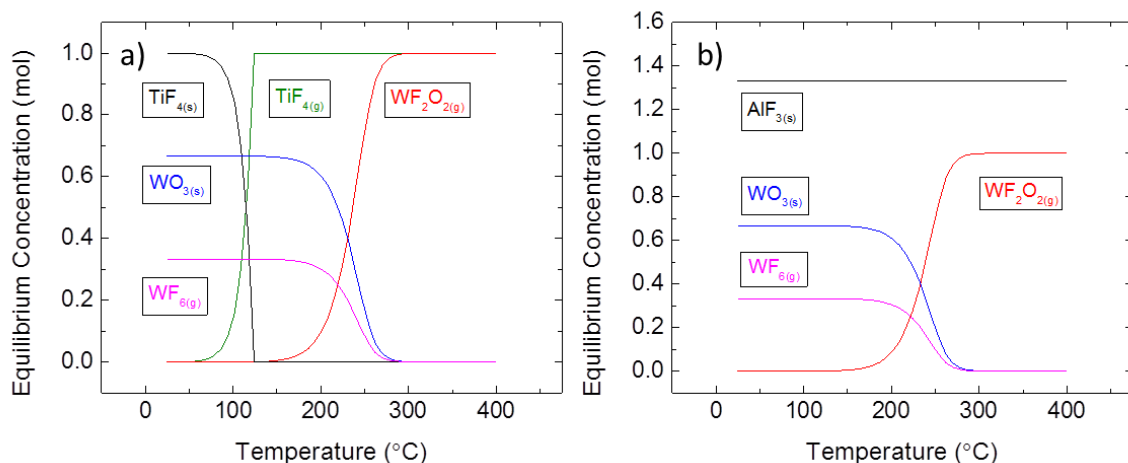


Figure 8.2: Equilibrium concentrations of species from 25 to 400°C for a system initially containing a) 1 mole WF_6 and 1 mole TiO_2 and b) 1 mole WF_6 and 0.667 mole Al_2O_3 .

Similar modeling results for Al_2O_3 shown in Figure 8.2b suggests that WF_6 reacts at room temperature with Al_2O_3 to form solid WO_3 and solid AlF_3 . At higher temperatures, like the case of TiO_2 , the solid WO_3 reacts further with WF_6 to form volatile WF_2O_2 . The AlF_3 remains nonvolatile between 25 to 400°C. The solid AlF_3 layer likely passivates the surface, preventing etching.^{81,82,256} Similar trends were modeled for ZnO , ZrO_2 , and HfO_2 , and all showed favorable free energy changes for fluorination by WF_6 , forming non-volatile metal fluorides. This shows that favorable etching reactions require both favorable surface reactions as well as volatile product formation.

The etching behavior of TiO_2 by WF_6 was assessed experimentally at different temperatures to collaborate the thermodynamic analysis. Data from QCM analysis in Figure 8.3a shows that when the temperature was reduced from 220°C to 120°C, the initial 1-5 WF_6 doses result in a mass gain on the TiO_2 surface. Additional WF_6 doses are accompanied by

relatively small mass increases, which plateau with time. The enlarged view in Figure 8.3b further shows the response to the WF_6 doses at 220°C and 120°C , in which there are clear mass losses following the WF_6 doses at 220°C .

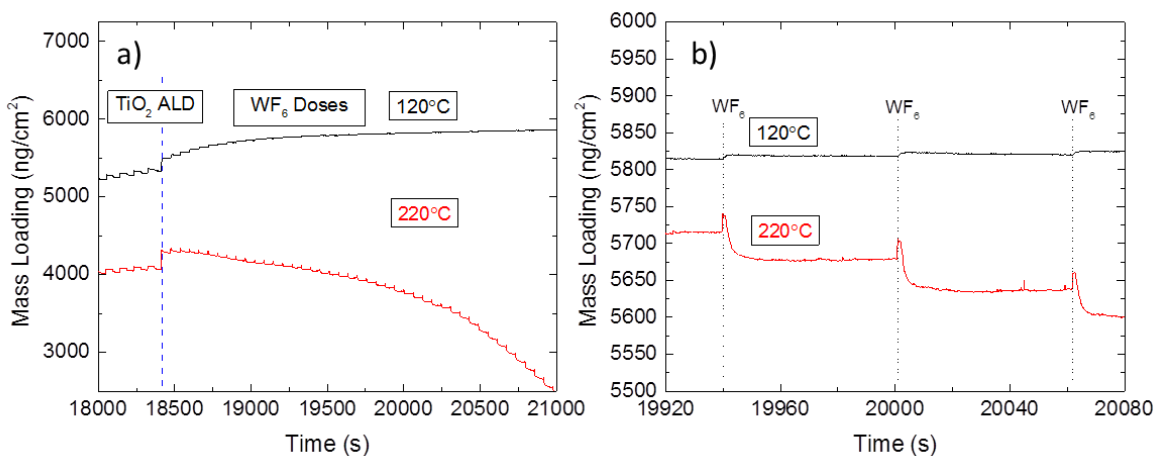


Figure 8.3: a) QCM analysis TiO_2 ALD followed by 50 WF_6 doses at 120 and 220°C and b) an enlarged view of the mass loading during the WF_6 doses, showing net mass loss during each WF_6 step at 220°C and little to no change at 120°C .

8.4.3 TiO_2 Surface Characterization following Etching by WF_6

The composition of the TiO_2 surfaces following the initial few WF_6 cycles, i.e. prior to significant TiO_2 mass loss, was analyzed with ex-situ XPS analysis. Figure 8.4 shows high resolution XPS scans of TiO_2 surfaces after 0, 1, 5 and 15 WF_6 doses. For this analysis, the initial TiO_2 film was sufficiently thin (i.e. ~ 6.5 nm) to allow detection of the underlying Si substrate. In addition, the starting TiO_2 shows evidence for fluorine at ~ 690 eV, consistent with fluoride from the reactor, likely remaining from previous WF_6 etch experiments. Figure 8.4a shows the Ti 2p signal decreases slightly following 1, 5, and 15 WF_6 doses, but

the Si 2p signal intensity in Figure 8.4b stays relatively constant. This suggests that there is minimal TiO₂ etching following 15 or fewer WF₆ doses of 1 s each. The decrease in the Ti 2p signal is attributed to the deposition of species (tungsten and fluorides) on the TiO₂ surface which scatter some Ti 2p photoelectrons. The presence of surface tungsten and fluorides is confirmed by results in Figure 8.4c and d, showing W 4f and F 1s peaks on the TiO₂ surface after 1 WF₆ dose. The tungsten signal stays relatively constant between 1 and 15 WF₆ doses, whereas the F 1s peak at 685 eV (associated with metal fluorides) progressively increases. This is consistent with WF₆ fluorinating the TiO₂ surface and with fluorine diffusion into the TiO₂ subsurface.^{254,280}

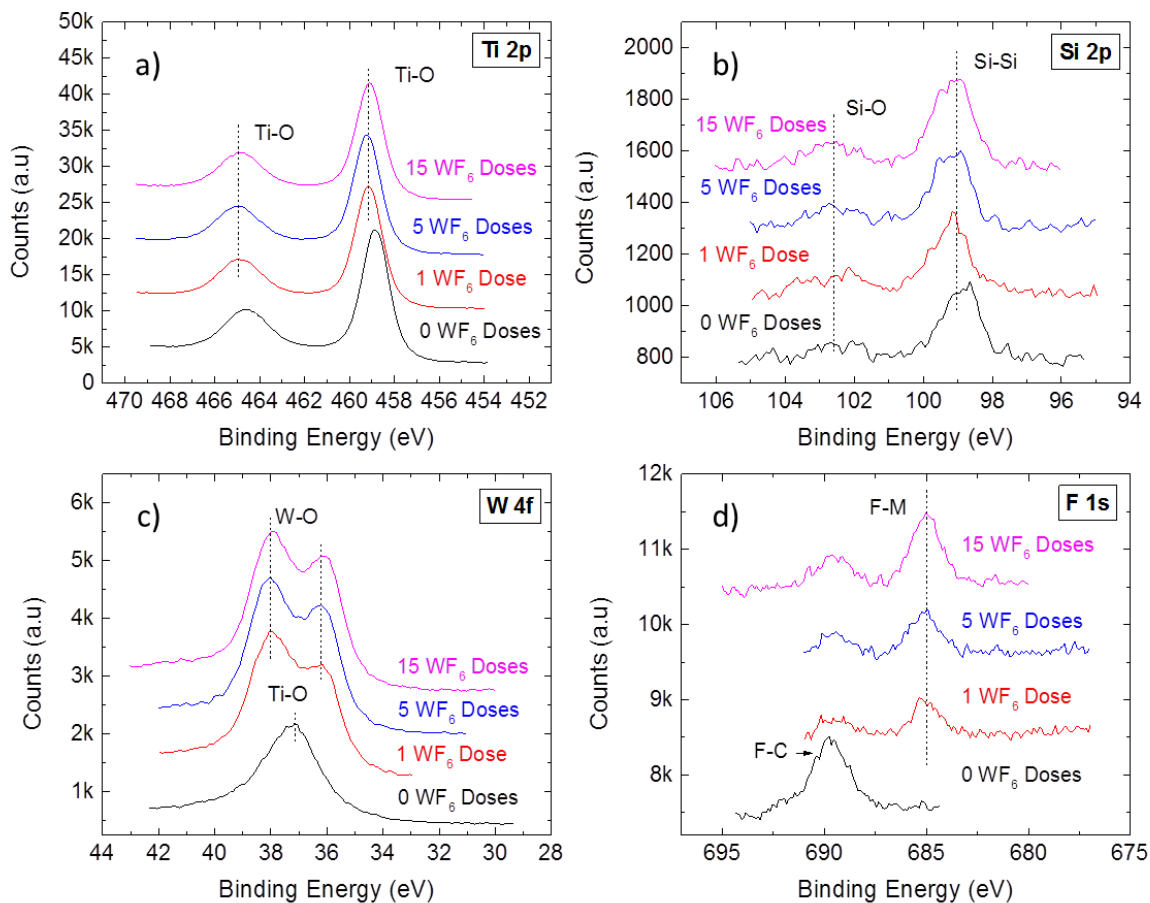


Figure 8.4: High resolution XPS scans of a) Ti 2p, b) Si 2p, c) W 4f, and d) F 1s regions for ~ 6.5 nm TiO_2 films exposed to 0, 1, 5 and 15 WF_6 doses at 220°C .

The relative location of the XPS peaks provides additional information concerning the etching mechanisms. For example, after 15 WF_6 doses, the Ti 2p doublet shifts by ~ 0.4 eV to higher binding energy (i.e., the Ti $2p_{3/2}$ peak shifts from 459.2 to 458.8 eV). This increase in binding energy is consistent with highly electronegative tungsten and fluorides on the TiO_2 surface. Full titanium fluorination to TiF_3 or TiF_4 would produce a much larger shift in the Ti $2p_{3/2}$ peaks to 462 and 464 eV respectively.²⁸⁰ In addition, the W 4f doublet peaks at 37.9

and 36 eV are shifted ~ 0.5 eV to higher binding energy compared to oxidized tungsten (37.6 and 35.5 eV),^{18,13} again consistent with surface fluorides.²⁸¹

Figure 8.5a shows the Ti 2p and Si 2p peak intensity values collected from the high resolution XPS scans plotted versus number of WF₆ dose steps (i.e. WF₆ exposure) after 0, 15, 25, 50, and 100 WF₆ doses. More WF₆ exposures lead to a decrease in the Ti signal and an increase in signal from the silicon substrate, clearly demonstrating the removal of TiO₂. The W 4f signal associated with oxidized tungsten (Figure 8.5b) stays constant, even up to 100 WF₆ doses. Figure 8.5b also shows that the F 1s signal increases significantly within the first 10 WF₆ doses followed by saturating behavior with additional WF₆ exposure.

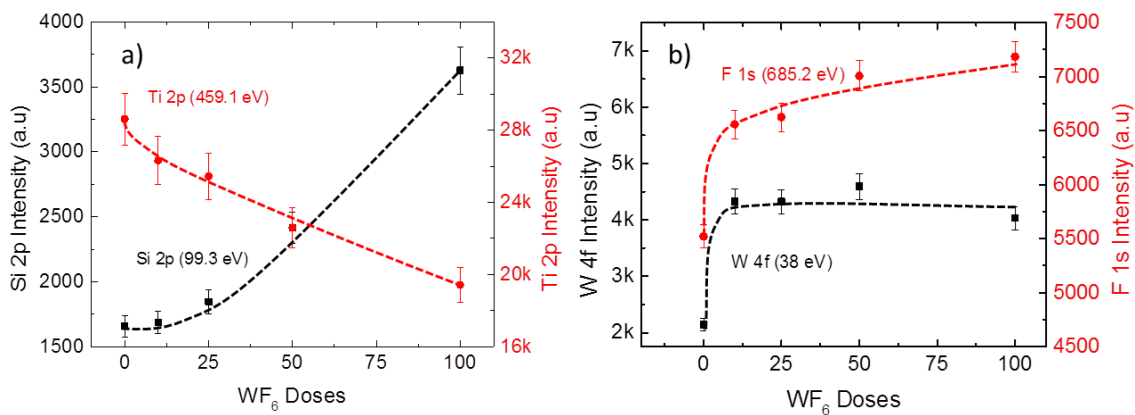


Figure 8.5: Peak intensity of high resolution XPS scans of a) Ti 2p (459.1 eV) and Si 2p (99.3 eV) and b) W 4f (38 eV) and F 1s (685.2 eV) for 5.5 nm TiO₂ films exposed to 0, 10, 25, 50, 100 WF₆ doses at 220°C. Lines are meant to guide eyes.

The film thickness for the samples Figure 8.5 was further analyzed by spectroscopic ellipsometry, and results are shown in Figure 8.6. Figure 8.6a shows that as the number of WF₆ doses increase, the TiO₂ film thickness decreases, consistent with the in-situ QCM and

XPS analysis in Figures 8.1, 8.3, and 8.5. Furthermore, the refractive index at 632.8 nm for the TiO₂ films is ~2.3 after 0 and 10 WF₆ doses, but decreases to ~1.9 with 25-100 WF₆ doses. The decrease in refractive index can be correlated with a decrease in film density. The observed decrease suggests that the WF₆ exposure promotes formation of a porous WO₃ film^{279,255} or the formation of a low density WO_xF_y^{236,261} surface layer.

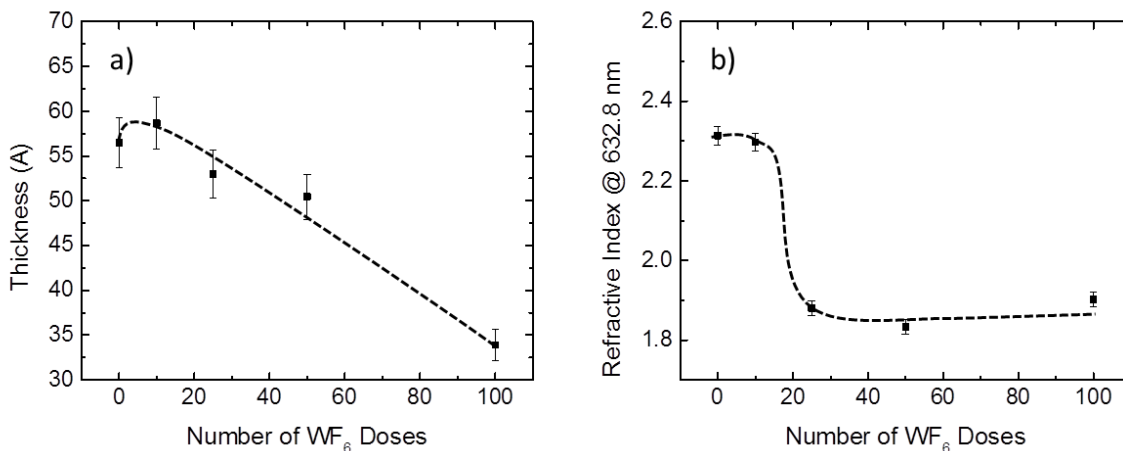


Figure 8.6: a) Thickness and b) refractive index at 632.8 nm of samples with 5.5 nm TiO₂ followed by 0, 15, 25, 50, and 100 WF₆ doses at 220°C, measured with spectroscopic ellipsometry. Lines are meant to guide eyes.

8.4.4 Effect of TiO₂ Thickness on Vapor Etch Rate

In the course of our experiments, we noted that the etch rate of TiO₂ by WF₆ depended on the thickness of the initial TiO₂ layer. This result is shown by the QCM results in Figure 8.7. The plot shows QCM results collected during 50, 100, and 200 TiO₂ ALD cycles at 220°C (estimated to be 10, 25, 55 Å thick), each followed by 50 WF₆/Ar dose steps. The traces for 200 TiO₂ ALD cycles + 50 WF₆ doses is reproduced from Figures 8.1 and 8.3. Note that

these experiments required continuous data collection over 3-5 hours, and the long-period fluctuations in the QCM data result from small instabilities in the controlled reactor temperature.

Examining the results in Figure 8.7b after 100 TiO₂ ALD cycles, there is an initial mass gain during the first WF₆ dose, similar to that after 200 TiO₂ cycles. However, further WF₆ doses result in a more rapid mass loss. The accelerated mass loss is even more pronounced for the thin 50 cycle TiO₂ film. The thinnest TiO₂ also shows a mass gain of only 28 ng/cm² during the initial WF₆ doses, in contrast to ~250 ng/cm² for the thicker 100 and 200 cycle TiO₂ films. Finally, for the thin 50 cycle TiO₂ only 8-10 WF₆ doses were necessary before no additional etching was observed, indicating complete removal of the deposited TiO₂.

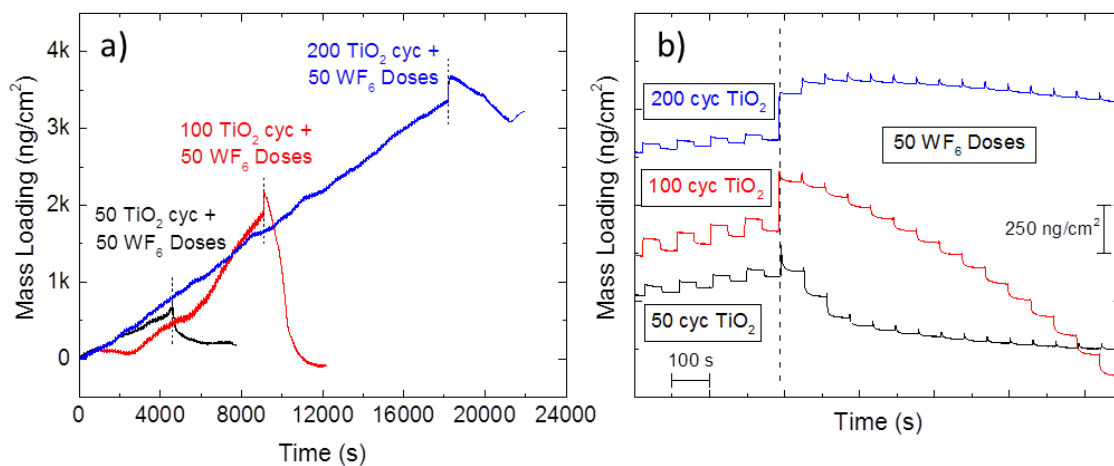


Figure 8.7: QCM analysis of WF₆ etching following 50, 100, and 200 TiO₂ ALD cycles on a bare Au QCM crystal at 220°C and 1.75 Torr.

8.4.5 Schematic of the WF_6 Vapor Etch Reaction Process

Figure 8.8 shows the proposed WF_6 etching mechanism of TiO_2 films at $220^\circ C$ based on QCM, XPS, and ellipsometric analysis. First, during the initial WF_6 doses, WF_6 adsorbs and reacts with the TiO_2 surface, forming a low density WO_xF_y layer. Based on QCM analysis of the mass increase during the first WF_6 dose, the WO_xF_y layer is estimated to be $\sim 6 \text{ \AA}$ thick, assuming a density comparable to reported low density WO_3 ALD films of $\sim 3.6 \text{ g/cm}^3$.²⁷⁹ In contrast, attenuation of the Ti 2p 3/2 XPS signal suggests a thinner WO_xF_y film of $\sim 1.6 \text{ \AA}$ after 1 WF_6 pre-exposures. The different calculated thicknesses are likely a result of the assumed film physical properties. It is also possible that the surface-bound species are a mix of nonvolatile TiF_3 ,^{254,255} $TiOF_2$,²⁵⁹ and WO_3 .^{236,261,255,260}

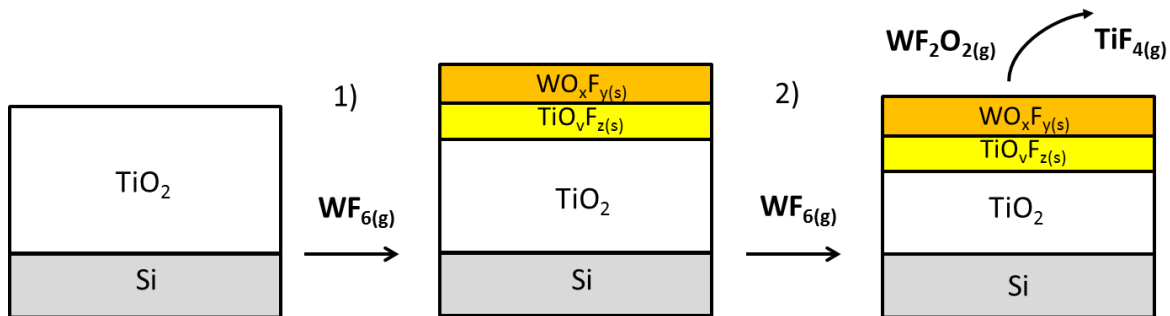


Figure 8.8: Proposed etching mechanism for TiO_2 films exposed to WF_6 at $220^\circ C$: 1) WF_6 adsorbs on thick TiO_2 surface, forming surface-bound TiO_vF_z and WO_xF_y . 2) Additional WF_6 exposure further fluorinates the TiO_vF_z and WO_xF_y , creating volatile WF_2O_2 and TiF_4 , etching the TiO_2 film.

Following the initial WF_6 adsorption and formation of WO_xF_y , subsequent WF_6 doses further fluorinate the TiO_2 and surface-bound WO_xF_y . The critical amount of fluorination to achieve volatilization and etching depends on the initial TiO_2 thickness as shown by QCM analysis in

Figure 8.7. Fluoride can readily diffuse into metallic titanium^{254,280} and titanium oxide.^{282,283} In the case of TiO₂, the extent of fluoride diffusion depends on the TiO₂ polymorph²⁸³ and surface plane, but fluoride implantation tends to be more favorable at surface over subsurface sites.²⁸² We propose that once a critical fluoride concentration is achieved, volatile WF₂O₂ and TiF₄ are formed, leading to etching. This is consistent with the work showing that WF₆ reacts with SiO₂ to form volatile WOF₄ and SiF₄.²³⁶ Furthermore, in similar systems, WF₆ etched WO₃ films²⁶¹ and NbCl₅ was observed to etch Nb₂O₅ films by forming volatile NbOCl₃.²⁶²

8.4.6 *Addition of Surface Modifiers to Increase Etching Rate*

Based on the XPS analysis in Figure 8.4 and 8.5, the TiO₂ etching by WF₆ produce a thin layer of WO_xF_y on the etched TiO₂ surfaces that remains after etch completion. To explore approaches to avoid this layer formation, we performed several experiments. As one approach, Sn(acac)₂ was incorporated into the etch sequence. Sn(acac)₂ has been observed to assist in metal fluoride volatilization in similar atomic layer etching processes.^{80-82,84} For this experiment, we deposited 200 cycles of TiO₂ at 220°C, then etched at the same temperature using WF₆/Ar/Sn(acac)₂/Ar with duration of 1/60/1/60 s for 0, 15, and 25 cycles. Figure 8.9 shows high resolution XPS scans collected after this exposure sequence. Comparing the measured XPS intensities in Figure 8.9 to those in Figure 8.5 (with only WF₆ exposure steps), the addition of Sn(acac)₂ significantly increases the etch rate for a ~6.5 nm TiO₂ film, so that after 25 WF₆/Sn(acac)₂ cycles the Ti 2p signal is near the detection limit (~0.5 at.%). We also note the presence of surface tin after 15 and 25 cycles at 220°C. After 25

WF₆/Sn(acac)₂ cycles, the amount of surface fluorine and tungsten is also less than observed in Figure 8.5 after 25 WF₆ cycles. These results suggest that the addition of Sn(acac)₂ into the WF₆/Ar sequential etch process increases the etch rate by creating more volatile etch products such as TiO(acac)₂ or TiF₂(acac)₂.⁸⁰

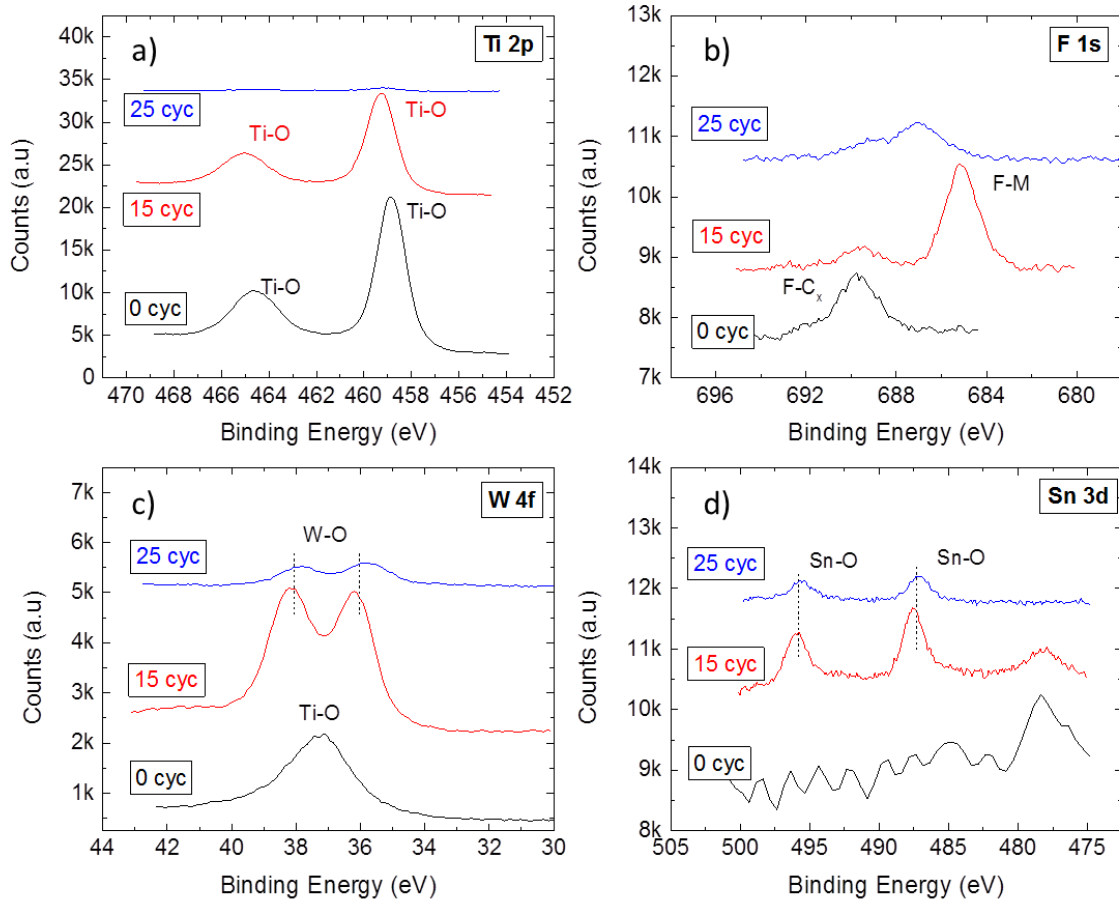


Figure 8.9: High resolution XPS scans of a) Ti 2p, b) F 1s, c) W 4f, and d) Sn 3d regions for 6.5 nm TiO₂ films following 0, 15, 25 WF₆/Ar/Sn(acac)₂/Ar cycles at 220°C and 1.75 Torr.

8.4.7 *TiO₂ Atomic Layer Etching using WF₆/BCl₃*

As shown above in Figures 8.5 and 8.6, the extent of TiO₂ etching depended on the number of WF₆ doses, and the etching proceeds nearly continuously without evidence for self-limiting behavior. A self-limiting atomic layer etching (ALE) process, consisting of two self-limiting adsorption and activation steps, is more desirable in that it will allow the extent of etching to be well controlled and defined. Therefore, we worked to modify the WF₆/Ar/Sn(acac)₂/Ar reaction sequence to identify possible ALE conditions. Using the results in Figures 8.2, 8.3, and 8.8, we: 1) reduced the process temperature from 220°C to 170°C to prevent uncontrolled WF₆ etching; and 2) explored BCl₃ as an alternative co-reagent in place of Sn(acac)₂ to volatilize surface-adsorbed product species.

Figure 8.10a shows QCM results collected at 170 °C when freshly deposited TiO₂ films were subsequently exposed to: i) BCl₃/Ar doses; ii) WF₆/Ar doses; iii) WF₆/Ar/Sn(acac)₂/Ar cycles; and iv) WF₆/Ar/BCl₃/Ar cycles. At 170°C, without the additional co-reagent, WF₆ shows mass gain consistent with surface adsorption, but the mass plateaus indicating little to no TiO₂ etching. Dosing only BCl₃ appears to initially etch the TiO₂, but like the WF₆, additional BCl₃ does not lead to substantial etching. In contrast, the WF₆/Sn(acac)₂ sequence produces an initialization period in which the mass increases, followed by controlled layer-by-layer etching. The WF₆/BCl₃ sequence also shows step-wise linear etching, but unlike the WF₆/Sn(acac)₂ sequence, it starts immediately from the first BCl₃ exposure step. An expanded view of the WF₆/BCl₃ etching process in Figure 8.10b shows a 21 ng/cm² mass gain during the WF₆ dose, followed by a net mass loss of 53 ng/cm²/cyc upon the subsequent

BCl₃ exposure. By contrast the mass gain measured during our TiO₂ ALD process is 26 ng/cm²/cyc, indicating that the WF₆/BCl₃ etch process removes the equivalent of ~2 ALD layers per cycle.

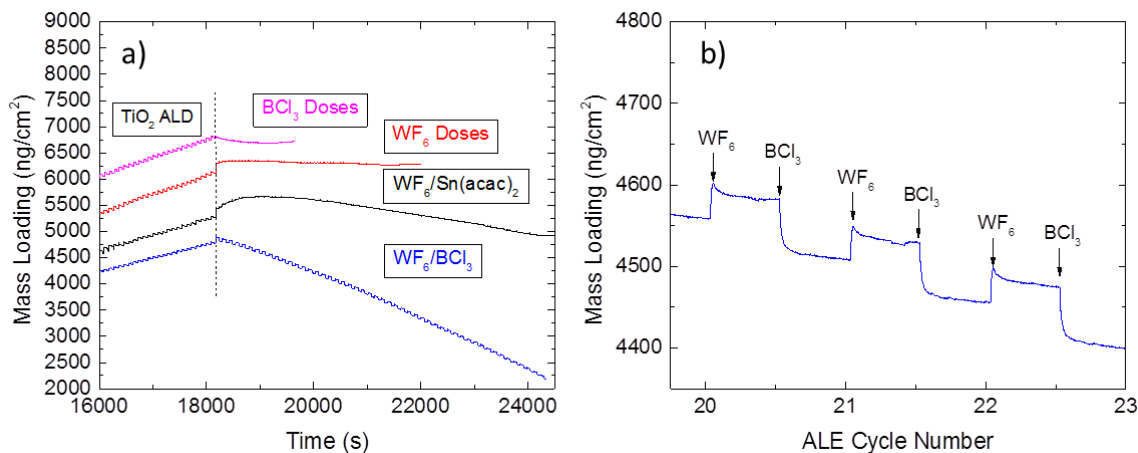


Figure 8.10: a) QCM analysis at 170°C and 1.75 Torr of TiO₂ ALD followed by 25 BCl₃/Ar doses (pink), 50 WF₆/Ar doses (red), 50 WF₆/Ar/Sn(acac)₂/Ar cycles (black), or 50 WF₆/Ar/BCl₃/Ar cycles (blue). b) Expanded view of the WF₆/Ar/BCl₃/Ar etch sequence.

The etch rate for the WF₆/BCl₃ process at 170°C was also analyzed with spectroscopic ellipsometry. Figure 8.11 shows that with increasing number of etch cycles, the TiO₂ thickness decreases linearly in agreement with the QCM results shown in Figure 8.10, with an etch rate per cycle of ~0.3 Å/cyc which is approximately 1 TiO₂ ALD layer per etch cycle. Spectroscopic ellipsometry also shows that the refractive index remains relatively constant with increasing number of ALE cycle number. The constant refractive index during etching indicates a clean TiO₂ surface after each WF₆/BCl₃ atomic layer etch cycle. This contrasts with the results from WF₆ vapor etching (Figure 8.6), where the decrease in refractive index was attributed to formation of a low density WO_xF_y layer during etching. In the ALE process,

the WO_xF_y layer formed after each WF_6 dose is removed by BCl_3 , producing the clean TiO_2 surface after each cycle.

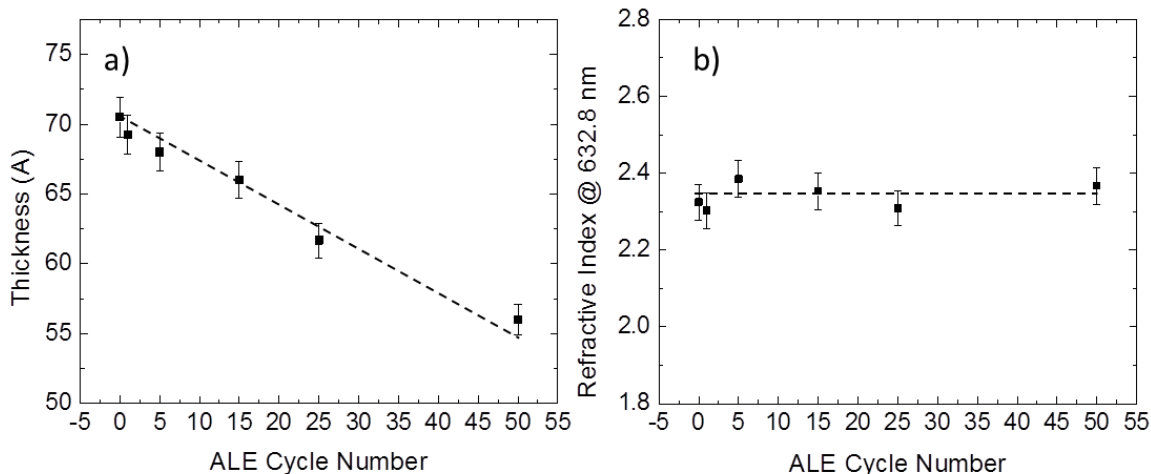


Figure 8.11: a) Thickness and b) refractive index of 7 nm TiO_2 versus WF_6/BCl_3 ALE cycle number as measured by spectroscopic ellipsometry. The TiO_2 ALD and ALE were performed at 170°C with an ALE dosing sequence of $\text{WF}_6/\text{Ar}/\text{BCl}_3/\text{Ar}$ (1/60/2.5/60 s). Lines are meant to guide eyes.

In addition, XPS analysis of TiO_2 films after the WF_6/BCl_3 etch process (Figure 8.12) shows that tungsten and fluorine content were comparable to the amount on the initial TiO_2 surface. The boron and chlorine content are also below the XPS detection limit, further confirming a clean surface after each WF_6/BCl_3 cycle, consistent with the refractive index results in Figure 8.11b.

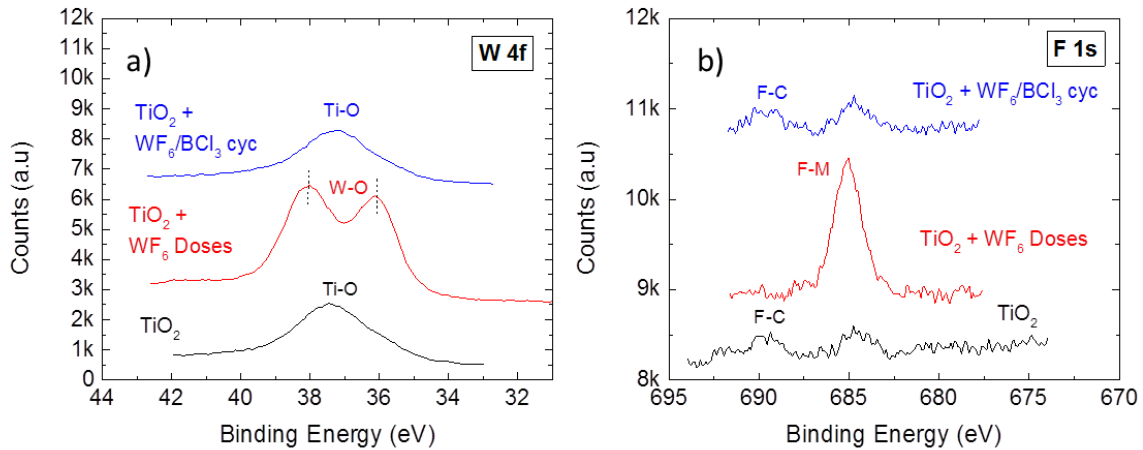


Figure 8.12: High resolution XPS scans of a) W 4f and b) F 1s regions for 7 nm TiO₂ film (black), 7 nm TiO₂ following 50 WF₆/BCl₃ cycles at 170°C (red), and 5.5 nm TiO₂ following 50 WF₆ doses at 220°C (blue).

To determine if the surface reactions during the WF₆/BCl₃ etch process showed self-limiting behavior indicative of thermal atomic layer etching (ALE), we used QCM to characterize the effect of process temperature and reactant exposure on the resulting etch rate. Figure 8.13a shows results when the WF₆/Ar/BCl₃/Ar dose was fixed at 1/60/2.5/60 s and the etch temperature was adjusted between 110 and 190°C. The etch rate generally increased with temperature, going from 6.3 to 55.6 ng/cm²/cycle as temperature increases from 110 to 190°C. The higher temperature enhances the rate of etch product volatilization, leading to an overall faster etch rate. Furthermore, the etch rate between 110 and 150°C changes relatively little with temperature, consistent with a desirable “ALE window” in this range. This range corresponds to limited volatility of TiF₄,^{284,285} suggesting that product elimination is a likely rate-limiting step for the ALE reaction mechanism.

The results of reactant saturation studies for the WF_6/BCl_3 ALE process are shown in Figure 8.13b. For this test, the reactant exposure consisted of sequential sub-doses of the WF_6 and BCl_3 precursors (i.e. 10 WF_6/Ar doses followed by 10 BCl_3/Ar doses). We monitored the change in mass uptake after each sub-dose step, in which a plateau in the mass change during the sub-dose sequence would indicate complete consumption of the available active sites and reaction saturation. Results in Figure 8.13b show evidence for saturation for both the WF_6 and BCl_3 half-reaction steps, where the first sub-dose produces a large mass change, followed by decreasing changes for subsequent sub-doses. In the low temperature range, 110–150°C, reducing the process temperature may promote a more self-limiting process, but longer exposures are needed to attain full saturation. This is attributed to a reduced rate of fluorine diffusion into the TiO_2 film at the lower temperature.

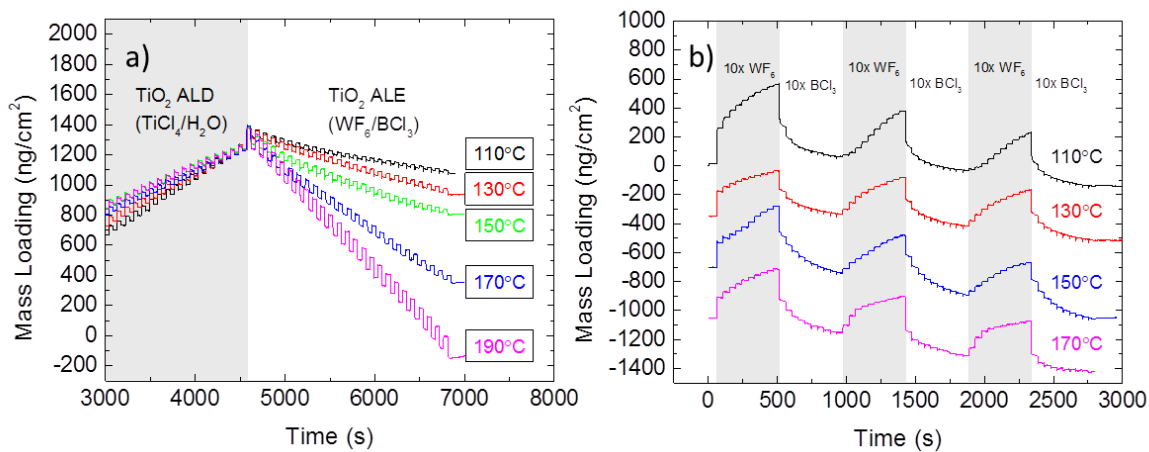


Figure 8.13: QCM analysis of a) $\text{WF}_6/\text{Ar}/\text{BCl}_3/\text{Ar}$ sequence at 110, 130, 150, 170 and 190°C and b) 10 WF_6/Ar followed by 10 BCl_3/Ar (repeated 3 times), at 110, 130, 150, and 170°C.

8.4.8 Schematic of the WF_6/BCl_3 ALE Reaction Process

The proposed WF_6/BCl_3 ALE process is shown in Figure 8.14. First, like the chemical vapor etching mechanism, the WF_6 adsorbs and fluorinates the TiO_2 surface. At the lower process temperatures, the WF_6 alone will not eventually etch the TiO_2 , unlike the chemical vapor etching shown in Figure 8.8. The modified surface, consisting of WO_xF_y and TiO_vF_z species are then volatilized by the subsequent BCl_3 exposure, likely through a halogen exchange reaction.²⁸⁰ XPS analysis suggests that following the BCl_3 exposure, the TiO_2 is pristine, effectively regenerating the initial TiO_2 surface.

The QCM results in Figure 8.10a show that at $170^\circ C$, exposing ALD TiO_2 to repeated doses of either WF_6 or BCl_3 leads to no mass loss (i.e. no etching). However, at the same $170^\circ C$, Figure 13b shows that the WF_6/BCl_3 dosing sequence does etch TiO_2 . Moreover, each half-reaction in the WF_6/BCl_3 etch process exhibits self-limiting saturation behavior, consistent with atomic layer etching. As indicated by the XPS results in Figures 8.4 and QCM results in Figure 8.10, exposing the TiO_2 to WF_6 produces a fluorinated surface layer containing WO_xF_y and TiO_vF_z . We expect that this fluorinated layer impedes fluorine diffusion into the TiO_2 ,^{80-83,282,283} leading to the reaction saturation behavior in Figure 8.13. Results in Figure 8.13 also show that when process temperature is reduced (and the rate of F diffusion is decreased) a larger WF_6 exposure is needed to saturate the WF_6 half-reaction.

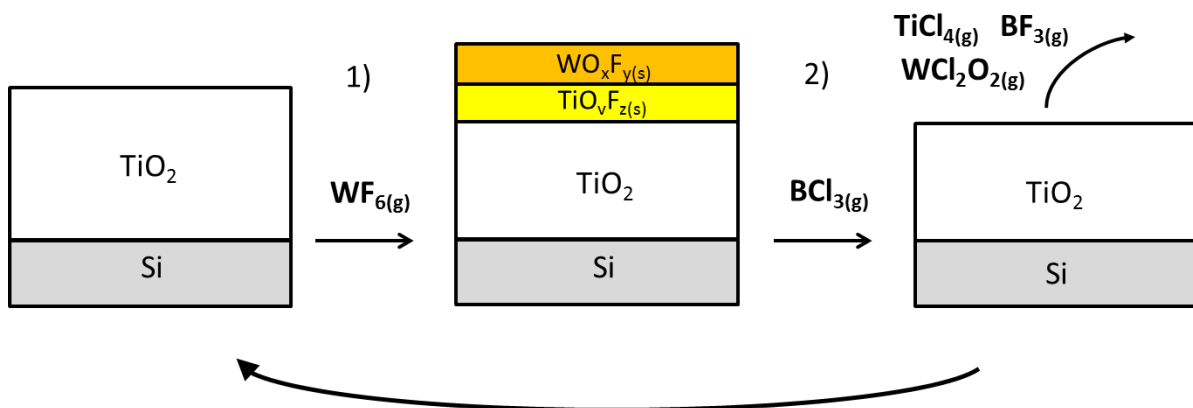


Figure 8.14: Proposed etch mechanism for the TiO₂ ALE process using WF₆ and BCl₃ at 170°C: 1) WF₆ adsorbs on thick TiO₂ surface, forming surface-bound TiO_vF_z and WO_xF_y. 2) BCl₃ volatilizes the surface metal oxy fluoride species, forming TiCl₄, WCl₂O₂ and BF₃.

8.5 Summary and Conclusions

In this article, we investigate how WF₆, WF₆/Sn(acac)₂, and WF₆/BCl₃ processes can be used for the controlled removal of TiO₂ films. WF₆ selectively etches TiO₂ over other oxides including Al₂O₃ as result of the relative volatility of the formed metal fluorides. Using ex-situ XPS and ellipsometry analysis, we confirm WF₆ etching of TiO₂ films and provide evidence that etching proceeds through TiO₂ fluorination and formation of a low density WO_xF_y region. Incorporating co-reagents such as Sn(acac)₂ and BCl₃ increased the etch rate and enabled the development of atomic layer etching processes at lower process temperatures. For the ALE process using WF₆ and BCl₃, the rate of etching per cycle decreases at lower temperatures, due to reduced volatilization of etches products. Furthermore, the WF₆/BCl₃ ALE process exhibited saturation behavior, in part due to the formation of a non-volatile WO_xF_y layer at the lower process temperatures. Exploring alternative fluorinating or

adsorption species is significant for the further development of thermally-driven etching processes.

8.6 *Acknowledgements*

The work included in this manuscript was funded by EMD Performance Materials (SAFC). The authors acknowledge the use of the Analytical Instrumentation Facility (AIF) at North Carolina State University, which is supported by the State of North Carolina and the National Science Foundation.

REFERENCES

- (1) Nucleation-Crystallography.
- (2) Mousa, M. B. M.; Oldham, C. J.; Jur, J. S.; Parsons, G. N. Effect of Temperature and Gas Velocity on Growth per Cycle during Al₂O₃ and ZnO Atomic Layer Deposition at Atmospheric Pressure. *J. Vac. Sci. Technol. a* **2012**, *30*, 01A155-01A155.
- (3) Hyde, G. K.; Park, K. J.; Stewart, S. M.; Hinstroza, J. P.; Parsons, G. N. Atomic Layer Deposition of Conformal Inorganic Nanoscale Coatings on Three-Dimensional Natural Fiber Systems: Effect of Surface Topology on Film Growth Characteristics. *Langmuir* **2007**, *23*, 9844–9849.
- (4) Peng, Q.; Sun, X.-Y.; Spagnola, J. C.; Hyde, G. K.; Spontak, R. J.; Parsons, G. N. Atomic Layer Deposition on Electrospun Polymer Fibers as a Direct Route to Al₂O₃ Microtubes with Precise Wall Thickness Control. *Nano Lett.* **2007**, *7*, 719–722.
- (5) George, S. M. Atomic Layer Deposition: An Overview. *Chem. Rev.* **2010**, *110*, 111–131.
- (6) Arvidson, S. A.; Wong, K. C.; Gorga, R. E.; Khan, S. A. Structure, Molecular Orientation, and Resultant Mechanical Properties in Core/ Sheath Poly(lactic Acid)/polypropylene Composites. *Polymer (Guildf)*. **2012**, *53*, 791–800.
- (7) Miikkulainen, V.; Leskelä, M.; Ritala, M.; Puurunen, R. L. Crystallinity of Inorganic Films Grown by Atomic Layer Deposition: Overview and General Trends. *J. Appl. Phys.* **2013**, *113*, 21301-021301–101.
- (8) Klesko, J. P.; Thrush, C. M.; Winter, C. H. Thermal Atomic Layer Deposition of Titanium Films Using Titanium Tetrachloride and 2-Methyl-1,4-Bis(trimethylsilyl)-2,5-Cyclohexadiene or 1,4-Bis(trimethylsilyl)-1,4-Dihydropyrazine. *Chem. Mater.* **2015**, *27*, 4918–4921.
- (9) Klesko, J. P.; Kerrigan, M. M.; Winter, C. H. Low Temperature Thermal Atomic Layer Deposition of Cobalt Metal Films. *Chem. Mater.* **2016**, *28*, 700–703.
- (10) Atanasov, S. E.; Kalanyan, B.; Parsons, G. N. Inherent Substrate-Dependent Growth Initiation and Selective-Area Atomic Layer Deposition of TiO₂ Using “water-Free” Metal-Halide/metal Alkoxide Reactants. *J. Vac. Sci. Technol. A Vacuum, Surfaces, Film.* **2016**, *34*, 01A148.
- (11) Kalanyan, B.; Losego, M. D.; Oldham, C. J.; Parsons, G. N. Low-Temperature Atomic Layer Deposition of Tungsten Using Tungsten Hexafluoride and Highly-Diluted Silane in Argon. *Chem. Vap. Depos.* **2013**, *19*, 161–166.
- (12) Kim, S.-H.; Hwang, E.-S.; Kim, B.-M.; Lee, J.-W.; Sun, H.-J.; Hong, T. E.; Kim, J.-K.; Sohn, H.; Kim, J.; Yoon, T.-S. Effects of B[₂H₆] Pretreatment on ALD of W Film Using a Sequential Supply of WF₆ and SiH₄. *Electrochem. Solid-State Lett.* **2005**, *8*, C155.

- (13) Lemaire, P. C.; King, M.; Parsons, G. N. Understanding Inherent Substrate Selectivity during Atomic Layer Deposition: Effect of Surface Preparation, Hydroxyl Density, and Metal Oxide Composition on Nucleation Mechanisms during Tungsten ALD. *J. Chem. Phys.* **2017**, *146*, 52811.
- (14) Grubbs, R. K.; Nelson, C. E.; Steinmetz, N. J.; George, S. M. Nucleation and Growth during the Atomic Layer Deposition of W on Al₂O₃ and Al₂O₃ on W. *Thin Solid Films* **2004**, *467*, 16–27.
- (15) Klaus, J. .; Ferro, S. .; George, S. . Atomic Layer Deposition of Tungsten Using Sequential Surface Chemistry with a Sacrificial Stripping Reaction. *Thin Solid Films* **2000**, *360*, 145–153.
- (16) Elam, J. .; Nelson, C. .; Grubbs, R. .; George, S. . Kinetics of the WF₆ and Si₂H₆ Surface Reactions during Tungsten Atomic Layer Deposition. *Surf. Sci.* **2001**, *479*, 121–135.
- (17) Mane, A. U.; Elam, J. W. Atomic Layer Deposition of W:Al₂O₃ Nanocomposite Films with Tunable Resistivity. *Chem. Vap. Depos.* **2013**, *19*, 186–193.
- (18) Kalanyan, B.; Lemaire, P. C.; Atanasov, S. E.; Ritz, M. J.; Parsons, G. N. Using Hydrogen To Expand the Inherent Substrate Selectivity Window During Tungsten Atomic Layer Deposition. *Chem. Mater.* **2016**, *28*, 117–126.
- (19) Ferguson, J. D.; Weimer, A. W.; George, S. M. Atomic Layer Deposition of Al₂O₃ Films on Polyethylene Particles. *Chem. Mater.* **2004**, *16*, 5602–5609.
- (20) Spagnola, J. C.; Gong, B.; Arvidson, S. A.; Jur, J. S.; Khan, S. A.; Parsons, G. N. Surface and Sub-Surface Reactions during Low Temperature Aluminium Oxide Atomic Layer Deposition on Fiber-Forming Polymers. *J. Mater. Chem.* **2010**, *20*, 4213–4222.
- (21) Hyde, G. K.; Scarel, G.; Spagnola, J. C.; Peng, Q.; Lee, K.; Gong, B.; Roberts, K. G.; Roth, K. M.; Hanson, C. A.; Devine, C. K.; *et al.* Atomic Layer Deposition and Abrupt Wetting Transitions on Nonwoven Polypropylene and Woven Cotton Fabrics. *Langmuir* **2010**, *26*, 2550–2558.
- (22) Gong, B.; Parsons, G. N. Quantitative in Situ Infrared Analysis of Reactions between Trimethylaluminum and Polymers during Al₂O₃ Atomic Layer Deposition. *J. Mater. Chem.* **2012**, *22*, 15672–15682.
- (23) Jur, J. S.; Spagnola, J. C.; Lee, K.; Gong, B.; Peng, Q.; Parsons, G. N. Temperature-Dependent Subsurface Growth during Atomic Layer Deposition on Polypropylene and Cellulose Fibers. *Langmuir* **2010**, *26*, 8239–8244.
- (24) Saito, Y.; Takagi, T. Effects of Plasma Excitation and Chemical Pretreatment on Adsorption of Tungsten Hexafluoride on Silicon and Silicon Dioxide Studied by X-Ray Photoelectron Spectroscopy. *J. Electrochem. Soc.* **1996**, *143*, 3670.
- (25) Desatnik, N. Nucleation on SiO₂ during the Selective Chemical Vapor

- Deposition of Tungsten by the Hydrogen Reduction of Tungsten Hexafluoride. *J. Electrochem. Soc.* **1994**, *141*, 3532.
- (26) Chang, K. M.; Wang, S. W.; Li, C. H.; Tsai, J. Y.; Yeh, T. H. Reduction of Selectivity Loss Probability on Dielectric Surface during Chemical Vapor Deposition of Tungsten Using Fluorinated Oxide and Removing Silanol Units on Dielectric Surface. *Jpn. J. Appl. Phys.* **1996**, *35*, 6555–6561.
- (27) Kannan Selvaraj, S.; Parulekar, J.; Takoudis, C. G. Selective Atomic Layer Deposition of Zirconia on Copper Patterned Silicon Substrates Using Ethanol as Oxygen Source as Well as Copper Reductant. *J. Vac. Sci. Technol. A Vacuum, Surfaces, Film.* **2014**, *32*, 10601.
- (28) Chen, R.; Kim, H.; McIntyre, P. C.; Bent, S. F. Investigation of Self-Assembled Monolayer Resists for Hafnium Dioxide Atomic Layer Deposition. *Chem. Mater.* **2005**, *17*, 536–544.
- (29) Hong, J.; Porter, D. W.; Sreenivasan, R.; McIntyre, P. C.; Bent, S. F. ALD Resist Formed by Vapor-Deposited Self-Assembled Monolayers. *Langmuir* **2007**, *23*, 1160–1165.
- (30) Avila, J. R.; Demarco, E. J.; Emery, J. D.; Farha, O. K.; Pellin, M. J.; Hupp, J. T.; Martinson, A. B. F. Real-Time Observation of Atomic Layer Deposition Inhibition: Metal Oxide Growth on Self-Assembled Alkanethiols. *ACS Appl. Mater. Interfaces* **2014**, *6*.
- (31) Chopra, S. N.; Zhang, Z.; Kaihlanen, C.; Ekerdt, J. G. Selective Growth of Titanium Nitride on HfO₂ across Nanolines and Nanopillars. *Chem. Mater.* **2016**, *28*, 4928–4934.
- (32) Zacher, D.; Baunemann, A.; Hermes, S.; Fischer, R. A. Deposition of Microcrystalline [Cu₃(btc)₂] and [Zn₂(bdc)₂(dabco)] at Alumina and Silica Surfaces Modified with Patterned Self Assembled Organic Monolayers: Evidence of Surface Selective and Oriented Growth. *J. Mater. Chem.* **2007**, *17*, 2785–2792.
- (33) Hermes, S.; Schröder, F.; Chelmoski, R.; Wöll, C.; Fischer, R. A. Selective Nucleation and Growth of Metal–Organic Open Framework Thin Films on Patterned COOH/CF₃-Terminated Self-Assembled Monolayers on Au(111). *J. Am. Chem. Soc.* **2005**, *127*, 13744–13745.
- (34) Biemmi, E.; Scherb, C.; Bein, T. Oriented Growth of the Metal Organic Framework Cu₃(BTC)₂(H₂O)₃·xH₂O Tunable with Functionalized Self-Assembled Monolayers. *J. Am. Chem. Soc.* **2007**, *129*, 8054–8055.
- (35) Ameloot, R.; Gobechiya, E.; Uji-i, H.; Martens, J. A.; Hofkens, J.; Alaerts, L.; Sels, B. F.; De Vos, D. E. Direct Patterning of Oriented Metal–Organic Framework Crystals via Control over Crystallization Kinetics in Clear Precursor Solutions. *Adv. Mater.* **2010**, *22*, 2685–2688.

- (36) Hashemi, F. S. M.; Prasittichai, C.; Bent, S. F. A New Resist for Area Selective Atomic and Molecular Layer Deposition on Metal–Dielectric Patterns. *J. Phys. Chem. C* **2014**, *118*, 10957–10962.
- (37) Hashemi, F. S. M.; Bent, S. F. Sequential Regeneration of Self-Assembled Monolayers for Highly Selective Atomic Layer Deposition. *Adv. Mater. Interfaces* **2016**, *3*, 1600464.
- (38) Chen, J.-R.; Zhang, W.; Suh, T.; Engstrom, J. Examination of Alternative Approaches to Self-Aligned, Selective Area Atomic Layer Deposition. In *16th International Conference on Atomic Layer Deposition*; 2016.
- (39) Minaye Hashemi, F. S.; Prasittichai, C.; Bent, S. F. Self-Correcting Process for High Quality Patterning by Atomic Layer Deposition. *ACS Nano* **2015**, *9*, 8710–8717.
- (40) George, S. M.; Lee, Y. Prospects for Thermal Atomic Layer Etching Using Sequential, Self-Limiting Fluorination and Ligand-Exchange Reactions. *ACS Nano* **2016**, *10*, 4889–4894.
- (41) Du, Y.; George, S. M. Molecular Layer Deposition of Nylon 66 Films Examined Using in Situ FTIR Spectroscopy. *J. Phys. Chem. C* **2007**, *111*, 8509–8517.
- (42) Atanasov, S. E.; Losego, M. D.; Gong, B.; Sachet, E.; Maria, J.-P.; Williams, P. S.; Parsons, G. N. Highly Conductive and Conformal Poly(3,4-Ethylenedioxythiophene) (PEDOT) Thin Films via Oxidative Molecular Layer Deposition. *Chem. Mater.* **2014**, *26*, 3471–3478.
- (43) Kim, D. H.; Atanasov, S. E.; Lemaire, P.; Lee, K.; Parsons, G. N. Platinum-Free Cathode for Dye-Sensitized Solar Cells Using Poly(3,4-Ethylenedioxythiophene) (PEDOT) Formed via Oxidative Molecular Layer Deposition. *ACS Appl. Mater. Interfaces* **2015**, *7*, 3866–3870.
- (44) Dameron, A. A.; Seghete, D.; Burton, B. B.; Davidson, S. D.; Cavanagh, A. S.; Bertrand, J. A.; George, S. M. Molecular Layer Deposition of Alucone Polymer Films Using Trimethylaluminum and Ethylene Glycol. *Chem. Mater.* **2008**, *20*, 3315–3326.
- (45) Yoon, B.; Seghete, D.; Cavanagh, A. S.; George, S. M. Molecular Layer Deposition of Hybrid Organic–Inorganic Alucone Polymer Films Using a Three-Step ABC Reaction Sequence. *Chem. Mater.* **2009**, *21*, 5365–5374.
- (46) Peng, Q.; Gong, B.; VanGundy, R. M.; Parsons, G. N. “Zincone” Zinc Oxide–Organic Hybrid Polymer Thin Films Formed by Molecular Layer Deposition. *Chem. Mater.* **2009**, *21*, 820–830.
- (47) Yoon, B.; Lee, B. H.; George, S. M. Highly Conductive and Transparent Hybrid Organic–Inorganic Zincone Thin Films Using Atomic and Molecular Layer Deposition. *J. Phys. Chem. C* **2012**, *116*, 24784–24791.
- (48) Abdulagatov, A. I.; Hall, R. A.; Sutherland, J. L.; Lee, B. H.; Cavanagh, A. S.; George, S. M. Molecular Layer Deposition of Titanicone Films Using TiCl₄ and

- Ethylene Glycol or Glycerol: Growth and Properties. *Chem. Mater.* **2012**, *24*, 2854–2863.
- (49) Lee, B. H.; Anderson, V. R.; George, S. M. Molecular Layer Deposition of Zirconium and ZrO₂/Zirconium Alloy Films: Growth and Properties. *Chem. Vap. Depos.* **2013**, *19*, 204–212.
- (50) Lee, B. H.; Anderson, V. R.; George, S. M. Growth and Properties of Hafnium and HfO₂/hafnium Nanolaminates and Alloy Films Using Molecular Layer Deposition Techniques. *ACS Appl. Mater. Interfaces* **2014**, *6*, 16880–16887.
- (51) Brown, J. J.; Hall, R. A.; Kladitis, P. E.; George, S. M.; Bright, V. M. Molecular Layer Deposition on Carbon Nanotubes. *ACS Nano* **2013**, *7*, 7812–7823.
- (52) Gong, B.; Peng, Q.; Parsons, G. N. Conformal Organic–Inorganic Hybrid Network Polymer Thin Films by Molecular Layer Deposition Using Trimethylaluminum and Glycidol. *J. Phys. Chem. B* **2011**, *115*, 5930–5938.
- (53) Klepper, K. B.; Nilsen, O.; Fjellvåg, H. Deposition of Thin Films of Organic–inorganic Hybrid Materials Based on Aromatic Carboxylic Acids by Atomic Layer Deposition. *Dalt. Trans.* **2010**, *39*, 11628–11635.
- (54) Klepper, K. B.; Nilsen, O.; Hansen, P.-A.; Fjellvåg, H. Atomic Layer Deposition of Organic–inorganic Hybrid Materials Based on Saturated Linear Carboxylic Acids. *Dalt. Trans.* **2011**, *40*, 4636–4646.
- (55) Klepper, K. B.; Nilsen, O.; Levy, T.; Fjellvåg, H. Atomic Layer Deposition of Organic–Inorganic Hybrid Materials Based on Unsaturated Linear Carboxylic Acids. *Eur. J. Inorg. Chem.* **2011**, *2011*, 5305–5312.
- (56) Abdulagatov, A. I.; Terauds, K. E.; Travis, J. J.; Cavanagh, A. S.; Raj, R.; George, S. M. Pyrolysis of Titanium Molecular Layer Deposition Films as Precursors for Conducting TiO₂/Carbon Composite Films. *J. Phys. Chem. C* **2013**, *117*, 17442–17450.
- (57) Chen, C.; Li, P.; Wang, G.; Yu, Y.; Duan, F.; Chen, C.; Song, W.; Qin, Y.; Knez, M. Nanoporous Nitrogen-Doped Titanium Dioxide with Excellent Photocatalytic Activity under Visible Light Irradiation Produced by Molecular Layer Deposition. *Angew. Chemie Int. Ed.* **2013**, *52*, 9196–9200.
- (58) Ishchuk, S.; Taffa, D. H.; Hazut, O.; Kaynan, N.; Yerushalmi, R. Transformation of Organic–Inorganic Hybrid Films Obtained by Molecular Layer Deposition to Photocatalytic Layers with Enhanced Activity. *ACS Nano* **2012**, *6*, 7263–7269.
- (59) Trucks, G. W.; Raghavachari, K.; Higashi, G. S.; Chabal, Y. J. Mechanism of HF Etching of Silicon Surfaces: A Theoretical Understanding of Hydrogen Passivation. *Phys. Rev. Lett.* **1990**, *65*, 504–507.
- (60) Kang, J. K.; Musgrave, C. B. The Mechanism of HF/H₂O Chemical Etching of SiO₂. *J. Chem. Phys.* **2002**, *116*, 275.

- (61) Hoshino, T.; Nishioka, Y. Etching Process of SiO₂ by HF Molecules. *J. Chem. Phys.* **1999**, *111*, 2109.
- (62) Ritala, M. Atomic Layer Deposition of Oxide Thin Films with Metal Alkoxides as Oxygen Sources. *Science (80-.)*. **2000**, *288*, 319–321.
- (63) Liu, J.; Lennard, W. N.; Goncharova, L. V.; Landheer, D.; Wu, X.; Rushworth, S. A.; Jones, A. C. Atomic Layer Deposition of Hafnium Silicate Thin Films Using Tetrakis(diethylamido)hafnium and Tris(2-Methyl-2-Butoxy)silanol. *J. Electrochem. Soc.* **2009**, *156*, G89.
- (64) Frank, M. M.; Chabal, Y. J.; Green, M. L.; Delabie, A.; Brijs, B.; Wilk, G. D.; Ho, M.-Y.; da Rosa, E. B. O.; Baumvol, I. J. R.; Stedile, F. C. Enhanced Initial Growth of Atomic-Layer-Deposited Metal Oxides on Hydrogen-Terminated Silicon. *Appl. Phys. Lett.* **2003**, *83*, 740.
- (65) Chaukulkar, R. P.; Agarwal, S. Atomic Layer Deposition of Titanium Dioxide Using Titanium Tetrachloride and Titanium Tetraisopropoxide as Precursors. *J. Vac. Sci. Technol. A* **2013**, *31*, 31509.
- (66) Park, K. J.; Terry, D. B.; Stewart, S. M.; Parsons, G. N. In Situ Auger Electron Spectroscopy Study of Atomic Layer Deposition: Growth Initiation and Interface Formation Reactions during Ruthenium ALD on Si–H, SiO₂, and HfO₂ Surfaces. *Langmuir* **2007**, *23*, 6106–6112.
- (67) Holmes, P. J.; Snell, J. E. A Vapour Etching Technique for the Photolithography of Silicon Dioxide. *Microelectron. Reliab.* **1966**, *5*, 337–341.
- (68) McIntosh, R.; Kuan, T.-S.; Defresart, E. Hydrogen Fluoride Vapor Etching for Pre-Epi Silicon Surface Preparation. *J. Electron. Mater.* **1992**, *21*, 57–60.
- (69) Helms, C. R. Mechanisms of the HF/H₂O Vapor Phase Etching of SiO₂. *J. Vac. Sci. Technol. A Vacuum, Surfaces, Film.* **1992**, *10*, 806.
- (70) Miki, N.; Kikuyama, H.; Kawanabe, I.; Miyashita, M.; Ohmi, T. Gas-Phase Selective Etching of Native Oxide. *IEEE Trans. Electron Devices* **1990**, *37*, 107–115.
- (71) Droes, S. R.; Kodas, T. T.; Hampden-Smith, M. J. Etching of ZnO Films with Hexafluoroacetylacetone. *Adv. Mater.* **1998**, *10*, 1129–1133.
- (72) Steger, R.; Masel, R. Chemical Vapor Etching of Copper Using Oxygen and 1,1,1,5,5,5-Hexafluoro-2,4-Pentanedione. *Thin Solid Films* **1999**, *342*, 221–229.
- (73) Jain, A.; Kodas, T. T.; Hampden-Smith, M. J. Thermal Dry-Etching of Copper Using Hydrogen Peroxide and Hexafluoroacetylacetone. *Thin Solid Films* **1995**, *269*, 51–56.
- (74) Fonash, S. J. An Overview of Dry Etching Damage and Contamination Effects. *J. Electrochem. Soc.* **1990**, *137*, 3885.
- (75) Kanarik, K. J.; Lill, T.; Hudson, E. A.; Sriraman, S.; Tan, S.; Marks, J.; Vahedi, V.; Gottscho, R. A. Overview of Atomic Layer Etching in the Semiconductor Industry. *J.*

Vac. Sci. Technol. A Vacuum, Surfaces, Film. **2015**, *33*, 20802.

- (76) Schindler, P.; Logar, M.; Provine, J.; Prinz, F. B. Enhanced Step Coverage of TiO₂ Deposited on High Aspect Ratio Surfaces by Plasma-Enhanced Atomic Layer Deposition. *Langmuir* **2015**, *31*, 5057–5062.
- (77) T. Carver, C.; J. Plombon, J.; E. Romero, P.; Suri, S.; A. Tronic, T.; B. Turkot, R. Atomic Layer Etching: An Industry Perspective. *ECS J. Solid State Sci. Technol.* **2015**, *4*, N5005–N5009.
- (78) Faraz, T.; Roozeboom, F.; Knoops, H. C. M.; Kessels, W. M. M. Atomic Layer Etching: What Can We Learn from Atomic Layer Deposition? *ECS J. Solid State Sci. Technol.* **2015**, *4*, N5023–N5032.
- (79) Oehrlein, G. S.; Metzler, D.; Li, C. Atomic Layer Etching at the Tipping Point: An Overview. *ECS J. Solid State Sci. Technol.* **2015**, *4*, N5041–N5053.
- (80) Lee, Y.; Huffman, C.; George, S. M. Selectivity in Thermal Atomic Layer Etching Using Sequential, Self-Limiting Fluorination and Ligand-Exchange Reactions. *Chem. Mater.* **2016**, acs.chemmater.6b02543.
- (81) Lee, Y.; George, S. M. Atomic Layer Etching of Al₂O₃ Using Sequential, Self-Limiting Thermal Reactions with Sn(acac)₂ and Hydrogen Fluoride. *ACS Nano* **2015**, *9*, 2061–2070.
- (82) Lee, Y.; DuMont, J. W.; George, S. M. Mechanism of Thermal Al₂O₃ Atomic Layer Etching Using Sequential Reactions with Sn(acac)₂ and HF. *Chem. Mater.* **2015**, *27*, 3648–3657.
- (83) Lee, Y.; DuMont, J. W.; George, S. M. Trimethylaluminum as the Metal Precursor for the Atomic Layer Etching of Al₂O₃ Using Sequential, Self-Limiting Thermal Reactions. *Chem. Mater.* **2016**, *28*, 2994–3003.
- (84) Lee, Y.; DuMont, J. W.; George, S. M. Atomic Layer Etching of HfO₂ Using Sequential, Self-Limiting Thermal Reactions with Sn(acac)₂ and HF. *ECS J. Solid State Sci. Technol.* **2015**, *4*, N5013–N5022.
- (85) Zacher, D.; Shekhah, O.; Wöll, C.; Fischer, R. A. Thin Films of Metal–organic Frameworks. *Chem. Soc. Rev.* **2009**, *38*, 1418–1429.
- (86) Li, H.; Eddaoudi, M.; O’Keeffe, M.; Yaghi, O. Design and Synthesis of an Exceptionally Stable and Highly Porous Metal–Organic Framework. *Nature* **1999**, *402*, 276–279.
- (87) Schlichte, K.; Kratzke, T.; Kaskel, S. Improved Synthesis, Thermal Stability and Catalytic Properties of the Metal–Organic Framework Compound Cu₃(BTC)₂. *Microporous Mesoporous Mater.* **2004**, *73*, 81–88.
- (88) Shekhah, O.; Liu, J.; Fischer, R. A.; Woell, C. MOF Thin Films: Existing and Future Applications. *Chem. Soc. Rev.* **2011**, *40*, 1081–1106.

- (89) Wang, Z.; Cohen, S. M. Postsynthetic Modification of Metal-Organic Frameworks. *Chem. Soc. Rev.* **2009**, *38*, 1315–1329.
- (90) Britt, D.; Tranchemontagne, D.; Yaghi, O. M. Metal-Organic Frameworks with High Capacity and Selectivity for Harmful Gases. *Proc. Natl. Acad. Sci. U. S. A.* **2008**, *105*, 11623–11627.
- (91) Cavka, J. H.; Jakobsen, S.; Olsbye, U.; Guillou, N.; Lamberti, C.; Bordiga, S.; Lillerud, K. P. A New Zirconium Inorganic Building Brick Forming Metal Organic Frameworks with Exceptional Stability. *J. Am. Chem. Soc.* **2008**, *130*, 13850–13851.
- (92) Mondloch, J. E.; Bury, W.; Fairen-Jimenez, D.; Kwon, S.; DeMarco, E. J.; Weston, M. H.; Sarjeant, A. A.; Nguyen, S. T.; Stair, P. C.; Snurr, R. Q.; *et al.* Vapor-Phase Metalation by Atomic Layer Deposition in a Metal-Organic Framework. *J. Am. Chem. Soc.* **2013**, *135*, 10294–10297.
- (93) Moon, S.-Y.; Liu, Y.; Hupp, J. T.; Farha, O. K. Instantaneous Hydrolysis of Nerve-Agent Simulants with a Six-Connected Zirconium-Based Metal-Organic Framework. *Angew. Chemie Int. Ed.* **2015**, *54*, 6795–6799.
- (94) Kandiah, M.; Nilsen, M. H.; Usseglio, S.; Jakobsen, S.; Olsbye, U.; Tilset, M.; Larabi, C.; Quadrelli, E. A.; Bonino, F.; Lillerud, K. P. Synthesis and Stability of Tagged UiO-66 Zr-MOFs. *Chem. Mater.* **2010**, *22*, 6632–6640.
- (95) Zhao, J.; Lee, D. T.; Yaga, R. W.; Hall, M. G.; Barton, H. F.; Woodward, I. R.; Oldham, C. J.; Walls, H. J.; Peterson, G. W.; Parsons, G. N. Ultra-Fast Degradation of Chemical Warfare Agents Using MOF-Nanofiber Kebabs. *Angew. Chemie Int. Ed.* **2016**, *55*, 13224–13228.
- (96) Long, J.; Wang, S.; Ding, Z.; Wang, S.; Zhou, Y.; Huang, L.; Wang, X.; Yamashita, H.; Ariyuki, M.; Yoshizawa, K.; *et al.* Amine-Functionalized Zirconium Metal-organic Framework as Efficient Visible-Light Photocatalyst for Aerobic Organic Transformations. *Chem. Commun.* **2012**, *48*, 11656.
- (97) Luu, C. L.; Nguyen, T. T. Van; Nguyen, T.; Hoang, T. C. Synthesis, Characterization and Adsorption Ability of UiO-66-NH₂. *Adv. Nat. Sci. Nanosci. Nanotechnol.* **2015**, *6*, 25004.
- (98) Valenzano, L.; Civalleri, B.; Chavan, S.; Bordiga, S.; Nilsen, M. H.; Jakobsen, S.; Lillerud, K. P.; Lamberti, C. Disclosing the Complex Structure of UiO-66 Metal Organic Framework: A Synergic Combination of Experiment and Theory. *Chem. Mater.* **2011**, *23*, 1700–1718.
- (99) Platero-Prats, A. E.; Mavrandonakis, A.; Gallington, L. C.; Liu, Y.; Hupp, J. T.; Farha, O. K.; Cramer, C. J.; Chapman, K. W. Structural Transitions of the Metal-Oxide Nodes within Metal-Organic Frameworks: On the Local Structures of NU-1000 and UiO-66. *J. Am. Chem. Soc.* **2016**.
- (100) Wu, H.; Chua, Y. S.; Krungleviciute, V.; Tyagi, M.; Chen, P.; Yildirim, T.; Zhou, W.

Unusual and Highly Tunable Missing-Linker Defects in Zirconium Metal-Organic Framework UiO-66 and Their Important Effects on Gas Adsorption. *J. Am. Chem. Soc.* **2013**, *135*, 10525–10532.

- (101) Yang, D.; Bernales, V.; Islamoglu, T.; Farha, O. K.; Hupp, J. T.; Cramer, C. J.; Gagliardi, L.; Gates, B. C. Tuning the Surface Chemistry of Metal Organic Framework Nodes: Proton Topology of the Metal-Oxide-Like Zr₆ Nodes of UiO-66 and NU-1000. *J. Am. Chem. Soc.* **2016**, *138*, 15189–15196.
- (102) Gascon, J.; Aguado, S.; Kapteijn, F. Manufacture of Dense Coatings of Cu-3(BTC)(2) (HKUST-1) on Alpha-Alumina. *Microporous Mesoporous Mater.* **2008**, *113*, 132–138.
- (103) HKUST-1 Metal Organic Framework <http://www.chemtube3d.com/solidstate/MOF-HKUST-1.html> (accessed Mar 7, 2017).
- (104) Guerrero, V. V.; Yoo, Y.; McCarthy, M. C.; Jeong, H.-K. HKUST-1 Membranes on Porous Supports Using Secondary Growth. *J. Mater. Chem.* **2010**, *20*, 3938–3943.
- (105) Alaerts, L.; Séguin, E.; Poelman, H.; Thibault-Starzyk, F.; Jacobs, P. A.; De Vos, D. E. Probing the Lewis Acidity and Catalytic Activity of the Metal–Organic Framework [Cu₃(btc)₂] (BTC=Benzene-1,3,5-Tricarboxylate). *Chem. – A Eur. J.* **2006**, *12*, 7353–7363.
- (106) Panella, B.; Hirscher, M.; Pütter, H.; Müller, U. Hydrogen Adsorption in Metal–Organic Frameworks: Cu-MOFs and Zn-MOFs Compared. *Adv. Funct. Mater.* **2006**, *16*, 520–524.
- (107) Müller, A. J.; Balsamo, V.; Arnal, M. L. Nucleation and Crystallization in Diblock and Triblock Copolymers. In; Abetz, V., Ed.; *Advances in Polymer Science*; Springer Berlin Heidelberg, 2005; pp. 1–63.
- (108) Hermes, S.; Zacher, D.; Baunemann, A.; Wöll, C.; Fischer, R. A. Selective Growth and MOCVD Loading of Small Single Crystals of MOF-5 at Alumina and Silica Surfaces Modified with Organic Self-Assembled Monolayers†. *Chem. Mater.* **2007**, *19*, 2168–2173.
- (109) Kosmulski, M. The pH-Dependent Surface Charging and the Points of Zero Charge. *J. Colloid Interface Sci.* **2002**, *253*, 77–87.
- (110) Beverskog, B.; Puigdomenech, I. Revised Pourbaix Diagrams for Zinc at 25–300 °C. *Corros. Sci.* **1997**, *39*, 107–114.
- (111) Cook, W. G.; Olive, R. P. Pourbaix Diagrams for Chromium, Aluminum and Titanium Extended to High-Subcritical and Low-Supercritical Conditions. *Corros. Sci.* **2012**, *58*, 291–298.
- (112) Abdulagatov, A. I.; Yan, Y.; Cooper, J. R.; Zhang, Y.; Gibbs, Z. M.; Cavanagh, A. S.; Yang, R. G.; Lee, Y. C.; George, S. M. Al₂O₃ and TiO₂ Atomic Layer Deposition on Copper for Water Corrosion Resistance. *ACS Appl. Mater. Interfaces* **2011**, *3*, 4593–

4601.

- (113) Abbasi, A. R.; Akhbari, K.; Morsali, A. Dense Coating of Surface Mounted CuBTC Metal–Organic Framework Nanostructures on Silk Fibers, Prepared by Layer-by-Layer Method under Ultrasound Irradiation with Antibacterial Activity. *Ultrason. Sonochem.* **2012**, *19*, 846–852.
- (114) Pinto, M. da S.; Sierra-Avila, C. A.; Hinestroza, J. P. In Situ Synthesis of a Cu-BTC Metal–organic Framework (MOF 199) onto Cellulosic Fibrous Substrates: Cotton. *Cellulose* **2012**, *19*, 1771–1779.
- (115) Shekhah, O.; Wang, H.; Zacher, D.; Fischer, R. A.; Wöll, C. Growth Mechanism of Metal–Organic Frameworks: Insights into the Nucleation by Employing a Step-by-Step Route. *Angew. Chemie Int. Ed.* **2009**, *48*, 5038–5041.
- (116) Shekhah, O.; Wang, H.; Kowarik, S.; Schreiber, F.; Paulus, M.; Tolan, M.; Sternemann, C.; Evers, F.; Zacher, D.; Fischer, R. A.; *et al.* Step-by-Step Route for the Synthesis of Metal–Organic Frameworks. *J. Am. Chem. Soc.* **2007**, *129*, 15118–15119.
- (117) Stavila, V.; Volponi, J.; Katzenmeyer, A. M.; Dixon, M. C.; Allendorf, M. D. Kinetics and Mechanism of Metal–organic Framework Thin Film Growth: Systematic Investigation of HKUST-1 Deposition on QCM Electrodes. *Chem. Sci.* **2012**, *3*, 1531–1540.
- (118) Wittmann, T.; Siegel, R.; Reimer, N.; Milius, W.; Stock, N.; Senker, J. Enhancing the Water Stability of Al-MIL-101-NH₂ via Postsynthetic Modification. *Chemistry* **2015**, *21*, 314–323.
- (119) Nguyen, J. G.; Cohen, S. M. Moisture-Resistant and Superhydrophobic Metal–Organic Frameworks Obtained via Postsynthetic Modification. *J. Am. Chem. Soc.* **2010**, *132*, 4560–4561.
- (120) Aguilera-Sigalat, J.; Bradshaw, D. A Colloidal Water-Stable MOF as a Broad-Range Fluorescent pH Sensor via Post-Synthetic Modification. *Chem. Commun. (Camb)*. **2014**, *50*, 4711–4713.
- (121) Li, B.; Zhang, Y.; Ma, D.; Li, L.; Li, G.; Li, G.; Shi, Z.; Feng, S. A Strategy toward Constructing a Bifunctionalized MOF Catalyst: Post-Synthetic Modification of MOFs on Organic Ligands and Coordinatively Unsaturated Metal Sites. *Chem. Commun. (Camb)*. **2012**, *48*, 6151–6153.
- (122) Tanabe, K. K.; Cohen, S. M. Postsynthetic Modification of Metal–Organic Frameworks--a Progress Report. *Chem. Soc. Rev.* **2011**, *40*, 498–519.
- (123) Lalonde, M. B.; Mondloch, J. E.; Deria, P.; Sarjeant, A. A.; Al-Juaid, S. S.; Osman, O. I.; Farha, O. K.; Hupp, J. T. Selective Solvent-Assisted Linker Exchange (SALE) in a Series of Zeolitic Imidazolate Frameworks. **2015**.
- (124) Karagiari, O.; Bury, W.; Mondloch, J. E.; Hupp, J. T.; Farha, O. K. Solvent-Assisted

- Linker Exchange: An Alternative to the De Novo Synthesis of Unattainable Metal-Organic Frameworks. *Angew. Chemie Int. Ed.* **2014**, *53*, 4530–4540.
- (125) Deria, P.; Bury, W.; Hupp, J. T.; Farha, O. K. Versatile Functionalization of the NU-1000 Platform by Solvent-Assisted Ligand Incorporation. *Chem. Commun.* **2014**, *50*, 1965.
- (126) Deria, P.; Mondloch, J. E.; Tylianakis, E.; Ghosh, P.; Bury, W.; Snurr, R. Q.; Hupp, J. T.; Farha, O. K. Perfluoroalkane Functionalization of NU-1000 via Solvent-Assisted Ligand Incorporation: Synthesis and CO₂ Adsorption Studies. **2013**.
- (127) Kim, M.; Cahill, J. F.; Fei, H.; Prather, K. A.; Cohen, S. M. Postsynthetic Ligand and Cation Exchange in Robust Metal-Organic Frameworks. *J. Am. Chem. Soc.* **2012**, *134*, 18082–18088.
- (128) Klet, R. C.; Wang, T. C.; Fernandez, L. E.; Truhlar, D. G.; Hupp, J. T.; Farha, O. K. Synthetic Access to Atomically Dispersed Metals in Metal–Organic Frameworks via a Combined Atomic-Layer-Deposition-in-MOF and Metal-Exchange Approach. **2016**.
- (129) Schröder, F.; Esken, D.; Cokoja, M.; van den Berg, M. W. E.; Lebedev, O. I.; Van Tendeloo, G.; Walaszek, B.; Buntkowsky, G.; Limbach, H.-H.; Chaudret, B.; *et al.* Ruthenium Nanoparticles inside Porous [Zn₄O(bdc)₃] by Hydrogenolysis of Adsorbed [Ru(cod)(cot)]: A Solid-State Reference System for Surfactant-Stabilized Ruthenium Colloids. *J. Am. Chem. Soc.* **2008**, *130*, 6119–6130.
- (130) Chavan, S.; Vitillo, J. G.; Uddin, M. J.; Bonino, F.; Lamberti, C.; Groppo, E.; Lillerud, K.-P.; Bordiga, S. Functionalization of UiO-66 Metal–Organic Framework and Highly Cross-Linked Polystyrene with Cr(CO)₃: In Situ Formation, Stability, and Photoreactivity. *Chem. Mater.* **2010**, *22*, 4602–4611.
- (131) Decoste, J. B.; Peterson, G. W.; Smith, M. W.; Stone, C. A.; Willis, C. R. Enhanced Stability of Cu-BTC MOF via Perfluorohexane Plasma-Enhanced Chemical Vapor Deposition. *J. Am. Chem. Soc.* **2012**, *134*, 1486–1489.
- (132) Kim, I. S.; Borycz, J.; Platero-Prats, A. E.; Tussupbayev, S.; Wang, T. C.; Farha, O. K.; Hupp, J. T.; Gagliardi, L.; Chapman, K. W.; Cramer, C. J.; *et al.* Targeted Single-Site MOF Node Modification: Trivalent Metal Loading via Atomic Layer Deposition. *Chem. Mater.* **2015**, *27*, 4772–4778.
- (133) Peters, A. W.; Li, Z.; Farha, O. K.; Hupp, J. T. Atomically Precise Growth of Catalytically Active Cobalt Sulfide on Flat Surfaces and within a Metal-Organic Framework via Atomic Layer Deposition. *ACS Nano* **2015**, *9*, 8484–8490.
- (134) Jeong, M.-G.; Kim, D. H.; Lee, S.-K.; Lee, J. H.; Han, S. W.; Park, E. J.; Cychosz, K. A.; Thommes, M.; Hwang, Y. K.; Chang, J.-S.; *et al.* Decoration of the Internal Structure of Mesoporous Chromium Terephthalate MIL-101 with NiO Using Atomic Layer Deposition. *Microporous Mesoporous Mater.* **2015**.
- (135) Xiong, G.; Elam, J. W.; Feng, H.; Han, C. Y.; Wang, H.-H.; Iton, L. E.; Curtiss, L. A.;

- Pellin, M. J.; Kung, M.; Kung, H.; *et al.* Effect of Atomic Layer Deposition Coatings on the Surface Structure of Anodic Aluminum Oxide Membranes. *J. Phys. Chem. B* **2005**, *109*, 14059–14063.
- (136) Li, Z.; Schweitzer, N. M.; League, A. B.; Bernales, V.; Peters, A. W.; Getsoian, A. “Bean”; Wang, T. C.; Miller, J. T.; Vjunov, A.; Fulton, J. L.; *et al.* Sintering-Resistant Single-Site Nickel Catalyst Supported by Metal–Organic Framework. **2016**.
- (137) Ohring, M. *Materials Science of Thin Films*; 2nd ed.; Academic Press: San Diego, 2002.
- (138) Elam, J. W.; Groner, M. D.; George, S. M. Viscous Flow Reactor with Quartz Crystal Microbalance for Thin Film Growth by Atomic Layer Deposition. *Rev. Sci. Instrum.* **2002**, *73*, 2981–2987.
- (139) Nakamoto, K. *Infrared and Raman Spectra of Inorganic and Coordination Compounds*; 4th ed.; John Wiley & Sons, Inc: New York, 1986.
- (140) Pereira, D. C.; Faria, D. L. A. de; Constantino, V. R. L. CuII Hydroxy Salts: Characterization of Layered Compounds by Vibrational Spectroscopy. *J. Braz. Chem. Soc.* **2006**, *17*, 1651–1657.
- (141) Lemaire, P. C.; Zhao, J.; Williams, P. S.; Walls, H. J.; Shepherd, S. D.; Losego, M. D.; Peterson, G. W.; Parsons, G. N. Copper Benzenetricarboxylate Metal-Organic Framework Nucleation Mechanisms on Metal Oxide Powders and Thin Films Formed by Atomic Layer Deposition. *ACS Appl. Mater. Interfaces* **2016**, *8*, 9514–9522.
- (142) Kim, D. H.; Losego, M. D.; Hanson, K.; Alibabaei, L.; Lee, K.; Meyer, T. J.; Parsons, G. N.; O’Regan, B.; Grätzel, M.; Yella, A.; *et al.* Stabilizing Chromophore Binding on TiO₂ for Long-Term Stability of Dye-Sensitized Solar Cells Using Multicomponent Atomic Layer Deposition. *Phys. Chem. Chem. Phys.* **2014**, *16*, 8615–8622.
- (143) Dandley, E. C.; Needham, C. D.; Williams, P. S.; Brozena, A. H.; Oldham, C. J.; Parsons, G. N.; Lee, S.-M.; Pippel, E.; Gosele, U.; Dresbach, C.; *et al.* Temperature-Dependent Reaction between Trimethylaluminum and Poly(methyl Methacrylate) during Sequential Vapor Infiltration: Experimental and Ab Initio Analysis. *J. Mater. Chem. C* **2014**, *2*, 9416–9424.
- (144) Tikhonravov, A. V.; Trubetskov, M. K.; Masetti, E.; Krasilnikova, A. V.; Kochikov, I. V. <title>Sensitivity of the Ellipsometric Angles Psi and Delta to the Surface Inhomogeneity</title> In; Amra, C.; Macleod, H. A., Eds.; International Society for Optics and Photonics, 1999; pp. 173–182.
- (145) Chui, S. S. A Chemically Functionalizable Nanoporous Material [Cu₃(TMA)₂(H₂O)₃]_n. *Science* (80-.). **1999**, *283*, 1148–1150.
- (146) DeCoste, J. B.; Peterson, G. W. Metal-Organic Frameworks for Air Purification of Toxic Chemicals. *Chem. Rev.* **2014**, *114*, 5695–5727.
- (147) Prince, J. A.; Bhuvana, S.; Anbharasi, V.; Ayyanar, N.; Boodhoo, K. V. K.; Singh, G.

- Self-Cleaning Metal Organic Framework (MOF) Based Ultra Filtration Membranes--a Solution to Bio-Fouling in Membrane Separation Processes. *Sci. Rep.* **2014**, *4*, 6555.
- (148) Lee, J.; Farha, O. K.; Roberts, J.; Scheidt, K. A.; Nguyen, S. T.; Hupp, J. T. Metal-Organic Framework Materials as Catalysts. *Chem. Soc. Rev.* **2009**, *38*, 1450–1459.
- (149) Corma, A.; García, H.; Llabrés i Xamena, F. X. Engineering Metal Organic Frameworks for Heterogeneous Catalysis. *Chem. Rev.* **2010**, *110*, 4606–4655.
- (150) Farrusseng, D.; Aguado, S.; Pinel, C. Metal-Organic Frameworks: Opportunities for Catalysis. *Angew. Chem. Int. Ed. Engl.* **2009**, *48*, 7502–7513.
- (151) Morris, R. E.; Wheatley, P. S. Gas Storage in Nanoporous Materials. *Angew. Chem. Int. Ed. Engl.* **2008**, *47*, 4966–4981.
- (152) Ma, S.; Zhou, H.-C. Gas Storage in Porous Metal-Organic Frameworks for Clean Energy Applications. *Chem. Commun. (Camb)*. **2010**, *46*, 44–53.
- (153) Kreno, L. E.; Leong, K.; Farha, O. K.; Allendorf, M.; Van Duyne, R. P.; Hupp, J. T. Metal-Organic Framework Materials as Chemical Sensors. *Chem. Rev.* **2012**, *112*, 1105–1125.
- (154) Lu, G.; Hupp, J. T. Metal–Organic Frameworks as Sensors: A ZIF-8 Based Fabry–Pérot Device as a Selective Sensor for Chemical Vapors and Gases. *J. Am. Chem. Soc.* **2010**, *132*, 7832–7833.
- (155) Küsgens, P.; Siegle, S.; Kaskel, S. Crystal Growth of the Metal—Organic Framework Cu₃(BTC)₂ on the Surface of Pulp Fibers. *Adv. Eng. Mater.* **2009**, *11*, 93–95.
- (156) Meilikhov, M.; Yusenko, K.; Schollmeyer, E.; Mayer, C.; Buschmann, H.-J.; Fischer, R. A. Stepwise Deposition of Metal Organic Frameworks on Flexible Synthetic Polymer Surfaces. *Dalt. Trans.* **2011**, *40*, 4838–4841.
- (157) López-Maya, E.; Montoro, C.; Rodríguez-Albelo, L. M.; Aznar Cervantes, S. D.; Lozano-Pérez, A. A.; Cenís, J. L.; Barea, E.; Navarro, J. A. R. Textile/Metal-Organic-Framework Composites as Self-Detoxifying Filters for Chemical-Warfare Agents. *Angew. Chemie Int. Ed.* **2015**, n/a-n/a.
- (158) Arslan, H. K.; Shekhah, O.; Wohlgemuth, J.; Franzreb, M.; Fischer, R. A.; Wöll, C. High-Throughput Fabrication of Uniform and Homogenous MOF Coatings. *Adv. Funct. Mater.* **2011**, *21*, 4228–4231.
- (159) Seo, Y.-K.; Hundal, G.; Jang, I. T.; Hwang, Y. K.; Jun, C.-H.; Chang, J.-S. Microwave Synthesis of Hybrid Inorganic–organic Materials Including Porous Cu₃(BTC)₂ from Cu(II)-Trimesate Mixture. *Microporous Mesoporous Mater.* **2009**, *119*, 331–337.
- (160) Centrone, A.; Yang, Y.; Speakman, S.; Bromberg, L.; Rutledge, G. C.; Hatton, T. A. Growth of Metal-Organic Frameworks on Polymer Surfaces. *J. Am. Chem. Soc.* **2010**, *132*, 15687–15691.
- (161) Khaletskaya, K.; Turner, S.; Tu, M.; Wannapaiboon, S.; Schneemann, A.; Meyer, R.;

- Ludwig, A.; Van Tendeloo, G.; Fischer, R. A. Self-Directed Localization of ZIF-8 Thin Film Formation by Conversion of ZnO Nanolayers. *Adv. Funct. Mater.* **2014**, *24*, 4804–4811.
- (162) Bechelany, M.; Drobek, M.; Vallicari, C.; Abou Chaaya, A.; Julbe, A.; MIELE, P. Highly Crystalline MOF-Based Materials Grown on Electrospun Nanofibers. *Nanoscale* **2015**, *7*, 5794–5802.
- (163) Salmi, L. D.; Heikkilä, M. J.; Puukilainen, E.; Sajavaara, T.; Grosso, D.; Ritala, M. Studies on Atomic Layer Deposition of MOF-5 Thin Films. *Microporous Mesoporous Mater.* **2013**, *182*, 147–154.
- (164) Stassen, I.; Styles, M.; Greci, G.; Gorp, H. Van; Vanderlinden, W.; Feyter, S. De; Falcaro, P.; Vos, D. De; Vereecken, P.; Ameloot, R. Chemical Vapour Deposition of Zeolitic Imidazolate Framework Thin Films. *Nat. Mater.* **2015**, *15*, 304–310.
- (165) Ahvenniemi, E.; Karppinen, M. Atomic/molecular Layer Deposition: A Direct Gas-Phase Route to Crystalline Metal-Organic Framework Thin Films. *Chem. Commun. (Camb)*. **2016**, *52*, 1139–1142.
- (166) Zhao, J.; Losego, M. D.; Lemaire, P. C.; Williams, P. S.; Gong, B.; Atanasov, S. E.; Blevins, T. M.; Oldham, C. J.; Walls, H. J.; Shepherd, S. D.; *et al.* Highly Adsorptive, MOF-Functionalized Nonwoven Fiber Mats for Hazardous Gas Capture Enabled by Atomic Layer Deposition. *Adv. Mater. Interfaces* **2014**, *1*, n/a-n/a.
- (167) Zhao, J.; Gong, B.; Nunn, W. T.; Lemaire, P. C.; Stevens, E. C.; Sidi, F. I.; Williams, P. S.; Oldham, C. J.; Walls, H. J.; Shepherd, S. D.; *et al.* Conformal and Highly Adsorptive Metal–organic Framework Thin Films via Layer-by-Layer Growth on ALD-Coated Fiber Mats. *J. Mater. Chem. A* **2015**, *3*, 1458–1464.
- (168) Bunge, M. A.; Ruckart, K. N.; Leavesley, S.; Peterson, G. W.; Nguyen, N.; West, K. N.; Glover, T. G. Modification of Fibers with Nanostructures Using Reactive Dye Chemistry. *Ind. Eng. Chem. Res.* **2015**, *54*, 3821–3827.
- (169) Mao, Y.; Shi, L.; Huang, H.; Yu, Q.; Ye, Z.; Peng, X. Mesoporous Separation Membranes of {[Cu(BTC–H₂)₂·(H₂O)₂]·3H₂O} Nanobelts Synthesized by Ultrasonication at Room Temperature. *CrystEngComm* **2012**, *15*, 265–270.
- (170) Ma, Y.-H.; Ma, P.-Z.; Yao, T.; Hao, J.-T. Catena-Poly[[tri-Aqua-copper(II)]-?-5-Carb-Oxy-Benzene-1,3-Di-Carboxyl-Ato-?2 O 1:O 3]. *Acta Crystallogr. Sect. E Struct. Reports Online* **2013**, *69*, m538.
- (171) Zhuang, J.-L.; Ceglarek, D.; Pethuraj, S.; Terfort, A. Rapid Room-Temperature Synthesis of Metal–Organic Framework HKUST-1 Crystals in Bulk and as Oriented and Patterned Thin Films. *Adv. Funct. Mater.* **2011**, *21*, 1442–1447.
- (172) Haouas, M.; Volkringer, C.; Loiseau, T.; Férey, G.; Taulelle, F. In Situ NMR, Ex Situ XRD and SEM Study of the Hydrothermal Crystallization of Nanoporous Aluminum Trimesates MIL-96, MIL-100, and MIL-110. *Chem. Mater.* **2012**, *24*, 2462–2471.

- (173) Loiseau, T.; Lecroq, L.; Volkringer, C.; Marrot, J.; Férey, G.; Haouas, M.; Taulelle, F.; Bourrelly, S.; Llewellyn, P. L.; Latroche, M. MIL-96, a Porous Aluminum Trimesate 3D Structure Constructed from a Hexagonal Network of 18-Membered Rings and μ_3 -Oxo-Centered Trinuclear Units. *J. Am. Chem. Soc.* **2006**, *128*, 10223–10230.
- (174) Xu, L.; Choi, E.-Y.; Kwon, Y.-U. Ionothermal Syntheses of Six Three-Dimensional Zinc Metal–Organic Frameworks with 1-Alkyl-3-Methylimidazolium Bromide Ionic Liquids as Solvents. *Inorg. Chem.* **2007**, *46*, 10670–10680.
- (175) Yaghi, O. M.; Davis, C. E.; Li, G.; Li, H. Selective Guest Binding by Tailored Channels in a 3-D Porous Zinc(II)–Benzenetricarboxylate Network. *J. Am. Chem. Soc.* **1997**, *119*, 2861–2868.
- (176) Biswick, T.; Jones, W.; Pacuła, A.; Serwicka, E. Synthesis, Characterisation and Anion Exchange Properties of Copper, Magnesium, Zinc and Nickel Hydroxy Nitrates. *J. Solid State Chem.* **2006**, *179*, 49–55.
- (177) Aguirre, J. M.; Gutiérrez, A.; Giraldo, O. Simple Route for the Synthesis of Copper Hydroxy Salts. *J. Braz. Chem. Soc.* **2011**, *22*, 546–551.
- (178) Liu, B. One-Dimensional Copper Hydroxide Nitrate Nanorods and Nanobelts for Radiochemical Applications. *Nanoscale* **2012**, *4*, 7194–7198.
- (179) Newman, S. P.; Jones, W. Comparative Study of Some Layered Hydroxide Salts Containing Exchangeable Interlayer Anions. *J. Solid State Chem.* **1999**, *148*, 26–40.
- (180) Nikolic, R.; Zec, S.; Maksimovic, V.; Mentus, S. Physico-Chemical Characterization of Thermal Decomposition Course in Zinc Nitrate-Copper Nitrate Hexahydrates. *J. Therm. Anal. Calorim.* **2006**, *86*, 423–428.
- (181) Niu, H.; Yang, Q.; Tang, K. A New Route to Copper Nitrate Hydroxide Microcrystals. *Mater. Sci. Eng. B* **2006**, *135*, 172–175.
- (182) Chen, J.; Yu, T.; Chen, Z.; Xiao, H.; Zhou, G.; Weng, L.; Tu, B.; Zhao, D. Synthesis and Structure of a New 3D Porous Cu(II)–Benzene-1,3,5-Tricarboxylate Coordination Polymer, $[\text{Cu}_2(\text{OH})(\text{BTC})(\text{H}_2\text{O})]_n \cdot 2n\text{H}_2\text{O}$. *Chem. Lett.* **2003**, *32*, 590–591.
- (183) Schlesinger, M.; Schulze, S.; Hietschold, M.; Mehring, M. Evaluation of Synthetic Methods for Microporous Metal–organic Frameworks Exemplified by the Competitive Formation of $[\text{Cu}_2(\text{btc})_3(\text{H}_2\text{O})_3]$ and $[\text{Cu}_2(\text{btc})(\text{OH})(\text{H}_2\text{O})]$. *Microporous Mesoporous Mater.* **2010**, *132*, 121–127.
- (184) Loera-Serna, S.; Oliver-Tolentino, M. A.; de Lourdes López-Núñez, M.; Santana-Cruz, A.; Guzmán-Vargas, A.; Cabrera-Sierra, R.; Beltrán, H. I.; Flores, J. Electrochemical Behavior of $[\text{Cu}_3(\text{BTC})_2]$ Metal–organic Framework: The Effect of the Method of Synthesis. *J. Alloys Compd.* **2012**, *540*, 113–120.
- (185) Mao, Y.; Cao, W.; Li, J.; Sun, L.; Peng, X. HKUST-1 Membranes Anchored on Porous Substrate by Hetero MIL-110 Nanorod Array Seeds. *Chemistry* **2013**, *19*,

11883–11886.

- (186) Rajamathi, J. T.; Britto, S.; Rajamathi, M. Synthesis and Anion Exchange Reactions of a Layered Copper-Zinc Hydroxy Double Salt, $\text{Cu}_{1.6}\text{Zn}_{0.4}(\text{OH})_3(\text{OAc})\cdot\text{H}_2\text{O}$. *J. Chem. Sci.* **2005**, *117*, 629–633.
- (187) Meyn, M.; Beneke, K.; Lagaly, G. Anion-Exchange Reactions of Hydroxy Double Salts. *Inorg. Chem.* **1993**, *32*, 1209–1215.
- (188) Zhao, J.; Nunn, W. T.; Lemaire, P. C.; Lin, Y.; Dickey, M. D.; Oldham, C. J.; Walls, H. J.; Peterson, G. W.; Losego, M. D.; Parsons, G. N. Facile Conversion of Hydroxy Double Salts to Metal-Organic Frameworks Using Metal Oxide Particles and Atomic Layer Deposition Thin-Film Templates. *J. Am. Chem. Soc.* **2015**, *137*, 13756–13759.
- (189) Park, S.-H.; Kim, H. J. Unidirectionally Aligned Copper Hydroxide Crystalline Nanorods from Two-Dimensional Copper Hydroxy Nitrate. *J. Am. Chem. Soc.* **2004**, *126*, 14368–14369.
- (190) Thomas, N. Mechanochemical Synthesis of Layered Hydroxy Salts. *Mater. Res. Bull.* **2012**, *47*, 3568–3572.
- (191) Huang, K.; Wang, J.; Wu, D.; Lin, S. Copper Hydroxyl Sulfate as a Heterogeneous Catalyst for the Catalytic Wet Peroxide Oxidation of Phenol. *RSC Adv.* **2015**, *5*, 8455–8462.
- (192) Alvarez-Puebla, R. Copper Heterogeneous Nucleation on a Palygorskitic Clay: An XRD, EXAFS and Molecular Modeling Study. *Appl. Clay Sci.* **2004**, *25*, 103–110.
- (193) YAMANAKA, S. Anion Exchange Reactions in Layered Basic Copper Salts. *Solid State Ionics* **1992**, *53–56*, 527–533.
- (194) Grant Glover, T.; Peterson, G. W.; Schindler, B. J.; Britt, D.; Yaghi, O. MOF-74 Building Unit Has a Direct Impact on Toxic Gas Adsorption. *Chem. Eng. Sci.* **2011**, *66*, 163–170.
- (195) Caskey, S. R.; Wong-Foy, A. G.; Matzger, A. J. Dramatic Tuning of Carbon Dioxide Uptake via Metal Substitution in a Coordination Polymer with Cylindrical Pores. *J. Am. Chem. Soc.* **2008**, *130*, 10870–10871.
- (196) Katz, M. J.; Brown, Z. J.; Colón, Y. J.; Siu, P. W.; Scheidt, K. A.; Snurr, R. Q.; Hupp, J. T.; Farha, O. K. A Facile Synthesis of UiO-66, UiO-67 and Their Derivatives. *Chem. Commun. (Camb)*. **2013**, *49*, 9449–9451.
- (197) Gallington, L. C.; Kim, I. S.; Liu, W.-G.; Yakovenko, A. A.; Platero-Prats, A. E.; Li, Z.; Wang, T. C.; Hupp, J. T.; Farha, O. K.; Truhlar, D. G.; *et al.* Regioselective Atomic Layer Deposition in Metal–Organic Frameworks Directed by Dispersion Interactions. *J. Am. Chem. Soc.* **2016**, *138*, 13513–13516.
- (198) Li, Z.; Peters, A. W.; Bernales, V.; Ortuño, M. A.; Schweitzer, N. M.; DeStefano, M. R.; Gallington, L. C.; Platero-Prats, A. E.; Chapman, K. W.; Cramer, C. J.; *et al.* Metal–Organic Framework Supported Cobalt Catalysts for the Oxidative

- Dehydrogenation of Propane at Low Temperature. *ACS Cent. Sci.* **2016**, acscentsci.6b00290.
- (199) Tan, K.; Zuluaga, S.; Fuentes, E.; Mattson, E. C.; Veyan, J.-F.; Wang, H.; Li, J.; Thonhauser, T.; Chabal, Y. J.; Ferey, G.; *et al.* Trapping Gases in Metal-Organic Frameworks with a Selective Surface Molecular Barrier Layer. *Nat. Commun.* **2016**, *7*, 13871.
- (200) Abid, H. R.; Shang, J.; Ang, H.-M.; Wang, S. Amino-Functionalized Zr-MOF Nanoparticles for Adsorption of CO₂ and CH₄. *Int. J. Smart Nano Mater.* **2013**, *4*, 72–82.
- (201) Shen, L.; Liang, S.; Wu, W.; Liang, R.; Wu, L.; Gordon, T. R.; Cargnello, M.; Paik, T.; Mangolini, F.; Weber, R. T.; *et al.* Multifunctional NH₂-Mediated Zirconium Metal-Organic Framework as an Efficient Visible-Light-Driven Photocatalyst for Selective Oxidation of Alcohols and Reduction of Aqueous Cr(VI). *Dalton Trans.* **2013**, *42*, 13649–13657.
- (202) Garibay, S. J.; Cohen, S. M.; Yaghi, O. M.; O’Keeffe, M.; Ockwig, N. W.; Chae, H. K.; Eddaoudi, M.; Kim, J.; Kitagawa, S.; Kitaura, R.; *et al.* Isoreticular Synthesis and Modification of Frameworks with the UiO-66 Topology. *Chem. Commun.* **2010**, *46*, 7700.
- (203) Karabacak, M.; Cinar, M.; Unal, Z.; Kurt, M. FT-IR, UV Spectroscopic and DFT Quantum Chemical Study on the Molecular Conformation, Vibrational and Electronic Transitions of 2-Aminoterephthalic Acid. *J. Mol. Struct.* **2010**, *982*, 22–27.
- (204) Kandiah, M.; Usseglio, S.; Svelle, S.; Olsbye, U.; Lillerud, K. P.; Tilset, M.; Hoskins, B. F.; Robson, R.; Seo, J. S.; Whang, D.; *et al.* Post-Synthetic Modification of the Metal–organic Framework Compound UiO-66. *J. Mater. Chem.* **2010**, *20*, 9848.
- (205) Fernández López, E.; Sánchez Escribano, V.; Panizza, M.; Carnasciali, M. M.; Busca, G.; Hamon, D.; Vrinat, M.; Breyse, M.; Durand, B.; Beauchesne, F.; *et al.* Vibrational and Electronic Spectroscopic Properties of Zirconia Powders. *J. Mater. Chem.* **2001**, *11*, 1891–1897.
- (206) Tan, K.; Zuluaga, S.; Gong, Q.; Canepa, P.; Wang, H.; Li, J.; Chabal, Y. J.; Thonhauser, T. Water Reaction Mechanism in Metal Organic Frameworks with Coordinatively Unsaturated Metal Ions: MOF-74. *Chem. Mater.* **2014**, *26*, 6886–6895.
- (207) Zhong-Tao, J.; Liesegang, J.; James, B. D.; Skelton, B. W.; White, A. H. Atomic Charges and Structures of Some Hydrogen Bonded Substituted Anilinium Chloride Systems: Correlation with XPS. *J. Phys. Chem. Solids* **1996**, *57*, 397–404.
- (208) Clark, R. J. H.; Bradley, D. C.; Thornton, P. *The Chemistry of Titanium, Zirconium and Hafnium*; Pergamon Press: Oxford, 1975.
- (209) Kurtz, S. R.; Gordon, R. G. Chemical Vapor Deposition of Titanium Nitride at Low Temperatures. *Thin Solid Films* **1986**, *140*, 277–290.

- (210) HOJO, J.; KATO, A. Direct Observation of the Formation Process of TiN Particles by CVD Method. *J. Ceram. Assoc. Japan* **1981**, *89*, 277–279.
- (211) Allendorf, M. D.; Janssen, C. L.; Colvin, M. E.; Melius, C. F.; Nielsen, I. M. B.; Osterheld, T. H.; Ho, P. Thermochemistry of Gas-Phase Species Relevant to Titanium Nitride CVD, 1995.
- (212) Almenningen, A.; Halvorsen, S.; Haaland, A.; Pihlaja, K.; Schaumburg, K.; Ehrenberg, L. A Gas Phase Electron Diffraction Investigation of the Molecular Structures of Trimethylaluminium Monomer and Dimer. *Acta Chem. Scand.* **1971**, *25*, 1937–1945.
- (213) Jóvári, P.; Mészáros, G.; Pusztai, L.; Sváb, E. The Structure of Liquid Tetrachlorides CCl_4 , SiCl_4 , GeCl_4 , TiCl_4 , VCl_4 , and SnCl_4 . *J. Chem. Phys.* **2001**, *114*, 8082.
- (214) Huang, Y.; Qin, W.; Li, Z.; Li, Y.; D'Alessandro, D. M.; Smit, B.; Long, J. R.; Hunt, A. J.; Sin, E. H. K.; Marriott, R.; *et al.* Enhanced Stability and CO_2 Affinity of a UiO-66 Type Metal–organic Framework Decorated with Dimethyl Groups. *Dalt. Trans.* **2012**, *41*, 9283.
- (215) Van de Voorde, B.; Stassen, I.; Bueken, B.; Vermoortele, F.; De Vos, D.; Ameloot, R.; Tan, J.-C. C.; Bennett, T. D.; Furukawa, H.; Cordova, K. E.; *et al.* Improving the Mechanical Stability of Zirconium-Based Metal–organic Frameworks by Incorporation of Acidic Modulators. *J. Mater. Chem. A* **2015**, *3*, 1737–1742.
- (216) Puurunen, R. L. Correlation between the Growth-per-Cycle and the Surface Hydroxyl Group Concentration in the Atomic Layer Deposition of Aluminum Oxide from Trimethylaluminum and Water. *Appl. Surf. Sci.* **2005**, *245*, 6–10.
- (217) Hanson, K.; Losego, M. D.; Kalanyan, B.; Ashford, D. L.; Parsons, G. N.; Meyer, T. J. Stabilization of $[\text{Ru}(\text{bpy})_2(4,4'-(\text{PO}_3\text{H}_2)\text{Bpy})]^{2+}$ on Mesoporous TiO_2 with Atomic Layer Deposition of Al_2O_3 . *Chem. Mater.* **2013**, *25*, 3–5.
- (218) Hanson, K.; Losego, M. D.; Kalanyan, B.; Parsons, G. N.; Meyer, T. J. Stabilizing Small Molecules on Metal Oxide Surfaces Using Atomic Layer Deposition. *Nano Lett.* **2013**, *13*, 4802–4809.
- (219) Son, H.-J.; Prasittichai, C.; Mondloch, J. E.; Luo, L.; Wu, J.; Kim, D. W.; Farha, O. K.; Hupp, J. T. Dye Stabilization and Enhanced Photoelectrode Wettability in Water-Based Dye-Sensitized Solar Cells through Post-Assembly Atomic Layer Deposition of TiO_2 . *J. Am. Chem. Soc.* **2013**, *135*, 11529–11532.
- (220) Ghazaryan, L.; Kley, E.-B.; Tünnermann, A.; Szeghalmi, A. V. Stability and Annealing of Alucones and Alucone Alloys. *J. Vac. Sci. Technol. A* **2012**, *31*, 01A149.
- (221) Liang, X.; Yu, M.; Li, J.; Jiang, Y.-B.; Weimer, A. W. Ultra-Thin Microporous-Mesoporous Metal Oxide Films Prepared by Molecular Layer Deposition (MLD). *Chem. Commun. (Camb)*. **2009**, 7140–7142.

- (222) Zhao, Y.; Nakamura, R.; Kamiya, K.; Nakanishi, S.; Hashimoto, K. Nitrogen-Doped Carbon Nanomaterials as Non-Metal Electrocatalysts for Water Oxidation. *Nat. Commun.* **2013**, *4*, 2390.
- (223) Stevens, J. S.; Byard, S. J.; Muryn, C. A.; Schroeder, S. L. M. Identification of Protonation State by XPS, Solid-State NMR, and DFT: Characterization of the Nature of a New Theophylline Complex by Experimental and Computational Methods. *J. Phys. Chem. B* **2010**, *114*, 13961–13969.
- (224) Yang, Z.; Xu, M.; Liu, Y.; He, F.; Gao, F.; Su, Y.; Wei, H.; Zhang, Y. Nitrogen-Doped, Carbon-Rich, Highly Photoluminescent Carbon Dots from Ammonium Citrate. *Nanoscale* **2014**, *6*, 1890–1895.
- (225) Lee, K.; Jur, J. S.; Kim, D. H.; Parsons, G. N. Mechanisms for Hydrophilic/hydrophobic Wetting Transitions on Cellulose Cotton Fibers Coated Using Al₂O₃ Atomic Layer Deposition. *J. Vac. Sci. Technol. a* **2012**, *30*, 01A163–01A163.
- (226) Blundell, R. K.; Licence, P. Quaternary Ammonium and Phosphonium Based Ionic Liquids: A Comparison of Common Anions. *Phys. Chem. Chem. Phys.* **2014**, *16*, 15278–15288.
- (227) Bahlawane, N.; Arl, D.; Thomann, J.-S.; Adjeroud, N.; Menguelti, K.; Lenoble, D. Molecular Layer Deposition of Amine-Containing Alucone Thin Films. *Surf. Coatings Technol.* **2013**, *230*, 101–105.
- (228) Galvin, C. J.; Dimitriou, M. D.; Satija, S. K.; Genzer, J. Swelling of Polyelectrolyte and Polyzwitterion Brushes by Humid Vapors. *J. Am. Chem. Soc.* **2014**, *136*, 12737–12745.
- (229) Biesalski, M.; Ruhe, J. Swelling of a Polyelectrolyte Brush in Humid Air. *Langmuir* **2000**, *16*, 1943–1950.
- (230) Shi, M.; Feng, Y.-S. Titanium(IV) Chloride and Quaternary Ammonium Salt Promoted Baylis–Hillman Reaction. *J. Org. Chem.* **2001**, *66*, 406–411.
- (231) Islam, M. S.; Yusoff, R.; Ali, B. S.; Islam, M. N.; Chakrabarti, M. H. Degradation Studies of Amines and Alkanolamines during Sour Gas Treatment Process. *International Journal of Physical Sciences*, 2011.
- (232) Colomban, P.; Tomkinson, J. Novel Forms of Hydrogen in Solids: The ‘ionic’ Proton and the ‘quasi-Free’ Proton. *Solid State Ionics* **1997**, *97*, 123–134.
- (233) Nicolas-Debarnot, D.; Poncin-Epaillard, F. Polyaniline as a New Sensitive Layer for Gas Sensors. *Anal. Chim. Acta* **2003**, *475*, 1–15.
- (234) Kostas, T. T.; Hampden-Smith, M. J. *The Chemistry of Metal CVD*; John Wiley & Sons, 2008.
- (235) Yamamoto, Y.; Matsuura, T.; Murota, J. H-Termination Effects on Initial Growth Characteristics of W on Si Using WF₆ and SiH₄ Gases. *Le J. Phys. IV* **1999**, *9*, Pr8-

431-Pr8-436.

- (236) Kobayashi, N.; Nakamura, Y.; Goto, H.; Homma, Y. In Situ Infrared Reflection and Transmission Absorption Spectroscopy Study of Surface Reactions in Selective Chemical-Vapor Deposition of Tungsten Using WF₆ and SiH₄. *J. Appl. Phys.* **1993**, *73*, 4637.
- (237) Saito, Y. Effects of Plasma Excitation and Chemical Pretreatment on Adsorption of Tungsten Hexafluoride on Silicon and Silicon Dioxide Studied by X-Ray Photoelectron Spectroscopy. *J. Electrochem. Soc.* **1996**, *143*, 3670.
- (238) Bozack, M. J. Reaction of Tungsten Hexafluoride with Si and TiN Surfaces. *Thin Solid Films* **1992**, *221*, 55–60.
- (239) Kobayashi, N.; Goto, H.; Suzuki, M. Study on Mechanism of Selective Chemical Vapor Deposition of Tungsten Using in Situ Infrared Spectroscopy and Auger Electron Spectroscopy. *J. Appl. Phys.* **1991**, *69*, 1013.
- (240) Creighton, J. R. The Surface Chemistry and Kinetics of Tungsten Chemical Vapor Deposition and Selectivity Loss. *Thin Solid Films* **1994**, *241*, 310–317.
- (241) Creighton, J. R. A Mechanism for Selectivity Loss during Tungsten CVD. *J. Electrochem. Soc.* **1989**, *136*, 271.
- (242) Bell, D. A. Desorption of Tungsten Fluorides from Tungsten. *J. Electrochem. Soc.* **1995**, *142*, 2401.
- (243) Cheek, R. W. In Situ Monitoring of the Products from the SiH₄ + WF₆ Tungsten Chemical Vapor Deposition Process by Micro-Volume Mass Spectrometry. *J. Electrochem. Soc.* **1993**, *140*, 3588.
- (244) Powell, C. J.; Jablonski, A. NIST Standard Reference Database 82, 2011.
- (245) Fuentes, G. G.; Elizalde, E.; Yubero, F.; Sanz, J. M. Electron Inelastic Mean Free Path for Ti, TiC, TiN and TiO₂ as Determined by Quantitative Reflection Electron Energy-Loss Spectroscopy. *Surf. Interface Anal.* **2002**, *33*, 230–237.
- (246) Kalanyan, B.; Oldham, C. J.; Sweet, W. J.; Parsons, G. N. Highly Conductive and Flexible Nylon-6 Nonwoven Fiber Mats Formed Using Tungsten Atomic Layer Deposition. *ACS Appl. Mater. Interfaces* **2013**, *5*, 5253–5259.
- (247) Morrow, B. A.; McFarlan, A. J. Chemical Reactions at Silica Surfaces. *J. Non. Cryst. Solids* **1990**, *120*, 61–71.
- (248) Lei, W.; Henn-Lecordier, L.; Anderle, M.; Rubloff, G. W.; Barozzi, M.; Bersani, M. Real-Time Observation and Optimization of Tungsten Atomic Layer Deposition Process Cycle. *J. Vac. Sci. Technol. B Microelectron. Nanom. Struct.* **2006**, *24*, 780.
- (249) Hoyas, A. M.; Whelan, C. M.; Schuhmacher, J.; Celis, J. P.; Maex, K. Effect of Surface Reactive Site Density and Reactivity on the Growth of Atomic Layer Deposited WN_xC_Y Films. *Electrochem. Solid-State Lett.* **2006**, *9*, F64.

- (250) Groenen, P. A. C.; Tekcan, Ö. F.; Hölscher, J. G. A.; Brongersma, H. H. Loss of Selectivity during W Chemical Vapor Deposition on Si Using the WF₆/SiH₄ Process. *J. Vac. Sci. Technol. A Vacuum, Surfaces, Film.* **1994**, *12*, 737.
- (251) Sneh, O.; George, S. M. Thermal Stability of Hydroxyl Groups on a Well-Defined Silica Surface. *J. Phys. Chem.* **1995**, *99*, 4639–4647.
- (252) O'Donnell, T. A.; Stewart, D. F. Reactivity of Transition Metal Fluorides. I. Higher Fluorides of Chromium, Molybdenum, and Tungsten. *Inorg. Chem.* **1966**, *5*, 1434–1437.
- (253) Broadbent, E. K. Nucleation and Growth of Chemically Vapor Deposited Tungsten on Various Substrate Materials: A Review. *J. Vac. Sci. Technol. B Microelectron. Nanom. Struct.* **1987**, *5*, 1661.
- (254) Ramanath, G.; Greene, J. E.; Carlsson, J. R. A.; Allen, L. H.; Hornback, V. C.; Allman, D. J. W Deposition and Titanium Fluoride Formation during WF₆ Reduction by Ti: Reaction Path and Mechanisms. *J. Appl. Phys.* **1999**, *85*, 1961.
- (255) Lee, Y. J.; Park, C.-O.; Kim, D.-W.; Chun, J. S. The Effects of Deposition Temperature on the Interfacial Properties of SiH₄ Reduced Blanket Tungsten on TiN Glue Layer. *J. Electron. Mater.* **1994**, *23*, 1075–1080.
- (256) Lee, Y.; DuMont, J. W.; George, S. M. Atomic Layer Etching of AlF₃ Using Sequential, Self-Limiting Thermal Reactions with Sn(acac)₂ and Hydrogen Fluoride. *J. Phys. Chem. C* **2015**, *119*, 25385–25393.
- (257) Lee, Y.; Sun, H.; Young, M. J.; George, S. M. Atomic Layer Deposition of Metal Fluorides Using HF-Pyridine as the Fluorine Precursor. *Chem. Mater.* **2016**, *28*, acs.chemmater.5b04360.
- (258) Lee, Y.; DuMont, J. W.; Cavanagh, A. S.; George, S. M. Atomic Layer Deposition of AlF₃ Using Trimethylaluminum and Hydrogen Fluoride. *J. Phys. Chem. C* **2015**, *119*, 150610114452004.
- (259) Louvain, N.; Karkar, Z.; El-Ghozzi, M.; Bonnet, P.; Guérin, K.; Willmann, P. Fluorination of Anatase TiO₂ towards Titanium Oxyfluoride TiOF₂: A Novel Synthesis Approach and Proof of the Li-Insertion Mechanism. *J. Mater. Chem. A* **2014**, *2*, 15308.
- (260) Baxter, D. V.; Chisolm, M. H.; Doherty, S.; Gruhn, N. E. Chemical Vapour Deposition of Electrochromic Tungsten Oxide Films Employing Volatile tungsten(VI) Oxo Alkoxide/?-Diketonate Complexes. *Chem. Commun.* **1996**, 1129.
- (261) Tägtström, P. Atomic Layer Epitaxy of Tungsten Oxide Films Using Oxyfluorides as Metal Precursors. *J. Electrochem. Soc.* **1999**, *146*, 3139.
- (262) Knapas, K.; Rahtu, A.; Ritala, M. Etching of Nb₂O₅ Thin Films by NbCl₅. *Chem. Vap. Depos.* **2009**, NA-NA.
- (263) Herner, S. B. Homogeneous Tungsten Chemical Vapor Deposition on Silane

- Pretreated Titanium Nitride. *Electrochem. Solid-State Lett.* **1999**, 2, 398.
- (264) Lantz, S. L. W Nucleation on TiN from WF₆ and SiH₄. *J. Vac. Sci. Technol. A Vacuum, Surfaces, Film.* **1994**, 12, 1032.
- (265) Zhuravlev, L. T. The Surface Chemistry of Amorphous Silica. Zhuravlev Model. *Colloids Surfaces A Physicochem. Eng. Asp.* **2000**, 173, 1–38.
- (266) Kim, D.; Wentorf, R. H.; Gill, W. N. Selective Deposition of Copper by Chemical Vapor Deposition Using Cu(HFA)₂. *J. Vac. Sci. Technol. A Vacuum, Surfaces, Film.* **1994**, 12, 153–157.
- (267) Kim, S.; Park, J.-M.; Choi, D.-J. The Carrier Gas and Surface Passivation Effects on Selectivity in Chemical Vapor Deposition of Copper Films. *Thin Solid Films* **1998**, 320, 95–102.
- (268) Kim, S.; Park, J.-M.; Choi, D.-J. Carrier Gas Effects on the Selectivity in Chemical Vapor Deposition of Copper. *Thin Solid Films* **1998**, 315, 229–237.
- (269) Chiou, J.-C.; Juang, K.; Chen, M. The Processing Windows for Selective Copper Chemical Vapor Deposition from Cu(hexafluoroacetylacetonate)trimethylvinylsilane. *J. Electrochem. Soc.* **1995**, 142, 177.
- (270) Kuse, R.; Kundu, M.; Yasuda, T.; Miyata, N.; Toriumi, A. Effect of Precursor Concentration in Atomic Layer Deposition of Al₂O₃. *J. Appl. Phys.* **2003**, 94, 6411.
- (271) Choi, H.-S.; Rhee, S. Effect of Carrier Gases on the Chemical Vapor Deposition of Tungsten from WF₆-SiH₄. *J. Electrochem. Soc.* **1994**, 141, 475.
- (272) Pan, D.; Li, T.; Chien Jen, T.; Yuan, C. Numerical Modeling of Carrier Gas Flow in Atomic Layer Deposition Vacuum Reactor: A Comparative Study of Lattice Boltzmann Models. *J. Vac. Sci. Technol. A Vacuum, Surfaces, Film.* **2014**, 32, 01A110.
- (273) Kajikawa, Y.; Tsumura, T.; Noda, S.; Komiyama, H.; Shimogaki, Y.; Ireland, P. J.; Lorenz, E. B. and J.; K. Hayakawa, M. K. Y. C. and M. M.; S.-H. Whang, J. K. K. J. W. P. D.-H. K. D.-L. C. and W.-J. L.; N. Kobayashi, H. G. and M. S.; *et al.* Nucleation of W during Chemical Vapor Deposition from WF₆ and SiH₄. *Jpn. J. Appl. Phys.* **2004**, 43, 3945–3950.
- (274) Aarik, J.; Aidla, A.; Kasikov, A.; Mändar, H.; Rammula, R.; Sammelselg, V. Influence of Carrier Gas Pressure and Flow Rate on Atomic Layer Deposition of HfO₂ and ZrO₂ Thin Films. *Appl. Surf. Sci.* **2006**, 252, 5723–5734.
- (275) Min, K. S.; Kang, S. H.; Kim, J. K.; Jhon, Y. I.; Jhon, M. S.; Yeom, G. Y. Atomic Layer Etching of Al₂O₃ Using BCl₃/Ar for the Interface Passivation Layer of III–V MOS Devices. *Microelectron. Eng.* **2013**, 110, 457–460.
- (276) Ikeda, K.; Imai, S.; Matsumura, M. Atomic Layer Etching of Germanium. *Appl. Surf. Sci.* **1997**, 112, 87–91.

- (277) Koutsospyros, A.; Braidia, W.; Dermatas, D.; Strigul, N. A Review of Tungsten: From Environmental Obscurity to Scrutiny. *J. Hazard. Mater.* **2006**, *136*, 1–19.
- (278) Vasilopoulou, M.; Kostis, I.; Vourdas, N.; Papadimitropoulos, G.; Douvas, A.; Boukos, N.; Kennou, S.; Davazoglou, D. Influence of the Oxygen Substoichiometry and of the Hydrogen Incorporation on the Electronic Band Structure of Amorphous Tungsten Oxide Films. *J. Phys. Chem. C* **2014**, *118*, 12632–12641.
- (279) Mouat, A. R.; Mane, A. U.; Elam, J. W.; Delferro, M.; Marks, T. J.; Stair, P. C. Volatile Hexavalent Oxo-Amidinate Complexes: Molybdenum and Tungsten Precursors for Atomic Layer Deposition. *Chem. Mater.* **2016**, *28*, 1907–1919.
- (280) Fracassi, F.; d’Agostino, R. Chemistry of Titanium Dry Etching in Fluorinated and Chlorinated Gases. *Pure Appl. Chem.* **1992**, *64*, 703–707.
- (281) Bestwick, T. D.; Oehrlein, G. S. Tungsten Etching Mechanisms in CF₄/O₂ Reactive Ion Etching Plasmas. *J. Appl. Phys.* **1989**, *66*, 5034.
- (282) Ortega, Y.; Lamiel-Garcia, O.; Hevia, D. F.; Tosoni, S.; Oviedo, J.; San-Miguel, M. A.; Illas, F. Theoretical Study of the Fluorine Doped Anatase Surfaces. *Surf. Sci.* **2013**, *618*, 154–158.
- (283) Tosoni, S.; Lamiel-Garcia, O.; Fernandez Hevia, D.; Illas, F. Theoretical Study of Atomic Fluorine Diffusion through Bulk TiO₂ Polymorphs. *J. Phys. Chem. C* **2013**, *117*, 5855–5860.
- (284) Mäntymäki, M.; Heikkilä, M. J.; Puukilainen, E.; Mizohata, K.; Marchand, B.; Räisänen, J.; Ritala, M.; Leskelä, M. Atomic Layer Deposition of AlF₃ Thin Films Using Halide Precursors. *Chem. Mater.* **2015**, *27*, 604–611.
- (285) Pilvi, T.; Puukilainen, E.; Munnik, F.; Leskelä, M.; Ritala, M. ALD of YF₃ Thin Films from TiF₄ and Y(thd)₃ Precursors. *Chem. Vap. Depos.* **2009**, *15*, 27–32.

APPENDICES

APPENDIX A. CO-AUTHORED PUBLICATIONS

A.1 *Highly Adsorptive, MOF-Functionalized Nonwoven Fiber Mats for Hazardous Gas Capture Enabled by Atomic Layer Deposition*

While metal-organic frameworks (MOFs) show great potential for gas adsorption and storage, their powder form limits deployment opportunities. Integration of MOFs on polymeric fibrous scaffolds will enable new applications in gas adsorption, membrane separation, catalysis, and toxic gas sensing. Here, we demonstrate a new synthesis route for growing MOFs on fibrous materials that achieves high MOF loadings, large surface areas and high adsorptive capacities. We find that a nanoscale coating of Al_2O_3 formed by atomic layer deposition (ALD) on the surface of nonwoven fiber mats facilitates nucleation of MOFs on the fibers throughout the mat. Functionality of MOFs is fully maintained after integration, and MOF crystals are well attached to the fibers. Breakthrough tests for HKUST-1 MOFs [$\text{Cu}_3(\text{BTC})_2$] on ALD-coated polypropylene fibers reveal NH_3 dynamic loadings up to 5.93 ± 0.20 mol/kg_(MOF+fiber). Most importantly, this synthetic approach is generally applicable to a wide range of polymer fibers (e.g., PP, PET, cotton) and MOFs (e.g., HKUST-1, MOF-74, and UiO-66).

*Junjie Zhao, Mark D. Losego, Paul C. Lemaire, Philip S. Williams, Bo Gong, Sarah E. Atanasov, Trent M. Blevins, Christopher J. Oldham, Howard J. Walls, Sarah D. Shepherd, Matthew A. Browe, Gregory W. Peterson, and Gregory N. Parsons

A.2 Conformal and Highly Adsorptive Metal–organic Framework Thin Films via Layer-by-Layer Growth on ALD-Coated Fiber Mats

Integration of metal–organic frameworks (MOFs) on textiles shows promise for enabling facile deployment and expanding MOF applications. While MOFs deposited on flat substrates can show relatively smooth surface texture, most previous reports of MOFs integrated on fibers show poor conformality with many individual crystal domains. Here we report a new low-temperature (<70 °C) method to deposit uniform and smooth MOF thin films on fiber surfaces using an energy enhanced layer-by-layer (LbL) method with an ALD Al₂O₃ nucleation layer. Cross-sectional TEM images show a well-defined core@shell structure of the MOF-functionalized fiber, and SEM shows a flat MOF surface texture. We analyze the thickness and mass increase data of LbL HKUST-1 MOF thin films on ALD-coated polypropylene fibers and find the growth rate to be 288–290 ng cm⁻² per LbL cycle. Unlike planar LbL MOF embodiments where adsorption capacities are difficult to quantify, the large volume quantity on a typical fiber mat enables accurate surface area measurement of these unique MOF morphologies. After 40 LbL cycles the MOFs on fibers exhibit N₂ adsorption BET surface areas of up to 93.6 m² g_{MOF+fiber}⁻¹ (~535 m²g_{MOF}⁻¹) and breakthrough test results reveal high dynamic loadings for NH₃ (1.37 mol_{NH₃}kg_{MOF+fiber}⁻¹) and H₂S (1.49 mol_{H₂S} kg_{MOF+fiber}⁻¹). This synthesis route is applicable to many polymer fibers, and the fiber@ALD@MOF structure is promising for gas filtration, membrane separation, catalysis, chemical sensing and other applications.

*Junjie Zhao, Bo Gong, William T. Nunn, Paul C. Lemaire, Eric C. Stevens, Fahim I. Sidi, Philip S. Williams, Christopher J. Oldham, Howard J. Walls, Sarah D. Shepherd, Matthew A. Browe, Gregory W. Peterson, Mark D. Losego and Gregory N. Parsons

A.3 Platinum-Free Cathode for Dye-Sensitized Solar Cells Using Poly(3,4-ethylenedioxythiophene) (PEDOT) Formed via Oxidative Molecular Layer Deposition

Thin ~20 nm conformal poly(3,4-ethylenedioxythiophene) (PEDOT) films are incorporated in highly conductive mesoporous indium tin oxide (m-ITO) by oxidative molecular layer deposition (oMLD). These three-dimensional catalytic/conductive networks are successfully employed as Pt-free cathodes for dye-sensitized solar cells (DSSCs) with open circuit voltage equivalent to Pt cathode devices. Thin and conformal PEDOT films on m-ITO by oMLD create high surface area and efficient electron transport paths to promote productive reduction reaction on the PEDOT film. Because of these two synergetic effects, PEDOT-coated m-ITO by oMLD shows power conversion efficiency, 7.18%, comparable to 7.26% of Pt, and higher than that of planar PEDOT coatings, which is 4.85%. Thus, PEDOT-coated m-ITO is an exceptional opportunity to compete with Pt catalysts for low-cost energy conversion devices.

*Do Han Kim, Sarah E. Atanasov, Paul Lemaire, Kyoungmi Lee, and Gregory N. Parsons

A.4 Wafer-Scale Selective-Area Deposition of Nanoscale Metal Oxide Features Using Vapor Saturation into Patterned Poly(methyl methacrylate) Templates

Patterned, chemically reactive poly(methyl)methacrylate can act as a chemical “sponge” via Lewis acid/base adduct formation with metal-organic reactants commonly used in atomic layer deposition. Extended reactant exposures saturate the reactant within the polymer, and subsequent oxidation removes the polymer and converts the saturated reactant to a metal oxide film that precisely mimics the lateral dimensions of the original polymer. Resulting oxide thickness scales with the starting polymer thickness. Regions without polymer are coated with less than 1 nm of metal oxide. Repeatable nanoscale features are formed simultaneously and uniformly across a 150 mm diameter silicon wafer.

*Erinn C. Dandley, Paul C. Lemaire, Zhongwei Zhu, Alex Yoon, Lubab Sheet, Gregory N. Parsons

A.5 Facile Conversion of Hydroxy Double Salts to Metal-Organic Frameworks Using Metal Oxide Particles and Atomic Layer Deposition Thin Film Templates

Rapid room-temperature synthesis of metal–organic frameworks (MOFs) is highly desired for industrial implementation and commercialization. Here we find that a (Zn,Cu) hydroxy double salt (HDS) intermediate formed in situ from ZnO particles or thin films enables rapid growth (<1 min) of HKUST-1 (Cu₃(BTC)₂) at room temperature. The space-time-yield reaches $>3 \times 10^4 \text{ kg} \cdot \text{m}^{-3} \cdot \text{d}^{-1}$, at least 1 order of magnitude greater than any prior report. The high anion exchange rate of (Zn,Cu) hydroxy nitrate HDS drives the ultrafast MOF formation. Similarly, we obtained Cu-BDC, ZIF-8, and IRMOF-3 structures from HDSs, demonstrating synthetic generality. Using ZnO thin films deposited via atomic layer deposition, MOF patterns are obtained on pre-patterned surfaces, and dense HKUST-1 coatings are grown onto various form factors, including polymer spheres, silicon wafers, and fibers. Breakthrough tests show that the MOF-functionalized fibers have high adsorption capacity for toxic gases. This rapid synthesis route is also promising for new MOF-based composite materials and applications.

*Junjie Zhao, William T. Nunn, Paul C. Lemaire, Yiliang Lin, Michael D. Dickey, Christopher J. Oldham, Howard J. Walls, Gregory W. Peterson, Mark D. Losego, and Gregory N. Parsons

A.6 Using Hydrogen to Expand the Inherent Substrate Selectivity Window During Tungsten Atomic Layer Deposition

Area-selective thin film deposition is expected to be important in achieving sub-10 nm semiconductor devices, enabling feature patterning, alignment to underlying structures, and edge definition. Atomic layer deposition (ALD) offers advantages over common chemical vapor deposition methods, such as precise thickness control and excellent conformality. Furthermore, several ALD processes show inherent propensity for substrate-dependent nucleation. For example, tungsten ALD using SiH_4 (or Si_2H_6) and WF_6 is more energetically favorable on Si than on SiO_2 , but selectivity is often lost after several ALD cycles. We show that modifying the W ALD process chemistry can decrease the W nucleation rate on SiO_2 , thereby expanding the ALD “selectivity window”. Specifically, we find that adding H_2 during the WF_6 dose step helps passivate SiO_2 against W nucleation without modifying W growth on silicon. Surface characterization confirms that H_2 promotes fluorine passivation of SiO_2 , likely through surface reactions with HF produced in the gas phase. This passivation affords at least 10 additional W ALD cycles, corresponding to ~ 6 nm of additional W growth, before substantial nucleation occurs on SiO_2 . We show that reactant modification also reduces undesirable nucleation due to substrate proximity or loading effects in patterned film growth. Further understanding of ALD reaction chemistry and film nucleation will lead to improved selective metal and dielectric film deposition, enabling ALD bottom-up patterning.

*Berç Kalanyan, Paul C. Lemaire, Sarah E. Atanasov, Mariah Ritz, and Gregory N. Parsons